

PRECISE DETERMINATION OF THE LUMINOSITY
WITH THE PANDA-LUMINOSITY DETECTOR
AND
IMPLEMENTATION OF THE HELICITY FORMALISM
FOR THE COMPWA FRAMEWORK
FOR AN EXTRACTION OF THE SCALAR WAVE
IN THE CHANNEL $J/\psi \rightarrow \pi^0 \pi^0 \gamma$

Dissertation
zur Erlangung des Grades eines
Doktors der Naturwissenschaften
in der Fakultät für Physik und Astronomie
der Ruhr-Universität Bochum

vorgelegt von
STEFAN PFLÜGER
aus Stuttgart

Bochum, Juli 2017

1. GUTACHTER: Prof. Dr. Miriam Fritsch
2. GUTACHTER: Prof. Dr. Ulrich Wiedner
DATUM DER DISPUTATION: 26. Oktober 2017

ABSTRACT

One of the main topics of interest in physics is the composition and structure of matter. Especially for hadrons, which are bound states of quarks and gluons such as the proton and neutron, the description is incomplete. Quantumchromodynamics (QCD), the theory of the strong interaction, is in accordance with most of the results from measurements. However QCD as well as derived effective theories or lattice-QCD calculations are unable to fully explain the rich hadron spectrum.

The isoscalar part of the hadron spectrum is particularly interesting, because states with a large gluon content are expected in this sector. In order to validate or invalidate theories, the precise measurement of the states is crucial. The mass and width of states can be measured by energy scans. With the method of partial wave analysis one is able to extract additional information such as the spin and parity of the states. In this respect, the BESIII experiment at IHEP in Beijing and the future PANDA experiment at FAIR in Darmstadt, will contribute with valuable information.

A key parameter for such experiments is the luminosity, which is needed for energy scans and the measurement of absolute cross sections. In this thesis the implementation of the versatile LuminosityFit software package is presented. It is responsible for the determination of the luminosity from the reconstructed tracks of the PANDA luminosity detector with high stability and an accuracy of below 0.5%. Essential for the small systematic uncertainty is the correction of influences from the accelerator beam and the target. In consequence a high accuracy for line shape measurements of resonances is ensured with the highly accurate luminosity determination.

Furthermore this thesis aims towards the extraction of the isoscalar mesons in the reaction $J/\psi \rightarrow \gamma\pi^0\pi^0$. The presence of many wide and interfering states makes a correct theoretical description difficult. To address this matter the implementation of the helicity formalism for the general partial wave analysis framework CompPWA is presented in this thesis. The goal of CompPWA is to establish the comparability of various theoretical models and formulations. The study of the isoscalar mesons can benefit from the direct comparison of different theories. This implementation of the helicity formalism takes the novel approach by using an expert system. An exhaustive validation of the implementation is performed on the basis of the $J/\psi \rightarrow \gamma\pi^0\pi^0$ reaction. With the availability of the helicity formalism in CompPWA, partial wave analysis can be performed with this first general model, that serves as a reference for comparisons with other implementations.

ZUSAMMENFASSUNG

Eine der zentralen Fragen der Physik ist die Zusammensetzung von Materie. Vor allem im Bereich der Hadronen, wozu die Protonen und Neutronen gehören, sind einige Phänomene bisher noch ungeklärt. Die Quantenchromodynamik (QCD), die theoretische Beschreibung der starken Wechselwirkung, ist in guter Übereinstimmung mit den meisten Messergebnissen. Allerdings sind weder die QCD selbst, noch effektive Theorien oder Berechnungen im Rahmen der Gitter-QCD in der Lage, alle bisher gefundenen Zustände zuzuordnen und deren interne Struktur aufzuklären.

Besonders interessant ist der isoskalare Sektor, da in diesem Zustände mit großem Gluonen-Anteil erwartet werden. Um theoretische Beschreibungen zu bestätigen oder auszuschließen, ist das präzise Vermessen der Zustände wesentlich. Energiescan-Messungen erlauben die genaue Bestimmung der Masse und Breite von Zuständen, während die Partialwellenanalyse die Extraktion von zusätzlichen Eigenschaften wie des Spins und der Parität ermöglicht. Hierzu liefern das BESIII-Experiment am IHEP in Peking und das künftige PANDA-Experiment an FAIR in Darmstadt wichtige Ergebnisse.

Eine grundlegende Messgröße für Experimente dieser Art ist die Luminosität, welche für Energiescan-Messungen oder der Bestimmung von absoluten Streuquerschnitten erforderlich ist. Im Rahmen dieser Arbeit wurde das umfangreiche LuminosityFit-Softwarepaket entwickelt, welches die Luminosität aus den rekonstruierten Spuren des PANDA-Luminositätsdetektors mit hoher Stabilität und einer geringen systematischen Unsicherheit von weniger als 0.5% bestimmt. Ausschlaggebend für das Erreichen dieser hohen Genauigkeit ist die Berücksichtigung der Abweichungen von einem idealen Strahl und Target. Damit ist von Seiten der Luminosität eine hohe Genauigkeit beim Vermessen der Linienform von Resonanzen sichergestellt.

Zudem befasst sich die Arbeit mit der Extraktion der isoskalaren Mesonen in der Reaktion $J/\psi \rightarrow \gamma\pi^0\pi^0$. Aufgrund der breiten und miteinander interferierenden Zustände ist deren korrekte Bestimmung eine komplizierte Aufgabenstellung. Hierzu wurde der Helizitätsformalismus für das allgemeine Partialwellenanalyse-Framework CompPWA implementiert. CompPWA hat zum Ziel, die Vergleichbarkeit von verschiedenen theoretischen Beschreibungen herzustellen. Dies ist für die Analyse der isoskalaren Mesonen von Vorteil, weil damit ein unmittelbarer Vergleich zwischen den unterschiedlichen Formalismen möglich wird. Mit der Verwendung eines Expertensystems bietet die Implementierung einen neuartigen Lösungsansatz. In Anlehnung an den Zerfall $J/\psi \rightarrow \gamma\pi^0\pi^0$ wird die Richtigkeit dieser Implementierung im Detail überprüft. Durch den Helizitätsformalismus in CompPWA steht das erste allgemeine Modell zur Verfügung, welches für weitere Implementierungen als Vergleichsmodell benutzt werden wird.

*We have seen that computer programming is an art,
because it applies accumulated knowledge to the world,
because it requires skill and ingenuity, and especially
because it produces objects of beauty.*

— Donald E. Knuth

ACKNOWLEDGMENTS

First of all I would like to thank Prof. Dr. Miriam Fritsch for giving me the opportunity of writing this thesis and her guidance and care over the years. I especially enjoyed the freedom which was given to me, allowing me to unfold my full potential.

For the successful accomplishment of my work, the computing cluster HIMSTER of the Helmholtz Institute Mainz was of great importance. In this respect I would like to thank Dr. Dalibor Djukanovic for his efforts in keeping the cluster running as smoothly as possible.

I am very grateful for the nice atmosphere among my co-workers, which served as a good foundation for the success of my work. I enjoyed the nice conversations during coffee and lunch breaks with my office colleagues Patric Kiese, Roman Klasen, Stephan Maldaner and Dr. Tobias Weber very much. Also coworkers from other workgroups contributed to this good spirit at the office, most notably Sebastian Bleser and Marcell Steinen from the hypernuclear group. A special thanks to Heinrich Leithoff, Dr. Mathias Michel, Dr. Christof Motzko, Dr. Andreas Pitka and Dr. Peter Weidenkaff for their interest, time and fruitful discussions.

Furthermore I am also thankful for meetings with Prof. Dr. Klaus Peters and Prof. Dr. Wolfgang Gradl and the valuable input.

I'm grateful to Dr. Malte Albrecht and Dr. Florian Feldbauer for helping me get acquainted with the graduation specifics at the Ruhr University Bochum.

Last but not least, I would like to thank my family, most importantly my wife 綺綺 and my parents Monika & Thomas for their constant backing and strengthening.

Thank you all!

CONTENTS

MOTIVATION	1
1 HADRON SPECTROSCOPY	7
1.1 Light Quark Sector	9
1.2 Charmonium	12
2 HADRON SPECTROSCOPY DETECTOR SYSTEMS	15
2.1 The BESIII Experiment	15
2.1.1 Physics Program	15
2.1.2 The BESIII Detector	16
2.2 The PANDA Experiment	19
2.2.1 The High-Energy Storage Ring (HESR)	20
2.2.2 Physics Program	23
2.2.3 The PANDA Detector	25
3 LUMINOSITY MEASUREMENT @ PANDA	31
3.1 Luminosity	31
3.2 Luminosity Measurements	33
3.3 The Elastic $\bar{p}p$ Scattering Model	33
3.4 The Luminosity Detector	36
3.4.1 The Vacuum Box and Transition Region	36
3.4.2 Detector Layout	38
3.4.3 DAQ System	39
3.5 Track Reconstruction	39
4 LUMINOSITY DETERMINATION - THE LUMINOSITY FIT FRAMEWORK	45
4.1 The Elastic Scattering Model	45
4.2 Coordinate Transformations	46
4.3 Divergence Smearing	47
4.4 Efficiency Correction	51
4.5 Detector Resolution Smearing	52
5 LUMINOSITY DETERMINATION RESULTS AND SYSTEMATIC STUDIES	55
5.1 Ideal Case Fit Results	55
5.2 Systematic Effects of the Beam and Target	59
5.2.1 IP Distribution	59
5.2.2 IP Displacements	64
5.2.3 Accelerator Beam Tilt	66
5.2.4 Accelerator Beam Divergence	68
5.3 Realistic Scenarios	72
5.4 Background Sources	76
5.5 Discussion & Outlook	78

6	HELICITY FORMALISM IN THE COMPWA FRAMEWORK	81
6.1	The Method of Partial Waves	81
6.2	Helicity Formalism	83
6.3	Helicity Formalism Implementation in CompPWA	86
6.3.1	Helicity Amplitude Module	87
6.3.2	Decay Tree Module and CompPWA Expert System	91
7	VALIDATION OF THE HELICITY FORMALISM IMPLEMENTATION	95
7.1	Test of the Expert System	95
7.2	Angular Distributions	96
7.3	First Validation with a Simple Model	100
7.4	Validation with Complex Model	107
7.5	Validation of the Complex Model using PAWIAN	111
7.6	A first Fit on the BESIII Data	114
7.7	Discussion & Outlook	120
	SUMMARY	121
A	APPENDIX - GENERAL	125
A.1	The Likelihood Estimators	125
A.1.1	Binominal, Poisson and Normal Distribution Relationship	125
A.1.2	Unbinned Loglikelihood	126
A.1.3	Extended Unbinned Loglikelihood	127
A.1.4	Extended Binned Loglikelihood	127
A.2	Introduction to Expert Systems	128
B	APPENDIX - LMD RELATED	131
B.1	Accelerator Beam Dynamics	131
B.2	From momentum transfer t to laboratory frame θ	132
B.3	Proton Recoil Energy	136
B.4	Convolution vs. Resolution Smearing Algorithm	137
C	APPENDIX - PWA RELATED	139
C.1	Dalitz Plot Kinematics	139
C.2	Single Channel $\gamma\pi^0\pi^0$ Kinematic Distributions	141
C.3	1D Kinematic Variable Comparisons	150
C.3.1	CompPWA $J/\psi \rightarrow \gamma\pi^0\pi^0$ benchmark model MC data and CompPWA best fit result	150
C.3.2	PAWIAN $J/\psi \rightarrow \gamma\pi^0\pi^0$ benchmark model MC data and CompPWA best fit result	151
C.4	Normalized residuals for CompPWA fits on $J/\psi \rightarrow \gamma\pi^0\pi^0$ MC data	152
C.4.1	Simple model data generated with CompPWA	152
C.4.2	Benchmark model data generated with CompPWA	153
C.4.3	Benchmark model data generated with PAWIAN	156
	BIBLIOGRAPHY	167

MOTIVATION

One of the fundamental questions that mankind is trying to find an answer to is “What is matter made of?”. Over centuries intense research efforts have shown that there is not a single answer to this question, but there exists a hierarchy of matter, ranging from very large composite objects such as planets or stars over molecules to atoms and finally to the fundamental building blocks of our universe. The latter is studied by the field of elementary particle physics with the Standard Model as our best understanding of the smallest scale of matter. It is summarized by figure 1. There are three particle categories: the

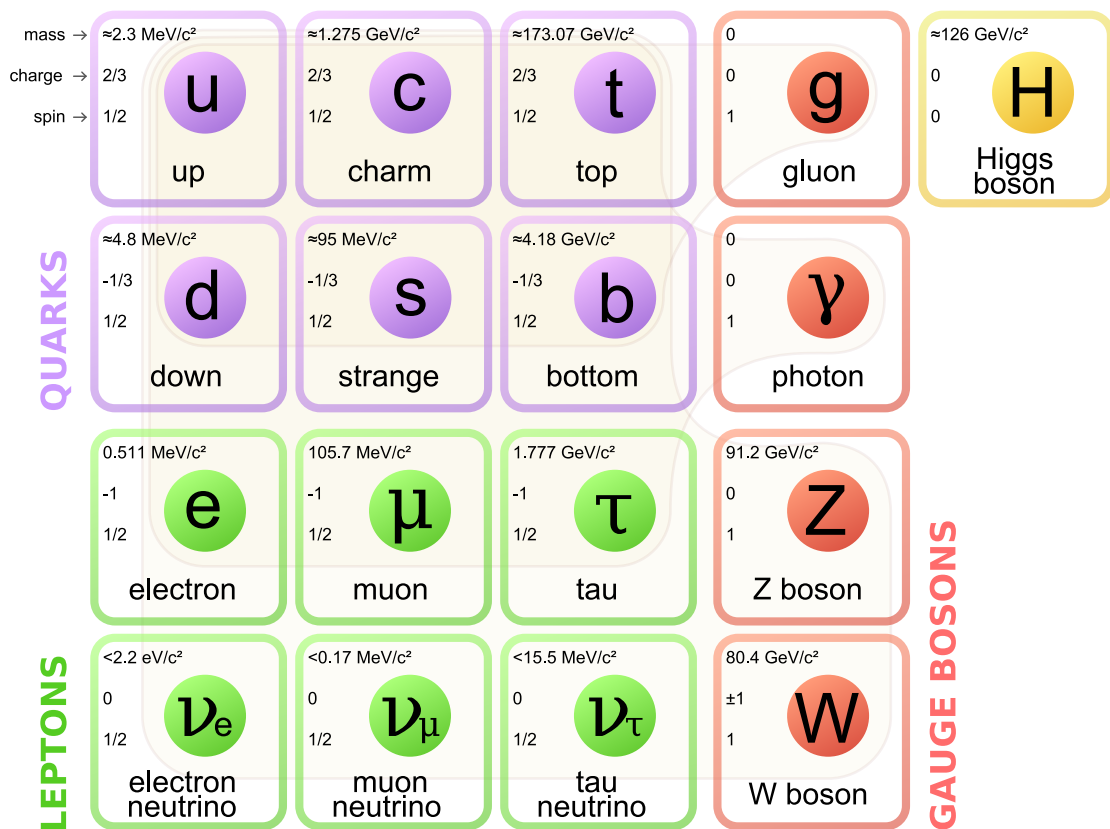


Figure 1: The Elementary Particles of the Standard Model [1].

quarks, the leptons, all of them being fermions of spin $S = \hbar/2$, and the interaction mediator bosons with integral spin. Both the quarks and leptons are categorized into three generations well separated in their mass which is indicated by the columns in figure 1. Each particle or state possesses a set of quantum numbers that uniquely identifies them. Quarks carry the additive baryon number $\mathcal{B} = 1/3$ while the leptons possess the lepton quantum number $\mathcal{L} = 1$. A total of six quark flavors are currently known, historically named up (u), down (d), strange (s), charm (c), bottom (b), and top (t), while each of the six flavors introduces a quantum number. For the four heavy quarks the assignment is straight forward, the s quark carries strangeness $S = -1$, the c quark charm $C = 1$, the b quark bottomness $B = -1$, and the top quark topness $T = 1$. Unlike these quarks,

the u and d quark have a similar mass and the isospin was introduced to express this symmetry. Analogous to the spin S it is also an $SU(2)$ group and the u and d quarks carry $I = 1/2, I_3 = \pm 1/2$, respectively.

Currently the Standard model contains three forces, the electromagnetic (EM), the weak and the strong force, which are described by their appropriate gauge quantum field theory (QFT). QFT combines special relativity and quantum mechanics predicting for example the existence of antiparticles as a consequence. Hence for every particle exists an antiparticle which has all internal quantum numbers inverted. Specifically, quantum electrodynamics (QED) describes the interactions of particles with electric charge with the photon as the force mediator. Because the photon is massless, the range of the EM force is infinite, but its strength drops off rapidly, more precisely the force drops with $1/r^2$. The small coupling constant $\alpha_{EM} \approx \frac{1}{137}$ of EM interactions together with the renormalizability of QED allows for analytic perturbation calculations that can be carried out with high precision, making it a well tested theory that is in excellent agreement with measurements [2]. It can be unified with the weak force, which is mediated by the massive W^\pm and Z^0 gauge bosons, to the electroweak theory [3–5]. All of the quarks and leptons carry weak charge and can therefore interact weakly. The interaction strength of the weak force is heavily suppressed by terms arising from the massive force mediator bosons. The mass of the weak interaction bosons seemed rather unesthetic until the 1960s, as gauge invariance also requires the W and Z bosons to be massless. The proposed Higgs mechanism was able to solve this mystery by the spontaneous symmetry breaking. However the theory remained indefinite over decades as no evidence for the Higgs particle was found by experiments. Only recently, in the year 2012, the long awaited Higgs particle was discovered [6, 7].

The third force of the standard model is the strong force with the gluons as the mediator bosons. Both the quarks and gluons possess color charge, which allows them to interact by the exchange of the gluons. The underlying renormalizable QFT [8], quantum chromodynamics (QCD), is able to describe two unique effects of the strong force with a four momentum transfer Q^2 dependent coupling constant in an elegant way. In general the coupling constant of a QFT is not constant, but vacuum polarization terms generate a Q^2 or interaction range dependence. The coupling constant decreases as Q^2 becomes smaller or the interaction distance becomes larger. This effect is also known as charge screening. In contrast to the photon the gluons themselves carry color that allows them to couple to other gluons. In return this results in a coupling constant α_s that increases as the interaction distance becomes larger or decreases for an increasing four momentum transfer Q^2 . For QCD this effect dominates over the charge screening one, so that the coupling constant dependency to Q^2 is governed by the self coupling feature (see figure 2). At large Q^2 or small distances it is very small and the quarks are quasi free and calculations can be performed via perturbation theory [10]. This effect is known as asymptotic freedom [11, 12]. On the contrary at large distances or small Q^2 it increases in a monotonic fashion, making it impossible to use the otherwise successful perturbation theory. As a result the existence of a free quark or antiquark is forbidden. This effect is known as confinement [13].

The observable bound states of quarks, the so called hadrons, are colorless and categorized within the constituent quark model (CQM) [14] into mesons ($\mathcal{B} = 0$) and baryons ($\mathcal{B} = 1$). Thus conventional mesons are simply a quark antiquark pair and baryons a three quark state. In contrast to the mesons, the antiparticles of baryons belong to the separate family of antibaryons ($\mathcal{B} = -1$). Apart from the quark flavor, further classifica-

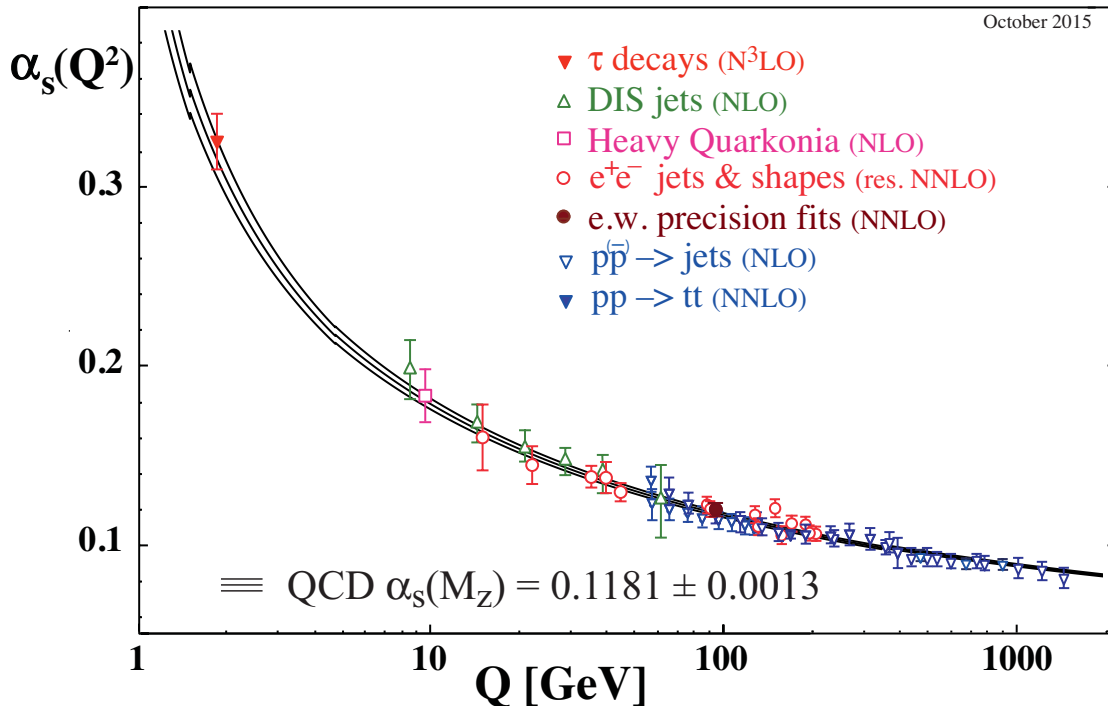


Figure 2: Summary of measurements of α_s as a function of the energy scale Q . The respective degree of QCD perturbation theory used in the extraction of α_s is indicated in brackets (NLO: next-to-leading order; NNLO: next-to-next-to leading order; res. NNLO: NNLO matched with resummed next-to-leading logs; N^3 LO: next-to-NNLO) [9].

tion is possible using the J^{PC} nomenclature, with the total spin J , the parity P and the C -parity. The total spin J is a coupling of the intrinsic spin S and the angular momentum L . The P and C -parity are multiplicative quantum numbers and describe the behavior of the particle state wave function under the spacial reflection transformation $\vec{x} \mapsto -\vec{x}$ and the particle to antiparticle transformation.

In order to gain insight into this rich particle spectrum one approach is trying to solve QCD numerically by discretizing spacetime, which is known as lattice QCD. Being computationally intensive, the use and precision of lattice QCD is still limited. However the steady increase of computation power over the years has accelerated this field of research, allowing to determine the hadron spectrum with increasing precision, e. g. the proton mass with 2% [15]. Otherwise one has to refer to effective field theories or approximating models, such as chiral perturbation theory [16] or the constituent quark model.

The classification and structure of the vast amount of experimentally discovered particles in the hadron spectrum is of high interest. With the discovery of several unexpected states in respect to the conventional hadron picture, the interest was drawn to the search for unconventional hadrons, so called exotics. For example in the charmonium sector ($c\bar{c}$ mesons), the recent measurement of the X, Y, Z states has caught the focus of attention [17–19]. Also parts of the meson spectrum remain understood relatively poor despite decades of investigation. In particular information of the light isoscalar spectrum with $J^{PC} = 0^{++}$, consisting of isospin singlet states ($I = 0$), proves to be difficult to extract due to many broad and overlapping states. The supernumerary amount of states also

makes this sector interesting with regard to the search for exotics. Additional precision measurements are needed to gain further insight on the nature of these states.

At this point one might ask, how exactly can such a bound state be measured in an experiment? Since all states except the energetic lowest ones are instable, they have to be produced first. In general this is achieved by the collision of particles, which are stable or are comparatively long-lived, e. g. protons, electrons, pions, kaons and muons. If an instable bound state is produced, it will decay into a set of particles that are stable or relatively long lived. These decay products are also known as the final state and can be measured. In the reverse order information about the instable bound states is obtained.

The mass and width of states can be extracted from the line shape. Energy scans are a simple yet precise method that measure the line shape of states produced directly in the initial particle collision. In this case the beam energy or the center of mass energy \sqrt{s} of the initial particle collisions is increased step by step, while the reaction rate is recorded. This obtained line shape spectrum will exhibit peaks at the masses of created instable states, as a result of their resonant production. The advantage of the energy scan is that merely the counting of a reconstructed final state is needed. The future experiment \bar{P} ANDA is able to make such measurements with its antiproton proton collisions. Depending on the reaction partners, e. g. electron positron collisions, the accessible states via direct production can be limited to a subset of the quark model states.

In addition, states with exotic quantum numbers can never be produced directly. Therefore one has to resort to another well established technique for extracting the information of states, the method of partial wave analysis (PWA). It allows the extraction of the properties of the states produced indirectly from subsequent decays. Partial wave models are created for the reaction processes, and by fitting the predicted kinematic variable distribution of the model for the given final state to the measured data, the instable intermediate particles and their parameters can be extracted. Apart from the mass and width of a state, also additional information e. g. the spin and parity are extracted. Important for such amplitude analysis is large amounts of data, in order to be able to notice small variations in the kinematic distributions. Currently experiments like BESIII are ideal for such analysis with their record amounts of collected data in the charm region, enabling unprecedented precision.

Line shape measurements require the information of the luminosity, which scales the overall reaction rate. Because the luminosity can vary with each individual measurement point of the energy scan, the knowledge of the relative luminosity is a vital aspect of the normalization and the correct measurement of the line shape [20]. Furthermore the absolute luminosity is mandatory for the determination of the absolute cross section of any process. One goal of this thesis is to determine the luminosity for the \bar{P} ANDA experiment from the reconstructed track information of the luminosity detector (LMD) with the highest possible accuracy. This high accuracy on the luminosity is achieved by studying the influence of the target and accelerator beams in detail.

When performing PWA, many different models can be used to extract properties of the states. The comparison of the various models is of high value, as it can provide more information on their interpretation, accuracy, limits, etc. Consequently the properties of states can be extract with higher accuracy and more insight on the composition of the states is gained. The second goal of the thesis is the implementation of the helicity formalism for the ComPWA framework. With this, a first general and well established model is made available, that serves as a foundation for the comparability of other models. In

this thesis the focus lies on the light isoscalar spectrum with the preparation of a partial wave analysis of the reaction channel $J/\psi \rightarrow \gamma\pi^0\pi^0$ using BESIII data. The attractiveness of this reaction lies in its simplicity, due to the restriction of the quantum numbers for the pseudoscalar-pseudoscalar pair.

The thesis begins with a summary of the current knowledge of hadronic resonances, open questions and possible theoretical interpretations. Chapter two presents the BESIII experiment at the Beijing Electron Positron Collider II (BEPCII) with its record-breaking amount of collected data in the charm sector and the PANDA experiment at the Facility for Antiproton and Ion Research (FAIR) currently under construction. Both setups are ideal machines for the study of the hadron spectrum. The third chapter introduces the concept of luminosity and guides towards the design of the luminosity detector (LMD) as well as the corresponding reconstruction software. In chapter four a detailed description of the luminosity extraction software is presented. Extensive systematic studies on the accuracy of the determined luminosity are performed in chapter five. Here influences of various sources of the luminosity extraction software, which affect the accurate determination of the luminosity, are studied in detail. These sources are the detector efficiency and resolution correction, the type of estimator used in the optimization problem, as well as the accelerator and target beam of the PANDA experiment. Chapter six then turns to the amplitude analysis of the $J/\psi \rightarrow \gamma\pi^0\pi^0$ reaction using data of the BESIII experiment. It starts with an theoretical introduction to partial wave analysis (PWA) and the helicity formalism. Afterwards the CompPWA framework is shortly presented in a general scope, while the following sections are devoted to the implementation of the helicity formalism with a unique approach by describing the physics model using an expert system. In chapter seven the implementation of the helicity formalism is validated exhaustively and closes with first results of the amplitude analysis of the BESIII dataset. At the end the results of the thesis are summarized in the final discussion chapter.

HADRON SPECTROSCOPY

Spectroscopy is a measurement technique in which observed intensity distributions of radiation properties, e. g. the energy, are extracted. It originates from the study of the interaction of electromagnetic radiation with matter. The recorded distributions are called spectra. In hadron spectroscopy, the intensity variation of certain kinematic variables observed in particle reactions are studied to obtain the interesting information of possibly created bound states. Properties of a state include its mass and width, but also its quantum numbers and internal structure. From the elementary constituents of these states, the quarks, a vast amount of composite particles are accessible. Their classification and internal structure is the core issue addressed by the field of hadron spectroscopy.

A well established theory for the understanding of the rich hadron spectrum is the constituent quark model (CQM). Historically it emerged from the previously developed eightfold way [21] that was introduced to organize the growing amount of states. The CQM asserts mesons being quark antiquark pairs and baryons three quark states, while all quarks carry color¹ and only colorless hadrons are allowed. Using the SU(3) symmetry group, the nine possible $q\bar{q}$ combinations containing the light u , d , and s quarks are grouped into an octet and a singlet of light quark mesons. This can be extended further to a SU(4) flavor symmetry group by including the charm quark c , which results in a 15-plet and a singlet, depicted in figure 3 for the ground states ($L = 0$) of the pseudoscalar ($S = 0$) and vector mesons ($S = 1$). Even though the SU(4) flavor symmetry group is broken strongly, due to the large mass difference of the charm quark, the qualitative classification and grouping of the mesons is possible. The states are commonly described by the J^{PC} quantum numbers, J being the spin, P the parity and C the charge conjugation parity² of the meson. The following selection rules apply

- $|L - S| \leq J \leq L + S$ with the orbital angular momentum L and sum of quark spins $S = 0, 1$
- $P = (-1)^{L+1}$
- $C = (-1)^{L+S}$ only defined for states which are their own antiparticle.

With $L = 0$ the pseudoscalar (0^{-+}) and the vector (1^{--}) states are addressed, similarly with an orbital excitation $L = 1$ the scalars (0^{++}), the axial vectors (1^{++}) and (1^{+-}), and the tensors (2^{++}). Despite its simplicity, the quark model is able to describe the observed hadron spectrum astonishingly well. Its power lies in the ability to categorize or organize the rich particle spectrum, which, especially at the time of its establishment, was of great importance to see structure and spawn new ideas for future models like QCD.

¹ In the CQM the quarks carry a color charge, which was introduced [22] because of the Δ^{++} baryon that has uuu constituent quark content and would be forbidden by fermi statistics.

² The charge conjugation operator \mathcal{C} changes a particle to its antiparticle, therefore inverting all its internal quantum numbers.

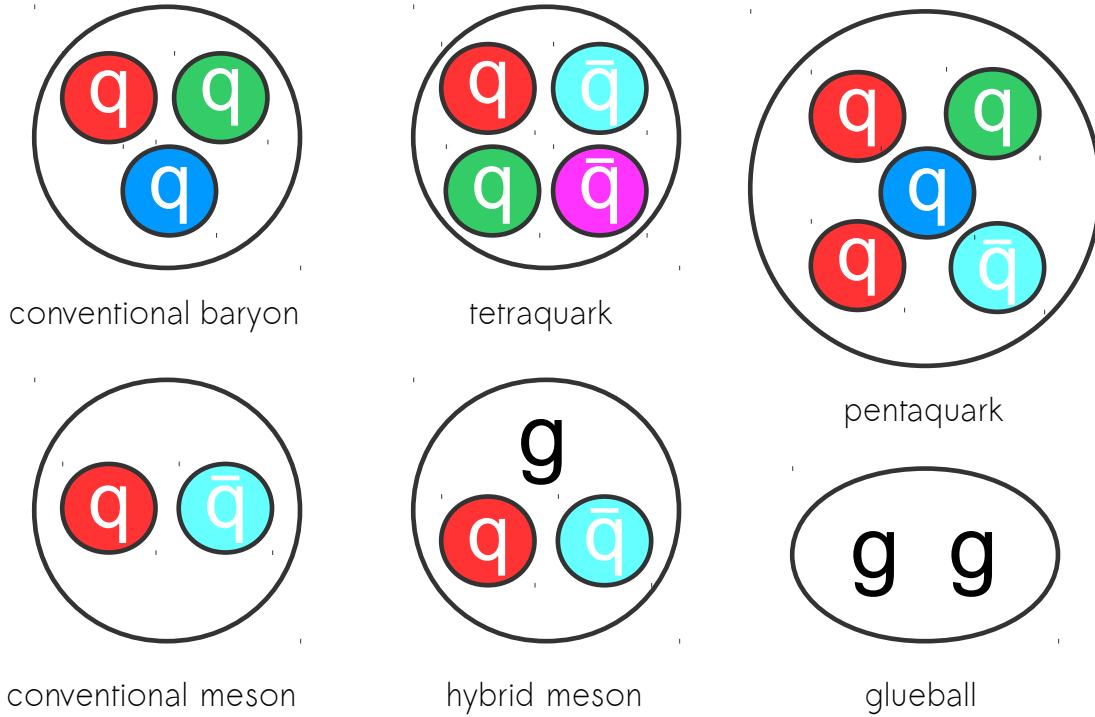


Figure 4: Simplest conventional and exotic components of hadron states within the constituent quark picture [23, p. 11].

1.1 LIGHT QUARK SECTOR

The light mesons are made up of the u , d and s quarks. Because their masses are small compared to the binding energy, the bound states of such quarks have to be treated relativistically. On the contrary the advantage is that their mass can be neglected as an approximation, allowing effective field theories to take over, as for example chiral perturbation theory (ChPT). In addition they are comparatively easy to measure from an experimental point of view, due to their low mass which allows an abundant production already at low beam energies.

Light mesons are categorized by the $SU(3)$ symmetry group, hence only states on the center planes of the diagrams in figure 3 are accessible, as we restrict the states to be charmless. The lightest mesons are the pseudoscalar pions which form an isospin $|I, I_z\rangle$ triplet [24, p. 47]

$$\begin{aligned}\pi^+ &= |1, +1\rangle = -u\bar{d} \\ \pi^0 &= |1, 0\rangle = \frac{1}{\sqrt{2}}(u\bar{u} - d\bar{d}) \\ \pi^- &= |1, -1\rangle = d\bar{u}.\end{aligned}$$

For a perfect symmetry between the quarks, all three quarks and states within a multiplet would be equal in mass. As measurements have shown, the states consisting of first generation quarks (u, d and their antiquarks), are indeed very similar in mass, therefore impose only a weak breaking of the underlying $SU(2)$ symmetry. Within $SU(3)$ there are

two isoscalar states with the same J^{PC} quantum numbers. These are the singlet ψ_1 and the octet state ψ_8

$$\begin{aligned}\psi_1 &= \sqrt{\frac{1}{3}}(u\bar{u} + d\bar{d} + s\bar{s}) \\ \psi_8 &= \sqrt{\frac{1}{6}}(u\bar{u} + d\bar{d} - 2s\bar{s}).\end{aligned}$$

They are defined by the orthogonality to each other and the neutral isospin triplet state ($\psi_3 = \sqrt{\frac{1}{2}}(u\bar{u} - d\bar{d})$). Since both of these states are isoscalar and have the same quantum numbers J^{PC} , they are allowed to mix and the physical states are orthogonal linear combination of these basis states. In fact for the ground state vector mesons ($L = 0, S = 1$), the physical states are

$$\begin{aligned}\phi(1020) &= \psi_8 \cos(\theta_V) - \psi_1 \sin(\theta_V) \approx s\bar{s} \\ \omega(782) &= \psi_8 \sin(\theta_V) + \psi_1 \cos(\theta_V) \approx \sqrt{\frac{1}{2}}(u\bar{u} + d\bar{d}).\end{aligned}$$

With a vector mixing angle of $\theta_V = 36.4^\circ$ [9], the mixing is nearly ideal, making the two physical states almost pure in the generation of quarks contributing to the state. The u , d , s quark masses and the mixing angles are actually determined from the masses of the states in the octet and singlet. The mixing angles and state masses suggest a heavier s quark, compared to u and d , therefore breaking the $SU(3)$ symmetry. Similarly this procedure can be applied to the pseudoscalars, namely the π^0 , η and η' states. However here the quark model reaches its limit, as measurements show a large mass difference between the η and η' , that cannot be explained with merely state mixing.

In addition the understanding in some parts of the light meson spectrum is relatively poor. The light isoscalar spectrum ($I = 0$) is particularly interesting, because the observed states are supernumerary with respect to predicted conventional isoscalar mesons. Figure 5 shows the light isoscalar mesons with $J^{PC} = 0^{++}$, comparing the 6 states predicted by the quark model with the 8 observed states. This suggests interpretations beyond the simple $q\bar{q}$ picture, such as molecules, glueballs and tetraquark systems. Owing to the fact that glueballs are isospin singlet states, this spectrum becomes even more intriguing. However as the majority of these states are broad and overlap, with widths between 100-450 MeV, both their correct theoretical description as well as their experimental extraction process is difficult.

A resonance is described by a pole s_{pole} in the S -matrix in the complex energy plane

$$\sqrt{s_{\text{pole}}} = Mc^2 - i\Gamma/2.$$

M and Γ denote the mass and width of the resonance. The location of this pole is only in agreement with the Breit-Wigner parameterization for narrow and well-separated resonances [26]. Also they should be far away from thresholds of decay channels. Specifically for the $f_0(500)/\sigma$, which is a very broad structure, this constraint is not given and the simple Breit-Wigner parameterization is not a valid approximation. In addition, the separation of the resonance from the background becomes impossible for such broad resonances. The pole position can be best extracted with state of the art dispersion relations [27] to about 450 – i275 MeV [26, 28]. Even though the $f_0(980)$ is a quite narrow

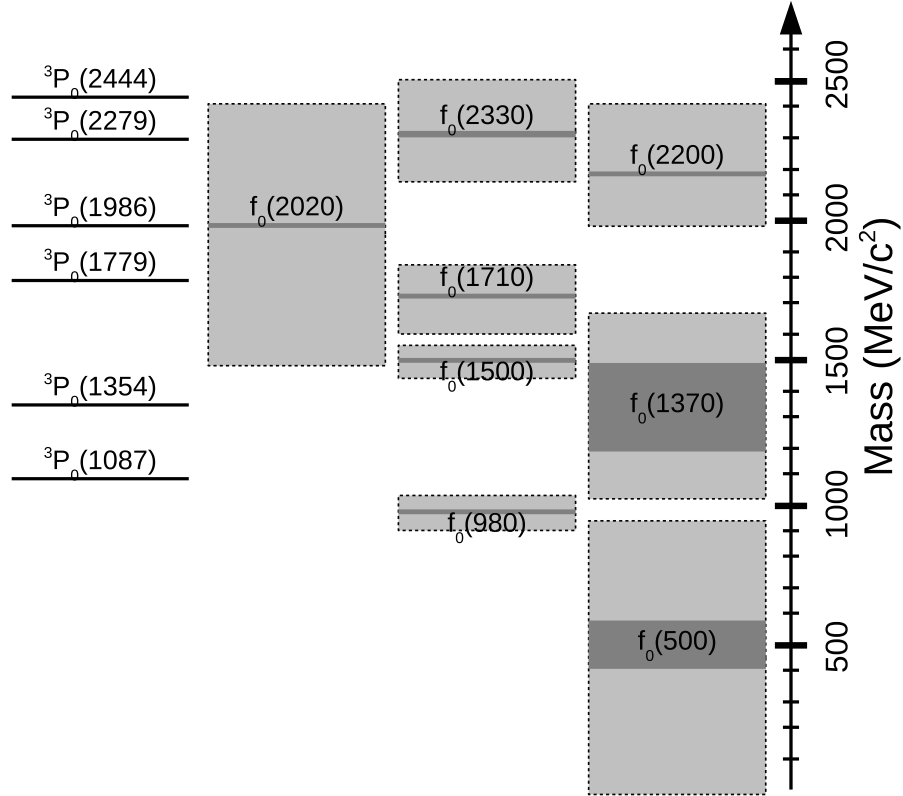


Figure 5: The spectrum of isoscalar mesons with $J^{PC} = 0^{++}$ [23]. The black bars represent quark model predictions [25, p.64f], while the gray shaded areas and bars show the experimental data [9] with the masses in dark and widths in light gray.

resonance, it overlaps strongly with the broad $f_0(500)$ and $f_0(1370)$, hence making the pole extraction with a Breit-Wigner problematic. The interference may shift the peak in the invariant mass spectrum and also the nearby $K\bar{K}$ threshold can create a dip or peak. In analogy also the strong overlapping for the f_0 resonances above $1 \text{ GeV}/c^2$, which is evident from figure 5, makes their correct pole extraction difficult.

The interpretation of these states is controversial, although some are supported with stronger evidence. For example the $f_0(980)$ can be associated with a $K\bar{K}$ molecule due to the unexpected strong coupling to $K\bar{K}$, even though the threshold is close [29, 30]. Also it is mainly seen in semi-leptonic D_s decays and decays of B/B_s -mesons, supporting this interpretation. Similar reasoning applies for the multiquark interpretation [31, 32]. When comparing the $f_0(1370)$ with the quark model predictions (see figure 5), a corresponding partner can be found and the $q\bar{q}$ picture appears suitable. Its decay into predominantly 2 and 4 pions also supports this view. For the $f_0(1500)$ and $f_0(1710)$ the interpretation is again more debated. Pure gauge quenched³ lattice QCD calculations show a glueball ground state with quantum numbers 0^{++} and its first excited state with 2^{++} [33] (see figure 6). The masses of these states are predicted to be at $1710 \pm 50 \pm 80 \text{ MeV}/c^2$ and $2390 \pm 30 \pm 120 \text{ MeV}/c^2$, while the first pure exotic glueball state has quantum numbers 2^{+-} at a mass of around $4 \text{ GeV}/c^2$. As the 0^{++} states for example are also accessible by conventional mesons, these states can mix with the glueball ground state. Possible mixing partners are the $f_0(1370)$, $f_0(1500)$ and the $f_0(1710)$ as their masses are similar [34, 35]. The $f_0(1500)$ couples strongly to $\pi\pi$ but not to $K\bar{K}$, unlike the $f_0(1710)$, which decays

³ In the quenched approximation, $q\bar{q}$ loops are neglected.

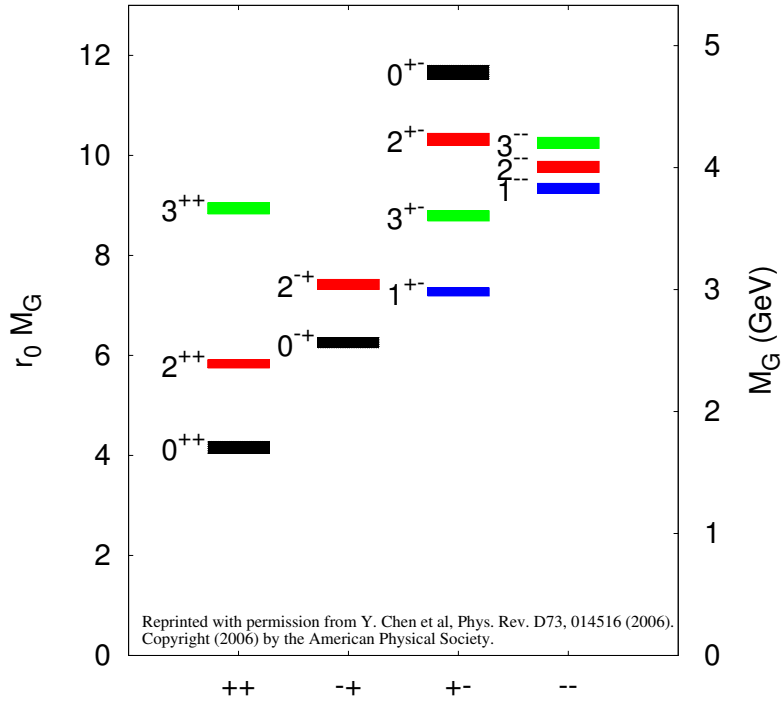


Figure 6: Predicted glueball mass spectrum from the lattice in quenched approximation [33].

mainly into kaons. This fact favors the $f_0(1500)$ for a dominant glueball content [35]. However simply comparing the mass of the $f_0(1710)$ and the predicted glueball mass from [33], this state seems like the more suitable candidate. It was found that the decay of a spin zero glueball G to light $q\bar{q}$ pairs is chirally suppressed by the mass ratio factor of $(m_q/m_G)^2$ [36]. This supports the glueball interpretation of the $f_0(1710)$ as this effect would result in a more dominant decay into kaons [25]. Since glueballs are expected to be produced in gluon rich decays, the production of the f_0 states in J/ψ radiative decays can help with the interpretation of these f_0 resonances. The J/ψ state belongs to a family of mesons known as the charmonia.

1.2 CHARMONIUM

When moving towards mesons build up from heavier constituent quarks, models can take advantage of this by treating them non-relativistically as an approximation. The charm (c), bottom (b) and top (t) quarks count as heavy, listed with increasing mass, but states consisting of top quarks were not seen since the t quark lifetime is shorter than the hadronization time scale. Therefore the charm and bottom quark meson spectrum is favored for searches in the heavy quark region. In general quarkonium designates a flavorless meson, constructed from a quark and its own antiquark ($q\bar{q}$), and hence Charmonium is a meson with $c\bar{c}$ content. Non-relativistic treatments can model the charmonium spectrum, with for example the Cornell potential [37]

$$V = -\frac{\hbar c \alpha}{r} + k \cdot r \quad (1)$$

with the distance between the quark and antiquark r , and the model parameters k and α . Because of the similar properties of the gluons compared to photons a coulomb-like potential, given by the first term in equation 1, is a reasonable choice and is compatible with asymptotic freedom. The second term is a linear growing string term which introduces the confinement feature. The level scheme of the charmonium spectrum is pictured in figure 7.

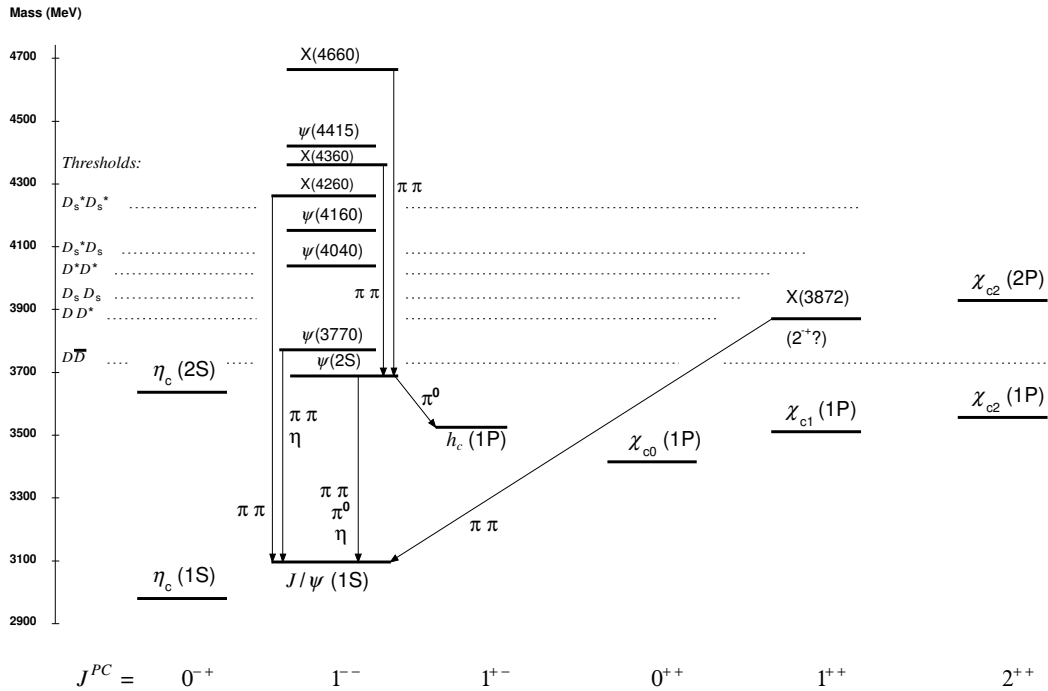


Figure 7: The level scheme of the $c\bar{c}$ states showing experimentally established states with solid lines. Singlet states are called η_c and h_c , spin triplet states ψ and χ_{cJ} , and unassigned charmonium-like states X . In parentheses it is sufficient to give the radial quantum number and the orbital angular momentum to specify the states with all their quantum numbers [9].

The lowest mass mesons with charm quark content are the D mesons. Below the threshold of $D\bar{D}$, the charmonium states are quite long living, due to the Okubo-Zweig-Iizuka (OZI) rule [38]. It states that Feynman diagrams, that can be cut in two by only slicing internal gluon lines, and not cutting any external particle lines, are suppressed. As a consequence these states are also narrow regarding their width, making them well separated in the mass spectrum, allowing a good approximation for the Breit-Wigner [39] model. For this reason the charmonium sector is also promising for the search of exotic mesons. The most prominent charmed state is the J/ψ , as with its discovery the charm quark was born.

Over the past few years several new charmonium-like states have been observed, now known as the X,Y,Z states. They challenge the conventional quark model due to their conflict with expectations. In charged sector the discovery of the $Z_c(3900)^\pm$ [17] shows exotic properties. They carry electric charge but also couple strongly to charmonium, as the decay to $\pi^\pm J/\psi$ preferred. This indicates a $c\bar{c}$ content with additional quarks to provide the necessary electric charge. Therefore the Z_c states are a strong candidates for tetraquarks or even higher quark states. The neutral ones are the $X(3872)$, $Y(4260)$,

$Y(4360)$ and $Y(4660)$ ⁴ and their masses and decay properties are still obscuring their internal structure. Even though the $X(3872)$ was discovered already in 2003 [40], its quantum numbers have only recently been measured to be 1^{++} by the Large Hadron Collider beauty (LHCb) experiment [41, 42]. Because it is very close to the $D^0\bar{D}^{*0}$ threshold, a possible explanation for this state is a $1^{++} D\bar{D}^*$ molecule. The strong isospin breaking that is predicted due to the nearby D^+D^{*-} threshold [43] is also verified by the ratios of the $J/\psi\omega$ and $J/\psi\rho$ decay channels [44]. Lattice QCD is making continuous improvements [45] and only recently a candidate for the $X(3872)$ state was found just below the $D\bar{D}^*$ threshold [46]. A tetraquark interpretation would also be possible but rather unlikely, since the charged partner of the $X(3872)$ has not been observed. Despite the immense efforts in uncovering the structure of the $X(3872)$, more experimental information is required and can be provided by the measurement of the line shape of the $X(3872)$, which can be performed by the PANDA experiment.

So far there are several candidates for exotic states or contributions to regular hadron states. For example in the light quark and the charmonium sector for the mesons, that have been discovered by experiments in the past years. However either their existence is questionable or more information on their properties are needed to reveal their true nature. Therefore new and more precise measurements are highly anticipated. Very recently the LHCb experiment reported to have discovered exotic hadrons consistent with a tetraquark interpretation [47]. In the future, experiments like the PANDA and BESIII experiment also play an important role.

⁴ Sometimes they are also referred to as X instead of Y in literature.

HADRON SPECTROSCOPY DETECTOR SYSTEMS

Beneficial for amplitude analyses are precise, clean and large data sets. Both the operating BESIII and the future PANDA experimental setup are ideal machines for this task with their high luminosities. Currently BESIII performs some of the most interesting measurements for hadron spectroscopy having collected a record amount of data. PANDA will give access to a broader spectrum of states with its anti-proton proton collisions. These two experiments are described in more detail in this chapter.

2.1 THE BESIII EXPERIMENT

The BESIII detector is located at the BEPCII of the Institute of High Energy Physics (IHEP) in Beijing. The BEPCII is a multi-bunch collider with two separate rings of a circumference of 237.5 m working at an energy range of $s = 2 \text{ GeV} - 4.6 \text{ GeV}$. Its high design luminosity of $\geq 10 \cdot 10^{33} \text{ 1/cm}^2 \text{ s}$ at a center of mass energy of $2 \cdot 1.89 \text{ GeV}$ is achieved by using a *top-off* injection system that enables the collider to reuse the remaining bunches. In addition the BEPCII can also be used as a source of synchrotron radiation, in which case only electrons are being accelerated. One of the strengths of the BESIII experiment is the high luminosity resulting in substantial amounts of data, which is crucial for precision measurements especially in the field of hadron spectroscopy. For example an uncontested amount of more than 1.5 billion J/ψ events are recorded as well as around 3 fb^{-1} at the $\psi(3770)$. Also large datasets at around 4.26 GeV exist.

2.1.1 Physics Program

The physics program of the BESIII experiment is versatile and can be divided into the following categories [48]:

CHARMONIUM PHYSICS: From the large amount of data, the total decay widths of the J/ψ and ψ' are measured with a precision below the percent level. Furthermore the many different decay modes of the J/ψ are studied much more precisely than before, giving insight to some of the problems such as the $\rho\pi$ puzzle, i.e. violations of the 12%-rule, and non- $D\bar{D}$ decays of the $\psi(3770)$ [48]. Also transitions between the different charmonium states are mapped out and more massive states such as the $Y(4260)$ are now accessible at BESIII. Cabbibo-suppressed J/ψ decay channels can be studied, which seem to have higher branching ratios as predicted by the Standard Model (SM) [48]. Unique explorations for physics beyond the SM are planned with the search for evidence of flavor-changing neutral currents.

SEARCH FOR NEW AND EXOTIC HADRONIC STATES: In the past four years the BESIII collaboration made some unexpected discoveries. At first a charged resonance de-

caying into a charged pion and a J/ψ was observed, now named $Z_c(3900)^\pm$ [17]. Intriguing about this particle is the decay into a J/ψ , which suggest $c\bar{c}$ content, and the non-zero charge implicating additional quark content. In the same year a partner to the $Z_c(3900)^\pm$ was found, the $Z_c(4020)^\pm$ [49]. It decays into a charged pion and h_c , which is also a charmonium state, suggesting a $c\bar{c}q\bar{q}$ content in consequence. Also the neutral partners to the Z_c states were observed recently, the $Z_c(3900)^0$ [18, 50] and the $Z_c(4020)^0$ [19], completing the two isospin triplets.

By studying the J/ψ decays, hadron spectroscopy and search for new hadronic states in the light quark sector is possible. Because the J/ψ 's almost always annihilate into gluons they are very useful for glueball searches and for probing the gluon contents of light hadrons. A radiative decay of the $J/\psi \rightarrow \gamma\pi^0\pi^0$ was studied to gain new insight in the controversial light isoscalar spectrum [51].

D-PHYSICS: Currently BESIII possesses the record data set of $\psi(3770)$, which allows high precision measurements. From purely leptonic decays of the produced D and D_s mesons, the decay constants f_D and f_{D_s} can be measured with expected systematic errors of 1.2 % and 2.1 % [48], respectively. Inclusive and exclusive semileptonic decays of D-mesons will also be studied to test various theoretical predictions. In addition from studying the D decays, one can extract the Cabibbo-Kobayashi-Maskawa (CKM) matrix elements V_{cs} and V_{cd} with an expected systematic error of around 1.6 %. Since theoretical predictions for $D - \bar{D}$ mixing and CP-violation are unreliable, BESIII can provide new experimental information about them. Rare or forbidden decays can be studied systematically and provide strict tests of the SM and have the potential of uncovering the effects of new physics beyond the SM. Their measured branching ratios can be improved significantly, while the precision on the upper limits of branching ratios for unseen modes can be improved by two orders of magnitude.

τ -PHYSICS: Experimental studies of inclusive hadronic τ decays can provide precise determinations of the strange quark mass and the CKM matrix element V_{us} , while the study of leptonic decays can test the universality of the electroweak interaction and give a possible hint of new physics. Also, due to the high statistics and low background fraction the measurement precision of the Michel parameters is improved by a factor of 2 to 4. Moreover the τ mass is measured with a higher precision of around 0.09 MeV. Amongst others the high statistics data sets of BESIII also allow for improvements on the SM uncertainty of the anomalous magnetic moment of the muon $(g - 2)_\mu$ [52]. In comparison with the high precision measurement of $(g - 2)_\mu$ [53], conclusions on the validity of the SM or possible physics beyond can be drawn. Similarly the large datasets of the reaction $e^+e^- \rightarrow p\bar{p}$ allow for improvements of the proton time-like form factors by around 30 % [54].

2.1.2 The BESIII Detector

The BESIII detector is optimized for the physics requirements discussed in the previous section. The average multiplicity lies in order of four charged particles and photons, with a typical momentum of charged particles of around 0.3 GeV/c, an average energy of photons of 100 MeV and an upper limit of 1.0 GeV for most particles. The complete

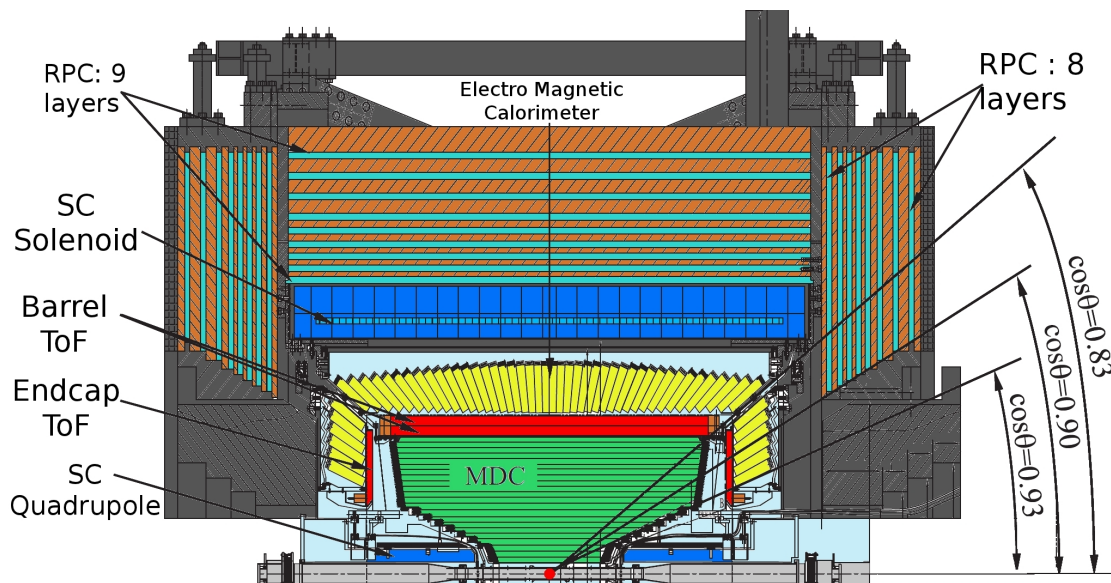


Figure 8: Side view of the upper half of the BESIII detector [55]

detector has an angular coverage 93%. The profile view is shown in figure 8. In the next paragraphs the individual detector components will be described in more detail [48].

MULTI-LAYER DRIFT CHAMBER (MDC) The conical shaped MDC surrounds the beam-pipe. Two superconducting quadrupoles are positioned in the MDC end caps and focus the beam onto the interaction point. With the help of the solenoidal magnetic field of 1 T the MDC measures the momentum of charged particle tracks by their curvature with a resolution of $\delta p/p = 0.5\%$ at $1.0 \text{ GeV}/c$. The single cell position resolution in the radial plane is $130 \mu\text{m}$ while the resolution in beam direction is 2 mm . The detector covers a θ -range down to $\cos(\theta) = 0.93$ and is split into an outer and inner chamber, while the latter can be replaced in case of radiation damage. A total of 43 layers of drift cells make up the MDC. Each drift cell consists of one tungsten gold plated sense wire that is surrounded by eight aluminum field wires. The cell volume is filled with a helium-propane mixture ($\text{He}/\text{C}_3\text{H}_8 = 60 : 40$) which optimizes the tradeoff between multiple scattering and a good dE/dx resolution. Altogether the energy loss resolution for particles is 6%.

TIME-OF-FLIGHT (TOF) By measuring the flight duration of particles from the IP the TOF system determines particle velocities that can be used for particle identification (PID). The TOF surrounds the MDC and consists of a barrel layer and two end caps that cover a solid angle of $|\cos(\theta)| < 0.83$ and $0.85 < |\cos(\theta)| < 0.95$ respectively. The barrel layer is built from two layers of staggered scintillating bars, while the end caps only have a single layer of scintillators. The scintillators are read out by fine mesh photomultiplier tubes and achieve a timing resolution of 90 ps in the barrel and 70 ps in the end caps. This allows for a $3\sigma \pi/K$ separation up to momenta of $0.7 \text{ GeV}/c$.

ELECTROMAGNETIC CALORIMETER (EMC) The energy and flight direction of photons, electrons and positrons will be measured by the EMC. It is located between the TOF system and the superconducting solenoid and is also split into a barrel region covering a solid angle of $|\cos(\theta)| < 0.82$ and the two end caps covering the

larger polar angles of $0.83 < |\cos(\theta)| < 0.93$. The sensor material consists of 28 cm long CsI(Tl) crystals, which corresponds to 15 radiation lengths, and are read out by two silicon photo-diodes. With an energy resolution of $2.3\%/\sqrt{E(\text{GeV})}$ and a position resolution of below $6\text{ mm}/\sqrt{E(\text{GeV})}$, the EMC can separate electrons and pions for momenta higher than 200 MeV/c.

MUON SYSTEM Most outward from the IP the muon system, occupying the space within the iron flux return of the superconducting magnet, discriminates and identifies muon tracks, by making use of the penetration power of the muons. The system consists of multiple interleaving detection and absorption layers. In this case the latter are iron plates, which are also responsible for the magnetic field return, and stop most of the created particles except the muons. Resistive plate chambers (RPCs) are responsible for the actual tracking of the muons, which consist of two electrodes separated by an isolating gas, in which a charged particle will ionize the gas and create a signal. Signals in all detection layers will therefore identify a muon. The barrel part consists of 9 such layer pairs, while the endcaps only have 8. Due to the bending of muon tracks in the magnetic field and the energy loss in the EMC crystals, the muon system becomes effective for energies starting at 0.4 GeV.

TRIGGER SYSTEM AND EVENT FILTER Because of the high interaction rates, which are dominated by background reactions, an event filtering is necessary, realized with a two level trigger system. The first level (L1) is a hardware trigger that processes the information from the subdetectors with the global trigger logic. The L1-trigger clock is synchronized to the accelerator and operates at 41.65 MHz. The second trigger level (L2) is a software trigger, which runs on a server farm, and reduces the background further by partially reconstructing the events. The BESIII DAQ runs at a rate of 4 kHz, with a overall background rate suppression from 40 MHz to below 2 kHz.

LUMINOSITY DETERMINATION The luminosity is determined by using three QED processes, for which cross sections are well known and very large. After correcting for detector efficiency and acceptance, the luminosity is determined from the rate of these processes with a precision of 1%. Luminosity monitors near the interaction point additionally measure the relative bunch-by-bunch luminosity using the rate of incident photons from radiative Bhabha scattering.

2.2 THE PANDA EXPERIMENT

The international research center FAIR is located at the GSI Helmholtzzentrum für Schwerionenforschung GmbH (GSI) in Darmstadt (Germany) and is currently under construction. It is a versatile particle accelerator complex hosting several experiments on its site and is funded by 16 countries. Figure 9 gives an overview on the research center. The

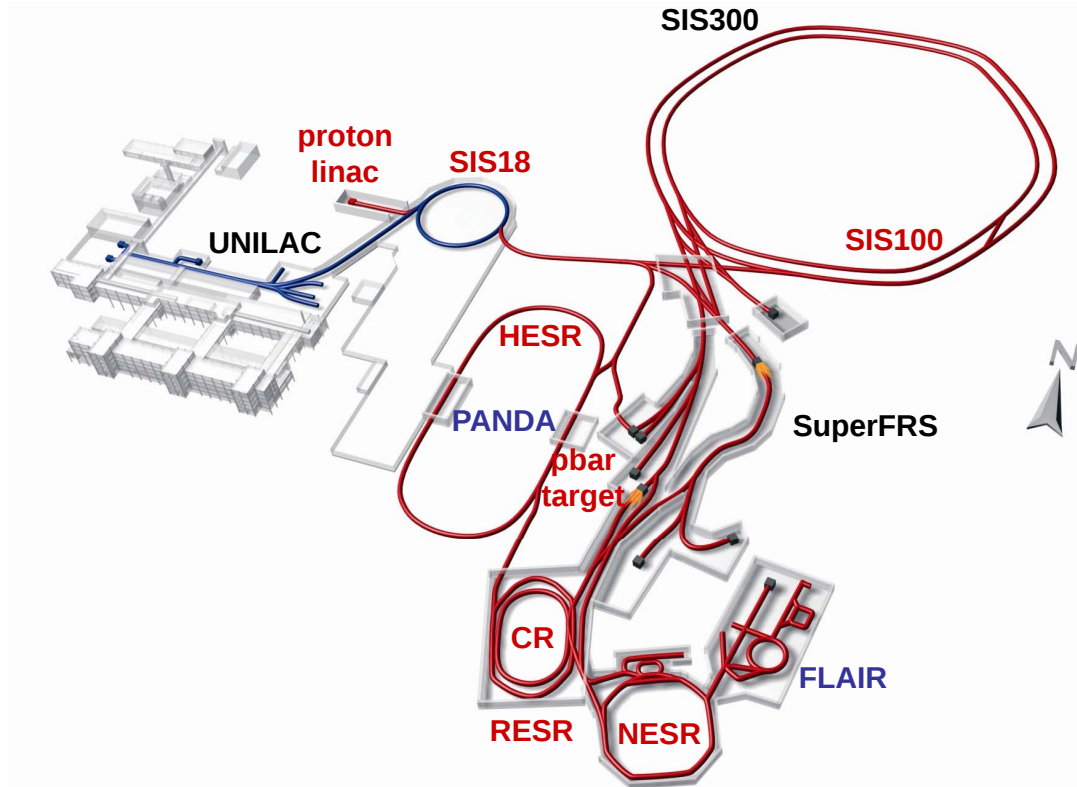


Figure 9: The accelerator complex FAIR [56].

starting point of all future particle beams is in main parts the already existing GSI accelerator complex with its universal linear accelerator (UNILAC) and the Schwerionen Synchrotron (SIS) 18. For the complete description of the facility please refer to [57]. The PANDA experiment will be located at the High-Energy Storage Ring (HESR). One key aspect that makes the PANDA experiment powerful and unique, is the use of the antiproton beam provided by HESR. The antiproton beam, which is fed into the HESR, is created in a multi step procedure. At first protons are created and accelerated by a chain of the proton linear accelerator (p-LINAC), the SIS 18 and the SIS 100 to a final energy of 29 GeV [58]. Then the high energetic protons from the SIS 100 are shot in bunches on a nickel (or iridium) antiproton production target [59] producing a large diversity of secondary particles via hard processes. A magnetic horn in combination with a momentum separation station will extract antiprotons with high efficiency on the transfer way to the Collector Ring (CR). The CR provides full acceptance of those separated antiprotons and its main task is the collection, cooling and debunching of the antiproton beam [60]. In the first years of operation, the pre-cooled beam will be directly fed into the HESR. A later upgrade involves the construction of the recuperated experimental storage ring (RESR) [56, 61]. The need for a high intensity beam requires an accumulation of antipro-

tons coming from the CR before it is transferred to the HESR [62]. During accumulation the beam emittance is further reduced by stochastic cooling.

2.2.1 The High-Energy Storage Ring (HESR)

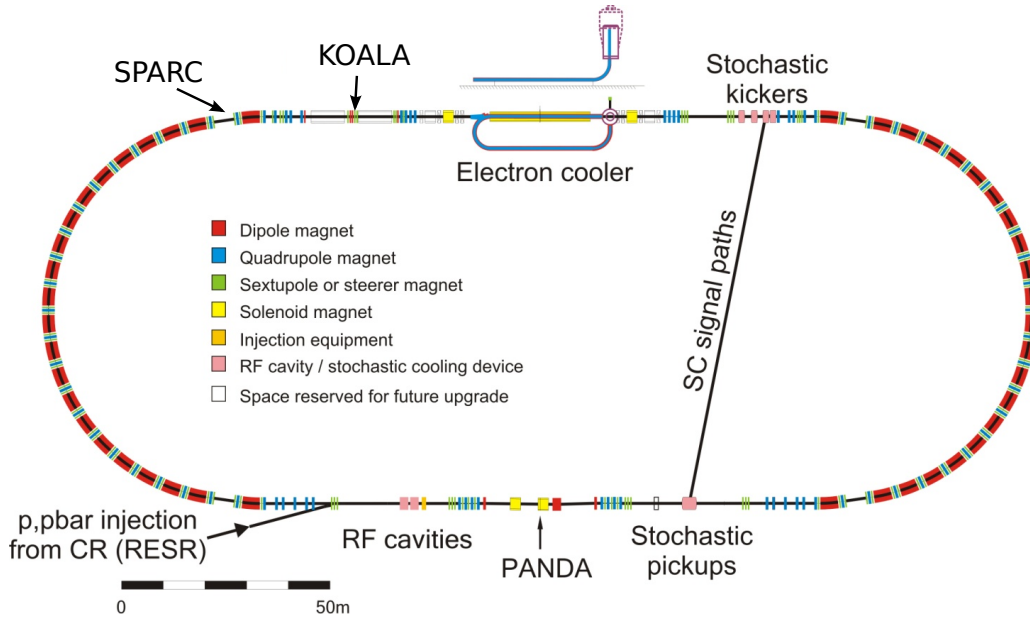


Figure 10: Illustration of the HESR setup with a length of 250 m and a width of 120 m. The racetrack shaped storage ring is equipped with RF cavities for beam acceleration and deceleration and stochastic pickups as well as kickers in the straights. While interactions of the stored antiproton beam with a perpendicular target beam are studied with the PANDA experiment in the lower straight section, the opposite straight will be equipped in a later stage with an electron cooler to reduce the beam emittance. Possible locations for the KOALA and SPARC experiment are indicated [63].

The HESR is going to host not solely the PANDA experiment, but also the KOALA [64] and SPARC [65] experiment (see figure 13). The exact locations of the latter two experiments are not fixed yet. The HESR RF-cavities allow for the beam to be acc- or decelerated in the momentum range of $1.5 \text{ GeV}/c$ – $15.0 \text{ GeV}/c$. One of the prominent features of the HESR is its cooling system. On the one hand stochastic cooling will be applied [66]. As indicated in figure 13 the stochastic pickups and kickers will get the particles with larger emittance closer to the ideal orbit. For a high intensity beam a momentum resolution in the order of $\Delta p/p \approx 10^{-4}$ will be achieved. By temporarily inserting cold electrons into the antiproton beam, additional cooling for particles with already low emittance can be achieved. The electron beam is slightly tilted with respect to the \bar{p} bunch to achieve the highest cooling power¹. This two stage cooling system achieves the highest momentum resolution of $\Delta p/p \geq 3 \cdot 10^{-5}$, crucial for energy scan experiments.

The expected luminosity profile is shown in figure 11. It can be divided in a preparation time t_{prep} and the experimental time t_{exp} . Preparation time includes injection, pre-cooling, acc- or decelerating the beam, beam steering as well as recuperation of remaining antiprotons after experimental time as long as the beam is not dumped after

¹ Note that the electron cooling process only increases the emittance for particles with a certain degree of the emittance. For particles with higher emittance than this threshold the correction will actually be counterproductive.

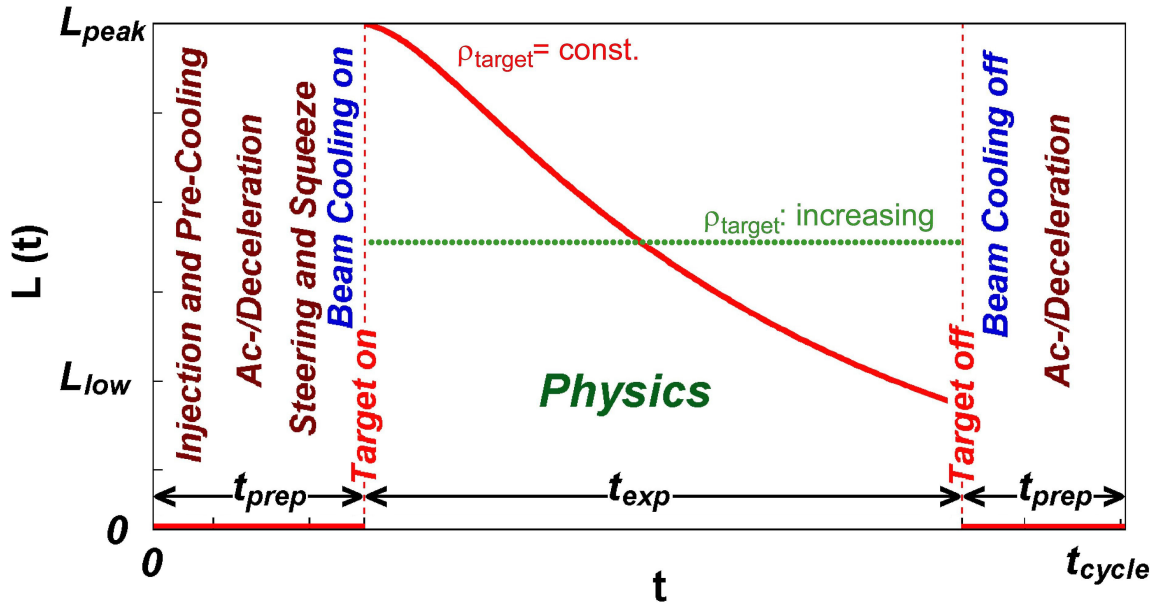


Figure 11: A typical cycle in the operation of the HESR with RESR[67].

each run. During the preparation time the target beam (see section 2.2.3) is switched off. Once the target beam is switched on, it marks the beginning of the experimental time, and the luminosity profile will follow the exponential decay of the form

$$L(t) = L_0 \cdot \exp\left(-\frac{t}{\tau}\right). \quad (2)$$

The total beam lifetime τ is defined as the time at which point the luminosity has reached $1/e$ of the peak luminosity L_0 . The most dominating effect for the beam loss or beam lifetime is the hadronic interaction. Next to first dominating effects are the small angle or coulomb scattering and the energy straggling. The Touschek Effect, which describes losses due to single large-angle intra-beam scattering [68], is fourth largest. Particles that have not exited the beam pipe will be reintegrated into the antiproton beam by the powerful cooling system.

For the two foreseen operation modes, the high resolution (HR) and the high luminosity (HL) mode, the specifications of the HESR are summarized in table 1. Without the

beam parameters	HL mode	HR mode
p [GeV/c]	1.5 - 15	1.5 - 8.9
$\Delta p/p$ (rms)	$\approx 10^{-4}$	$\geq 3 \cdot 10^{-5}$
N antiprotons	10^{11}	10^{10}
$\mathcal{L}_{\text{peak}}$ [$\text{cm}^{-2} \text{s}^{-1}$]	$2 \cdot 10^{32}$	$2 \cdot 10^{31}$

Table 1: Design goal antiproton beam parameters for the HESR in the HR and HL mode of operation [69]. A target density of $4 \cdot 10^{15} \text{ atoms/cm}^2$ was assumed.

RESR and the electron cooling system at the beginning of PANDA, only the high resolution mode will be available with a slightly worse momentum resolution of $\geq 5 \cdot 10^{-5}$.

p_{beam}	1.5 GeV/c	4.06 GeV/c	8.9 GeV/c	15 GeV/c
emittance (rms) [mm mrad]	1.45	0.53	0.244	0.145
spot size (rms) [mm]	0.8	0.8	0.8	0.8
divergence (rms) [mrad]	1.81	0.67	0.31	0.18

Table 2: Expected HESR beam parameters HL mode with $N = 10^{11}$ antiprotons

ADDITIONAL BEAM PARAMETERS Several aspects of the antiproton beam can introduce systematic effects that are crucial for the determination of the luminosity with the luminosity detector (LMD) and will be mentioned in the following. Ideally every antiproton would travel on the same trajectory throughout the beam line. This would correspond to a single point in the phase space x, y, p_x, p_y, p_z (see appendix B.1). However in reality the particles are distributed around this ideal value. This distribution can have two possible variations from the ideal value, mean and variance. Naturally the phase space can be split into the longitudinal p_z and transversal x, y, p_x, p_y phase space. The transversal phase space can further be divided into x, y and p_x, p_y . It is now of high interest to obtain realistic values for the mean and variance of these values. Variations of p_z are called the momentum resolution σ_p as usually the z axis is aligned with the beam line, carrying the largest contribution of the total particle momentum. The magnitude of transversal variations can be expressed with the beam emittance ϵ , which is very common in accelerator dynamics. The design goals for the emittance $\epsilon_{x,y}$ and the momentum spread σ_p of the HESR antiproton beam during physics data taking are

$$\epsilon_{x,y} = \frac{1 \text{ mm mrad}}{\beta\gamma} \left(\frac{N}{N_0} \right)^{4/5} \text{ (RMS)} \quad (3)$$

and

$$\frac{\sigma_p}{p} = \frac{1.33 \cdot 10^{-3}}{\beta\gamma} \left(\frac{N}{N_0} \right)^{2/5} \text{ (RMS)} \quad (4)$$

with the reference number $N_0 = 3.5 \cdot 10^{10}$. Note that the beam emittance and momentum spread are not only depending on the number of antiprotons N , but is also reduced by the momentum boost in form of the $\beta\gamma$ Lorentz factor. This effect is called adiabatic damping [70, p.48].

From the emittance the variation of the subspaces x, y and p_x, p_y can be calculated. They are also known as the beam spot and divergence. In order to have a high interaction rate the RMS beam spotsize should be roughly 0.8 mm [71], and is assumed as fixed. With the emittance and the beam spotsize, the divergence can be calculated as explained in the appendix B.1. These beam parameters are summarized in tables 2 and 3 for the two running modes. It should be noted that the beta function is adjustable in the range from 1 m to 20 m, and describes the trajectories of particles in the accelerator. In the case of the HL mode the desired spotsize of 0.8 mm would therefore not be possible, but a slightly larger spotsize of 1.2 mm has to be used. As a consequence the divergence becomes smaller to about 1.2 mrad. Similarly for the highest beam momentum in the HR mode the beta value of 20 m will be exceeded and the actual spotsize and divergence would vary slightly from the values given in table 3. The mean variations of the antipro-

p_{beam}	1.5 GeV/c	4.06 GeV/c	8.9 GeV/c	15 GeV/c
emittance (rms) [mm mrad]	0.23	0.08	0.04	0.023
spot size (rms) [mm]	0.8	0.8	0.8	0.8
divergence (rms) [mrad]	0.29	0.11	0.05	0.03

Table 3: Expected HESR beam parameters HR mode with $N = 10^{10}$ antiprotons

ton distribution from the ideal accelerator trajectory in the phase space are the mean position, the mean angle and the mean momentum. Variations in position and angle will be referred to as beam offset and beam tilt. The beam position will be measured with so called beam positioning monitors (BPM), that are located upstream and downstream of the PANDA experiment, roughly 20 m apart. Those devices measure the center of gravity of a beam charge distribution with a resolution in the order of $100 \mu\text{m}$ [72]. This leads to uncertainties of the beam offset of roughly $200 \mu\text{m}$ and the tilt of the beam of about $20 \mu\text{rad}$, neglecting component position uncertainties.

Taking all these effects together, combined upper bounds can be estimated for the individual beam properties, based on the beam losses on the walls of the beampipe. Since the non-interacting beam travels without any focusing along the PANDA experiment, the bottleneck is located roughly 11 m behind the IP, where the beampipe diameter is 70 mm. Obviously the beam spot size is almost irrelevant, as the beampipe diameter is much greater than the typical beam spot size at the IP. Assuming the beam is point-like in x, y at the IP and normal distributed in p_x, p_y , the beam loss rate is given by

$$\tau^{-1} = -\ln \left(\text{erf} \left(\frac{3.2 \text{ mrad} - 0.9 \cdot r_{\text{offset}} \frac{\text{mrad}}{\text{cm}} - \theta_{\text{tilt}}}{\sigma_{\text{div}}} \right)^f \right). \quad (5)$$

erf is Gauss error function and f represents the revolution frequency which is roughly 450 kHz. The value $3.2 \text{ mrad} \approx \frac{35 \text{ mm}}{11 \text{ m}}$ is the maximal angular acceptance of the antiproton beam calculated from the bottleneck values of the beampipe at the LMD stated above. Keeping the beam loss rate from the beampipe interaction an order of magnitude below the typical beam loss rates of $1 \cdot 10^{-4}$, we can determine critical upper bounds for the beam offset, tilt and divergence $r_{\text{offset}}^{\text{crit}} = 0.5 \text{ cm}$, $\theta_{\text{tilt}}^{\text{crit}} = 0.5 \text{ mrad}$, $\sigma_{\text{div}}^{\text{crit}} = 0.5 \text{ mrad}^2$.

While momentum resolution can be very high due to the powerful cooling system of the HESR the trueness or absolute precision depends on beam momentum measurement methods. The measurement of particle revolution frequencies by Schottky noise spectrum analysis and the orbit length via BPM readings gives direct access to the momentum spread and its absolute value, with an beam energy uncertainty of 100 keV in the charmonium region [73].

2.2.2 Physics Program

The PANDA experiment is a multi purpose experiment in the field of hadron and nuclear physics [74–76]. Thus it addresses a rich spectrum of physics topics:

² Note that these critical values are shared amongst each other, therefore, if the beam offset is smaller, higher values in the divergence and tilt may be possible.

HADRON SPECTROSCOPY: Hadron spectroscopy is dedicated to the search for exotic particles and the measurement of hadron properties. Exotic particles do not simply consist of 2 or 3 constituent quarks, but carry additional degrees of freedom either by more quark content or gluon contributions. They shed light on the full allowed particle space of QCD. Also there are discovered particles which do not fit very well into the current model predictions, with especially large deviations in the charmonium, D-meson and baryon sector. For this purpose \bar{P} ANDA has exceptional capabilities due to its antiproton beam and variable beam energy allowing the direct productions of a large variety of particles via formation reactions. Their line shape information is accessible by using the method of energy scans.

IN-MEDIUM EFFECTS: The origin of hadron masses in the context of spontaneous chiral symmetry breaking in QCD and its partial restoration in a hadronic environment can be studied with \bar{P} ANDA. So far the light quark sector was the primary focus, but with the higher center of mass energies \bar{P} ANDA can extend these studies to the hidden and open charm region. In addition the J/ψ nucleus dissociation cross section can be deduced by comparing measurements of J/ψ and D meson production cross sections in $\bar{p}p$ annihilation on a series of nuclear targets. It is a fundamental parameter for understanding of the J/ψ suppression in relativistic heavy ion collisions interpreted as a signal for quark-gluon plasma formation.

NUCLEON STRUCTURE: Exclusive $\bar{p}p$ annihilation into two photons at large s and t can be described with generalized parton distributions (GPDs) [77, 78]. It is proposed to measure the crossed-channel Compton scattering and the related exclusive annihilation processes with a scalar meson, a vector meson, or a lepton pair in the final state. The comparison of the differential cross sections of the various processes and the comparison with GPD based models will allow new insights into the annihilation process in terms of quark models and QCD. Via the process $\bar{p}p \rightarrow e^+e^-$ it is possible to determine the electromagnetic form factor of the proton in the time-like region. In the low Q^2 region down to threshold several experiments have measured the proton form factor, while at high Q^2 , of up to $15 \text{ GeV}^2/c^2$, only few measurements with limited statistics exist. Unlike the other experiments \bar{P} ANDA is able to determine the form factors $|G_M|$ and $|G_E|$ separately over a wide Q^2 range from threshold to $20 \text{ GeV}^2/c^2$ with significant improvements on the results in the high Q^2 region.

HYPERNUCLEI: Replacing an up or down quark with a strange quark in a proton or neutron of a nucleus leads to the formation of a hypernucleus. With the introduction of the quantum number strangeness in the nucleus a third dimension is added to the nuclear chart. Even though single and double Λ -hypernuclei were discovered roughly 60 years ago, only 8 double Λ -hypernuclei are presently known, in spite of considerable experimental effort. With its \bar{p} beam copious production is expected at \bar{P} ANDA. The determination of the $\Lambda\Lambda$ strong interaction strength will be the first result, which is not feasible by direct scattering experiments. Because the hyperons are not restricted by the Pauli principle to populate all possible nuclear states, they are an excellent probe for the structure of the nucleus and the hyperon-nucleon interaction. Furthermore, the $\Lambda - N$ weak interaction can be studied with four-baryon, strangeness non-conserving reactions like $\Lambda N \rightarrow NN$ and $\Lambda\Lambda \rightarrow \Lambda N$ in the nucleus [76, p.140].

2.2.3 The PANDA Detector

Due to the broad spectrum of the physics program a universal experimental setup with a 4π angular coverage is needed. The targeted precision of the measurements sets high demands on the track reconstruction resolution and particle identification capabilities. Furthermore the high interaction rates require corresponding radiation hardness of the detector subsystems, which also have to be able to handle the high data rates. As shown in figure 12 the PANDA detector guarantees a large angular coverage with its target/barrel and forward spectrometer part. Its detector subsystems will be introduced in more detail in the following.

PANDA TARGET To achieve high luminosities the PANDA experiment has a fixed target in the heart of the target spectrometer. The target system varies depending on the physics measurements that will be performed and can be roughly divided in solid state and “gaseous state” targets. Solid targets will be used for studies of antiproton-nucleon reactions and hypernuclei productions and consist of wires or foils. The high density “gaseous” targets which will be used during the first years of PANDA operation. Two different target systems are being developed for PANDA: A cluster-jet target and a pellet target [80].

The cluster-jet is produced by expansion of pre-cooled gas through a special convergent-divergent nozzle into vacuum. With accurate pressure and temperature settings condensation into clusters is observed. The dimensions of the jet are small enough to achieve a high overlap with the antiproton beam. The target jet beam density can be parameterized according to the formula

$$\rho_T(x, z) = \rho_0 \cdot \frac{\operatorname{erf}\left(\frac{b_z/2-z}{s}\right) - \operatorname{erf}\left(\frac{-b_z/2-z}{s}\right)}{2} \cdot \frac{\operatorname{erf}\left(\frac{b_x/2-x}{s}\right) - \operatorname{erf}\left(\frac{-b_x/2-x}{s}\right)}{2} \quad (6)$$

where erf is the error function. b_x and b_z denote the widths of the beam with the highest beam density ρ_0 at its center. Within this distribution the density is homogeneous, which is another advantage of the cluster jet target as it results in a more constant luminosity over time. Prototype measurements have led to target densities of up to $\rho_0 = 1.7 \cdot 10^{15} \text{ atoms/cm}^3$ with beam dimensions of $b_z = 13.1 \text{ mm}$, $b_x = 3.3 \text{ mm}$ and $s = 1.39 \text{ mm}$ [81]. The dimensions along y are infinite for a constant target beam.

The main part of a pellet target is a triple-point chamber. There a jet of a cryogenic liquid is injected through a nozzle into a gas of the same element or helium, which is kept near the triple-point. The nozzle is vibrating periodically, driven by a piezoelectric transducer, what in turn leads to drop production. Those drops are further cooled before exiting the chamber as a very stable frozen pellet stream through a thin capillary into the antiproton beam. With 10 pellets in average at the interaction point and a typical pellet size of $30 \mu\text{m}$ an effective thickness of up to $5 \cdot 10^{15} \text{ atoms/cm}^2$ is reached. This corresponds to the maximum interaction rate at PANDA. Due to relatively slow target beam speed of currently about 60 m/s its divergence is harder to control as in comparison for the cluster jet target. With an optical tracking system to record the beam direction the pellet position can be determined with an accuracy of better than 0.1 mm at the in-

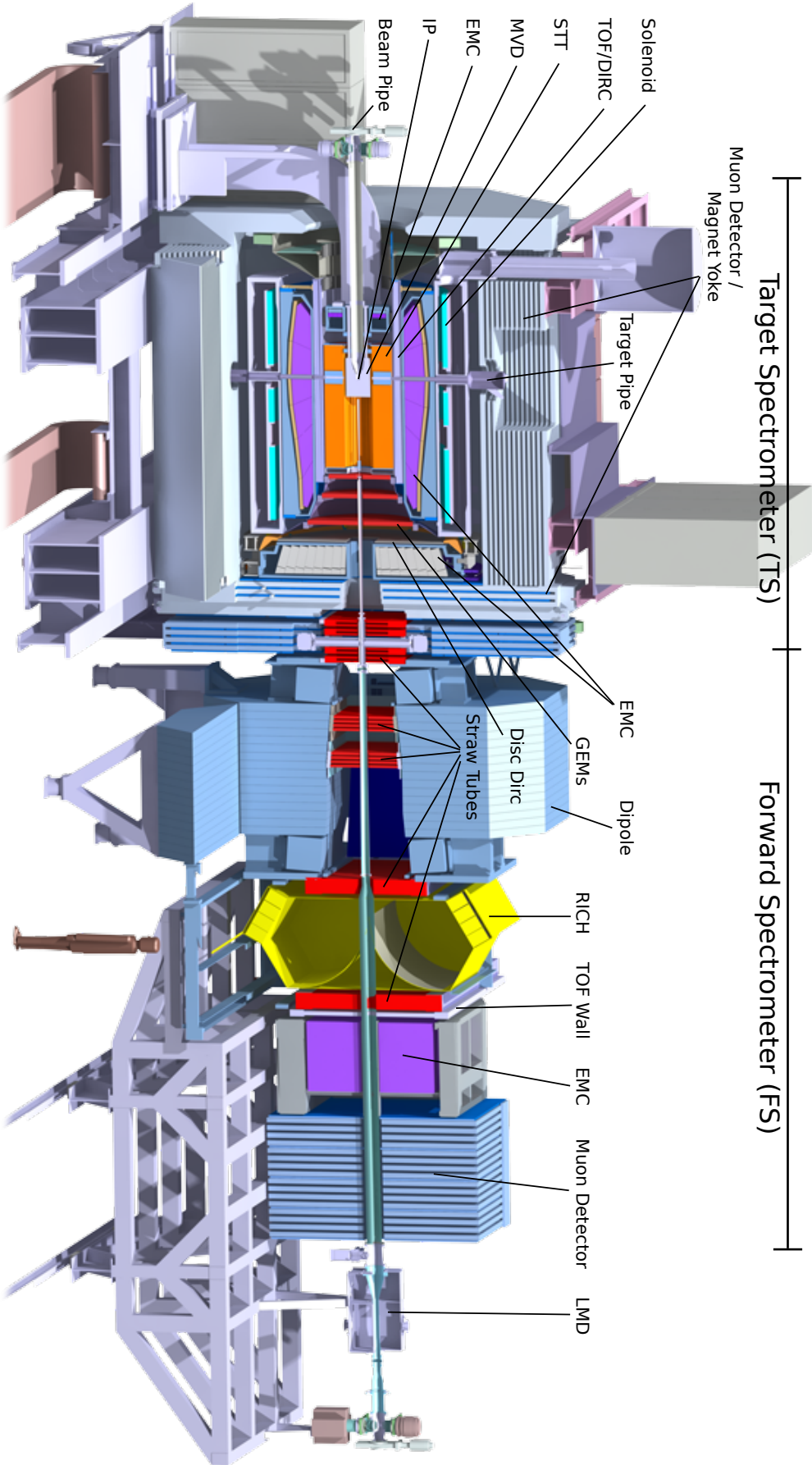


Figure 12: Side view of the complete PANDA experiment [79]

teraction region, which benefits the reconstruction of certain charmonium and Hyperon decays [82]. However the diameter of pellets has to be increased and the frequency has to be reduced such that in average only one pellet crosses the antiproton beam. The effective target thickness is reduced down to $2 \cdot 10^{15} \text{ atoms/cm}^2$. The target beam will have approximately a cylindrical shape with a full width diameter of about 3 mm.

	cluster target	pellet target
eff. thickn. [atoms/cm^2]	$\leq 2 \cdot 10^{15}$	$\geq 4 \cdot 10^{15}$
size transverse	2 – 3 mm	≤ 3 mm
size longitudinal	15 mm	≤ 3 mm

Table 4: Properties of the target beams for the PANDA experiment. Numbers are based on already achieved results [80, 81].

The specifications of these two target systems are summarized in table 4. For a constant instantaneous luminosity, which is under discussion, either the target density or the overlap between the antiproton beam and the target beam has to be constantly increased starting with a low density or small overlap. That way the decreasing number of antiprotons in the HESR is compensated. Both solutions require a fast measurement of the relative instantaneous luminosity as a feedback for the target systems. The variation of the antiproton beam and target is foreseen by the hypernuclei setup [83, 84], with a primary target that consists of a thin carbon fiber allowing the produced Ξ particles to escape. To obtain reaction rates in the order of $1 \cdot 10^6 \text{ s}^{-1}$, the target is placed on the edge of the accelerator beam spot. To keep the average luminosity as high as possible the target will be shifted to the antiproton beam center over time.

THE TARGET SPECTROMETER For the determination of momenta of charged particles one requires tracking detectors and a magnetic field. The barrel part has a solenoid magnet with a magnetic field strength of 2 T around the IP and several tracking detectors. The most inner detector surrounding the IP is the micro vertex detector [85]. It is a combination of semiconductor strip sensors and pixel sensors in the regions of high track multiplicities delivering the high vertex resolution of below $100 \mu\text{m}$. Both the primary interaction vertex and secondary vertices of short lived particles and delayed decays rely on information of the micro vertex detector (MVD). Furthermore it improves the momentum resolution and PID. Just surrounding the MVD is the central tracker, the straw tube tracker (STT) [86] consisting of a total of 4636 straws. A straw is a 10 mm thick aluminised mylar tube, which is operated with an ArCO_2 gas mixture at an overpressure of 1 bar, making it self-supporting. Each straw tube contains a single anode wire in the centre, collection the generated charge clouds. They are arranged in planar layers around the beam pipe at radial distances 15 cm-41.8 cm and an overall length of 150 cm. The detector delivers position resolutions of less than $150 \mu\text{m}$ with a material budget of 1.2 % of one radiation length at a momentum range from about a few 100 MeV/c up to 8 GeV/c. In addition energy loss (dE/dx) for the particle trajectories can be calculated, which is needed in particular to separate protons, kaons and pions in the momentum region below 1 GeV/c. Particles emitted at angles below 20° are not covered by the STT and will be tracked by three planar gas electron multiplier (GEM) stations placed approximately 1.1 m, 1.4 m and 1.9 m downstream of the target. The GEMs are able to sustain the high

particle rates in the forward direction due to the relativistic boost of the fixed target setup and enable unambiguous tracking with a position resolution below $100\ \mu\text{m}$.

Going further, for the detection of neutral particles and the identification of light charged particles the electromagnetic calorimeter (EMC) is a crucial detector. The EMC is made up of the barrel part, the forward and the backward endcap. Here lead tungstate PbWO_4 crystals are mostly read out by large area avalanche photodiodes. On the one hand this enables good energy resolution of $1.54\%/\sqrt{E(\text{GeV})} + 0.3\%$ for photon and electron detection under the compact design conditions of the target spectrometer. On the other hand short decay times of less than $20\ \text{ns}$ and a good radiation hardness have been achieved [87]. The crystals are aligned to the proximity of the IP.

Several state of the art PID systems establish the last group of subsystems, which are responsible for classifying a large variety of particles over a wide kinematic range. The time-of-flight (TOF) system achieves the best classification for low momentum particles and is located just outside of the central tracker. For the intended time resolution of $100\ \text{ps}$, a three standard deviation separation for π/K of up to $430\ \text{MeV}/c$ at 90° and $760\ \text{MeV}/c$ at a polar angle of 22° is achievable. In addition it can deliver timing information that can improve the performance of the trigger for the hypernuclei program and help reduce background and correct for dispersion effects in the detector of internally reflected Cherenkov light (DIRC) subsystem. The DIRC uses the emitted Cherenkov radiation to provide π/K separation up to about $4\ \text{GeV}/c$ in the target spectrometer at polar angles between 22° - 140° . Particles crossing the solid fused silica slabs with a thickness of $1.7\ \text{cm}$, surrounding the beam line at a radial distance of $48\ \text{cm}$, create the Cherenkov light, that is then detected by micro-channel plate photomultiplier tubes (MCP-PMTs). The DIRC also serves for the distinction between gammas and relativistic charged particles entering the EM-calorimeter behind. In the forward direction another DIRC in shape of a large disc is located in the endcap. It will provide π/K identification in the higher momentum range at polar angles of 5° - 22° .

Since muons are extremely penetrable compared to other particles, they are detected in a typical absorber-detector combination. The PANDA muon system consists of alternating detection and absorber layers, introducing enough material budget to absorb remaining pions. Hence only muons will fully pass the detection system and can therefore be successfully identified. The barrel part consists of 13 sensitive layers, each $3\ \text{cm}$ thick, surrounded with iron absorbers of $3\ \text{cm}$ - $6\ \text{cm}$ thickness. For the forward end cap more material is required, due to the occurring higher energetic particles. Therefore, six detection layers are placed around five $6\ \text{cm}$ thick iron layers. The sensors itself are rectangular aluminum mini drift tubes (MDTs). Behind the forward end cap a removable muon filter with four additional layers of $6\ \text{cm}$ iron and corresponding detection layers is placed between the solenoid and the dipole magnets. This also acts as an additional magnetic screen between the two magnetic fields.

THE FORWARD SPECTROMETER The target spectrometer has an opening in the forward direction for particles with polar angles below 5° and 10° in vertical and horizontal z -direction. Charged particle tracking is done with the dipole magnetic field of $1\ \text{T}$ ($2\ \text{T m}$ bending power) and the forward tracker (FT). The FT consists of six tracking stations each equipped with 2 detection planes. Similar to the central tracker, they are based on straw tube detectors of $10\ \text{mm}$ thickness. Every detection plane consists of 32 straws arranged side by side in two layers, making up 4 straw planes per tracking station. The two inner straw planes are inclined by $\pm 5^\circ$ with respect to the outer planes, allowing to

handle multi-track events while the average track multiplicity in the FT is about 1 per event. With the position resolution of 0.1 mm per detection layer and a material budget of 0.3% X_0 for each tracking station, a momentum resolution of below 1% is achieved. Also the tracking stations should stand high local particle fluxes in the vicinity of the beam pipe with rates of about $2 \cdot 10^7 \text{ s}^{-1}$ in the high luminosity mode.

Photons and electrons in the forward direction will be measured by a Shashlyk-type EMC with high resolution and efficiency about 7-8 m downstream of the target. Each Shashlyk module is made up of alternating lead and scintillator plates with embedded wavelength shifting fibers. Then the scintillation photons can pass to a photomultiplier tubes (PMTs), which is attached to the fibers. This is a well established and successfully used detector with an energy resolution of $4\%/\sqrt{E}$.

Finally, also the forward spectrometer has additional particle identification detectors. The forward TOF are walls of plastic scintillator slabs, which are read out on both ends by fast PMTs. It ensures a 3σ π/K and K/p separation at momenta below 2.8 GeV/c and 4.7 GeV/c respectively. One wall is placed in front of the forward EMC and another inside the dipole magnet opening, to detect low momentum particles which do not exit the dipole magnet. At the higher momenta a ring imaging Cherenkov (RICH) detector gives the necessary separation for pions, kaons and protons. Charged particles traveling through the silica aerogel and C_4F_{10} gas mixture produce Cherenkov radiation, which is reflected onto PMTs with a lightweight mirror. This enables particles separation in the momentum range 2-15 GeV/c, while keeping the material budget as low as possible. Similar to the muon system of the target spectrometer the muon range system, placed 9 m from the target, consists of interleaved absorber and rectangular aluminium mini drift tube (MDT) layers. The system allows discrimination of pions from muons, detection of pion decays and, with moderate resolution, also the energy determination of neutrons and anti-neutrons.

The last component in forward direction is the luminosity detector (LMD), which will be explained in detail in the next chapter.

PANDA TRIGGER AND DAQ Because the high precision physics goals of the PANDA experiment require a substantial amount of data, the PANDA data acquisition (DAQ) system has to handle high data rates of up to 200 GB/sec at an average interaction rate of 20 MHz [88]. To deal with the large fraction of background a sophisticated event filtering and trigger system are mandatory. One unique feature of PANDA is that no global hardware trigger will be used, but instead solely a partial reconstruction of the events will lead to the trigger decision. Every detector front end is running independently and employs feature extraction algorithms to select relevant data. It is collected by data concentrators and sent to a two stage event building network. Compute nodes reconstruct the reactions on the fly in order to form a trigger decision and write the interesting events to tape. To synchronize the DAQ system across all sub-detectors the synchronization of data acquisition (SODA) protocol[89] will be used. It offers a global clock with a jitter of less than 20 ps and timestamps coupled to the HESR beam structure. This way it is possible to assemble a complete event out of the information from individual detector components within the event building network.

LUMINOSITY MEASUREMENT @ PANDA

3.1 LUMINOSITY

In contrast to classical mechanics, no predictions for an individual reaction can be made in quantum theory. Instead each possible outcome has a certain probability to occur. Hence multiple identical and independent measurements have to be performed, in order to determine the probabilities. An experimental physicist determines the probability for a reaction in form of the cross section σ . The cross section denotes the interaction probability per flux and relates, together with particle flux or *instantaneous luminosity* \mathcal{L} , to the reaction rate

$$R = \mathcal{L} \cdot \sigma. \quad (7)$$

Because particle rates for processes are measured by counting N events over a period of time dt a time-integration of equation 7 has to be performed to

$$N = L \cdot \sigma \quad (8)$$

with

$$L = \int \mathcal{L} dt \quad (9)$$

the *time-integrated luminosity*. From this definition the luminosity can also be put in di-

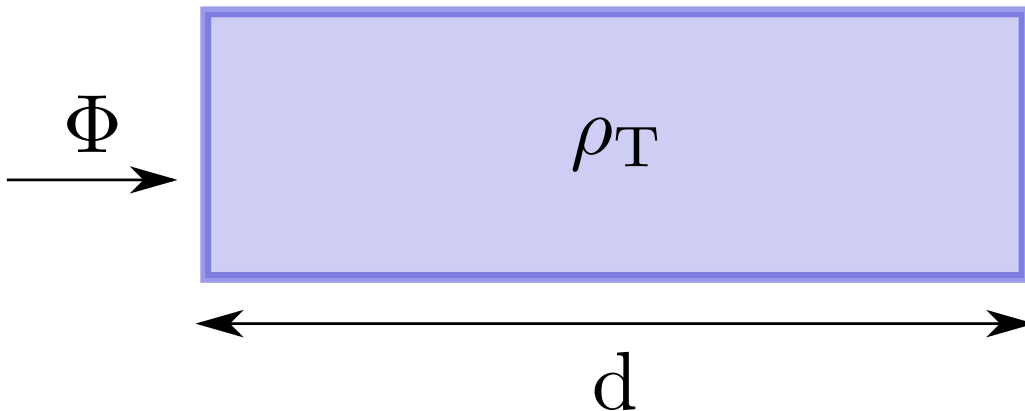


Figure 13: Illustration of luminosity for a beam of flux Φ impinging on a fixed target with density ρ_T and length d .

rect relation with the interacting particle bunches. The number of possible interactions depends on the amount of independently created initial states, which are controlled by

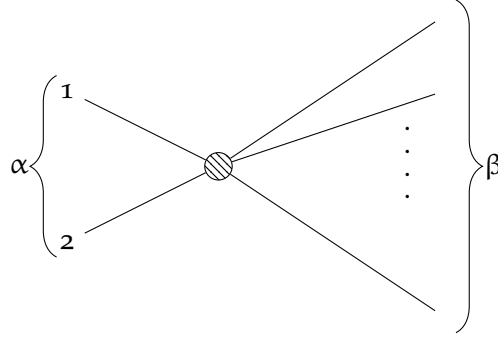


Figure 14: Illustration of a general scattering process from a two particle initial state α to a final state β .

the amount of colliding particles. For a fixed target experiment it can be shown that the luminosity[90] is equal to

$$\mathcal{L} = \Phi \rho_T d. \tag{10}$$

Here Φ is the accelerator beam flux, ρ_T the target density and d the target thickness. This assumes that all of the accelerator beam actually overlaps with the target.

The importance of luminosity can be directly concluded from equation 7. In quantum theory [91, p.134f] the S-matrix $S_{\alpha\beta}$ contains all of the interesting physics information and gives the probability amplitude for the transition from the initial state α to the final state β . Therefore the main physics interest lies in determining these matrix elements. For the case of a two particle initial state, the measured cross section stands in relation to the scattering matrix as

$$d\sigma(\alpha \rightarrow \beta) = (2\pi)^4 u_\alpha^{-1} |M_{\alpha\beta}|^2 \delta^4(p_\beta - p_\alpha) d\beta \tag{11}$$

with $S_{\alpha\beta} = -2\pi i \delta^4(p_\beta - p_\alpha) M_{\alpha\beta}$ and the relative velocity between the two particles in the initial state $u_\alpha = |\frac{\vec{p}_1}{E_1} - \frac{\vec{p}_2}{E_2}|$. The delta function ensures momentum and energy conservation as p_α and p_β are the four momenta of the initial and final state. Notice that in general the cross section is a differential, which gives the interaction probability per flux, in which the final state particles are in an infinitesimal phase space region $d\beta$ around the value β as described by

$$\frac{dN(\alpha \rightarrow \beta)}{d\beta} = \mathcal{L} \cdot \frac{d\sigma(\alpha \rightarrow \beta)}{d\beta}. \tag{12}$$

Experiments measure the number of events for the final state β in the proximity $d\beta$, $\frac{dN(\alpha \rightarrow \beta)}{d\beta}$. Therefore no absolute cross section values or S-matrix elements can be determined without the luminosity. However for probability ratios of two processes the case is slightly different. There the luminosity is not required, which is obvious from equation 12 by constructing the ratio of two cross sections.

3.2 LUMINOSITY MEASUREMENTS

In principle there are only two possible ways to measure the luminosity. One possibility is to use equation 10 directly, for which the target density and thickness as well as the accelerator beam flux information is needed. The latter can be determined from the accelerator side. When a charged particle passes through matter it loses energy through electromagnetic processes and this is also true inside a storage ring where a coasting beam goes through a thin target a very large number of times. The energy loss, which is proportional to the target thickness, builds up steadily in time and causes a shift in the revolution frequency in the machine which can be measured through the study of the Schottky spectra [92]. This allows the effective target thickness to be deduced and has been investigated with an internal proton beam of energy 2.65 GeV at the COSY accelerator using the ANKE spectrometer and a hydrogen cluster-jet target [93]. It yields luminosity values with a precision of about 5% and is also planned for the PANDA experiment. Unfortunately this method only works for a coasting beam, which is not accelerated to its nominal energy on each turn, but is continuously losing energy [93]. This means that only punctual measurements for separate runs can be performed and not simultaneously to the recording of the physics data.

Alternatively the luminosity can be obtained indirectly by the measurement of a reaction rate, while the luminosity can simply be determined by formula 12. This requires the knowledge of the cross section for the process. The more precise the cross section model is known, the smaller the systematic uncertainty from the model on the determined luminosity value. In e^+e^- annihilation experiments the preferred channel is Bhabha scattering ($e^+e^- \rightarrow e^+e^-$) for which the absolute cross section can be calculated accurately from QED [90]. On the contrary such a precisely known channel is not present in hadronic reactions, since QCD cannot be solved analytically in general. For the E760/E835 experiment the choice of the reference cross section was $\bar{p}p$ elastic scattering. By measuring the energy of the recoil protons in dependence on the scattering angle as close as possible to the limiting polar angle, the luminosity was determined [94]. Similarly, elastic $\bar{p}p$ reactions are used by the PANDA luminosity detector (LMD) to determine the luminosity. However only the anti-protons are measured, because most recoil protons cannot exit the beampipe or the solenoid magnetic field due to the low energies [85].

3.3 THE ELASTIC $\bar{p}p$ SCATTERING MODEL

The elastic scattering of $\bar{p}p$ contains two interfering processes. One is the long range force via the exchange of photons, coupling to the electric charge, and the other is the exchange of hadrons and gluons at shorter distances. The corresponding cross section is therefore expanded to

$$\frac{d\sigma_{\text{el}}}{dt} = \frac{1}{16\pi} |f_{\text{had}} + f_{\text{coul}} e^{i\delta(t)}|^2 = \frac{d\sigma_{\text{coul}}}{dt} + \frac{d\sigma_{\text{had}}}{dt} + \frac{d\sigma_{\text{int}}}{dt} \quad (13)$$

where t denotes the four momentum transfer and δ the Coulomb phase. Note that the value of t is defined as a negative number. f_{had} and f_{coul} denote the scattering amplitudes for the two interaction types that results in the respective cross sections σ_{had} and σ_{coul} and the interference part σ_{int} .

The coulomb cross section

$$\frac{d\sigma_{\text{coul}}}{dt} = \frac{4\pi\alpha_{\text{EM}}^2 G^4(t)(\hbar c)^2}{\beta^2 t^2} \quad (14)$$

is well understood and analytically calculable within QED. Here $\beta = v/c$ is the ratio of the velocity v to the speed of light c and \hbar denotes the reduced Plank constant. α_{EM} is the fine structure constant and $G(t) = (1 + \Delta)^{-2}$ the proton dipole form factor, with $\Delta = |t|/(0.71 \text{ GeV}/c)$. As evident from formula 14, the Coulomb part of the cross section ($t \rightarrow 0$) is divergent by virtue of the infinite range of the EM force. However, screening effects actually prevent the cross section from going to infinity. In addition the antiprotons will be measured starting at some minimal scattering angle by the experiment. This naturally implicates a cutoff for the lower t region and a correct description close to $t \rightarrow 0$ is not required. As EM force allows long distance interactions, it is the dominating process at small scattering angles where small momentum is transferred.

The hadronic part, dominating at larger scattering angles, cannot be calculated analytically, due to the self-coupling feature of the mediating gluons. Therefore only approximate empirical models can be used to parametrize this part of the elastic cross section. In the momentum transfer range $-t > 0.0001 \text{ GeV}^2/c^2$, where the hadron interaction is dominating, the description

$$\frac{d\sigma_{\text{had}}}{dt} = \frac{\sigma_{\text{had}}^2 (1 + \rho^2)}{16\pi(\hbar c)^2} e^{Bt} \quad (15)$$

is suitable [95]. σ_{had} is the total hadronic cross section, B the slope parameter and ρ the ratio of real to imaginary part of the hadronic scattering amplitude at zero momentum transfer. The parameters σ_{had} , B and ρ are obtained from fits to $\bar{p}p$ elastic scattering data from various experiments. Because the E760 collaboration has used this parameterization, we also refer to this model as the ‘‘E760 model’’.

The interference term

$$\frac{d\sigma_{\text{int}}}{dt} = \frac{\alpha_{\text{EM}}\sigma_{\text{had}}}{\beta|t|} G^2(t) e^{\frac{1}{2}Bt} (\rho \cos(\delta) + \sin(\delta)) \quad (16)$$

plays a minor role in the total cross section, as it is dominated at low t by the Coulomb cross section and similarly at larger t by the hadronic elastic cross section. The Coulomb phase δ depends on the momentum transfer t and the slope parameter B

$$\delta(t) = \alpha_{\text{EM}} \left[0.577 + \ln \left(\frac{B|t|}{2} + 4\Delta \right) + 4\Delta \ln(4\Delta) + 2\Delta \right]. \quad (17)$$

In the PANDA collaboration the dual parton model (DPM) generator is used to simulate the background from a large variety of inelastic antiproton proton reactions [96]. In addition it also simulates elastic scattering and provides a hadronic part that is valid over a wider t range [97] modeled by

$$\frac{d\sigma_{\text{had}}}{dt} = A_1 \cdot \left[e^{t/2t_1} - A_2 \cdot e^{t/2t_2} \right]^2 + A_3 \cdot e^{t/t_2}. \quad (18)$$

Unlike the ‘‘E760 model’’ it is not motivated by physics, and the parameters A_i and t_i are again obtained from existing measurements. Altogether the DPM generator implements

the full elastic cross section given by equation 13 and uses the Coulomb and Interference parameterizations specified by equations 14 and 16.

HADRON PART PARAMETERIZATION COMPARISON One of the systematic uncertainties on the luminosity measurement can arise directly from inaccuracies of the hadronic part of the elastic $\bar{p}p$ scattering cross section. They were studied extensively in [98], which includes a comparison of the DPM elastic hadronic model (equation 18) and the “E760 model” (equation 15). The relative uncertainty after integration of the luminosity over

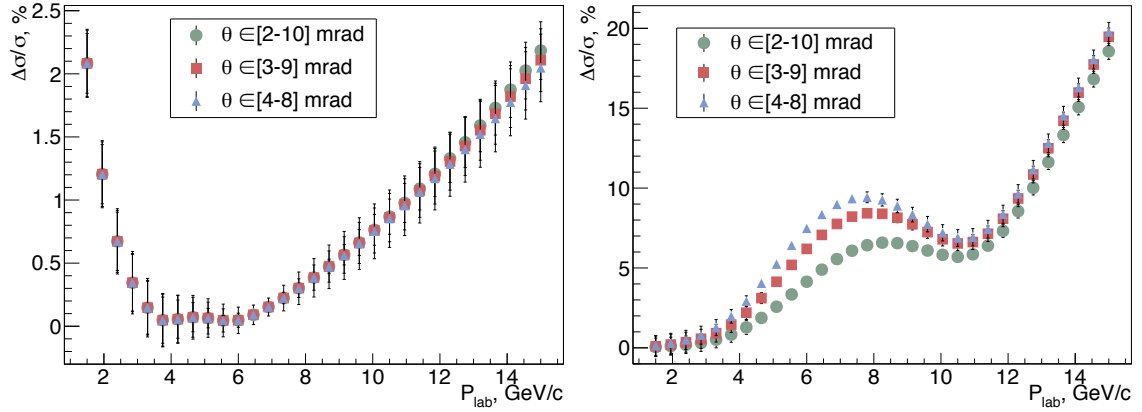


Figure 15: The relative uncertainty of the cross section integrated over different polar angles ranges in dependence on the beam momentum p_{lab} (left: E760 model; right: DPM model) [98, p.44 f].

three different angular ranges is shown in figure 15. The chosen integral ranges are close to the angular range covered by the LMD of ≈ 3 mrad – 9 mrad. Clearly, the E760 model was tuned to the beam momenta data between 3 GeV/c and 7 GeV/c, visible by the small uncertainties in this range. Below and above this range the uncertainty increases due to the extrapolation. The data from previous experiments, which are used for the two model parameterizations, are shown in figure 16. On the contrary the DPM parameterization

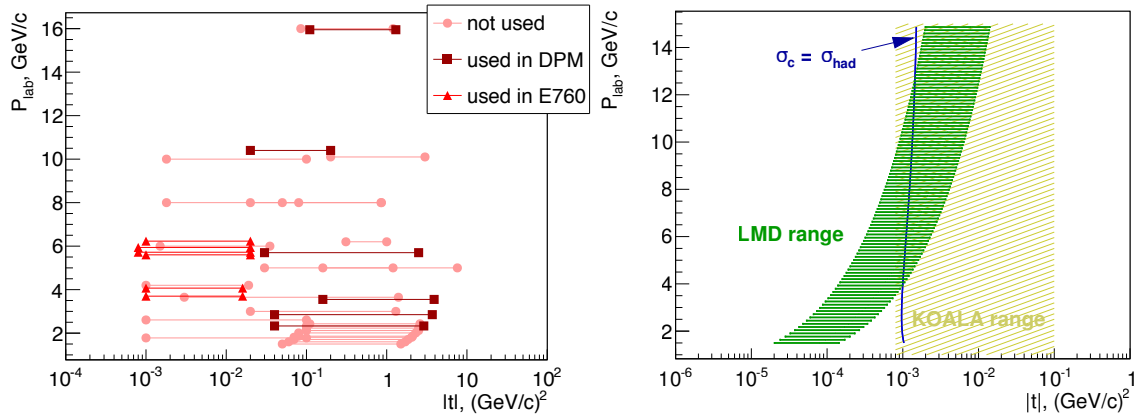


Figure 16: Left: $|t|$ ranges for previous $\bar{p}p$ elastic scattering measurements [98, p.48] Right: Measurement region for the luminosity detector at PANDA (green) and for the KOALA experiment (golden) in terms of momentum transfer $|t|$ [98, p.40].

tries to model the hadronic elastic cross section over a larger momentum range by using also information from previous measurements at higher momenta. As figure 16 shows, the used measurement points unfortunately lie even more above the four-momentum

transfer range of the LMD than the data used by the E760 parameterization. This leads to even larger uncertainties of the elastic cross section. However as both parameterizations lack experimental information in the LMD momentum and momentum transfer range, a more precise measurement is needed for the luminosity determination at PANDA.

For this reason the KOALA experiment will measure both the recoil protons as well as the elastically scattered antiprotons in the relevant four-momentum range (see figure 16) for various momenta [64], in order to precisely determine the hadronic part of the elastic scattering. A special beampipe in the interaction region was designed specifically for KOALA, which allows the measurement of the recoil protons. In the forward direction the luminosity detector (LMD) measures the scattered antiprotons from the elastic $\bar{p}p$ scattering, implying small momentum transfers or small scattering angles θ , due to the forward boost from the fixed target setup.

3.4 THE LUMINOSITY DETECTOR

In order to minimize the systematic uncertainty from the hadronic part of the elastic scattering model, the measurement is performed at low momentum transfers where the Coulomb cross section is dominant. Therefore the placement of the LMD should be as close as possible to the non-interacting beam and as far away as possible from the interaction point (IP). Hence the LMD is placed 10.5 m-12.5 m behind the target measuring at the angular range of approximately 3 mrad to 9 mrad. Unfortunately, the low momentum transfers prevent the measurement of the recoil protons, as the kinetic energies are too low to penetrate the beam pipe or the protons are curling in the solenoid magnet field at very low radii [85]. Consequently the tracks of the antiprotons have to be measured precisely to ensure a high luminosity precision and accuracy.

The elastically scattered antiprotons will travel inside the beampipe along the entire PANDA setup through the magnetic fields of the solenoid and dipole magnet until they reach the LMD. This is possible as the diameter of the beampipe is stepwise increasing upto the entrance of the LMD to ensure the desired angular acceptance. The placement behind the PANDA experiment is advantageous as the dipole magnetic field drastically reduces the background since only particles with negative charge and the correct momentum will get the needed deflection. This is crucial for the background suppression as neither the momentum nor the ID of particles are measured by the LMD.

3.4.1 *The Vacuum Box and Transition Region*

The complete setup of the LMD is shown in the figure 17. Inside the LMD vacuum box the beampipe tapers from a diameter of 200 mm to a diameter of 70 mm at the transition cone, allowing the elastically scattered particles at polar angles between ≈ 3 mrad and ≈ 9 mrad to enter the LMD volume. The transition cone is a laminate of a robust biaxially-oriented polyethylene terephthalate (boPET) foil and a conducting aluminum foil, shielding the electromagnetic fields of the non-interacting antiproton beam. Its diameter changes smoothly to minimize distortions of the beam from rapid conductivity changes. Due to the dimensions of the LMD and the out-gassing of various detector components, the high grade vacuum of the beampipe of $1 \cdot 10^{-9}$ mbar is not feasible for the LMD. The transition foil separates the two vacua and allows an about 2 orders of magnitude worse vacuum in the LMD box, without altering the performance of the

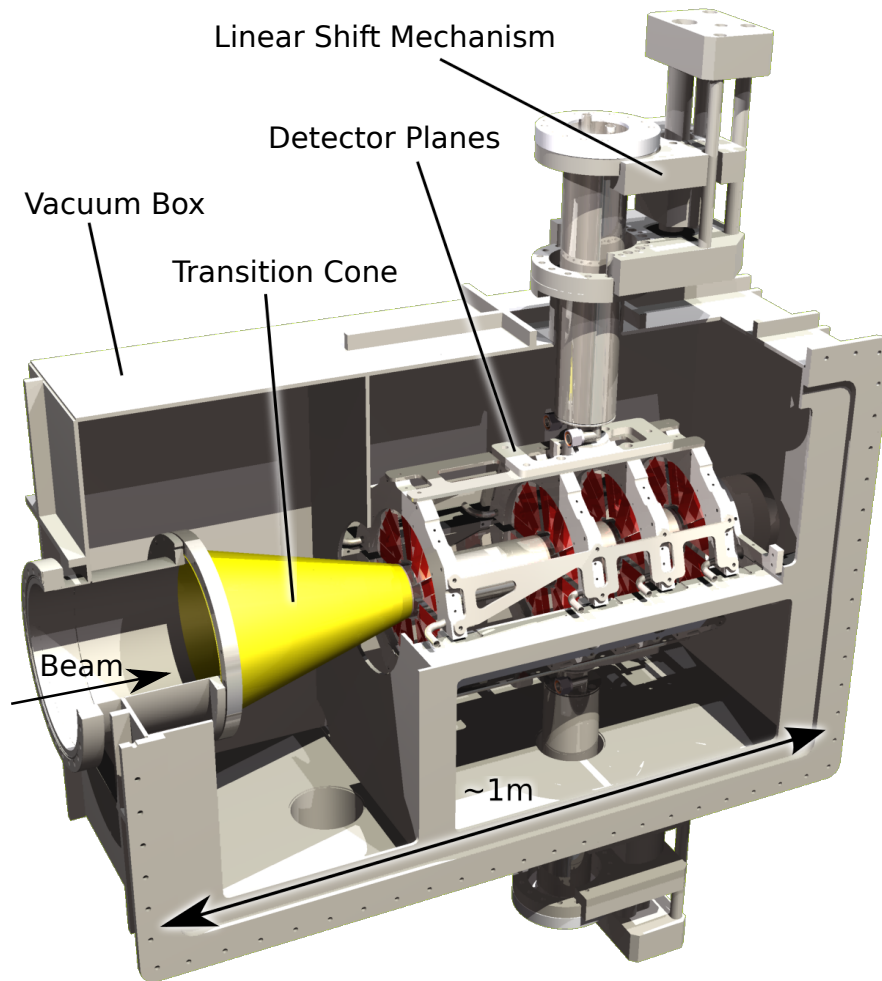


Figure 17: CAD Side view of the complete luminosity detector (LMD) [79].

detector. To prevent the transition foil from ripping, communication of both vacuum volumes, specially during evacuation, is important. This is achieved by a coupled pumping system of the beam pipe and the vacuum box itself [79].

Once the particles are inside the LMD vacuum, they will travel through 4 detector planes, where the first plane is placed at $z=11.24$ m and the following 3 with distances of 20 cm, 10 cm and 10 cm in between. Multiple scattering is proportional to the material budget, thus it is kept as low as possible in order to have a good angular resolution. For the LMD a total of 4 planes was chosen to be able to perform a track fit and obtain errors on the track parameters for validation reasons. In principle three layers would suffice, but in case of a missing hit in a detection layer a fourth layer recovers these events. As each plane introduces additional multiple scattering, the first two planes have the largest impact on the angular track resolution and their distance was chosen to be larger to generate a large lever arm. A minimal distance of 10 cm between planes is a trade-off between the compact design and mechanical spacing requirements.

3.4.2 Detector Layout

State of the art pixel sensors [99], the high voltage monolithic active pixel sensors (HV-MAPS), are used for the actual particle track detection. They convert the raw analog signals to digital row and column hit information directly on the chip. The main difference of HV-MAPS to normal MAPS technology is the relatively high bias voltage of 50 V and above, resulting in a larger number of charges and a faster charge collection in the order of nano-seconds. In addition the sensors can be thinned down to 50 μm making the material budget very low. The layout scheme of a single sensor can be seen in figure 18. A sensor has the dimension of 2 cm by 2 cm with pixel dimensions of 80 μm by 80 μm . Even though the majority of the sensor area is active, the guard ring on the border (100 μm) and also the digitization part (500 μm) will lead to some inefficiencies. Naturally the pixel design is able to handle high count rates and is read out in time-frames of 25 ns.

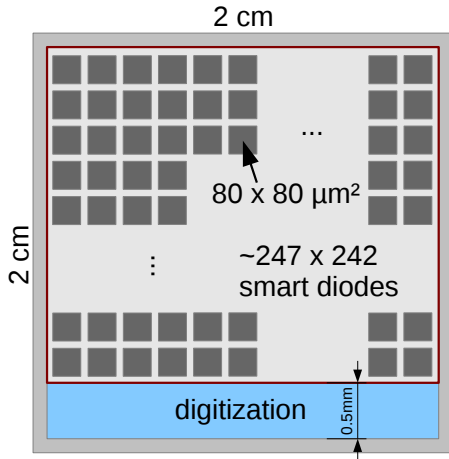


Figure 18: Illustration of the layout of a single HV-MAPS chip.

For beam instability reasons the detector is divided in an upper and lower half that can be retracted from the beam to avoid unnecessary radiation damage, e.g. during the injection phase of the beam. Each half plane consists of 5 modules and is depicted in figure 19. A module consists of a chemical vapor deposition (CVD) diamond wafer that has 5 sensors glued on each side optimizing the azimuthal coverage, making it a total of 400 sensors for the entire detector. The main disadvantage of the active pixel sensors is their heat generation of the on-chip

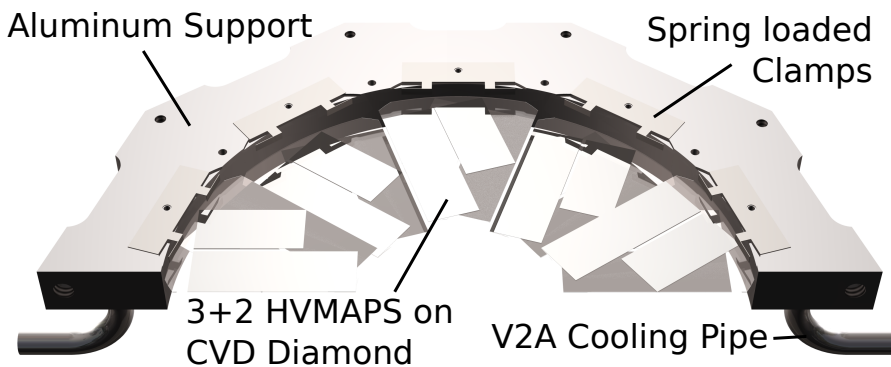


Figure 19: Illustration of a half plane acting as a cooling support of 5 modules. The aluminum structure contains a stainless steel cooling pipe. Electrical components which are attached to the surface of the cooling structure as well as the sensors on the back side of each module are not visualized.

electronics. As a result the sensors have to be cooled and diamond, with its superior heat conductivity, has been chosen as a cooling support structure. Altogether the radiation length of a single plane is $X/X_0 = 0.3735\%$, while next to the diamond, sensors and glue,

also the power and signal cables for the sensors will contribute to this value [79]. An aluminum structure holds the diamond wafers and maintains their temperature below 50 °C with the integrated cooling circuit.

3.4.3 DAQ System

The data from the 400 HV-MAPS is send to the LMD data acquisition (DAQ) system, where it is sorted, filtered and fast track reconstruction software decides which tracks should be stored. Time information from the SODA system, which sends common timing signals to all \bar{P} ANDA sub-detectors to correlate individual signals, are included in the data before it is transferred to the \bar{P} ANDA DAQ system. As mainly elastic scattering events will be reconstructed by the LMD, most \bar{P} ANDA physics events will be not or anti-correlated to the LMD and hence LMD event building can be regarded as independent¹[79]. For a controlled operation of the \bar{P} ANDA experiment, online information of the luminosity is essential and for this purpose a simplified instantaneous luminosity determination will be implemented. Together with the luminosity values of the HESR accelerator group absolute precision of about 10% for the online monitoring will be reached.

3.5 TRACK RECONSTRUCTION

The LMD software is developed for the extraction of the time-integrated luminosity from raw data, the individual pixel hits. During measurements the detector will deliver this information directly, however for simulation studies this pixel hit information has to be artificially generated. All simulations in the first part of this thesis have been performed with the PandaRoot [100] software package, which uses the geometry and tracking (Geant4) software [101]. It is initialized with realistic computer models or geometries of the important parts of the experiment setup. Because only a small fraction of particles in the forward direction is able to reach the LMD, only a few components of the entire detector setup are needed for the simulations. These are the geometries of the LMD, the beam pipe, the solenoid and the dipole magnet. High precision field maps are used in the simulation software for both magnets. The magnetic field strength of the dipole varies continuously with the beam energy, while the solenoid is operated at its full current or half current for beam momenta above or below 3.0 GeV/c.

The geometry of the LMD (figure 20) is composed of the vacuum box, the beampipe including the transition cone and the half planes including the aluminum support and cooling structures. Each module consists of a diamond wafer, layer of glue, the sensors and cables for the signal and power transmission. The cables are modeled by a layer of aluminum and kapton with an effective thickness. After the simulation the generated charge distributions in the active sensor material are digitized into pixel hits, using the geometrical layout of a sensor as shown in figure 18. Hereby individual thresholds for the deposited charge of each pixel can be set, which determine if the pixel information is used further. The row and column information of all of these fired pixels are calculated. At this point the simulated data will be processed with the same track reconstruction software as the real data.

¹ Few correlated events will be used to calibrate the LMD time constant in respect to \bar{P} ANDA.

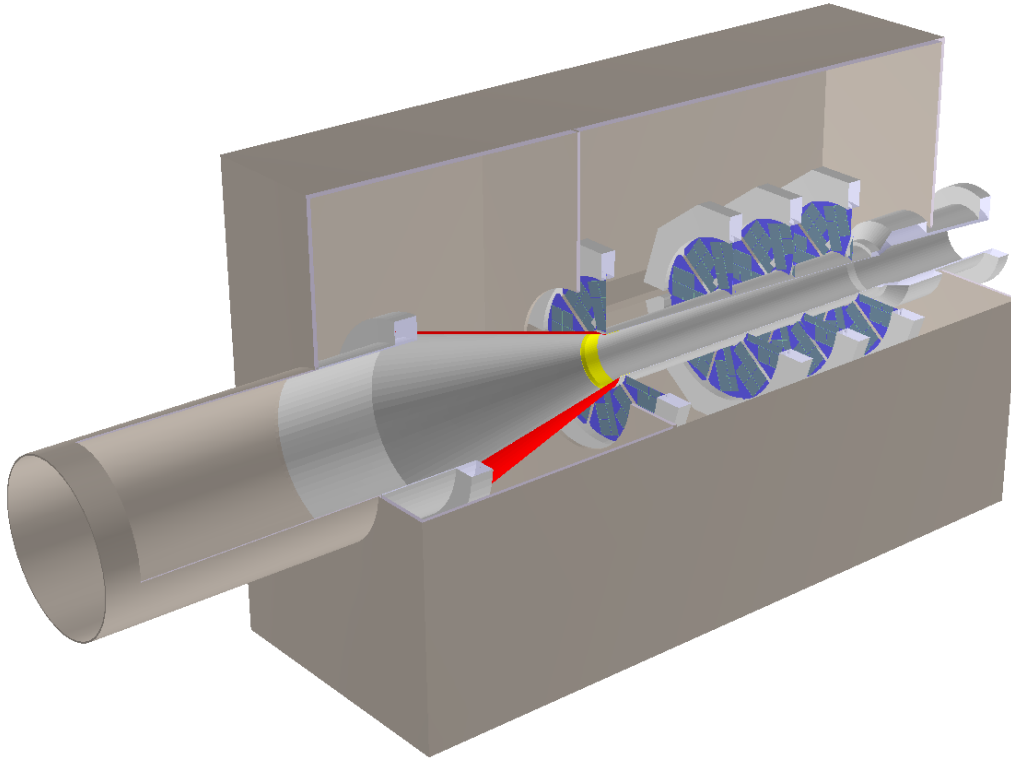


Figure 20: Simulation model of the luminosity detector.

By looking at the complete flow-chart of the software package (figure 21) one can see the workflow of the LMD software. The LMD fit procedure, which determines the luminosity from the angular antiproton distribution, requires three essential inputs: the reconstructed tracks arising from the actual measured detector hits, the detector acceptance and the detector resolution. In order to obtain this information several data processing steps are required, that can be categorized into three stages.

ALIGNMENT STAGE: At first in the so called alignment stage the misalignment of each individual sensor has to be detected with respect to its reference position in the PANDA coordinate system. The alignment itself consists of three parts, the alignment of the sensors on a module, the alignment of modules within a corridor and the alignment of the corridors to the global PANDA reference frame [102]. Usually the alignment procedure only has to be performed once after the detector has been physically undergone changes, i.e initial setup or retraction/insertion of the detector halves. While the first two alignment parts are crucial for the correct reconstruction of particle track parameters, the third part is elementary for correct determination of the displacement of the IP and the accelerator beam tilt.

ACCEPTANCE AND RESOLUTION PARAMETERIZATIONS: As a second step the detector acceptance and detector resolution parameterization are computed by using a MC data sample and by using the IP position information from the first stage.

DATA RECONSTRUCTION The third stage consists of the track reconstruction from the measured data, which has to be corrected for the misalignment of the sensors.

Note that the second and third step are only dependent on step 1, hence they are not time-ordered with respect to each other. All three stages share the same track recon-

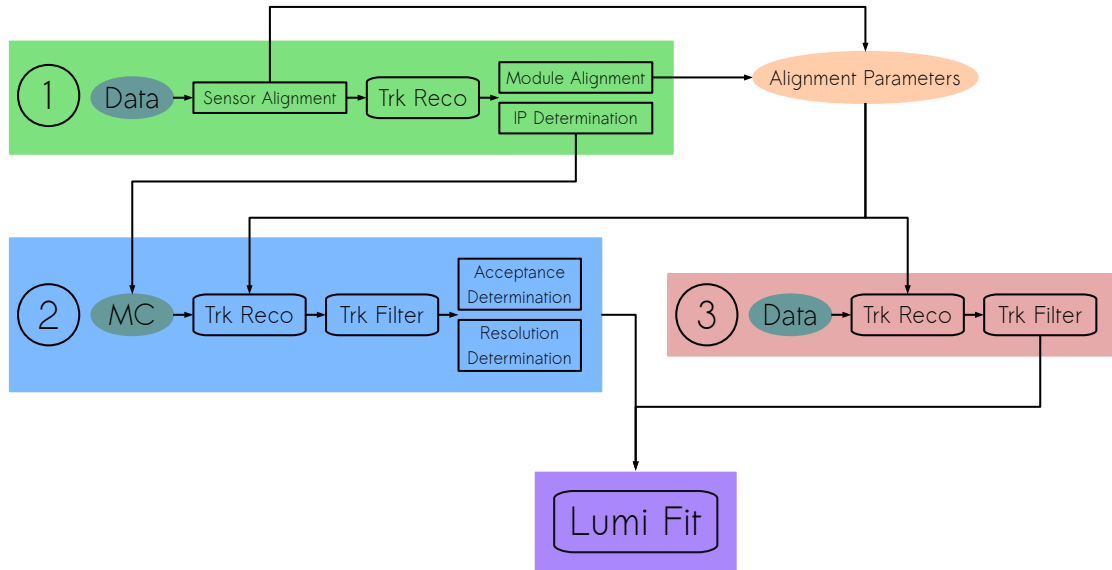


Figure 21: Flow-chart of the LMD software for the extraction of the luminosity starting from raw data.

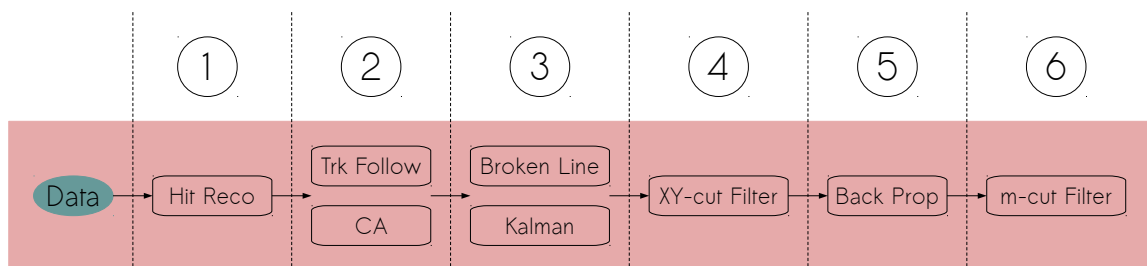


Figure 22: Data reconstruction software flow of the LMD software starting from raw data.

struction software. Figure 22 provides a zoom-in into stage 3 of figure 21. The complete reconstruction chain is separated into 6 steps, each performing a specific task going from the raw pixel data to the fully reconstructed track at the IP [98].

As a very first step the pixel hits can be filtered for hot pixels as an example. Then the row and column information of a sensor hit is converted into a hit in the PANDA coordinate system, that is further clustered with neighboring hits. Since the modules are mounted with sensors on both sides, certain areas of the modules have overlaps of front and back sensors (see figure 23). Clusters with a partner cluster in their proximity on the other side are merged together into a single cluster. In the next step track search algorithms try to find tracks in the collection of hits. Both the track-follower [103] and cellular automaton (CA) [98, 104] algorithms are implemented, while the latter is used as the default track finding method. The hits combined to a track candidate by the track finder are then fitted via a broken line fit, extracting the track parameters such as position and direction. In the broken line fit each segment between two detector planes is modeled as a straight line that are connected at the detector planes [105]. This model is able to describe the multiple scattering in the detector planes. Also a Kalman filter implementation is available, which was used mainly for testing as its track fitting speed is slower. The entity of the steps 1 to 3 are expressed by the boxes labeled with “Trk Reco” in figure 21.

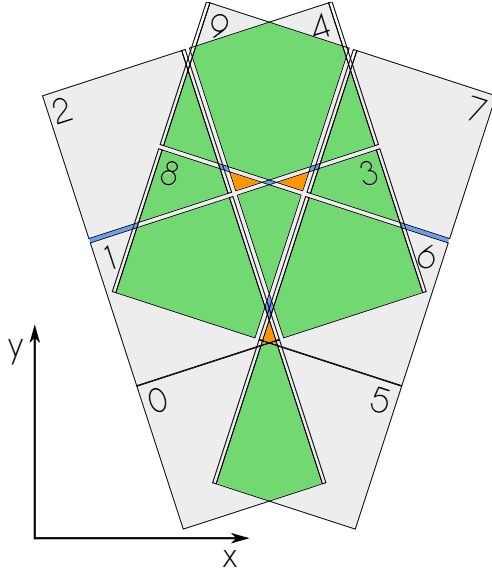


Figure 23: Sensor placement scheme of a single sensor module. Large overlapping areas are marked in green and smaller ones in red. Completely inactive areas are filled in blue.

Analogous, the remaining steps fall in the category of track filtering with the combined label “Trk Filter”. Note that the track filtering only appears in the stages 2 and 3 (see figure 21). The objective of the filtering is the removal of background tracks that do not correspond to elastic scattering events. Such background tracks can be identified by their characteristic position and angular distribution of the reconstructed track parameters with respect to the elastically scattered antiprotons. By cutting off the non-elastic scattering areas a large fraction of the background can be removed. This filter is labeled here as the “XY-cut Filter” [98]. Finally the reconstructed tracks at the LMD are propagated back to the IP using average tracking and error propagation package (Geane)[106]. This step is necessary as the elastic scattering model is defined at the production vertex and is perturbed by the magnetic fields. Since the LMD cannot measure the momentum of tracks, the beam

momentum is used for the back-tracking procedure as an approximation. The largest relative deviation to the true momentum is in the order of 10^{-4} and is negligible, see appendix B.3. Additional filtering can be performed on the back-propagated tracks, further reducing the background to a percent level [98]. Figure 24 shows an exemplary two dimensional angular distribution of reconstructed tracks at the IP by the LMD.

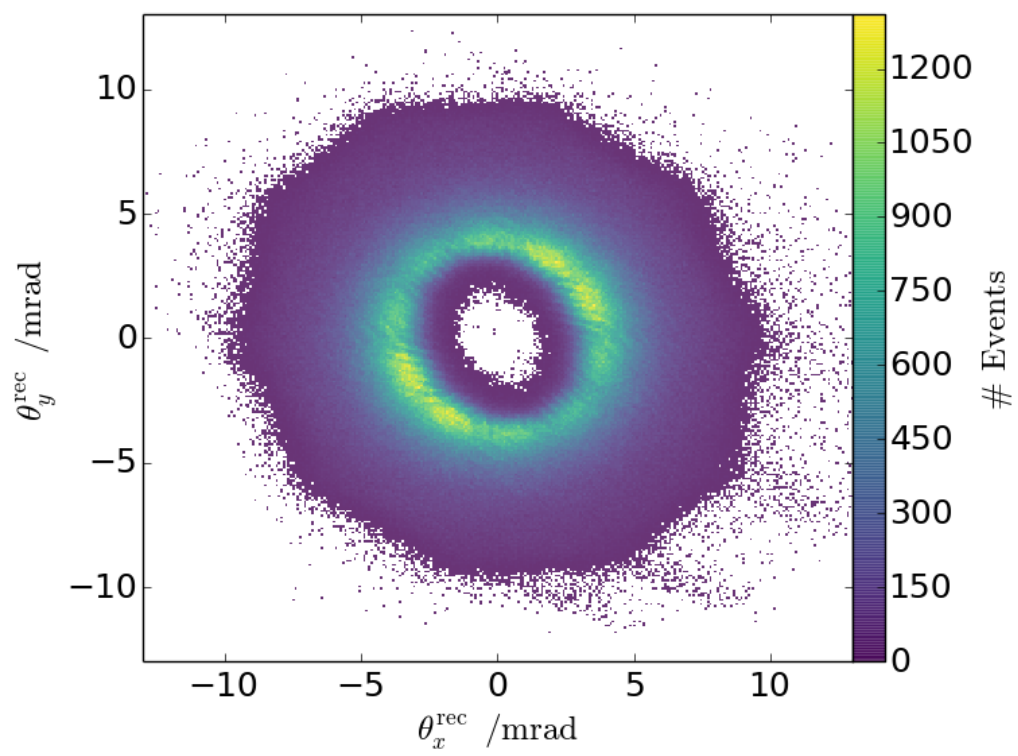


Figure 24: Exemplary reconstructed track 2D angular distribution at 1.5 GeV/c.

LUMINOSITY DETERMINATION - THE LUMINOSITY FIT FRAMEWORK

This chapter presents the LuminosityFit software, which counts as major work effort of this thesis, and can be found on the github platform [107]. It is responsible for the determination of the luminosity with the highest possible precision from the reconstructed data of the LMD. Recalling chapter 3, this is achieved by comparing the measured elastic scattering angular distribution with the theoretical model distribution. The normalization variable is the absolute luminosity L . However the measured angular distribution $N(\theta)$ cannot simply be compared to the theoretical model $\sigma(\theta)$, because several inevitable measurement effects alter the original pure elastic scattering distribution. There are two possible paths to overcome this obstacle. One possibility is to correct the measured data for the effects introduced by the PANDA spectrometer, which then allows a direct comparison with the pure elastic scattering model. Alternatively, the pure model can be modified to include all of the effects that arise during the measurement, so that is directly comparable with the data. The first option is in practice not feasible as required operations such as deconvolutions, which undo the detector resolution of the data, require very large amounts of data and a constant resolution to work reliably. On these grounds the second option was chosen, allowing for far more flexibility, extraction power and precision. The construction of the fit model with all of the transformations and correction procedures of the elastic scattering cross section is presented in detail in the following. Results on the extracted luminosity precision and studies of systematic uncertainties are presented in the next chapter.

4.1 THE ELASTIC SCATTERING MODEL

The cross section for elastic $\bar{p}p$ scattering was introduced in section 3.3. Apart from the calculable coulomb part of the total elastic cross section, two possible parameterizations for the description of the hadronic part exist. Both parameterizations are implemented in the LuminosityFit software. Despite the fact that the E760 parameterization is more suitable, because it uses more measurements in the four momentum range of the LMD, the DPM parameterization was chosen for the studies in this thesis (see equation 18). The reasoning is that the DPM generator is the only official generator for the PANDA experiment that includes elastic $\bar{p}p$ processes¹. Moreover the operability of the LuminosityFit software and the validity of its extraction precision and studies on systematic uncertainties are not influenced by the chosen parameterization, as long as the behavior of the true physics cross section is described approximated. To ensure meaningful results

¹ The official version of the DPM generator unfortunately uses 32bit floating point precision. For the small excerpt of the angular spectrum of the LMD, the numerical precision was not good enough. Therefore a special 64bit precision version of this generator is used in the simulation studies

of the systematic effects, the parameterization of the event generator and the fit model of the luminosity extraction software are identical.

4.2 COORDINATE TRANSFORMATIONS

In general the kinematics of the elastic scattering process is defined by the momentum transfer t and the center of mass energy \sqrt{s} or the beam momentum p_{lab} . However the latter can be omitted because for measurements of the $\bar{\text{P}}\text{ANDA}$ experiment the beam momentum will be fixed and measured with a relative precision of a few hundred keV/c. Hence it can be regarded as a constant and only the momentum transfer t remains as a phase space variable. In order to relate the measured quantities, the scattering angles θ_{lab}

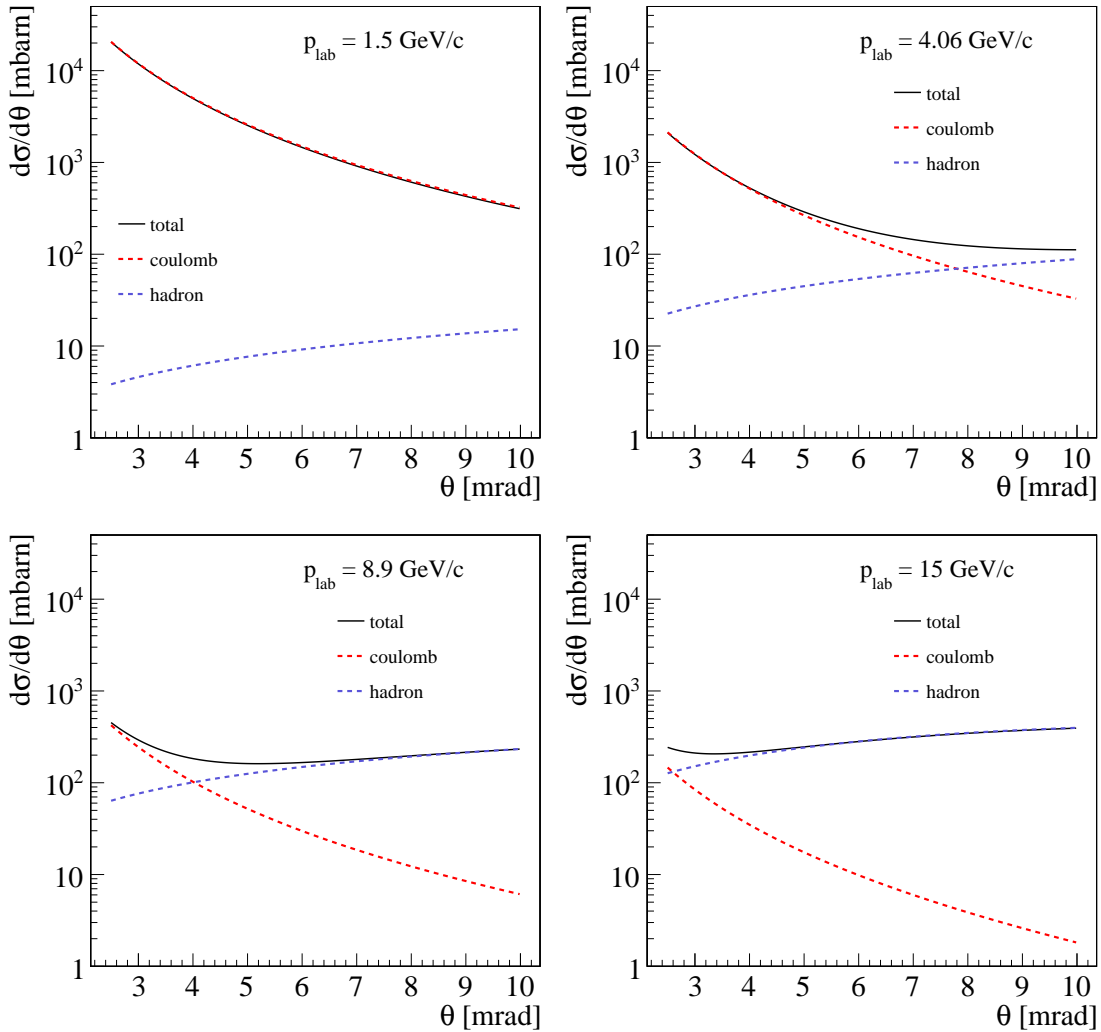


Figure 25: Elastic $\bar{p}p$ scattering cross section contributions in the LMD measurement range for various beam momenta. For these beam momenta accurate magnetic field maps exist in the simulation software.

and ϕ_{lab} in the laboratory system, to the momentum transfer t a coordinate transforma-

tion is necessary. The relation between the four momentum transfer and the scattering angle θ_{lab} (defined with respect to the incoming antiproton) is

$$t(\theta_{\text{lab}}) = -2p_{\text{cms}}^2 \left(1 - \cos \left(\text{atan} \left(\frac{\sin \theta_{\text{lab}}}{\gamma (\cos \theta_{\text{lab}} - \beta \frac{E_{\text{lab}}}{p_{\text{lab}}})} \right) \right) \right). \quad (19)$$

This is an approximation for small momentum transfers, because the kinetic energy of the recoiling proton is neglected, but can be used without concerns as demonstrated in appendix B.2. The coordinate transformation also shows that the cross section is independent of ϕ , hence the scattering probability is symmetric in this variable. As a consequence the measurement of ϕ would not be relevant. The elastic cross section in dependence on the scattering angle θ_{lab} is depicted for several beam momenta in figure 25.

So far the laboratory system and the accelerator reference system are assumed to be aligned in this derivation. In reality the beam can have a certain inclination on the target, resulting in a tilted reference system and the observed angular distribution is no longer symmetric in ϕ^{lab} . Hence its measurement becomes important (see section 5.2.3). Taking these facts into account, relation 12 expands to

$$\begin{aligned} \frac{dN(\theta^{\text{lab}}, \phi^{\text{lab}})}{d\theta^{\text{lab}} d\phi^{\text{lab}}} = & L \cdot \det(J_R(\theta^{\text{lab}}, \phi^{\text{lab}})) \\ & \cdot \det(J_t(\theta)) \cdot \frac{d\sigma(t(\theta(\theta^{\text{lab}}, \phi^{\text{lab}})))}{dt}. \end{aligned} \quad (20)$$

Here σ is the total elastic cross section as defined in 13. $\theta(\theta^{\text{lab}}, \phi^{\text{lab}})$ describes the rotation transformation going from the laboratory system to the tilted accelerator reference system. In this system the model is again ϕ symmetric, however the scattering angle θ has still to be transformed into the momentum transfer $t(\theta)$ which corresponds to equation 19. Since the cross section is a differential also the angular elements are changed under the transformations. The Jacobian determinants $\det(J_R(\theta^{\text{lab}}, \phi^{\text{lab}}))$ and $\det(J_t(\theta))$ supply the necessary correction factors for the rotation transformation of the laboratory system and the transformation into the momentum transfer frame. They are calculated using numerical differentiation of the transformation equations.

4.3 DIVERGENCE SMEARING

As a next step, the divergence of the antiproton beam has to be taken into account. This means that the antiprotons no longer all have the same inclination on the target, but are distributed around a mean value, the beam tilt. It turns out that the overall fit performance is heavily penal-

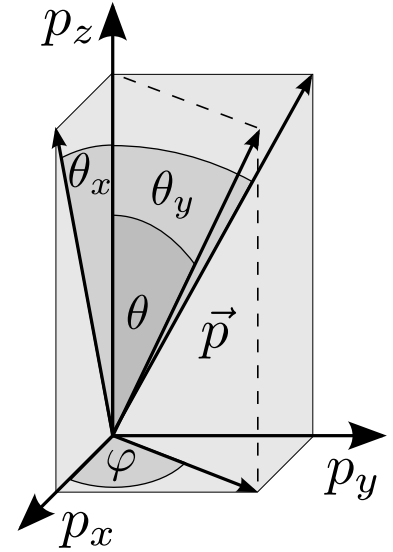


Figure 26: The $\theta_x \theta_y$ coordinate system.

ized by the tilt rotation transformations in the $\theta\phi$ -coordinate system. For this reason the $\theta_x\theta_y$ -coordinate system, as illustrated in figure 26 and defined by

$$\theta_x^{\text{lab}} = \frac{p_x}{p_z} \quad (21)$$

$$\theta_y^{\text{lab}} = \frac{p_y}{p_z}, \quad (22)$$

is introduced. The crucial difference to the $\theta\phi$ spherical coordinates are the transformations of the angle variables from the laboratory system into the physics system, which are now simple differences

$$\theta_x = \theta_x^{\text{lab}} - \text{tilt}_x$$

$$\theta_y = \theta_y^{\text{lab}} - \text{tilt}_y$$

with

$$\vec{\text{tilt}} = (\text{tilt}_x, \text{tilt}_y, 1)$$

and

$$\theta(\theta_x^{\text{lab}}, \theta_y^{\text{lab}}; \text{tilt}_x, \text{tilt}_y) = \sqrt{\theta_x^2 + \theta_y^2} \quad (23)$$

$$\phi(\theta_x^{\text{lab}}, \theta_y^{\text{lab}}; \text{tilt}_x, \text{tilt}_y) = \text{atan}(\theta_y/\theta_x). \quad (24)$$

This is a small angle approximation, but for the very small forward angles relevant for the LMD these errors are negligible. The severity of the approximation is visualized in figure 27. In this example a tilt of 0.5 mrad in both the θ_x and θ_y direction was chosen, which already resembles the worst expected setting of the HESR (see 2.2.1). Plotted is the relative difference of θ calculated by equation 23 and the exact solution calculated using rotations specified by Euler angles. It can be seen that the relative difference varies by less than $0.2 \cdot 10^{-6}$ in the measurement range of the LMD. In this new coordinate system equation 20 changes to

$$\frac{dN(\theta_x^{\text{lab}}, \theta_y^{\text{lab}})}{d\theta_x^{\text{lab}} d\theta_y^{\text{lab}}} = L \cdot \det(J_R(\theta_x^{\text{lab}}, \theta_y^{\text{lab}})) \det(J_t(\theta)) \cdot \frac{d\sigma(t(\theta(\theta_x^{\text{lab}}, \theta_y^{\text{lab}}; \text{tilt}_x, \text{tilt}_y)))}{dt}. \quad (25)$$

With these much simpler transformations, occurring especially frequently in the convolution algorithms needed for the beam divergence smearing and detector resolution smearing, the computation times of the luminosity fit are reduced dramatically². Now the coordinate system rotation Jacobi determinant is relatively simple and can be calculated analytically as

$$J_R(\theta_x^{\text{lab}}, \theta_y^{\text{lab}}) = \frac{1}{\sqrt{(\theta_x^{\text{lab}})^2 + (\theta_y^{\text{lab}})^2}}.$$

In addition the periodicity in ϕ is removed also making some algorithms simpler. Finally the visualization of the results is more intuitive and easier to understand. In the following an example will be worked out to clarify the actual divergence smearing con-

² The run-time performance improves by a factor of about 100

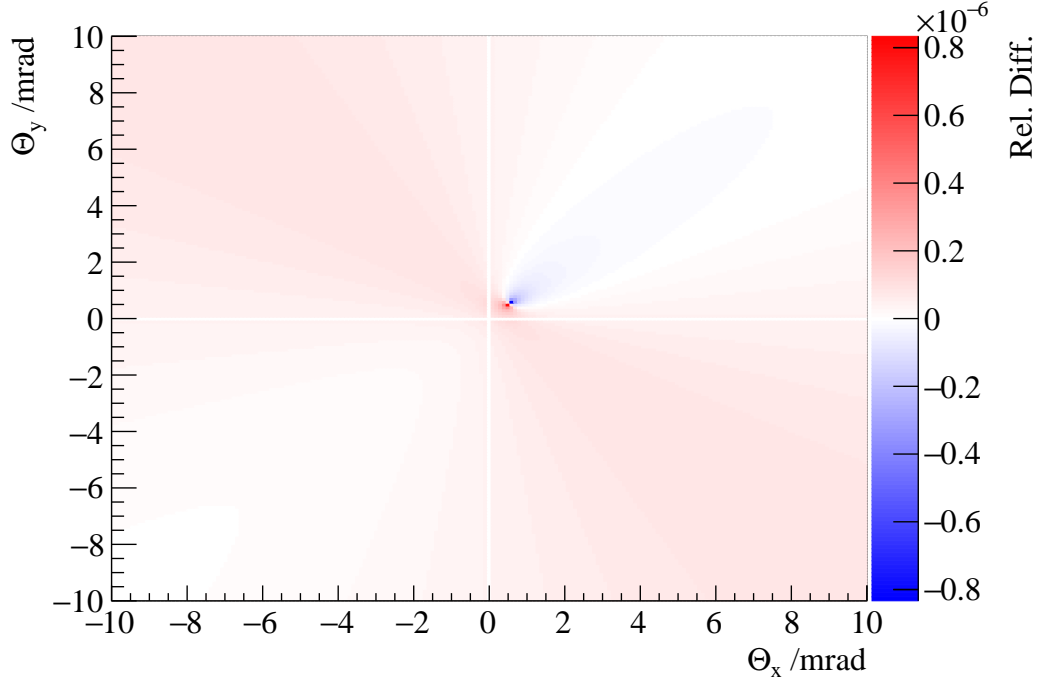


Figure 27: Relative difference of θ in the $\theta_x \theta_y$ approximation and the exact solution for a beam tilt setting of 0.5 mrad in both θ_x and θ_y . The exact solution is calculated using rotations specified by Euler angles.

volution algorithm. It works on a two dimensional grid and has two input models³ and outputs a smeared model. In the example the signal function that will undergo the effect of divergence smearing is a uniform function defined in the range from -2.0 mrad to 2.0 mrad in both dimensions θ_x and θ_y . For the divergence model a normalized 2D gaussian function is used. These are depicted in figure 28. The algorithm now discretizes both models on a specified grid, concretely in this example 14 chunks on each dimension. The divergence model grid is adjusted so that the grid constant is equivalent to the one of the signal model. Now for each 2D bin in the signal model space, an integral of its content is performed and distributed to the neighboring bins according to the integral values of the divergence model bins. The integrals are evaluated with MC integration. Pictorially speaking the divergence model center is placed on top of each signal model bin, so that the bin boundaries match, and the previously mentioned content distribution is performed. The divergence smeared result can be seen in figure 28.

Putting this in mathematical terms we can define the divergence smeared elastic cross section in the $\theta_x^{\text{lab}}, \theta_y^{\text{lab}}$ coordinate system as

$$\frac{d\sigma(\theta_x^{\text{lab}}, \theta_y^{\text{lab}})}{d\theta_x^{\text{lab}} d\theta_y^{\text{lab}}} = \int d\theta_{x'}^{\text{lab}} \int d\theta_{y'}^{\text{lab}} \text{div}(\theta_x^{\text{lab}}, \theta_y^{\text{lab}}, \theta_{x'}^{\text{lab}}, \theta_{y'}^{\text{lab}}) \cdot \det(J_R(\theta_{x'}^{\text{lab}}, \theta_{y'}^{\text{lab}})) \cdot \det(J_t(\theta)) \cdot \frac{d\sigma(t(\theta(\theta_{x'}^{\text{lab}}, \theta_{y'}^{\text{lab}}; \vec{\alpha})))}{dt}. \quad (26)$$

³ Note that the words model and function are used interchangeably.

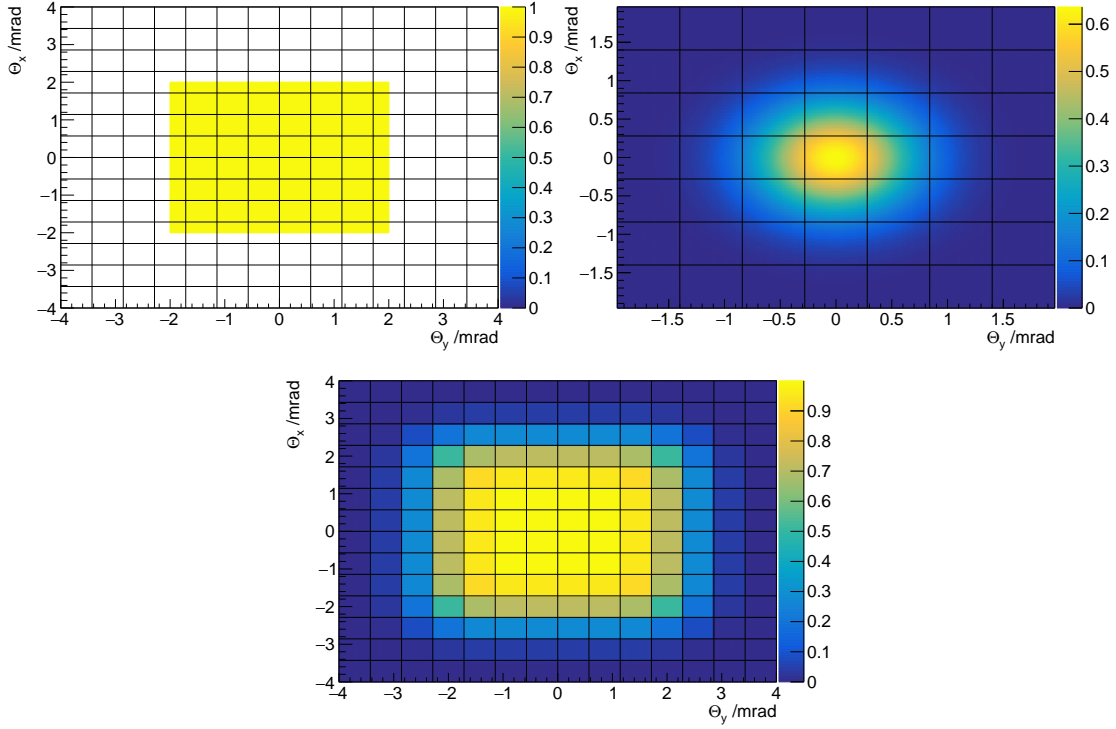


Figure 28: Example of the divergence smearing algorithm illustrating the procedure. In all figures the black lines span the grid that was used within the smearing algorithm.

Top left: The signal model before the smearing process, here a uniform model in the range from -2.0 mrad to 2.0 mrad in both dimensions is used.

Top right: The divergence smearing model, which is a 2D normal distribution.

Bottom: Resulting signal model after the smearing process, clearly showing smudged edges of the original model from the gaussian smearing model.

Here the $\text{div}(\theta_x^{\text{lab}}, \theta_y^{\text{lab}}, \theta_{x'}^{\text{lab}}, \theta_{y'}^{\text{lab}})$ is the function for the beam divergence that depends on not only the initial space parameters $\theta_{x'}^{\text{lab}}, \theta_{y'}^{\text{lab}}$, but also the final ones $\theta_x^{\text{lab}}, \theta_y^{\text{lab}}$. The $\theta_{x'}^{\text{lab}}, \theta_{y'}^{\text{lab}}$ variables are being integrated over. Usually the divergence can be expressed with the differences of the variables from the primed and unprimed coordinate system and the divergence changes to $\text{div}(\theta_x^{\text{lab}} - \theta_{x'}^{\text{lab}}, \theta_y^{\text{lab}} - \theta_{y'}^{\text{lab}})$, then the operation is more commonly referred to as the convolution. This description in terms of differences is of course only valid as long as the divergence has this symmetry. For a more thorough discussion of this topic see appendix B.4. Luckily this is very often the case, and specifically for the LMD a 2D normal distribution is used for the divergence function. All parameters of the model are absorbed by the vector $\vec{\alpha} = (\text{tilt}_x, \text{tilt}_y, \text{div}_x, \text{div}_y)$.

On the one hand the divergence gives the angular distribution of the antiproton beam particles around its mean tilt. This means that the physics coordinate system is different for each individual scattering event, as it is defined by the direction of flight of the initial state. However, because the scattering process is invariant under rotations⁴, the beam divergence is identical to a smearing of the elastic cross section by the divergence distribution. Therefore it can also be interpreted as the probability density function for a particle, which is initially within the angular element in the direction $\theta_{x'}^{\text{lab}}, \theta_{y'}^{\text{lab}}$, to wind up in the neighboring direction $\theta_x^{\text{lab}}, \theta_y^{\text{lab}}$.

⁴ Invariant under rotations means that the scattering process can be rotated as a whole and the physics outcome is not altered by this transformation.

Using this definition, the relation of the measured angular distribution can be rewritten as

$$\frac{dN(\theta_x^{\text{lab}}, \theta_y^{\text{lab}})}{d\theta_x^{\text{lab}} d\theta_y^{\text{lab}}} = L \cdot \frac{d\sigma(\theta_x^{\text{lab}}, \theta_y^{\text{lab}}; \vec{\alpha})}{d\theta_x^{\text{lab}} d\theta_y^{\text{lab}}}. \quad (27)$$

4.4 EFFICIENCY CORRECTION

Next the so called efficiency correction has to be applied. The efficiency gives the probability for successful reconstruction of a track with the generated MC values of $\theta_x \theta_y$. This is necessary due to the partial angular coverage of the LMD detector of the complete angular range. Furthermore detection inefficiencies of the sensors or the unsuccessful track reconstruction can lead to additional reductions of the efficiency. The true detector acceptance can never be known, but only an approximation can be determined by using simulated data. The efficiencies used in the LuminosityFit software are determined from simulations and track reconstruction with the PandaRoot software as described in section 3.5. An event/track⁵ is regarded as accepted if the reconstruction software was able to build a track from the sensor hits. The ratio between all accepted tracks and all generated tracks is the efficiency ϵ . Specifically for the LuminosityFit the generated values of the track parameters $\theta_x \theta_y$ ⁶ are used for the angular efficiency $\epsilon(\theta_x, \theta_y)$, which is shown in figure 29. Here the visualization advantage of the $\theta_x \theta_y$ coordinate system

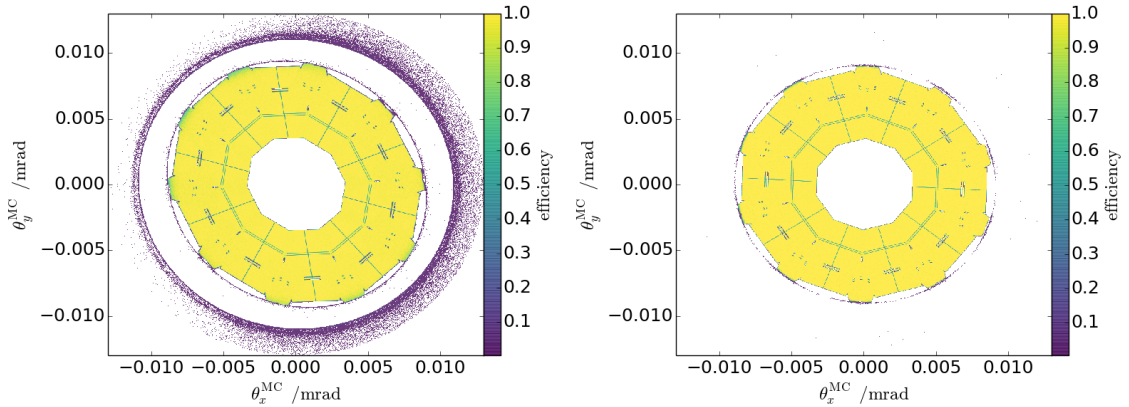


Figure 29: Angular acceptance of the LMD in the $\theta_x \theta_y$ coordinate system for fully reconstructed tracks at a beam energy of 1.5 GeV/c (left) and 15 GeV/c (right).

becomes apparent. The 10 modules on each plane of the detector can easily be seen, as they are separated by thin inefficiency gaps. Most areas of a module region show a very high efficiency of 99%, except for 4 pairs of holes in the center region of the module, as well as two pairs of longer areas of inefficiency on each edge of the module that reaches towards its center. These inefficiencies can be explained by the arrangement of the individual sensors on the module as shown in figure 23 with the mentioned areas are shaded in blue. In addition the electronical layout of the sensors (see figure 18) enhances the inactive areas on the module, as every sensor is surrounded by a guard ring and one edge also contains digitization components. The pairwise occurrence of the these

⁵ Single track events were used in these simulations.

⁶ Since all $\theta_x \theta_y$ angles appearing in the following will be in the laboratory coordinate system, the labels $^{\text{lab}}$ are dropped.

inefficiencies is clarified by figure 30. Since all four detection planes are identical, any

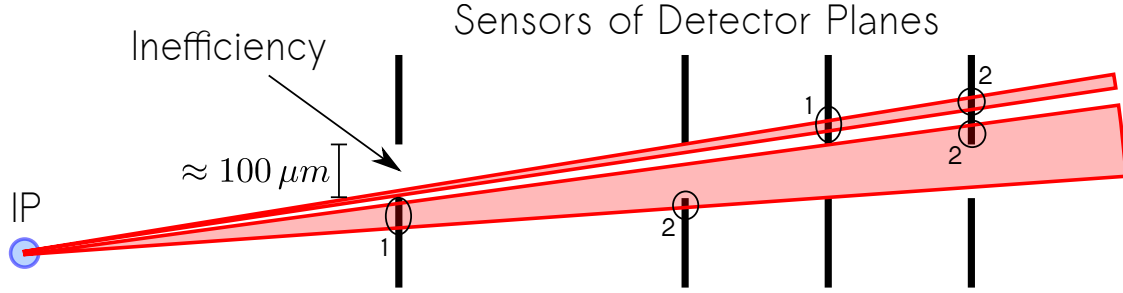


Figure 30: Sketch of four LMD planes sections with a inefficiency gap in the order of $100 \mu\text{m}$ diameter in each plane. On every detection plane the inefficiency locations are matching, because the arrangement of the sensors is identical. The two red angular ranges illustrate regions for tracks that cannot be reconstructed, due to insufficient track hits (less than 3).

area that is not covered by any sensor appears repeatedly in every detector plane. As a consequence there exist two nearby angular ranges, for which tracks that will traverse more than one of these inefficient areas, leading to unsuccessful track reconstruction, because the software requires hits from three or four detector planes (see 3.5). For radial angles between $11 \text{ mrad} < \sqrt{\theta_x^2 + \theta_y^2} < 13 \text{ mrad}$ a ring of minor efficiency is visible at a beam momentum of $1.5 \text{ GeV}/c$. Antiprotons in this angular region are able to reflect off the beampipe wall and enter the detector. Finally also noticeable when comparing the two beam momenta scenarios is the more skewed and rotated acceptance for $1.5 \text{ GeV}/c$, arising from the larger ratio of the solenoid field strength and momentum⁷.

For the acceptance correction of the elastic scattering model, this binned two dimensional efficiency, with the option of bilinear interpolation [108] based on the four nearest bin centers, is used. When using the same binning for the acceptance as for the definition of the model, an interpolation is not necessary. In case of a different binning the interpolation has only to performed once at the construction of the two dimensional efficiency object, since it is a static component of the final model. This avoids very costly interpolation operations during the fitting procedure. To incorporate the efficiency the formula for the elastic scattering, equation 27 changes to

$$\frac{dN(\theta_x, \theta_y)}{d\theta_x d\theta_y} = L \cdot \epsilon(\theta_x, \theta_y) \cdot \frac{d\sigma(\theta_x, \theta_y; \vec{\alpha})}{d\theta_x d\theta_y}. \quad (28)$$

4.5 DETECTOR RESOLUTION SMEARING

Finally the imprecision of the measured track parameters by the LMD, more specifically the angles θ_x, θ_y , has to be taken into account. This finite resolution for the angles arises mainly from two factors. The reconstructed track hits vary from the true values because of the intrinsic sensor resolution and the multiple scattering in the modules and the transition cone. The latter is dominant at low beam energies. Figure 31 shows the two dimensional angular resolution distributions for the two extreme momenta of the $\bar{\text{P}}\text{ANDA}$ experiment. It can be seen that the resolution distributions can be rotated and skewed, because of the solenoid and dipole magnetic fields. By fitting the resolution distributions

⁷ The solenoid is reduced to half current for beam momenta below $3.0 \text{ GeV}/c$

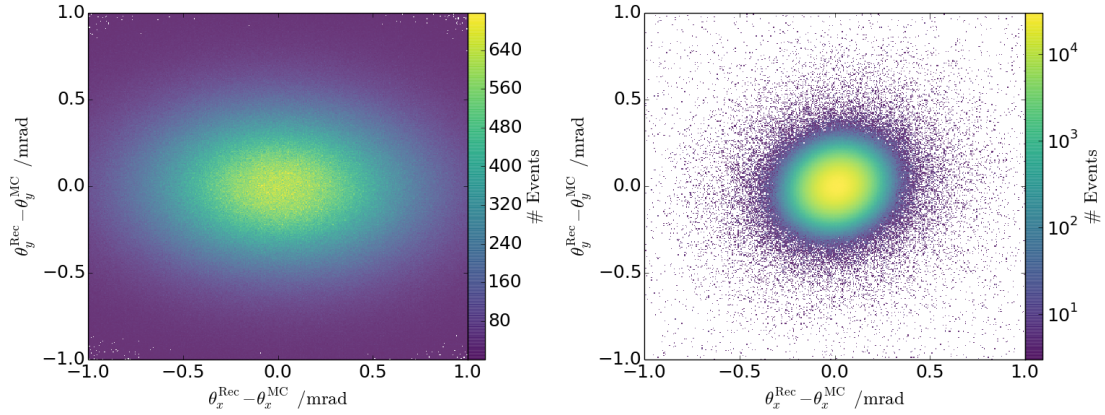


Figure 31: Global two dimensional angular resolution of the LMD at 1.5 GeV/c (left) and 15 GeV/c (right).

of various beam momenta with a 2D multivariate gaussian model, the parameters of the resolution as a function of the momentum in the laboratory frame can be extracted and are depicted in figure 32. Clearly the dominance of multiple scattering towards lower energies is visualized by the increase of the width of the resolution distributions, which are an effect of the reduced track “stiffness” for lower momentum antiprotons.

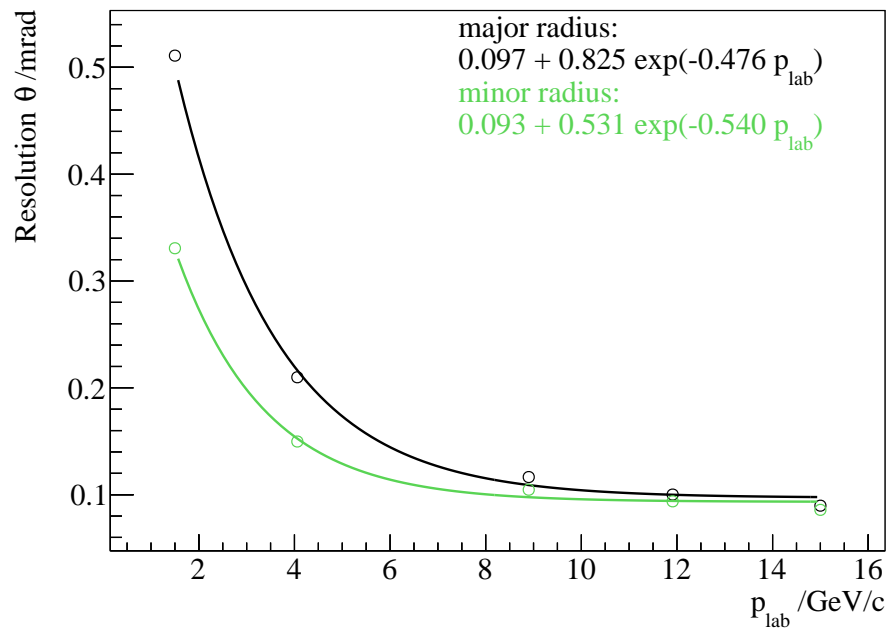


Figure 32: Momentum dependence of the LMD two dimensional angular resolution. The major and minor width (σ) of the resolution are shown in black and green.

Similar to the approach of the divergence smearing correction in 4.3, the detector resolution correction modifies the current two dimensional LMD fit model from equation 28 to

$$\frac{dN(\theta_x^{\text{rec}}, \theta_y^{\text{rec}})}{d\theta_x^{\text{rec}} d\theta_y^{\text{rec}}} = L \cdot \int d\theta_x^{\text{MC}} \int d\theta_y^{\text{MC}} \text{Res}(\theta_x^{\text{rec}}, \theta_y^{\text{rec}}, \theta_x^{\text{MC}}, \theta_y^{\text{MC}}) \epsilon(\theta_x^{\text{MC}}, \theta_y^{\text{MC}}) \frac{d\sigma(\theta_x^{\text{MC}}, \theta_y^{\text{MC}}; \vec{\alpha})}{d\theta_x^{\text{MC}} d\theta_y^{\text{MC}}}. \quad (29)$$

The function $\text{Res}(\theta_x^{\text{rec}}, \theta_y^{\text{rec}}, \theta_x^{\text{MC}}, \theta_y^{\text{MC}})$ contains all the information of the detector smearing. Its domain is 4 dimensional and it gives the probability density for reconstructing particles at angles $\theta_x^{\text{rec}} \theta_y^{\text{rec}}$ initially generated at the IP with angles $\theta_x^{\text{MC}} \theta_y^{\text{MC}}$. Simulations done with PandaRoot can give insight to this resolution function as both the generated and reconstructed angles are available.

There are two possibilities to extract this information from the simulation results and construct a resolution function. The first solution tries to parameterize the resolution as a function of the generated (MC) angles $\theta_x^{\text{MC}} \theta_y^{\text{MC}}$, by first splitting the simulated resolution information into bins of these angles and then fitting each of these local two dimensional resolution distributions with an appropriate model extracting the resolution parameters. When applying the smearing, the resolution model, here a 2D normal distribution, is initialized with the correct parameters dependent on the angles $\theta_x^{\text{MC}} \theta_y^{\text{MC}}$. Unfortunately it turns out that the resolution parameterization is extremely complex, as the resolution is not constant along the generated angles $\theta_x^{\text{MC}} \theta_y^{\text{MC}}$. Also the resolution at specific $\theta_x^{\text{MC}} \theta_y^{\text{MC}}$ proximities can have additional contributions to the 2D normal distribution. These complications arise due to an inhomogeneous material budget of the detector and edge effects. The problem of the resolution parameterization can be avoided in the second solution, in which simulation data is used directly by storing the required information within a 4D histogram. Due to the better compatibility and reliability, the latter solution was chosen. However it imposes other difficulties that are related to statistics and storage. In order to obtain equal statistical uncertainties for the resolution smearing probabilities when increasing the binning or density of these 4D histograms, the needed amount of data has to be increased with the fourth power. A similar statement holds for the storage of the resolution information, which can quickly exceed several gigabytes. From this point of view the histogram binning constant should be chosen as coarse as possible.

To be able to systematically study this large chain of sophisticated correction algorithms and allow the flexible extension for further corrections, the need for a framework for the construction of general functions of arbitrary dimensionality and complexity arose. This led to the development of an additional software package, the ModelFramework [109], which is a dependency of the LuminosityFit software⁸.

⁸ Both software packages are written purely in C++.

LUMINOSITY DETERMINATION RESULTS AND SYSTEMATIC STUDIES

This chapter presents the performance and accuracy of the LuminosityFit framework including systematic studies of the influence of the accelerator and target beam parameterization on the accuracy. At first the runtime settings of the luminosity fit are given followed by results of the luminosity determination for the ideal scenario. In this scenario merely the parameterizations of the accelerator beam momentum and IP distributions are idealistic, which use delta functions $\delta_3(\vec{p}_{\text{lab}})$ with $\vec{p}_{\text{lab}} = (0, 0, p_{\text{lab}})$ and $\delta_3(\vec{IP})$ with $\vec{IP} = (0, 0, 0)$. The parameters for realistic distributions are the shift and width of the IP distribution and the tilt and divergence of the accelerator beam. They are studied systematically, with both expected parameter values as well as an extreme case. Those values are taken from section 2.2.1, in which these parameters are discussed and summarized.

Because the detector resolutions (figure 32) and elastic scattering cross sections (figure 25) between the lab momenta of 4.06 GeV and 15 GeV/c are similar, most of the following studies were only performed for the two extreme values for the antiproton beam momentum of 1.5 GeV/c and 15 GeV/c. However results of several realistic scenarios with non-trivial accelerator and target beam parameters as well as different beam momenta are shown afterwards.

All data shown in this chapter has been simulated with the PandaRoot framework with only pure elastic $\bar{p}p$ scattering events and no background from inelastic channels. All relevant background sources are discussed at the end of this chapter.

5.1 IDEAL CASE FIT RESULTS

Before any fit results are shown, some general information on the determination procedure has to be provided. The fits are performed with the LuminosityFit software using an extended binned log-likelihood estimator. With the typical data sample size of 10^6 events and a 2D histogram binning of roughly 300 in each dimension a binned estimator is favored.

It was discovered that fits with a chi-square estimator give a systematic error on the luminosity in the order of 0.1%. The reason for this is the assumption of a normal distributed bin content, which is not well enough satisfied for the used sample sizes and poisson statistics is preferable [110]. This systematic error mainly effects the normalization constant, but for the luminosity determination this is precisely the crucial parameter. A complete description of the likelihood estimator is given in section A.1.

When using a binned estimator it is important to compare the bin content with the integral of the model within the bin boundaries. This is in general a quite computation expensive calculation, especially if the model changes with the fit parameters. In the limit of fine binnings the function can be regarded as constant within the boundaries of a single bin and a single function evaluation normalized to the area of bin provides an

accurate value for the integral. The two dimensional integrals for the luminosity fit are calculated by evaluating the model on a 3×3 grid within each bin, giving the necessary precision without large speed penalties. These integrals are cached and the luminosity fit model is now discretized according to the histogram of the data.

The binning of the luminosity fit model introduces an approximation at the stage of the efficiency correction, defined by equation 28. Here both the elastic scattering model and the efficiency is assumed to be constant inside each bin, which is only valid for large number of divisions of the binned model. When performing luminosity fits with

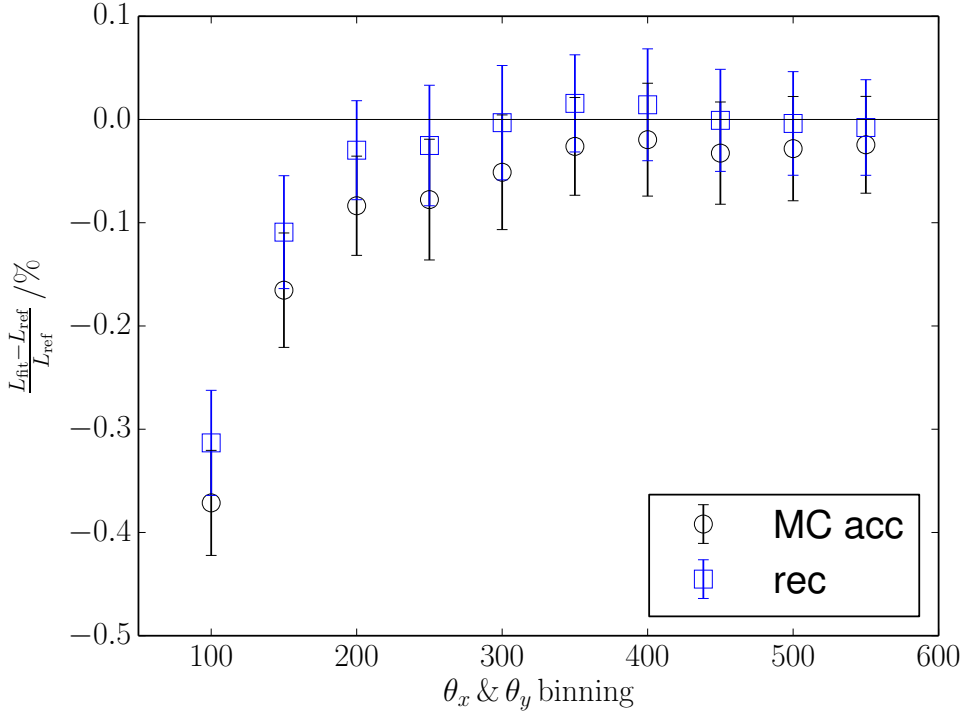


Figure 33: Relative luminosity as a function of the fit model and data binning in the θ_x, θ_y space. The black circles are fit results in which only accepted generated MC angular distributions are fitted. In this case the detector resolution smearing correction is not applied. The blue squares are fit results of reconstructed angular distributions. All mean and error values were calculated from the luminosity parameter fit result distributions of 100 bootstrapped data samples. The RMS value is used as an error estimate.

different binnings the optimal size can be determined, which is shown in figure 33. Here two different types of data are fitted with the appropriate model: the reconstructed data and accepted generated MC data. The former is the track information, arising from the simulation and track reconstruction software, resembling realistic data. On the contrary the accepted generated MC data is the information of the generated MC tracks the at the IP, that resulted in a reconstructed track. In this case the resolution smearing of the elastic scattering model was not used to ensure a valid description of this data. For each chosen binning, 100 bootstrapped data samples were fitted and the mean and RMS values of the relative luminosity distribution are displayed by the graphs in figure 33.

Clearly at low binnings the approximations of the model yield systematic uncertainties of several permille. Note that the binning approximation is already introduced at the stage of the efficiency correction. Once binnings of 300 are reached, this effect becomes negligible for both the reconstructed data and accepted generated MC data fit. Then an

excellent accuracy of the extracted luminosity is achieved, as they are compatible with the actual generated luminosities L_{ref} with respect to the statistical errors of about 0.05%. The fits on angular distributions with binnings of 600 and above were not tested, due to limited statistics for the resolution parameterization, its memory consumption and the runtime of the fits. A binning of 300 has been chosen for all other performed luminosity fits, as the computation times are the lowest here and no penalties on the accuracy of the extracted luminosity are present. In the following a single high statistics sample will be used instead of the 100 bootstrapped samples, due to reasons of feasibility. The mean and error of fit parameters, such as the luminosity, are obtained directly from the minimizer Function Minimization and Error Analysis 2 (MINUIT2). Figure 34 shows the two dimensional angular distributions of both the simulated large data sample and the corresponding optimized luminosity model for the two extreme beam momentum values. The bin-wise normalized residuals of the luminosity fit models and the reconstructed angular distributions indicate that the model is able to perfectly describe the data, as no distinct regions of over- or underestimation are visible. For the 15 GeV/c beam momentum case the angular distributions reveal a grid-like substructure, which are a consequence of the pixel sensors. Recalling the design of the detector each pixel has the dimensions of $80 \mu\text{m} \times 80 \mu\text{m}$. Most hits on the sensors are reconstructed from a single activated pixel [20], as the charge deposition is low, making the center of the pixel the reconstructed hit position. From the spacing between the detector planes, which is either 20 cm or 10 cm, the angular resolution of the detector is limited to $80 \mu\text{m}/20 \text{ cm} = 0.4 \text{ mrad}$. The grid constant visible in the angular distribution for the 15 GeV/c case in figure 34 is in perfect agreement with this value. For the regions of overlapping sensors (green area in figure 23), this grid structure is not as prominent, which is clearly visible in the reconstructed angular distribution. The reason for this is the only partial overlap of the pixels of the front and back sensors, yielding an improved resolution after performing hit merging of the two sides. For lower beam momenta this discrete structure is not visible anymore, as it is smeared by the larger detector resolution from multiple scattering. Similar to the bootstrapped data sampled case above, the accuracy of the extracted luminosity is below the permille level and is statistically compatible with generated value.

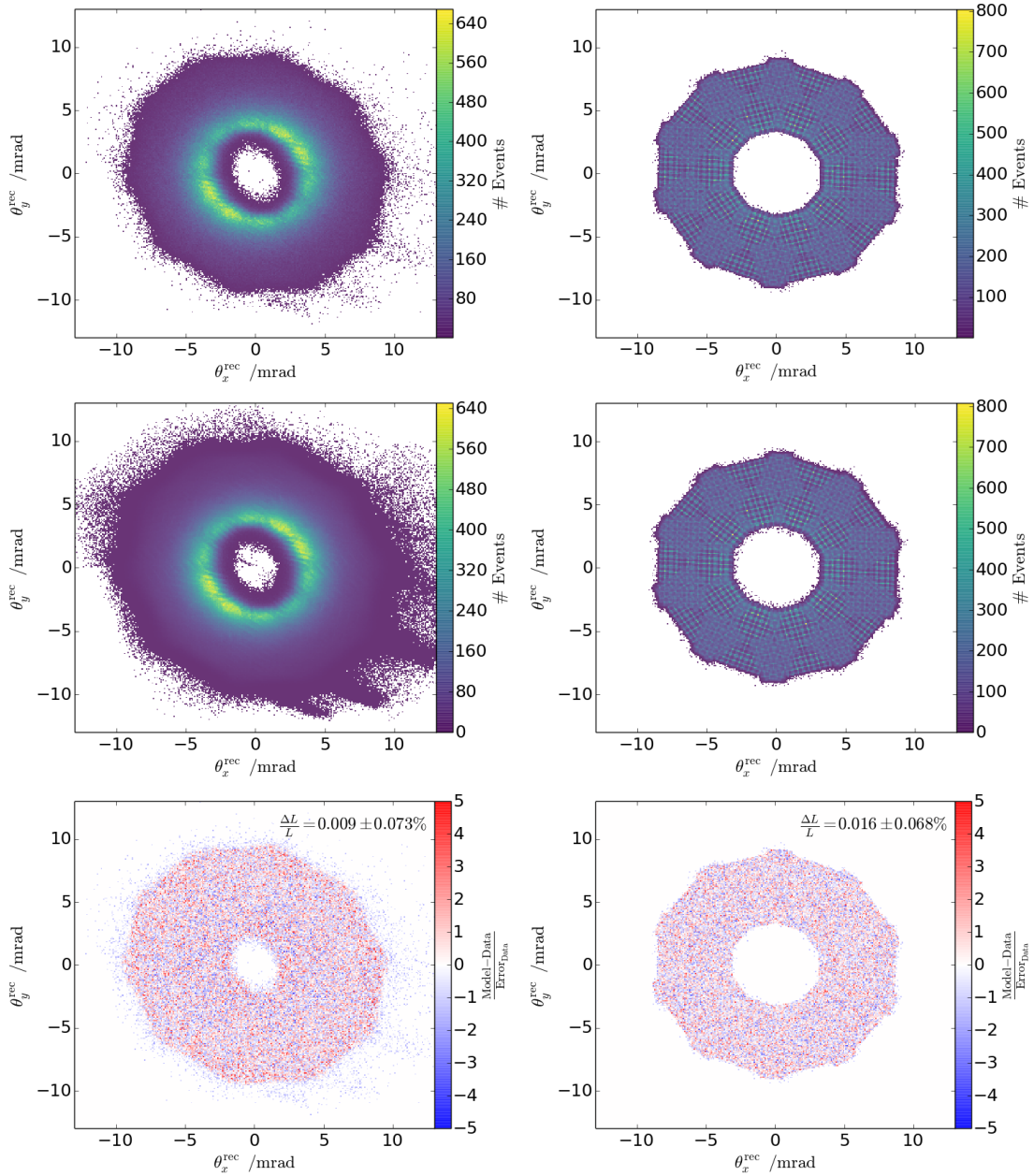


Figure 34: Fit results for the ideal scenario with the antiproton momenta aligned with the z-axis and the IP coincides with the \bar{P} ANDA origin. The left column shows results at a beam momentum of 1.5 GeV/c while the right column for 15 GeV/c.

Top: reconstructed angular distribution simulated with the PandaRoot software
Center: luminosity fit model w/o divergence smearing and with the luminosity parameter obtained from the fit while the accelerator beam tilt parameters are fixed to zero
Bottom: bin-wise normalized residuals of the luminosity fit model and the reconstructed angular distribution

5.2 SYSTEMATIC EFFECTS OF THE BEAM AND TARGET

So far idealistic parameterizations for the accelerator beam momentum and IP distribution in form of the delta functions $\delta_3(\vec{p}_{\text{lab}})$ with $\vec{p}_{\text{lab}} = (0, 0, p_{\text{lab}})$ and $\delta_3(\vec{IP})$ with $\vec{IP} = (0, 0, 0)$ were used. Now realistic parameterizations are examined. Figure 35 shows a sketch of a scattering process with a displaced interaction point and for a tilted incoming beam particle with respect to the z-axis.

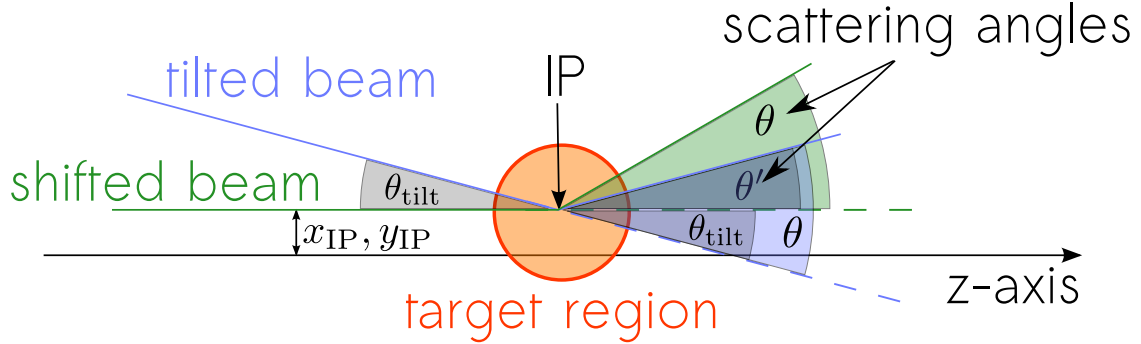


Figure 35: Beam shift and tilt sketch. A shifted IP scenario is shown in green, while the case drawn in blue arises from a tilted accelerator beam.

Obviously for position changes of the IP the angular distribution of the scattering process is not effected. However even though the scattering angles of the outgoing antiprotons are identical, the paths of the individual particles through the experimental setup are now different. As a consequence, the detector efficiency changes since previously reconstructed particles on the edge of the detector may now miss the sensor planes and vice versa. It is crucial that the magnetic field maps of the PandaRoot software represent the magnetic fields of the experiment, otherwise systematic errors in the luminosity determination can occur. The \bar{P} ANDA experiment will perform a high precision scan measurement of the magnetic fields [111]. Hence this influence is classified as uncritical.

For an incoming particle with an inclination to the z-axis, its scattering angle in the laboratory system θ' now differs from the one of the physics process θ . The physics and laboratory coordinate systems are no longer aligned, hence the angular distribution of a scattering process is directly effected. However only the amount of particles scattered into the angular elements change and the individual particle paths remain the same. Therefore the detector acceptance remains unchanged. Strictly speaking the antiproton paths originating from the same angular scattering region before and after a tilt may vary, since they have different momenta due to the different momentum transfer to the proton.

In general this shift and tilt is different for each event and will follow distributions described by the IP distribution and accelerator beam divergence.

5.2.1 IP Distribution

The IP distribution is the overlap of the accelerator beam distribution and the target beam distribution, while mean displacements of the IP distribution are neglected in this section. For a correct description one relies on the information of these two distributions, either from simulations or measurements. For the accelerator beam position a normal distribution in the xy plane is used. Estimations on the accelerator beam parameters are

summarized in tables 2 and 3. For the target beams there are two possible systems, the cluster jet target and pellet target. As the former will be used in the beginning of the PANDA runtime and measurements for the target beam distribution exist, this system was chosen in this study. The target hydrogen clusters follow the distribution given in equation 6, with a slightly elongated shape in the z direction, while newest measurements even suggest a wider gaussian distribution[112]. Because the antiproton beam is costly to create and high reaction rates are desired, the target beam is usually broadened in the xy plane to have a good overlap with the antiproton beam. Therefore the dimensions of the IP distribution in the x and y direction are dictated by the size of the more narrow accelerator beam when performing the overlap. Hence a normal distribution for x and y with widths of $\sigma_x = \sigma_y = 0.8$ mm is used. Along the beam direction the distribution is dominated by the target beam profile and would be described best by equation 6. However for reasons of simplicity a gaussian distribution with a similar width was used instead. The 2σ interval of the normal distribution should roughly equal the 13.1 mm size in z direction, therefore $4\sigma_z \approx 13.1$ mm $\rightarrow \sigma_z = 3.5$ mm. The distribution of the pellet target beam is similar in xy , and therefore also the IP distribution parameterization.

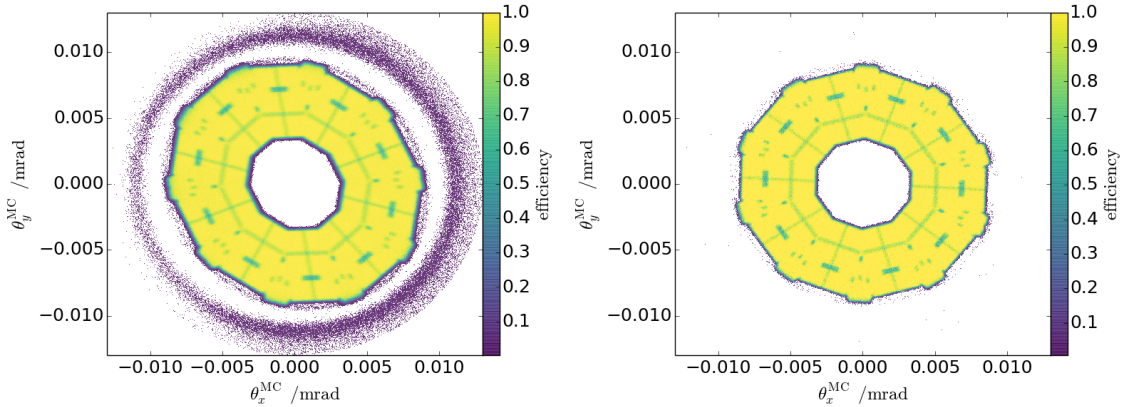


Figure 36: Angular acceptance of the LMD in the $\theta_x\theta_y$ coordinate system for fully reconstructed tracks at a beam energy of 1.5 GeV/c (left) and 15 GeV/c (right). The interaction vertices follow normal distributions in all three dimensions with standard deviations of $\sigma_x = \sigma_y = 0.8$ mm and $\sigma_z = 3.5$ mm.

The angular acceptances of the LMD with the gaussian IP distribution are shown in figure 36 for both extreme beam momentum cases. At a first glance the acceptances look similar to the ones with a delta function like IP distribution shown in figure 29, showing all of the previously discussed shapes and detector layout features (see 4.4). On a more precise comparison a difference becomes apparent. Now the acceptances are smeared, which can be seen from the borders as well as the inefficient areas of the detector indicated by the blue areas in figure 23. The previously appearing two-fold structure of the inefficiencies is no longer visible due to the smearing from the IP distribution.

Figure 37 shows a reconstructed angular distribution at 1.5 GeV/c generated with the IP distribution as mentioned above. Two luminosity fit models are shown, one assumes a point-like IP and the other uses the efficiency with the correct IP distribution. When comparing these two models no difference is visible by eye. Only when performing luminosity fits a systematic error of roughly 0.4% becomes apparent in the case of not correcting for the IP distribution.

If the distribution of the IP is taken into account in the fit model, the deviation of the reconstructed luminosity in comparison to the generated luminosity is below 0.1%. Of course determining the true IP distribution is a difficult task, because of the smearing from the detector resolution. But since even a dramatically wrong description, here using a delta function instead of a gaussian function, the systematic error stays well below the percent level. Hence a rough knowledge of the IP description suffices.

The same study has been performed for the beam momentum of 15 GeV/c and the results are shown in figure 38. Different to the 1.5 GeV/c case is that the IP distribution does not influence the precision on the luminosity determination.

As both the target system and the accelerator will be adjusted to create this desired IP distribution in order to achieve the design luminosity, this parameterization parameters for the IP distribution are used for all further studies.

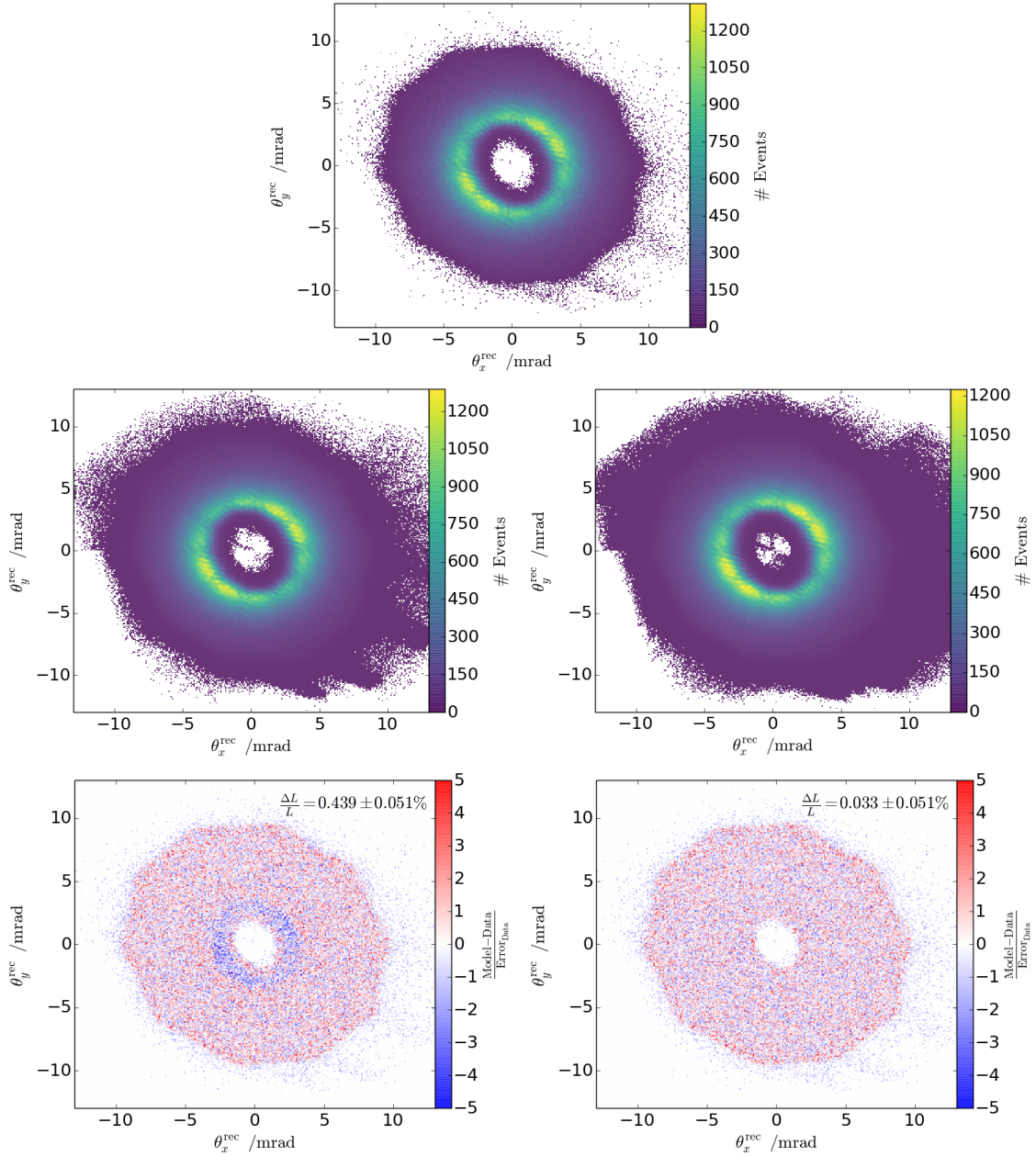


Figure 37: Fit results with the IP mean at the origin and no antiproton beam divergence and tilt at 1.5 GeV/c. The left column shows results for with the point-like IP model, while the right column shows the results with the correct IP distribution.

Top: reconstructed angular distribution simulated with the PandaRoot software with the IP distribution (same for both cases)

Center: luminosity fit model

Bottom: bin-wise normalized residuals of the luminosity fit model and the reconstructed data

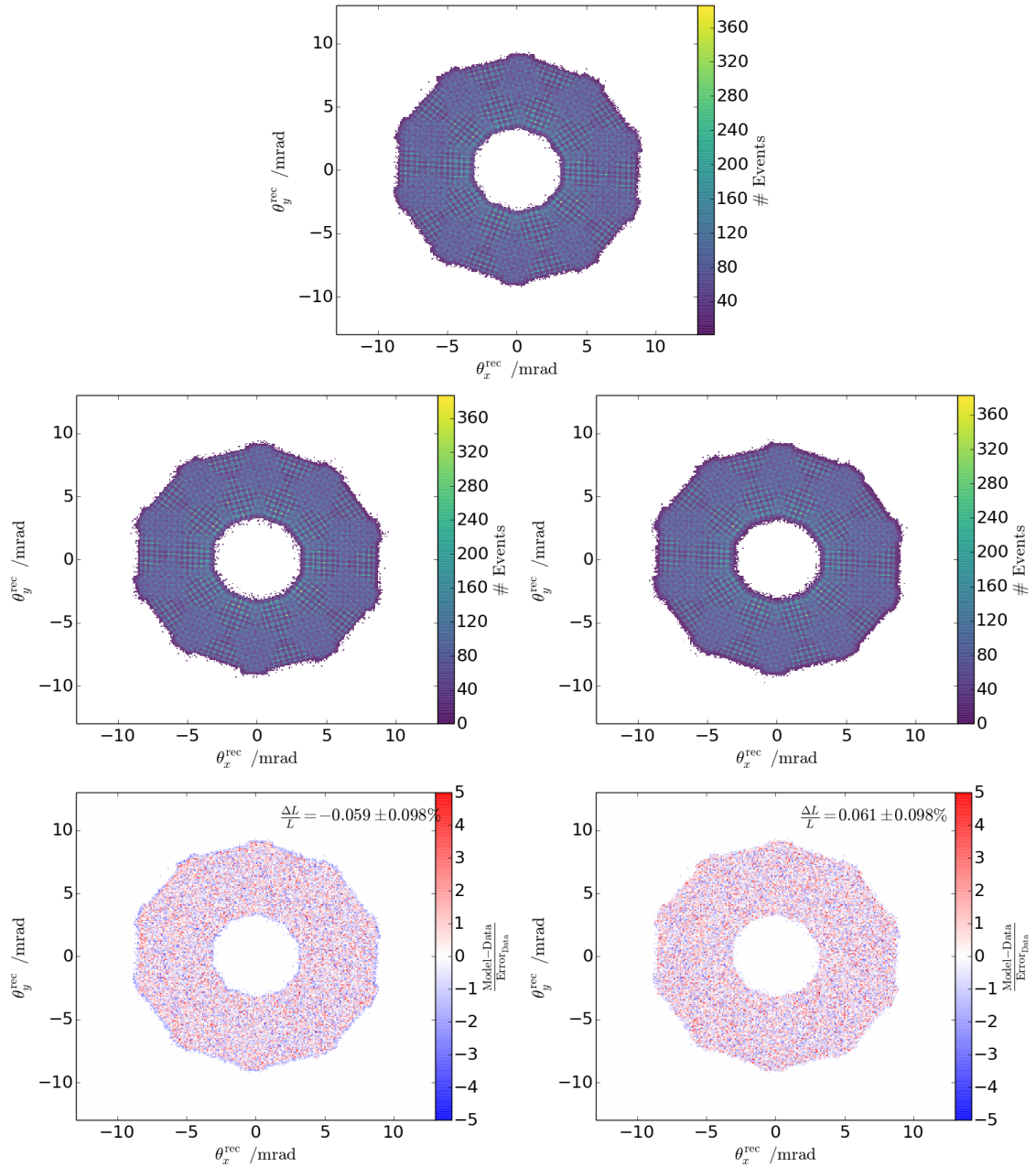


Figure 38: Fit results with the IP mean at the origin and no antiproton beam divergence and tilt at 15 GeV/c. The left column shows results for with the point-like IP model, while the right column shows the results with the correct IP distribution.

Top: reconstructed angular distribution simulated with the PandaRoot software with the IP distribution (same for both cases)

Center: luminosity fit model

Bottom: bin-wise normalized residuals of the luminosity fit model and the reconstructed data

5.2.2 IP Displacements

In addition to a distribution of the interaction point, it can also exhibit a mean displacement with respect to the origin of the PANDA laboratory frame. This is visualized in figure 35, in which a shifted¹ beam scenario is drawn in green. In general, both the target and antiproton beam have to be shifted as a unit to achieve a IP displacement without changing the interaction rate or the IP profile. During the operation of the experiment, both beams will be positioned to achieve a maximal overlap giving the highest interaction rates. With their finite positioning resolutions an offset of several hundred μm up to the order of mm can be expected (see section 2.2.1). To probe the influence of the IP offset on the luminosity determination, various simulations with a shifted IP in the xy plane, were generated. The magnitudes of the displacements are either 1 mm or 3.5 mm, while the same IP distribution as in the previous section was used. Those values resemble an expected and extreme shift of the IP. The strong forward angles of the scattered antiprotons suppress the influence of shifts in the z direction. Also only minor systematic effects in the xy position are introduced due to this approximation. Therefore it is possible to work without the determined mean offset in the z dimension.

At first these simulated angular distributions with IP offsets are fitted assuming there was no displacement to determine the severity of the systematic effects on the extracted luminosity. The results are shown in figure 39. Immediately visible is the point symmetry

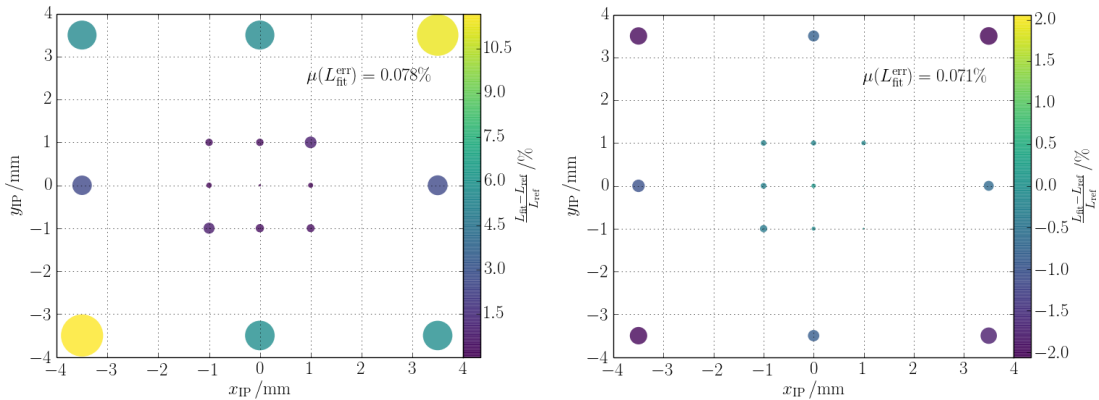


Figure 39: Relative precision of the fitted luminosity for various displacements of the IP without applying correction procedures (left: $p_{\text{lab}} = 1.5 \text{ GeV}/c$; right: $p_{\text{lab}} = 15 \text{ GeV}/c$). 1 mm and 3.5 mm magnitudes for the offsets were simulated, while the former is an expected shift and the latter an extreme scenario. The diameter of the points are scaled with an arbitrary factor to additionally visualize the severity of the deviation of the luminosity between various displacements. $\mu(L_{\text{fit}}^{\text{err}})$ is the mean statistical error on the obtained luminosity from the fit for all displacement scenarios.

around the origin, with the largest relative deviations of up to 10% on the diagonal at $x_{\text{ip}} = y_{\text{ip}} = \pm 3.5 \text{ mm}$. For expected displacements of 1 mm the systematic uncertainty of the luminosity determination is in the order of 1%, precise to about 0.08%. This states the need for a correction procedure. If the offsets of the IP can be extracted from the reconstructed measured tracks, a data sample with these displacement values can be simulated and used to determine the acceptance and resolution. Even though only the scattered antiproton track is measured the displacement of the IP can still be determined,

¹ The terms displacement, offset and shift are used interchangeably for IP displacements.

by studying the xy distribution of the reconstructed tracks in the proximity of the origin. From the backtracking procedure the interaction vertex is determined via the closest point of approach (CPA) with respect to the origin of the \bar{P} ANDA laboratory frame. The distributions of the reconstructed x and y IP positions for an exemplary data sample are shown in figure 40. The mean displacements are determined by fitting gaussian

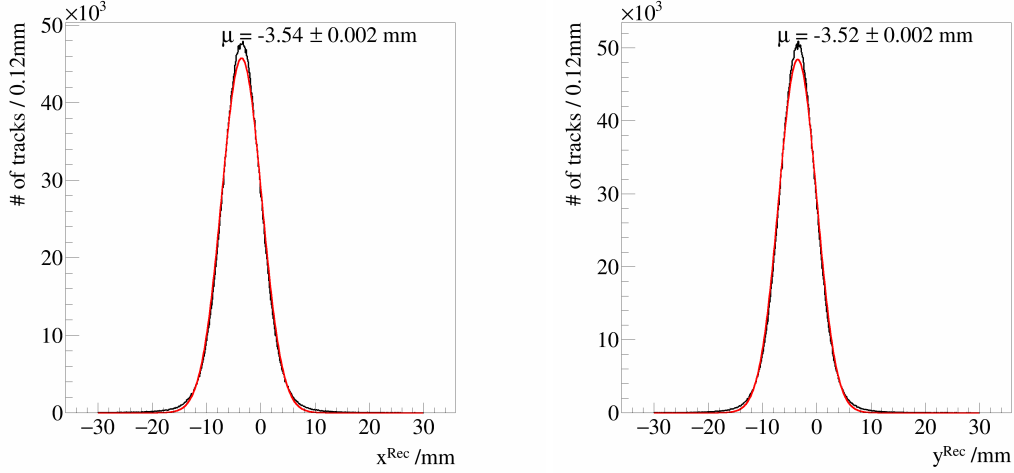


Figure 40: Reconstructed IP distributions of x_{IP} (left) and y_{IP} (right) using the CPA during backtracking for a shifted IP scenario simulated with $\mu(x_{IP}) = \mu(y_{IP}) = -3.5$ mm. The red lines indicate a gaussian function fit, with the mean of the gaussian and statistical error listed.

functions to these distributions and only small deviations between the functions and the distributions can be recognized. The description of the gaussians is appropriate and the extraction of the mean only shows a small systematic uncertainty from the true value. When performing this procedure on all of the previously cases in figure 39, the precision on the IP determination can be studied.

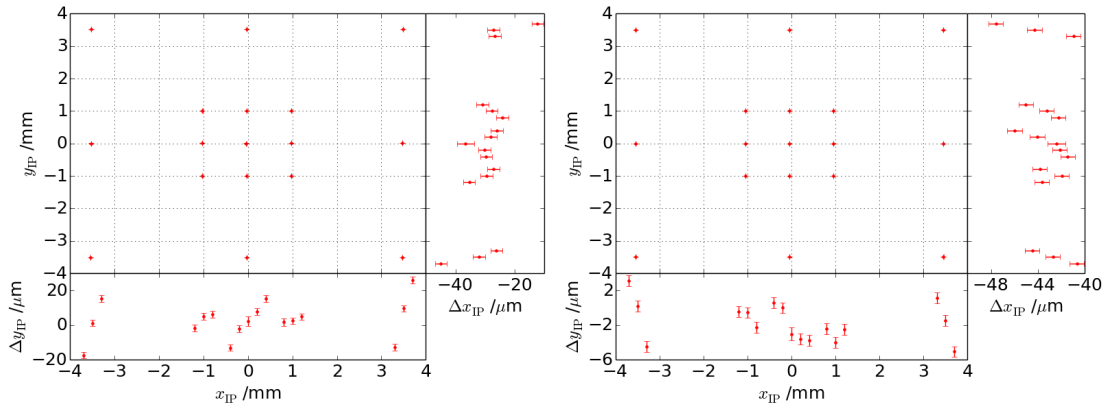


Figure 41: Reconstructed mean displacements x_{IP} , y_{IP} and the statistical errors obtained from the gaussian fits (left: $p_{lab} = 1.5$ GeV/c, right: $p_{lab} = 15$ GeV/c). The attached graphs on the right and bottom show the difference Δx and Δy to the generated mean IP displacements. A small constant spacing between points with identical true x_{IP} or y_{IP} was introduced. The order of the points is defined by the less than relation of the values in the other dimension, e. g. y_{IP} for Δx .

Figure 41 summarizes the results. The accuracy of the measured offset in y direction is below $20 \mu\text{m}$ and $6 \mu\text{m}$ for the lab momenta 1.5 GeV/c and 15 GeV/c respectively. Also

no mean systematic deviation is visible. However it can be seen that the deviation to the ideal value is dependent on the y displacement itself, as the shift is in general overestimated for positive values and vice versa. On the contrary the measured offset in the x direction does not show this dependency as prominently. Though, in this case the measured values for x_{ip} are systematically underestimated with about $-30 \mu\text{m}$ for $1.5 \text{ GeV}/c$, and slightly worse for $15 \text{ GeV}/c$ with $-43 \mu\text{m}$. The reason for this underestimation is the false assumption of the momentum of the tracks in the back propagation procedure, as discussed in section 3.5. Since the reconstructed tracks possess a momentum slightly smaller than the beam momentum, their deflection would be stronger in reality. Overall the mean positions of the IP can be extracted with a precision of below $50 \mu\text{m}$.

Finally, simulations with the measured IP displacements are used to obtain the corrected angular acceptance information, which is used in the luminosity fits. The overview of the fit results when using the offset corrected angular acceptances is shown in figure 42. The original accuracy on the determined luminosity of below 0.1% is restored. Further-

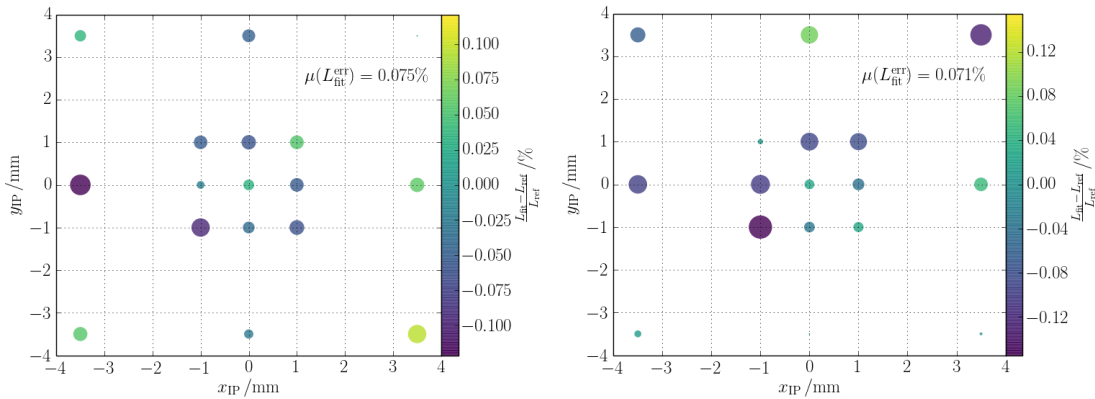


Figure 42: Relative precision of the fitted luminosity for various displacements of the IP using the correction procedure (left: $p_{\text{lab}} = 1.5 \text{ GeV}/c$; right: $p_{\text{lab}} = 15 \text{ GeV}/c$). 1 mm and 3.5 mm magnitudes for the offsets were simulated. The diameter of the points are scaled with an arbitrary factor to additionally visualize the severity of the deviation of the luminosity between various displacements. Note that a different color scale is used here. $\mu(L_{\text{fit}}^{\text{err}})$ is the mean statistical error on the obtained luminosity from the fit for all displacement scenarios.

more the deviation from the generated luminosity for all offset scenarios is compatible with the statistical error of 0.07% obtained from the minimizer Minuit2 [113]. However figure 42 also suggests a small underestimation of the luminosity after the offset correction, as the relative differences appear slightly more frequently below zero.

5.2.3 Accelerator Beam Tilt

Similar to the offsets of the two beams, their tilts can influence the precision of the extracted luminosity. Since the target beam velocities are by magnitudes smaller than the velocities of the accelerator beam particles, the target can be viewed as fixed without concerns and possible tilts of the target beam can be neglected. A scenario of a tilted accelerator beam is sketched in figure 35, indicated with the blue tracks. Obviously the measured angular track distribution is directly altered, since the physics reference frame no longer coincides with the laboratory system, but are instead rotated with respect to each other. The beam tilt effect can be studied by generating data for various scenarios in

the $\theta_x\theta_y$ tilt plane and fitting with the assumption of a nonexistent accelerator beam tilt. In the simulations the standard IP distribution is used, but the mean of the IP distribution is kept at the origin.

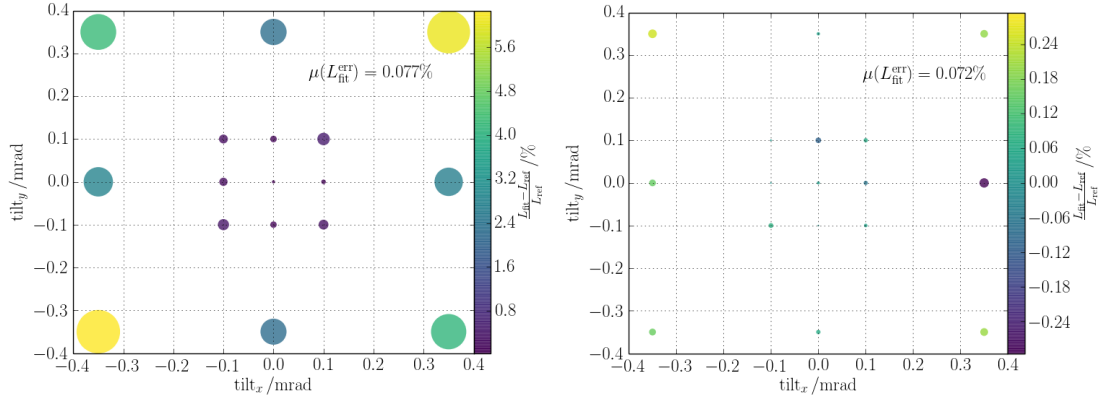


Figure 43: Relative precision of the fitted luminosity for various accelerator beam tilts without applying correction procedures (left: $p_{\text{lab}} = 1.5 \text{ GeV}/c$; right: $p_{\text{lab}} = 15 \text{ GeV}/c$). 0.1 mrad and 0.35 mrad magnitudes for the tilts were simulated, while the former is an expected tilt and the latter an extreme scenario. The diameter of the points are scaled with an arbitrary factor to additionally visualize the severity of the deviation of the luminosity between various tilts. $\mu(L^{\text{errfit}})$ is the mean statistical error on the obtained luminosity from the fit for all scenarios.

Figure 43 gives an overview of the effect of a tilted beam, which produce systematic relative differences of the luminosity of up to 6% for the larger tilts of 0.35 mrad at $p_{\text{lab}} = 1.5 \text{ GeV}/c$. At higher beam momenta the systematic deviations are reduced to about 0.2%. The higher accuracy of the extracted luminosity for the higher beam momenta is based on the flattening of the elastic cross section (see figure 25). Similar to the studies of the shift of the interaction point, a point symmetry is present. Furthermore for the low beam momentum case all of the scenarios overestimate the actual luminosity.

The tilt of the accelerator beam merely implicates a rotation of the coordinate system. Once the tilting of the accelerator beam is introduced into the model according to equations 23 and 24, the tilted measured angular distribution can now be described correctly. In addition, also the accelerator beam tilt parameters are a result of the luminosity fit. The extracted tilt parameters and their errors for all of the scenarios are shown in figure 44.

For both the lowest and highest beam momentum case no systematic deviations from the generated tilt values can be seen. An upper bound for the accuracy is $3 \mu\text{rad}$ and $30 \mu\text{rad}$ respectively. Regarding the statistical errors obtained from the fit, the actual accuracy is likely below this upper bound. In addition no dependency on the beam tilts of the relative luminosity is visible. Despite the lower sensitivity of beam tilts on the luminosity with respect to IP offsets, the beam tilt parameters are determined with excellent accuracy.

The overview of the relative luminosity uncertainties are shown in figure 45. Again, the luminosity is determined correctly and the deviations to the generated values are compatible with the statistical errors of 0.07%. Also judging from figure 45 the determined luminosity is slightly underestimated on a sub per-mille level. With the two tilt parameters the estimator space is increased to three dimensions, and the minimization problem becomes more complex, thus reducing the fitting speed.

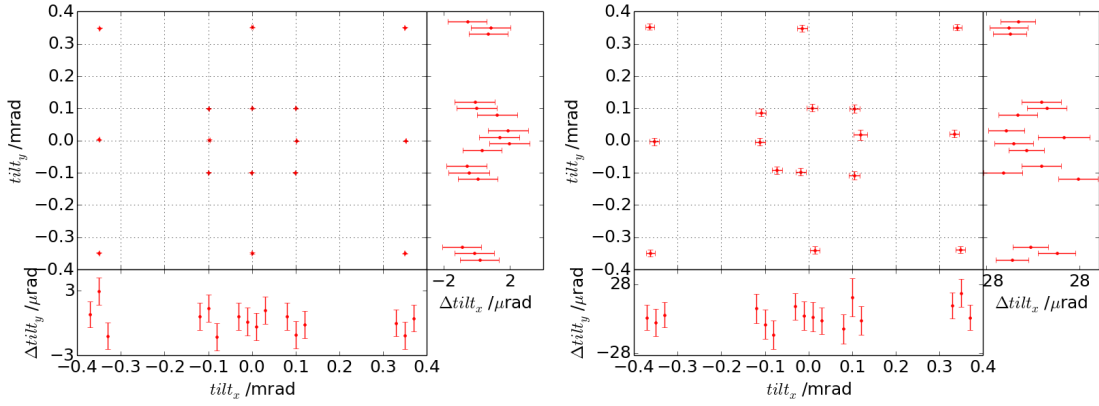


Figure 44: Reconstructed beam tilt tilt_x , tilt_y and their statistical errors obtained from the luminosity fits (left: $p_{\text{lab}} = 1.5 \text{ GeV}/c$, right: $p_{\text{lab}} = 15 \text{ GeV}/c$). The attached graphs on the right and bottom show the difference Δtilt_x and Δtilt_y to the generated beam tilts. A small constant spacing between points with identical generated tilt_x or tilt_y was introduced. The order of the points is defined by the less than relation of the values in the other dimension, e.g. tilt_y for Δtilt_x .

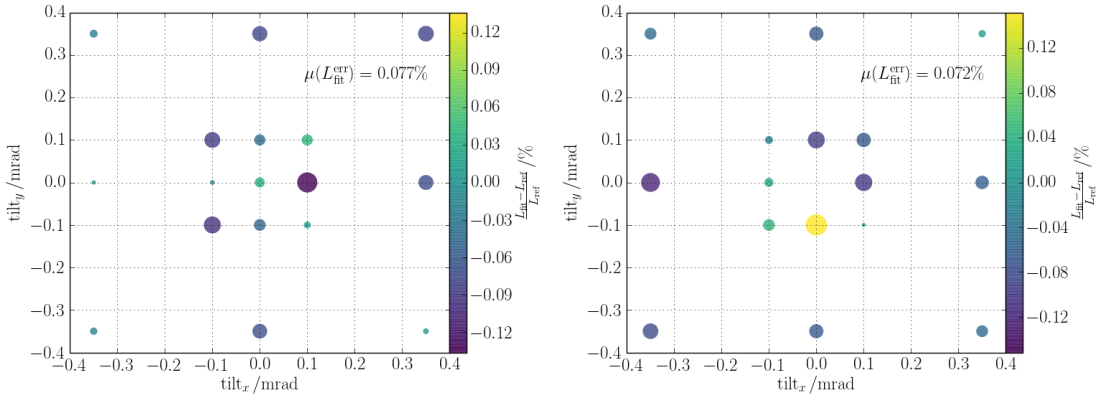


Figure 45: Relative precision of the fitted luminosity for various accelerator beam tilts using the correction procedure (left: $p_{\text{lab}} = 1.5 \text{ GeV}/c$; right: $p_{\text{lab}} = 15 \text{ GeV}/c$). 0.1 mrad and 0.35 mrad magnitudes for the tilts were simulated. The diameter of the points are scaled with an arbitrary factor to additionally visualize the severity of the deviation of the luminosity between various tilts. Note that a different color scale is used here. $\mu(L_{\text{fit}}^{\text{err}})$ is the mean statistical error on the obtained luminosity from the fit for all scenarios.

5.2.4 Accelerator Beam Divergence

In analogy to the distribution of the interaction point, the accelerator beam particles are distributed around the mean tilt. This distribution is also known as the beam divergence. Similar to the tilt, the beam divergence will also directly influence the elastic cross section. More precisely, the physics coordinate system is now no longer the same for the individual beam particles, as it has to be aligned to the flight direction. Because the physics scattering process is independent on the orientation of the coordinate system, the beam divergence is identical to a smearing of the elastic cross section by the divergence distribution in the reference frame aligned to the mean beam tilt.

Again the influence of the beam divergence on the accuracy of the luminosity determination can be studied by generating data samples from simulations with various

divergences, while assuming no divergence when performing the luminosity fit. For the parameterization of the divergence a two dimensional normal distribution was chosen, as this is to be expected. Additional insight about the parameterization of the divergence can later be gained from beam measurements by the HESR group. Three different values for the standard deviation of the distributions $\text{div}_{x,y} = 0.1, 0.2, 0.35$ mrad, independently in the θ_x and θ_y dimension, were simulated.

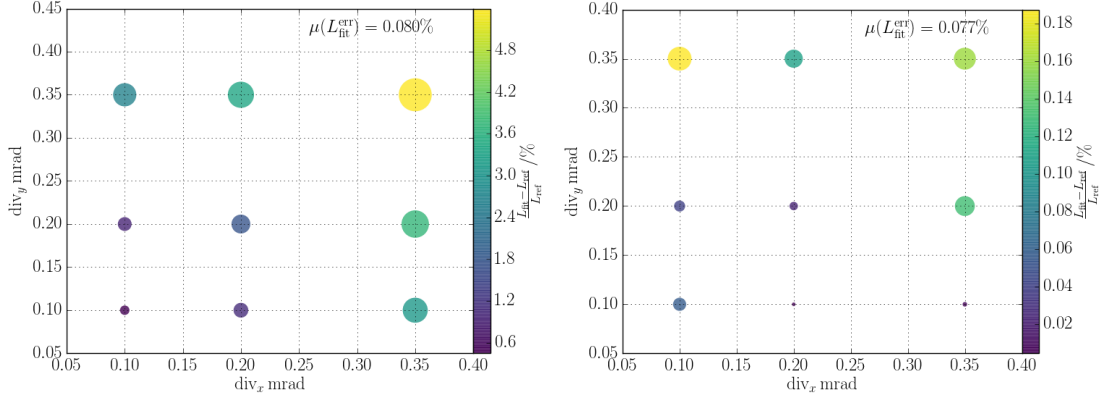


Figure 46: Relative precision of the fitted luminosity for various accelerator beam divergences without applying correction procedures (left: $p_{\text{lab}} = 1.5$ GeV/c; right: $p_{\text{lab}} = 15$ GeV/c). A two dimension normal distribution is used for the parameterization of the divergence. Multiple scenarios with three different standard deviations, 0.1 mrad, 0.2 mrad and 0.35 mrad, were simulated. The diameter of the points are scaled with an arbitrary factor to additionally visualize the severity of the deviation of the luminosity between various divergences. A different scaling factor for the two momentum cases was used. $\mu(L_{\text{err}}^{\text{fit}})$ is the mean statistical error on the obtained luminosity from the fit for all scenarios.

The fit results for these scenarios are shown in figure 46. In the 1.5 GeV/c case the relative deviation of the luminosity changes with the divergence as expected. For the largest beam divergence of $\text{div}_x = \text{div}_y = 0.35$ mrad also the largest systematic deviation from the generated luminosity of 5.4% can be observed. The systematic overestimation of the luminosity is below 2.0% for realistic divergences of 0.2 mrad or lower. On the other hand the influence of the beam divergence for beam momenta of 15 GeV/c is almost negligible. The largest observed relative deviation is 0.18% at $\text{div}_{x,y} = (0.1, 0.35)$ mrad. Analogous to the case with only the tilted beam, the reason for the varying severity of this systematic influence at the different beam momenta is the shape of the elastic scattering cross section in the angular range of the LMD. In general, the more structure and asymmetry is present in the elastic scattering cross section, the stronger the modifications from the divergence smearing. While the cross section has a large slope at scattering angles in the LMD range for 1.5 GeV/c beam momentum, it is comparatively flat at higher momenta (see figure 25). This flattening already occurs at a beam momentum of 4.06 GeV/c, so that the influence of the divergence on the extracted luminosity becomes negligible.

The extension of the fit model to include the beam divergence was presented in section 4.3. Similar to the correction for the IP distribution, the parameterization of the divergence has to be known for this procedure. Here also a two dimensional normal distribution is used, which is defined to be zero outside of the $\pm 5\sigma$ region. When performing the luminosity fit with the divergence correction, the variables of the divergence parameterization, in this case the two standard deviations, do not have to be known.

Rather they can be promoted to fit parameters and simultaneously be extracted with the luminosity.

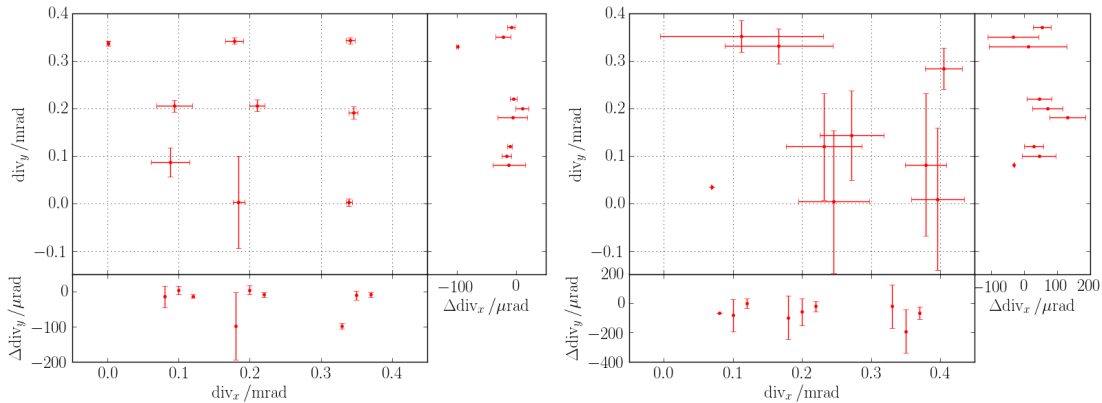


Figure 47: Reconstructed beam divergence div_x , div_y and the statistical errors obtained from the luminosity fits (left: $p_{\text{lab}} = 1.5 \text{ GeV}/c$, right: $p_{\text{lab}} = 15 \text{ GeV}/c$). The attached graphs on the right and bottom show the difference Δdiv_x and Δdiv_y to the generated beam divergences. A small constant spacing between points with identical true div_x or div_y was introduced. The order of the points is defined by the less than relation of the values in the other dimension, e. g. div_y for Δdiv_x . Because the errors on some of the fits are so large that they would distort the plot scale, these errors are limited to 0.15 mrad.

Figure 47 shows the results of the determined divergences with respect to the generated values. Immediately visible is the comparatively bad precision of the extracted divergences, especially in the high beam momentum case. Furthermore the accuracy is lower for asymmetric distributions, in which the divergence is different in both dimensions. For example in the case ($\text{div}_x = 0.35 \text{ mrad}$, $\text{div}_y = 0.1 \text{ mrad}$) at the beam momentum of $1.5 \text{ GeV}/c$, the divergence is determined well in the div_x dimension but poorly in the div_y dimension. Also the error estimations from the minimizer are no longer valid. At higher momenta the accurate extraction of the divergence is not possible. However this is expected from the small influence of the divergence on the extracted luminosity (see figure 46).

The stability of the fit was initially reduced when using the divergence correction and several adjustments in the fitting process were mandatory. Recall that the binned extended log-likelihood estimator was used for the optimization process (see section A.1). Crucial for a better convergence behavior was the normalization of the log-likelihood. The absolute log-likelihood values of the luminosity fit are usually large numbers in the order of 10^7 . However in the proximity of the minimum this value only changes slightly with absolute differences below 10^{-3} . In general the location of the minimum does not change² when adding an arbitrary constant to the estimator function. By subtracting the log-likelihood value of the initial or start parameters during the minimization process, this numerical issue can be resolved and the convergence behavior of the fits improves greatly. However since the initial parameters can be far away from the minimum, the log-likelihood values may vary several orders of magnitude when reaching the neighborhood of the minimum. This restores the original problem, but can be resolved by interrupting the fit several times on the way to the minimum and using the last parameter set as new initial parameters of the next iteration.

² Because the minimum is located at the position at which the derivative is equal to zero.

Additional stability can be gained by choosing good start parameters in the first place. Initially a fit without divergence is performed to obtain good values for the beam tilts. These values are then used in a second level fit with the divergence correction. The two divergence start parameters are determined by scanning a crude grid of the log-likelihood space in these variables. After normalizing all log-likelihood scan values to their mean again, the best divergence parameter set is used as start parameters of the second level fit.

When using all these fit adjustments the convergence of all fits was restored. The divergence parameters can be successfully extracted, although with varying accuracy of between $10 \mu\text{rad}$ and $200 \mu\text{rad}$ depending on the scenario. The influence of the divergence correction on the extracted accuracy of the luminosity can be seen in figure 48. The luminosity can be extracted with an accuracy of below $0.40 \pm 0.17 \%$ for $1.5 \text{ GeV}/c$

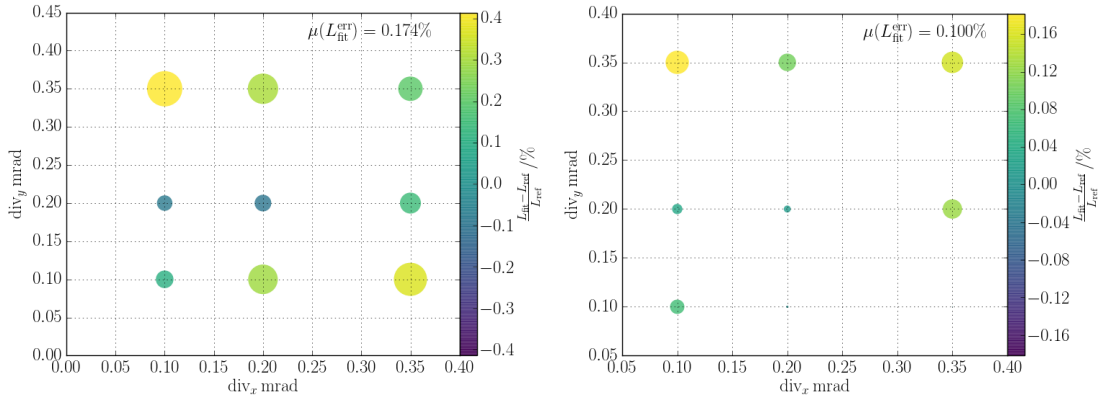


Figure 48: Relative precision of the fitted luminosity for various divergenc values using the correction procedure (left: $p_{\text{lab}} = 1.5 \text{ GeV}/c$; right: $p_{\text{lab}} = 15 \text{ GeV}/c$). 0.1 mrad and 0.35 mrad magnitudes for the divergences were simulated. The diameter of the points are scaled with an arbitrary factor to additionally visualize the severity of the deviation of the luminosity between various divergences. $\mu(L_{\text{fit}}^{\text{err}})$ is the mean statistical error on the obtained luminosity from the fit for all scenarios.

and $0.16 \pm 0.10 \%$ for $15 \text{ GeV}/c$. Most problematic are the asymmetric divergence distributions, in which one dimension has a stronger divergence than the other. Especially for very small divergences below 0.1 mrad , the divergence smearing algorithm becomes ineffective and the fit is unable to estimate the divergence parameter. Therefore the stated accuracy can be regarded as upper bounds.

When comparing the accuracy with the mean statistical error estimate of 0.17% from the minimizer, the upper bound of 0.4% is rather tolerant.

The reason for this insensitivity is that the correction procedure operates on a grid, which discretizes the models (see section 4.3). This introduces an artificial resolution of the smearing algorithm and depends on the grid constant, here $26 \text{ mrad}/300 = 0.087 \text{ mrad}$. The extreme case of a small divergence illustrates this nicely. In the correction algorithm the integrals of the divergence function for the bins defined by the grid give the basis for the redistribution of the corrected elastic cross section. These modifications vanish, once the divergence distribution is completely contained within a single bin. For the 2D normal distribution used here, the changes by the divergence correction become negligible at the one σ threshold of $\text{div}_\sigma^{\text{thres}} = 0.043 \text{ mrad}$. At this point the minimizer loses the sensitivity to the divergence parameters and is unable to deter-

mine them accurately. However for small divergences, the influence on the luminosity is insignificant and the divergence correction is no longer required.

5.3 REALISTIC SCENARIOS

p_{lab} /GeV/c	IP_x	IP_y	IP_z	σ_x	σ_y	σ_z	tilt_x	tilt_y	div_x	div_y	$\Delta L/L$ /%
	/mm						/ μrad				
1.5	0.2	-1.3	-0.1	0.8	0.5	3.1	160	140	160	140	0.49 ± 2.47
	0.17	-1.29	0.0	0.8	0.8	3.5	160	138	11	44	
	-0.6	1.8	0.8	0.6	0.5	3.1	160	-10	90	110	-0.16 ± 0.23
	-0.62	1.82	0.0	0.8	0.8	3.5	158	-14	1	97	
4.06	-1.3	0.3	1.3	0.6	0.5	3.8	170	90	150	130	0.59 ± 0.29
	-1.31	0.3	0.0	0.8	0.8	3.5	174	86	60	3	
	1.7	0.8	-1.4	0.4	1.1	3.7	-20	70	90	80	-0.25 ± 0.45
	1.69	0.81	0.0	0.8	0.8	3.5	-23	67	147	166	
	-1.5	-2.0	-1.9	0.8	1.0	3.4	170	-100	80	150	-0.61 ± 0.45
	-1.5	-2.01	0.0	0.8	0.8	3.5	172	-102	191	197	
8.9	1.0	-0.0	-0.1	0.8	1.1	3.6	-20	-150	110	100	0.09 ± 0.29
	1.01	-0.0	0.0	0.8	0.8	3.5	-30	-152	131	4	
8.9	0.1	-0.8	1.9	0.5	1.2	3.5	30	-140	190	180	-0.20 ± 0.23
	0.08	-0.79	0.0	0.8	0.8	3.5	21	-133	224	194	
15.0	1.8	1.9	0.3	0.7	0.4	3.7	60	-190	60	90	-0.07 ± 1.86
	1.75	1.9	0.0	0.8	0.8	3.5	61	-197	99	11	
	0.2	0.2	-1.3	0.8	0.4	3.3	-50	-30	80	140	-0.02 ± 0.12
	0.15	0.2	0.0	0.8	0.8	3.5	-86	-14	-	-	
	0.1	-1.2	-0.3	1.1	1.1	3.5	-140	60	100	140	-0.05 ± 0.12
	0.05	-1.19	0.0	0.8	0.8	3.5	-144	35	-	-	

Table 5: Ten fit results of the luminosity determination and the IP determination procedure are shown. Every pair of rows represents a scenario with a random generated accelerator beam momentum p_{lab} , tilt $\text{tilt}_{x,y}$, divergence $\text{div}_{x,y}$ and IP parameters $IP_{x,y,z}$ and $\sigma_{x,y,z}$. The first row shows the generated or true values, while the second row gives the values for all of the determined parameters. In the last column the relative deviation to the generated luminosity value with the statistical error obtained from the minimizer is shown. The values for IP_z , $\sigma_{x,y}$ and σ_z for the fit model are assumed and not extracted by the fit. Two fits at 15 GeV/c failed initially, after which the divergence correction was automatically turned off.

Previously the systematic influences of the accelerator beam and IP were studied independently. In reality these effects are coexistent and thus the robustness and accuracy of the luminosity fit has to be studied. Ten data samples with random values for the IP offset, IP distribution, beam momentum, tilt and divergence were generated. The parameters are randomly chosen from intervals that spread over the expected value ranges. For the beam momenta only four distinct possibilities 1.5, 4.06, 8.9 and 15 GeV/c are used, at which the magnetic field maps are known with the highest accuracy. Each of these

data sets resembles a realistic PANDA runtime scenario and contains $10 \cdot 10^6$ DPM elastic scattering events with a lower angular cut-off of 1 mrad. Because the integral of the elastic cross section in the LMD range changes with the beam momentum, the number of reconstructed tracks also varies for the different scenarios.

Table 5 compares the results of the luminosity fit procedure with the generated parameters. For each scenario only a single fit was performed. The interaction point shift is again determined with an accuracy of about $50 \mu\text{m}$ using the procedure mentioned above. The z-offset cannot be determined in this way and was assumed to be not present in the fit model. Normal distributions with fixed widths of $\sigma_{x,y} = 0.8 \text{ mm}$ and $\sigma_z = 3.5 \text{ mm}$ were used for the modeling of the interaction region.

The antiproton beam tilts and divergence are determined from the fit with varying accuracy, so that they need to be studied more detail. Furthermore for two of the 15 GeV beam momentum cases the fits failed to converge and had to be rerun without the divergence correction. Hence no divergence parameters are available for these scenarios. Additional fits with three different settings were performed on the ten scenarios to study the importance of including the tilt and divergence in the fit. Their influence on the luminosity, as well as their accuracy and precision are analyzed. One setting is without the divergence correction, another without the divergence correction and keeping the tilts fixed to zero and finally also a fit setting with values of the divergence fixed to the generated values. Table 6 compares the results of all fit settings.

case	p_{lab} /GeV/c	Δtilt_x / μrad	Δtilt_y / μrad	$\Delta L/L$ /%
normal	1.5	0 ± 3	-2 ± 3	0.49 ± 2.47
		-2 ± 3	-4 ± 3	-0.16 ± 0.23
	4.06	4 ± 4	-4 ± 4	0.59 ± 0.29
		-3 ± 4	-3 ± 4	-0.25 ± 0.45
		2 ± 4	-2 ± 4	-0.61 ± 0.45
		-10 ± 4	-2 ± 4	0.09 ± 0.29
	8.9	-9 ± 8	7 ± 9	-0.20 ± 0.23
	15.0	1 ± 21	-7 ± 20	-0.07 ± 1.86
		-36 ± 20	16 ± 20	-0.02 ± 0.12
		-4 ± 20	-25 ± 20	-0.05 ± 0.12
no div.	1.5	0 ± 3	-2 ± 3	0.53 ± 0.18
		-3 ± 3	-3 ± 3	0.04 ± 0.18
	4.06	4 ± 4	-4 ± 4	0.66 ± 0.23
		-1 ± 4	-2 ± 4	0.64 ± 0.23
		0 ± 4	-5 ± 4	0.74 ± 0.23
		-10 ± 4	-2 ± 4	0.43 ± 0.23
	8.9	-11 ± 9	-1 ± 9	0.25 ± 0.19
	15.0	3 ± 20	-7 ± 20	-0.07 ± 0.12
		-36 ± 20	16 ± 20	-0.02 ± 0.12
		-4 ± 20	-25 ± 20	-0.05 ± 0.12

no tilt & div.	1.5	-	-	-0.18 ± 0.17
		-	-	1.87 ± 0.17
	4.06	-	-	1.17 ± 0.23
		-	-	0.55 ± 0.23
		-	-	-0.28 ± 0.23
		-	-	1.01 ± 0.23
	8.9	-	-	0.44 ± 0.19
	15.0	-	-	-0.06 ± 0.12
		-	-	-0.01 ± 0.12
		-	-	-0.02 ± 0.12
with gen. div.	1.5	0 ± 3	-3 ± 3	-0.45 ± 0.17
		-4 ± 3	-4 ± 3	-0.40 ± 0.18
	4.06	3 ± 4	-6 ± 4	-0.06 ± 0.23
		-2 ± 4	-2 ± 4	0.36 ± 0.23
		0 ± 4	-2 ± 4	0.23 ± 0.23
		-10 ± 4	-1 ± 4	0.01 ± 0.23
	8.9	-10 ± 8	5 ± 8	-0.10 ± 0.19
	15.0	2 ± 20	-7 ± 20	-0.07 ± 0.12
		-35 ± 20	16 ± 20	-0.04 ± 0.12
		-2 ± 20	-23 ± 20	-0.07 ± 0.12

Table 6: Influence of various fit settings on the beam tilts and luminosity. In addition to the normal case identical to the results shown in table 5, the results of three other cases are given. These are luminosity fits without divergence correction, another with no divergence correction including the fixing of the beam tilt parameters to zero and finally a fit setting in which the divergence parameters are set to the generated values. The residuals for the two tilt parameters and the relative luminosity with respect to the generated value are denoted.

The accuracy of the tilt has to be classified into the lower and higher beam momenta. For all kinds of fits the tilt is extracted with an accuracy below $10 \mu\text{rad}$ for momenta up to about $4.06 \text{ GeV}/c$. Above, larger deviations to the generated tilts of up to $40 \mu\text{rad}$, as well as a lower precision, are evident. An identical behavior was already visible in the independent beam tilt study. The reason is the flattening of the elastic cross section in the angular range of the LMD. Because of this missing structure in the cross section distribution, the influence from the beam tilts decreases.

When comparing the determined tilt values from all fit settings, a high extraction stability is proven. In general the extracted luminosities are statistically compatible with the generated values and the deviations for the relative difference are below the percent level. Only for the case of fixing the tilts to zero, one can see larger deviations of up to 1.9% for the extracted luminosity. Therefore it is not recommended to fix the beam tilts, unless the values are well known from other measurements.

For the divergence also a separation of the results in the lower and higher beam momentum range has to be made. From the uniformity of the elastic cross section in the

LMD region, also a minor influence of the divergence on the extracted luminosity at larger beam momenta can be concluded. This fact is nicely supported from the results in table 6 and 5. Even though the divergence is determined poorly for all scenarios, the deviations of the luminosity relative to the generated value become smaller at higher antiproton momenta. However in accordance with section 5.2.4, the low accuracy of the determined divergence is to be expected.

The dependence of the divergence on the extracted luminosity accuracy increases in the lower momentum sector for momenta of about 4.06 GeV/c and below. An accurate extraction of the divergences is difficult for present divergences of 200 μ rad and below. This was already discussed in section 5.2.4. Table 6 shows that comparable results are achieved, when not using the divergence correction. Then also the statistical error estimation for the extracted luminosity is more stable. A higher accuracy for the luminosity can be achieved in the low beam momentum case, when using precise divergence values, for example from measurements by the HESR.

The single fit results shown in table 5 indicate that the luminosity is determined with an accuracy below the percent level. This is concluded from the largest deviations of approximately 0.6% in the 4.06 GeV/c case, which poses estimated statistical errors of about 0.29 and 0.45%. A more quantitative statement on the accuracy and also the correctness of the error estimation can be made, when performing a systematic study.

For this purpose the scenario with the largest deviation in the luminosity of -0.61% was selected³. The complete data of this scenario was bootstrapped to yield 120 samples each containing 70% of the data. All of these samples are fitted and the extracted parameters are compared with the generated values. The residuals for the parameters of the luminosity fit are shown in figure 49. Except tilt_y all parameters show a bias. Most importantly the accuracy for the extracted luminosity lies between 0.33%-0.49% with a 95% confidence level. Overall the minimizer estimates the statistical errors reasonably well. This can be seen when comparing the mean estimated errors with the RMS value of the residuals. More specifically for the luminosity, a slight overestimation is present. In summary it can be concluded that the luminosity is determined with an accuracy of below 0.5% in a stable manner.

³ This corresponds to the fifth scenario, counting from the top of the table

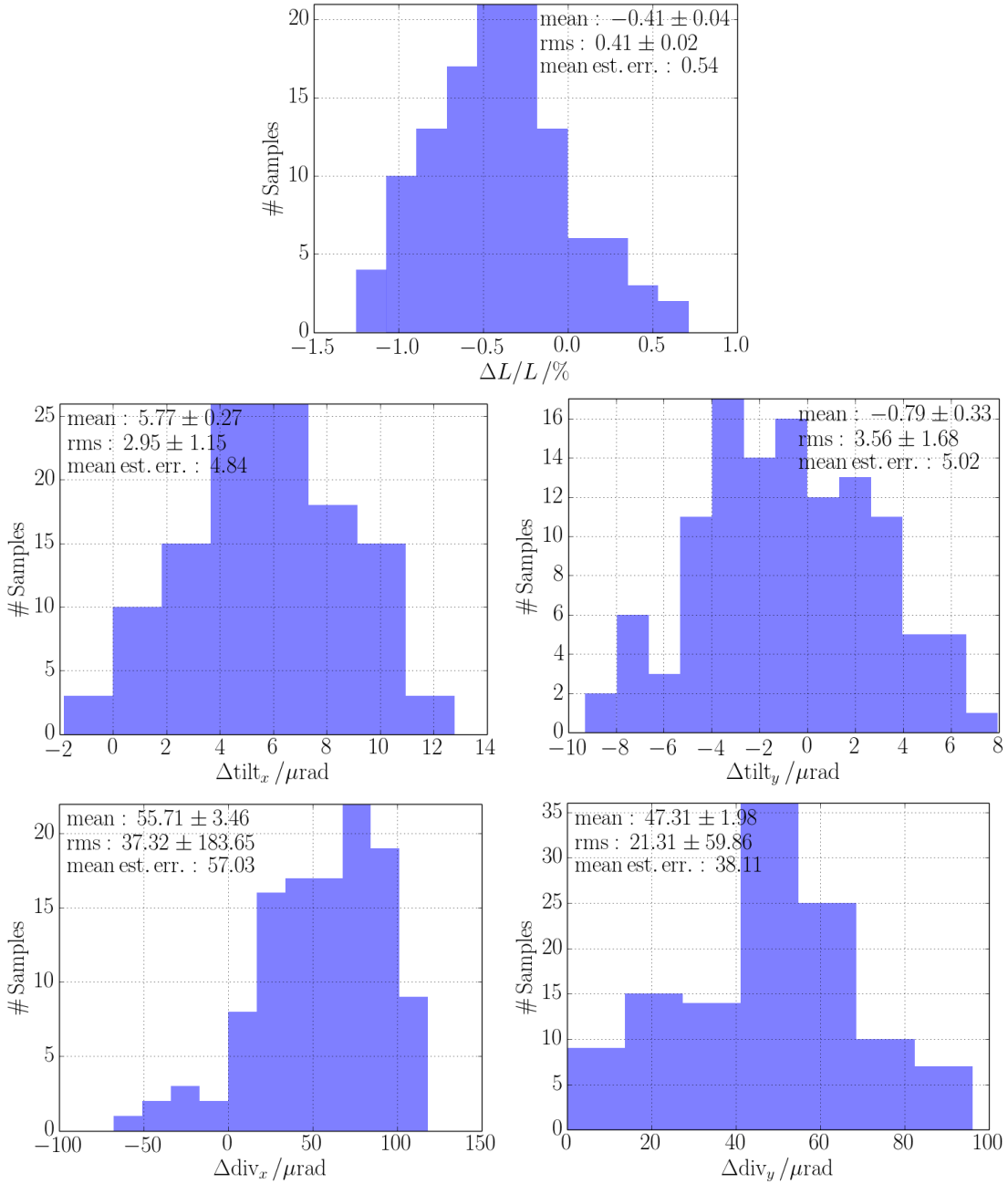


Figure 49: Residuals of all luminosity fit parameters of the 3rd 4.06 GeV/c realistic scenario from table 5 determined from 120 bootstrapped data samples. In the first row is the residual of the relative luminosity. The second row shows residuals of the $\text{tilt}_{x,y}$ parameters, while the residuals for $\text{div}_{x,y}$ are in the last row.

5.4 BACKGROUND SOURCES

Further systematic deviations of the luminosity can arise from background sources. Even though the background was studied in full detail in [98], each category is discussed briefly in connection with the LuminosityFit framework. The background can be classified into three categories, the inelastic, elastic and secondary background.

INELASTIC BACKGROUND: The inelastic background arises from all events in which the antiproton does not scatter elastically on the target, but undergoes an inelastic reaction. Because there is no PID information available for the particle tracks reconstructed by the LMD, all of the inelastic channels are possible background. This might seem like an immense source of background, fortunately the kinematic phase space of the inelastic and elastic channels have very little overlap. Hence the majority of particles from inelastic reactions are deflected into other directions by the magnetic fields. Studies with the DPM generator showed that only 5 % of the particles remain, which pass through the LMD [98, p.141]. After the two stage track filtering of the LMD track reconstruction software, this background is reduced to 0.2 %.

This fraction of inelastic background particles carries a similar momentum as the elastically scattered antiprotons and they cannot be distinguished. Further reduction is possible with the additional term to the elastic cross section in equation 13, which resembles the inelastic contribution of the total cross section

$$\frac{d\sigma}{dt} = \frac{d\sigma_{el}}{dt} + \frac{B}{S} \cdot \frac{d\sigma_{inel}}{dt}. \quad (30)$$

The factor $\frac{B}{S}$ is a ratio of the inelastic background with respect to the elastic signal cross section. Such an inelastic background function is already foreseen in the LuminosityFit software, but this has to be implemented. The parameterization of the inelastic background is a very difficult task. Measurements from the KOALA experiment are helpful. However, due to the low remaining background fraction of 0.2 %, the influence on the luminosity extraction is rated as uncritical.

ELASTIC AND SECONDARIES BACKGROUND: Another rather unexpected background source are elastically scattered antiprotons at larger angles, which are reflected on the beam pipe and are then successfully reconstructed by the LMD. Secondary particles are created by reactions of the particles and material along the path to the LMD, mostly created close to the LMD itself. Particles for either of these two categories mostly lie within a different region of the kinematic space and can therefore be removed with high purity and efficiency by the two stage track filtering parts of the LMD track reconstruction software. In total the background from these two sources can be reduced to about 1 % and is mostly elastic [98, p.156]. Furthermore, since these particles are also produced in simulations used for the generation of the 2D angular efficiency, this information is also contained within the efficiency and is therefore automatically corrected by the luminosity fit. This of course assumes the simulations resemble the physics realistically and that the modeling of the LMD is perfect. In conclusion the systematic deviation on the luminosity is expected to be well below the percent level and can be neglected.

MORE BACKGROUND SOURCES: An additional source of background can arise from noisy pixels that create ghost tracks. Since the noisy pixel rate corresponds to a single noise pixel per track reconstruction time frame [20, p.87], this background source is negligible. Furthermore the option of performing simulations with noisy pixels is available, which allows for corrections via the luminosity fit.

5.5 DISCUSSION & OUTLOOK

It was shown that for an ideal beam scenario, regarding the IP and antiproton beam momentum distribution, the LuminosityFit software is able to extract the luminosity with an accuracy of below the permille level. Also the cross section, corrected with the acceptance and detector resolution, is able to describe the angular distribution of the reconstructed tracks perfectly, as no systematic deviation between them is visible.

In addition the influence of the IP distribution and displacement, as well as the accelerator beam tilt and divergence, were studied systematically. If not correcting for the distribution of the interaction point, excluding a mean displacement, a systematic error of about 0.4% is present for the lowest beam momentum of 1.5 GeV/c. At higher beam energies the influence diminishes quickly and no systematic deviation was noticeable at 15 GeV/c. Even though the IP distribution cannot be determined by the LMD, an expected distribution can be used to obtain corrected results that push the accuracy of the luminosity fit again below the permille level. Later the PANDA experiment can deliver IP distribution information, which shall be used for a realistic parameterization.

Despite not being able to measure the mean displacements of the IP in beam direction (z-direction), it is possible to extract the information in x and y dimension with an accuracy of 50 μm . When not correcting for the IP shifts, the deviation of the determined luminosity is approximately 2% for realistic displacements of about 1.5 mm and can be as large as 10% for a very dramatic scenario of a 5 mm IP-offset. Again the effect in the high momentum case is much less profound. Applying the correction procedure the original accuracy of the determined luminosity below the 0.1% level is recovered. Further optimizations such as exploiting the missing IP_z information are possible, but were not pursued because the accuracy is already sufficient.

Analogously the influence of the accelerator beam tilt was studied systematically. At first no correction procedures were applied for the various data samples with tilted antiproton beams. Also the systematic shifts on the extracted luminosity are most dramatic for the 1.5 GeV/c case. Here the systematic deviations lie between 1.5% for expected beam tilts and 5.5% for extreme scenario tilts of 0.5 mrad. For the 15 GeV/c case the deviation of the extracted luminosity is still below 0.3%. Because the tilt-correction is simply a coordinate transformation, the beam tilt parameters are extracted from the fit with high accuracy of 3 μrad and 30 μrad for 1.5 GeV/c and 15 GeV/c respectively. Furthermore the accuracy of the luminosity again goes below 0.1% after this correction.

The studies of the beam divergence show similar results. When applying no corrections the systematic deviations range from 1.5% for realistic beam divergences to 5.5% for the extreme case at 1.5 GeV/c. The systematic error at 15 GeV/c beam momentum is less severe and lies below 0.2%. A normal distribution parameterization was used for the correction procedure, while the standard deviations are promoted to fit parameters. The conclusion here is that divergences are determined best for large divergences with an accuracy of about 20 μrad for the 1.5 GeV/c case. However the accuracy decreases quickly, the stronger the asymmetry in the divergence distribution becomes. In addition small beam divergences are difficult or impossible to extract in general, due to the discretization introduced by the correction algorithm. At higher beam momenta the beam divergence cannot be extracted. Despite the inaccurate extraction of the divergence parameters, the upper bounds of the systematic deviations of the luminosity after the correction are 0.4% and 0.15% for the two respective extreme beam momenta.

Finally realistic scenarios were studied, that combine all of the above IP and accelerator beam properties. Here also intermediate momenta of 4.06 and 8.9 GeV/c were examined. It was shown that the determination procedure is robust and delivers the luminosity with an accuracy of about 0.5 % for beam momenta up to 5 GeV and 0.1 % for the high momentum regime. The accuracy and momentum dependency of the IP offset, beam tilt and divergence are all in accordance with the individual systematic studies. In general it is recommended to use the LuminosityFit software with all correction procedures. However for higher beam momenta of about 9 GeV and above, the dependence of the beam divergence is negligible and the correction is ineffective. In consequence the divergence correction is not necessary and can be omitted in this case. When switching off the divergence correction the statistical error estimations from the minimizer also become more reliable. Furthermore the fitting procedure is less stable for smaller divergences of below 200 μrad , due to the discretization of the fit model. Improved luminosity results can be obtained in the low momentum sector when using accurate divergence parameters and fixing these in the luminosity fit. The HESR could supply this information.

Further systematic deviations in the determined luminosity can arise from various background sources and was studied in [98]. The background reduction during the track reconstruction is able to minimize the influence. Additionally two background sources are automatically handled by the efficiency correction procedure. The remaining inelastic background contribution amounts to 0.2 % [98, p.156]. Therefore the luminosity would be slightly overestimated by this fraction. To further minimize this contribution a corresponding correction term is already foreseen in the luminosity fit model.

Taking together the systematic effects presented here, the accuracy of the luminosity is dominated by the uncertainty of the hadronic elastic scattering part of the cross section of up to several percent. A more precise parameterization is of need and will be carried out by the KOALA experiment. With all remaining effects an upper bound of 0.5 % for the luminosity accuracy at beam momenta of about 5 GeV/c and below is reached. In the higher momentum range the accuracy is on the 0.1 % level. The statistical error on the luminosity depends on the dataset size. For the realistic scenarios the reconstructed dataset sizes are different, and the statistical errors lie between 0.1 %-0.5 %. This corresponds to roughly 3 seconds of data taking for the low beam momentum case, and 30 seconds of data taking for the high momentum case. For future studies, the influence of the magnetic fields and the detector geometry on the accuracy of the luminosity are interesting and should be examined in detail.

HELICITY FORMALISM IN THE ComPWA FRAMEWORK

When trying to extract information on bound states produced in particle reactions the partial wave expansion is a powerful method, which gives access to a broad spectrum of particles, since the theoretical formulation is general. Furthermore the extraction of the spin and parity of states, next to their mass and width, is possible.

However more than one theoretical description for such processes exist and the comparison between the results of these various models on data-sets is of high value, as it can provide information on their interpretation, accuracy, limits, etc. The Common Partial Wave Analysis (CompWA) framework can achieve such comparisons with its high modularity [23]. By providing this project with the helicity formalism, a first general and well established model is made available and serves as a foundation for diverse analysis. This allows the study of the isoscalar states f_0, f_2, f_4 in the radiative decay $J/\Psi \rightarrow \gamma\pi^0\pi^0$. In the scope of this thesis, the analysis of BESIII data for this process using the helicity formalism is prepared, starting with the implementation of the helicity formalism itself. For this channel a model independent study [23] as well as an analysis in the radiative basis [51] was already performed.

The implementation of the helicity formalism in CompWA is covered in this chapter. With the use of an expert system, a novel approach for the realization is presented. The extensive validation of the helicity formalism implementation is shown in the next chapter. This chapter begins with introduction of the theoretical fundamentals of the partial wave expansion and the helicity formalism.

6.1 THE METHOD OF PARTIAL WAVES

In order to probe the structure of particles, interaction with them, in form of scattering experiments, is indispensable. All of the interesting physics information is contained within the scattering matrix S . Often it is convenient to work in the basis of free particle states where all of their quantum numbers are discrete, except their momentum p_i and energy E_i [91, p.151f]. Defining the discrete quantum number free particle state as $|\Phi_{E,p,N}\rangle$, where all the discrete quantum numbers are absorbed in the label N , the S -matrix can be expressed as

$$\langle\Phi_{E',\vec{p}',N'}^-|S|\Phi_{E,\vec{p},N}^+\rangle = \delta(E' - E)\delta^3(\vec{p}' - \vec{p})S_{N',N}(E, \vec{p}). \quad (31)$$

$|\Phi_{E,\vec{p},N}^+\rangle$ and $\langle\Phi_{E',\vec{p}',N'}^-|$ are the *in* and *out* states defined at times $t \rightarrow -\infty$ and $t \rightarrow \infty$ with respect to the interaction. $S_{N',N}$ is a unitary matrix and is related to the matrix $\mathcal{M}_{N',N}$, which contains the complete interaction information, by

$$S_{N',N} = \delta_{N',N} - i2\pi\mathcal{M}_{N',N}(E, \vec{p}). \quad (32)$$

When the operator \mathcal{M} is rotation invariant, it commutes with the angular momentum operators J^2 and J_z , and the transition amplitude $A := \mathcal{M}_{fi} = \langle \Phi_{E',\vec{p}',N'}^- | \mathcal{M} | \Phi_{E,\vec{p},N}^+ \rangle$ can be expanded in terms of the orbital angular momentum L .

Especially useful are the two-particle states, which are discussed with the example of the two-body decay

$$1 \rightarrow 2 \ 3.$$

This derivation follows the definitions and conventions of reference [114]. Consider the decay of particle 1, with spin J and spin projection m_1 into two particles with spin s_2 and s_3 and projections m_2 and m_3 . All of the spin projections are defined with respect to an arbitrarily chosen quantization axis. The state of particle 1 at rest is denoted by $|Jm_1\rangle$. This also corresponds to the center-of-mass system for the particles 2 and 3, in which they have opposite momenta $\vec{p}_2 = -\vec{p}_3$ with the direction given by the angles (θ, ϕ) . Their free particle state is defined as $|\theta\phi m_2 m_3\rangle$. The spin quantum numbers, and others such as the electric charge, isospin etc., are now dropped for reasons of convenience. Previously they were included in the label N .

The amplitude of the two-body decay can be written as

$$\begin{aligned} A_P(s, \theta\phi; m_1, m_2, m_3) &= \langle \theta\phi m_2 m_3 | \mathcal{M}(s) | Jm_1 \rangle \\ &= \langle \theta\phi m_2 m_3 | JMLS \rangle \langle JMLS | \mathcal{M}(s) | Jm_1 \rangle \\ &\sim \sum_{L,S} (s_2 m_2, s_3 m_3 | Sm_S) (Lm_L, Sm_S | Jm_1) \\ &\quad \cdot Y_L^{m_L}(\theta, \phi) \cdot a_{L,S}^J(s) \end{aligned} \quad (33)$$

with

$$\langle \theta\phi m_2 m_3 | JMLS \rangle = \sum_{L,S} (s_2 m_2, s_3 m_3 | Sm_S) (Lm_L, Sm_S | Jm_1) Y_L^{m_L}(\theta, \phi)$$

and

$$a_{L,S}^J(s) = \langle JMLS | \mathcal{M}(s) | Jm_1 \rangle.$$

Here $|JMLS\rangle$ denotes the two particle state with total spin J and spin projection M . Together with the center-of-mass energy \sqrt{s} , the direction of flight of the decay products (θ, ϕ) defines the kinematics of the decay. The normalization was dropped here as it is not important when only the kinematic distribution of the transition amplitude is of interest. The spins of the two decay products s_2, s_3 form the total intrinsic spin S using the Clebsch-Gordan coefficient $(s_2 m_2, s_3 m_3 | Sm_S)$. In similar fashion this spin S can be coupled with the angular momentum L to the total spin of the two particle state $J = L \oplus S$. Since the spin projections of the initial and final state are given, the spin projections $m_S = m_1 + m_2$ and $m_L = m_J - m_S$ are defined by angular momentum conservation and hence their summation index is dropped.

Naturally there is a splitting of the angular part $Y_L^{m_L}(\theta, \phi)$ and the dynamical part which is encoded in the canonical matrix elements $a_{L,S}^J(s)$. As the latter contain the interesting information from a physical point of view, their properties are in the focus of attention.

6.2 HELICITY FORMALISM

In the helicity basis a particle state is defined by its spin J and the helicity λ , which quantizes the spin along the direction of flight. Because of the invariance of the helicity operator $\lambda = \vec{J} \cdot \frac{\vec{p}}{|\vec{p}|}$ under rotations and boost along $\frac{\vec{p}}{|\vec{p}|}$, this formalism is also suitable for relativistic problems. Returning to the two-body decay, the two particle final state is now defined by the helicities λ_2 and λ_3 as $|Jm_1\lambda_2\lambda_3\rangle$. They are correlated to the canonical two particle states by

$$|Jm_1\lambda_2\lambda_3\rangle = \sum_{LS} \left(\frac{2L+1}{2J+1} \right)^{1/2} (LOS\lambda|J\lambda)(s_2\lambda_2s_3-\lambda_3|S\lambda) |Jm_1LS\rangle \quad (34)$$

$$|Jm_1LS\rangle = \sum_{\lambda_2\lambda_3} \left(\frac{2L+1}{2J+1} \right)^{1/2} (LOS\lambda|J\lambda)(s_2\lambda_2s_3-\lambda_3|S\lambda) |Jm_1\lambda_2\lambda_3\rangle \quad (35)$$

and the decay amplitude in the helicity basis is given by

$$\begin{aligned} A_H(1 \rightarrow 23) &= \langle \theta\phi\lambda_2\lambda_3 | \mathcal{M}(s) | Jm_1 \rangle \\ &= \sum_{\lambda'_2\lambda'_3} \langle \theta\phi\lambda_2\lambda_3 | Jm_1\lambda'_2\lambda'_3 \rangle \langle Jm_1\lambda'_2\lambda'_3 | \mathcal{M}(s) | Jm_1 \rangle \\ &= \left(\frac{2J+1}{4\pi} \right)^{1/2} D_{m_1,\lambda}^{*J}(\phi, \theta, 0) F_{\lambda_2\lambda_3}^J(s) \end{aligned} \quad (36)$$

with

$$\langle \theta\phi\lambda_2\lambda_3 | Jm_1\lambda'_2\lambda'_3 \rangle = \left(\frac{2J+1}{4\pi} \right)^{1/2} D_{m_1,\lambda}^{*J}(\phi, \theta, 0) \delta_{\lambda'_2\lambda_2} \delta_{\lambda'_3\lambda_3}$$

and

$$F_{\lambda_2\lambda_3}^J = \langle Jm_1\lambda_2\lambda_3 | \mathcal{M}(s) | Jm_1 \rangle.$$

The Wigner-D function $D_{m_1,\lambda}^{*J}(\phi, \theta, \psi = 0)$ with $\lambda = \lambda_2 - \lambda_3$ carries the angular information of the decay, with a conventional choice of the third Euler angle $\psi = 0$ [115]. Meanwhile the information of the interaction is captured within the helicity amplitude $F_{\lambda_2\lambda_3}^J(s)$. It is rotation invariant and only depends on the helicities and the total spin J [114, p.16]. It should be noted that both the spin projection of the initial state m_1 and the helicities of the final state particles are regarded as known quantities in this decay amplitude, hence there is no sum over these variables.

For every two-body decay the helicities of the daughters 2 and 3 are restricted by

$$J \geq |\lambda_2 - \lambda_3|. \quad (37)$$

If parity is conserved in the decay, then

$$F_{-\lambda_2-\lambda_3}^J(s) = \eta_1\eta_2\eta_3(-1)^{s_2+s_3-J} F_{\lambda_2\lambda_3}^J(s) \quad (38)$$

with the intrinsic parities denoted as η_i . This relation reduces the number of independent amplitudes by a factor of almost 2. For the special case of a decay into two particles with

$\lambda_2 = \lambda_3 = 0$, the possibility of a vanishing amplitude $F_{00}^J = -F_{00}^J \rightarrow F_{00}^J = 0$ can exist. In the following equations the variable of the center-of-mass energy \sqrt{s} is dropped in the helicity amplitudes for reasons of convenience.

By definition the decay amplitude is independent of the projection of the angular momentum between the two product particles m_L [116], as its operator $\vec{L} = \vec{r} \times \vec{p}$ is perpendicular to the momentum and therefore the quantization axis. This also becomes noticeable when comparing equations 33 and 36. The sum over LS has vanished in the latter and is included in the amplitude $F_{\lambda_2\lambda_3}^J$. In other words an amplitude in one basis is a linear combination of amplitudes of the other basis and vice versa [114, p.11]. Using equations 34 and 35, equations 36 and 33 give the linear combinations

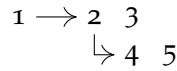
$$F_{\lambda_2\lambda_3}^J = \sum_{LS} \left(\frac{2L+1}{2J+1} \right)^{1/2} (LOS\lambda|J\lambda)(s_2\lambda_2s_3-\lambda_3|S\lambda)a_{L,S}^J \quad (39)$$

and

$$a_{L,S}^J = \sum_{\lambda_2\lambda_3} \left(\frac{2L+1}{2J+1} \right)^{1/2} (LOS\lambda|J\lambda)(s_2\lambda_2s_3-\lambda_3|S\lambda)F_{\lambda_2\lambda_3}^J. \quad (40)$$

Also the number of amplitudes in a specific transition is the same for both bases [116, p.6].

Compared to the canonical basis, the main advantage of the helicity formalism is that decay amplitudes can easily be extended to more complex decays with a larger number of final state particles. Using the assumption of the isobar model, which asserts that N particle decays are described by a number of successive two-body decays, the full decay into a three body final state is modeled as



and results in the decay amplitude

$$\begin{aligned} A(1 \rightarrow 345) &= \langle \theta_4 \phi_4 \lambda_4 \lambda_5 | \mathcal{M}_B | s_2 m_2 = \lambda_2 \rangle \langle \theta_2 \phi_2 \lambda_2 \lambda_3 | \mathcal{M}_A | J m_1 \rangle \\ &= \sum_{\lambda_2} \left(\frac{2J+1}{4\pi} \right)^{1/2} \left(\frac{2s_2+1}{4\pi} \right)^{1/2} \\ &\quad D_{m_1, \lambda_2 - \lambda_3}^{*J}(\phi_2, \theta_2, 0) F_{A, \lambda_2 \lambda_3}^J \\ &\quad D_{m_2, \lambda_4 - \lambda_5}^{*s_2}(\phi_4, \theta_4, 0) F_{B, \lambda_4 \lambda_5}^{s_2}. \end{aligned} \quad (41)$$

The angles ϕ_2, θ_2 are measured in the rest frame of 1 with respect to an arbitrarily chosen quantization axis for m_1 . A spherical coordinate system is used, while θ is the polar angle¹ and ϕ the azimuthal angle. On the contrary the angles ϕ_4, θ_4 are defined in the rest frame of particle 2 not to an arbitrary axis, but with respect to the momentum direction of particle 2 in the rest frame of particle 1 so that $m_2 = \lambda_2$. These angles are sketched in figure 50. A sum over all allowed intermediate state helicities according to the selection rule formulated in equation 37 is performed, in this example λ_2 . Similar to the extension of equation 36 to 41, the procedure can be applied to decays with an arbitrary number of final state particles.

¹ Also known as the helicity angle in literature.

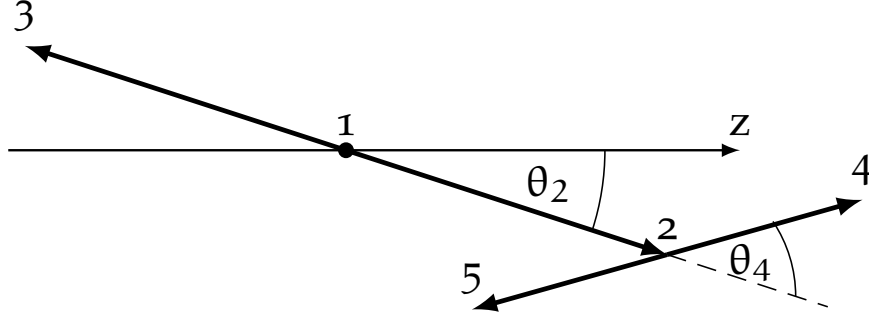


Figure 50: Sketch visualizing the definition of the angles for a sequential two-body decay in the helicity formalism.

So far it was assumed that the decay proceeds only over a single intermediate resonance, however in reality there can be several and equation 41 is extended to

$$\begin{aligned}
 A(1 \rightarrow 345) &= \langle \theta_4 \phi_4 \lambda_4 \lambda_5 | \mathcal{M}_B | s_2 m_2 = \lambda_2 \rangle \langle \theta_2 \phi_2 \lambda_2 \lambda_3 | \mathcal{M}_A | J m_1 \rangle \\
 &= \sum_{R, s_2, \lambda_2} \left(\frac{2J+1}{4\pi} \right)^{1/2} \left(\frac{2s_2+1}{4\pi} \right)^{1/2} \\
 &\quad D_{m_1, \lambda_2 - \lambda_3}^{*J}(\phi_2, \theta_2, 0) F_{A, \lambda_2 \lambda_3}^J \\
 &\quad D_{m_2, \lambda_4 - \lambda_5}^{*s_2}(\phi_4, \theta_4, 0) F_{B, \lambda_4 \lambda_5}^{R, s_2}.
 \end{aligned} \tag{42}$$

Next to the sum over the spin s_2 of the intermediate resonance, an additional summation index R is introduced to allow for multiple resonances of the same spin quantum numbers. In general this is not required as the amplitude $F_{B, \lambda_4 \lambda_5}^{R, s_2}$ could describe an arbitrary amount of states as long as their spin properties are equal. Nevertheless such a splitting into individual resonances is common and convenient, and valid as long as the resonances are well separated. In order to compare the model to measured angular final state distributions only the intensity of the decay amplitude

$$\begin{aligned}
 I &= \frac{2J+1}{4\pi} \frac{2s_2+1}{4\pi} \sum_{RR' s_2 s_2' \lambda_1 \lambda_2 \lambda_2' \lambda_3 \lambda_4 \lambda_5} \\
 &\quad D_{\lambda_1, \lambda_2 - \lambda_3}^{*J}(\phi_2, \theta_2, 0) D_{\lambda_1, \lambda_2' - \lambda_3}^J(\phi_2, \theta_2, 0) F_{A, \lambda_2 \lambda_3}^J F_{A, \lambda_2' \lambda_3}^{*J} \\
 &\quad D_{\lambda_2, \lambda_4 - \lambda_5}^{*s_2}(\phi_4, \theta_4, 0) D_{\lambda_2', \lambda_4 - \lambda_5}^{s_2'}(\phi_4, \theta_4, 0) F_{B, \lambda_4 \lambda_5}^{R s_2} F_{B, \lambda_4 \lambda_5}^{*R' s_2'}
 \end{aligned} \tag{43}$$

is relevant. In general the initial and final state particles can have several helicity configurations so that additional sums over their possible helicity orientations appear. However these sums are incoherent in contrast to the intermediate states, which are summed coherently [116, 117].

The parameterization of the helicity amplitudes F_A, F_B are the main interest, as they contain the physics information about the interaction. In general each such amplitude

$$F_i = g_i \cdot H_i$$

consists of a dynamical function H , describing the interaction, and a complex parameter g , composed of the magnitude A and phase ϕ . While the magnitude gives the general

strength of the amplitude, the phase adjusts the interference among different amplitudes. For a single resonance far from any open thresholds, the Breit-Wigner formula

$$H(s) = \frac{m_R c^2 \cdot \Gamma}{(m_R c^2)^2 - s - i\sqrt{s} \cdot \Gamma} \quad (44)$$

is a good approximation for the dynamical function and can be derived from almost the unitarity condition alone [9, p.563f]. Here m_R denotes the mass of the resonance, Γ its width and \sqrt{s} the center-of-mass energy of the two decay product particles. When open thresholds are near, the Breit-Wigner parameterization has to be modified, also known as the Flatté parameterization [9, p.563f]. For more than a single resonance in a single partial wave or amplitude, the sum of Breit-Wigner functions is in general an incorrect description as it violates unitarity. Nevertheless it can still be used in case the resonances have negligible overlap. However it is preferable to use other formalisms such as the K-matrix formalism [9, p.567f].

For a mathematically unique description and physics reasons several parts of the complex parameters g_i can be fixed. At first all except one complex parameter can be fixed for each amplitude product as they are mathematically redundant. Additionally for each coherent sum a global phase can be fixed as only the intensity can be observed, or in other words, only relative phases can be measured. In case of parity conservation, two complex parameters become related and the total number of independent parameters is further reduced. Finally one global magnitude can be fixed as the unbinned log likelihood estimator is insensitive to global scaling (see appendix A.1.2), therefore stabilizing the fitting procedure.

Now that the basic theoretical knowledge on the helicity formalism is complete, its implementation in the CompPWA framework can be discussed.

6.3 HELICITY FORMALISM IMPLEMENTATION IN COMPWA

CompPWA is a flexible and modular partial wave analysis (PWA) framework for various use-cases [118]. In contrast to most other available PWA frameworks or tools, CompPWA will not solely be used by a single experiment, but also for various other experiments, to provide a common tool which is stable, efficient and provides comparable results. It even allows combined fitting of data from different experiments. This is possible due to its high modularity, that was achieved by thorough planning and discussions with experts from different experiments and the testing of different technologies. Also instead of specializing the modules for a specific experiment the focus lies on generality of their implementation. The high standard that was required in the software design lead to a good foundation for the framework [23].

An overview of the CompPWA design is illustrated in figure 51. Quite naturally the framework consists of the following main categories of modules. The data modules handle experiment specific information, as for example data input and output, but also data generation. All physics models and formalisms, e.g. the helicity formalism, are contained in the physics category. When validating a theory, a comparison of the physics model with a measured data set has to be made, which is performed by estimator modules. Finally the optimizer modules are responsible for finding the optimal values of free parameters of a physics model to best match the observations. In general each of these categories consists of various modules.

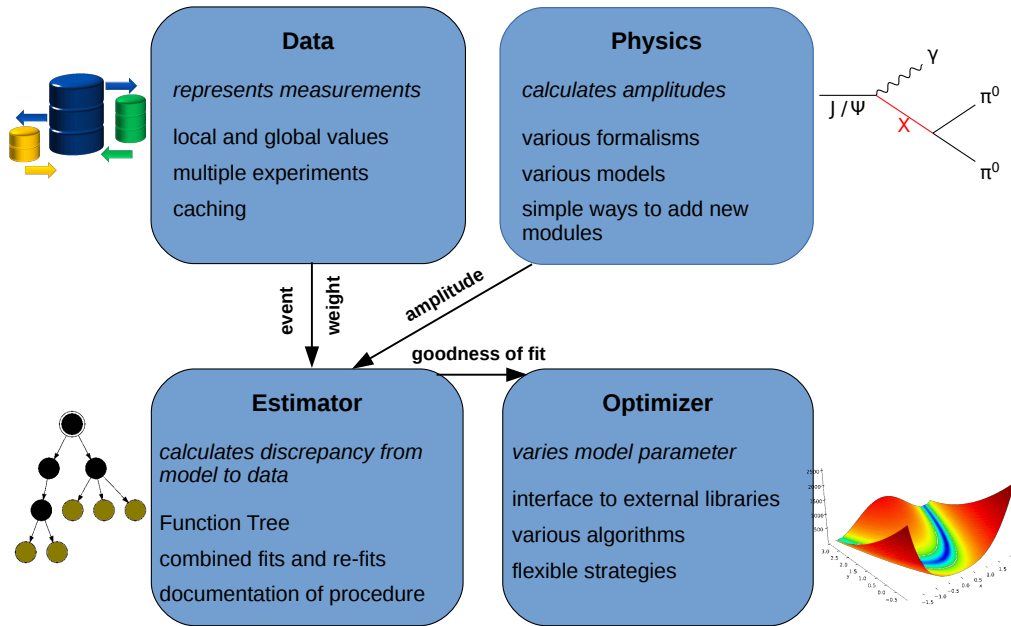


Figure 51: Modular design overview of the CompPWA project [118].

The helicity formalism of CompPWA belongs to the category of physics modules and is based on three sub-modules, the HelicityAmplitude, the DecayTree and the Dynamical-Functions. They are depicted in the overview figure 52. The DecayTree and HelicityAmplitude modules are the core constituents of the helicity formalism implementation. In the first module, basic information about the reaction which is to be analyzed, such as the initial and final state, is processed in the CompPWA expert system into decay trees. Each decay tree contains all of the relevant physics information of the reaction for a specific wave, representing a single element of the sum in equation 42. The HelicityAmplitude module uses the decay trees to create the corresponding amplitudes. During the construction of an amplitude, the DynamicalFunctions module is used to obtain requested parameterization of the dynamical parts from a selection. Currently only the Breit-Wigner parameterization is implemented. Both of the core modules are discussed in more detail below.

6.3.1 Helicity Amplitude Module

Following the high modularity and flexibility standard of CompPWA, the HelicityAmplitude module consists of several components, which belong to one of the two categories. In the first category the individual amplitude classes with varying granularity, ranging from the lower level two-body decay amplitude to the high level coherent amplitude are defined. The second category focuses on the automated construction of the various amplitudes. Altogether there are four levels in this amplitude hierarchy.

TWO-BODY DECAY AMPLITUDE: It describes the decay of a mother particle into two daughter particles. It is composed of an angular and a dynamical amplitude and a complex parameter, that specifies the strength of the decay (see equation 36). The angular amplitude is proportional to the Wigner D-function while the dynamical amplitude is generated by a factory within the DynamicalFunctions module. Currently only the Breit-Wigner parameterization as in equation 44 is used.

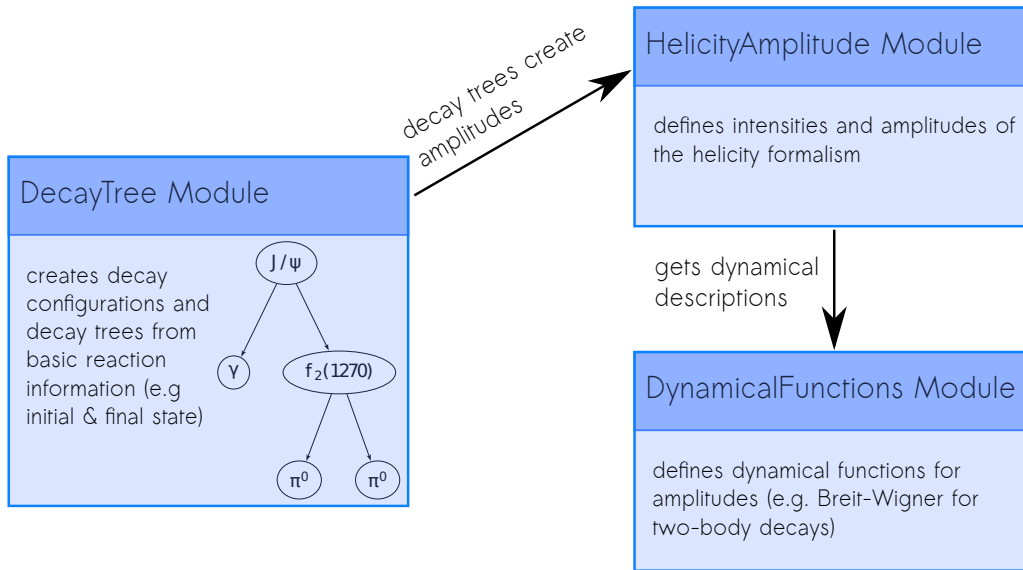


Figure 52: Overview of the CompPWA helicity formalism modules.

SEQUENTIAL TWO-BODY DECAY AMPLITUDE: This class defines a sequence of two-body decays, in form of a list of two-body decay amplitudes.

TOPOLOGY AMPLITUDE: Every two-body decay of a sequential decay is considered as a decay node. The decay topology is defined by assigning a list of the downward connected final state particles to every decay node. Here, downward connected means only going along the links to daughters and not upwards to the mother. Hence, for a three particle final state there are three decay topologies. In the special case of having two undistinguishable final state particles, the number of topologies is reduced to two. Using the $J/\psi \rightarrow \gamma\pi^0\pi^0$ decay as an example, they are

1.
$$J/\psi \rightarrow X \begin{matrix} \gamma \\ \searrow \\ \pi^0 \pi^0 \end{matrix}$$
2.
$$J/\psi \rightarrow X \begin{matrix} \pi^0 \\ \searrow \\ \gamma \pi^0 \end{matrix}$$

Each sequential two-body decay amplitude belongs to one of the possible decay topologies. This allows the topology amplitude to group together all sequential decay amplitudes with the same topology. Since the decay topologies have a unique set of kinematic variables for all of its decay nodes, the construction and evaluation of the full intensity can benefit from this. For example all sequential two-body decay amplitudes with the same topology can be evaluated with the identical set of kinematic variables.

COHERENT AMPLITUDE: Ultimately every decay process from an initial state to a final state is described by an intensity according to formula 43, the coherent amplitude. The coherency of this amplitude can be adjusted completely to the users needs.

An overview of this amplitude hierarchy is also depicted in figure 53.

The components belonging to the second category of the HelicityAmplitude module are responsible for the automated construction of the amplitude hierarchy for the requested decay from decay trees. The decay trees are created by the DecayTree module

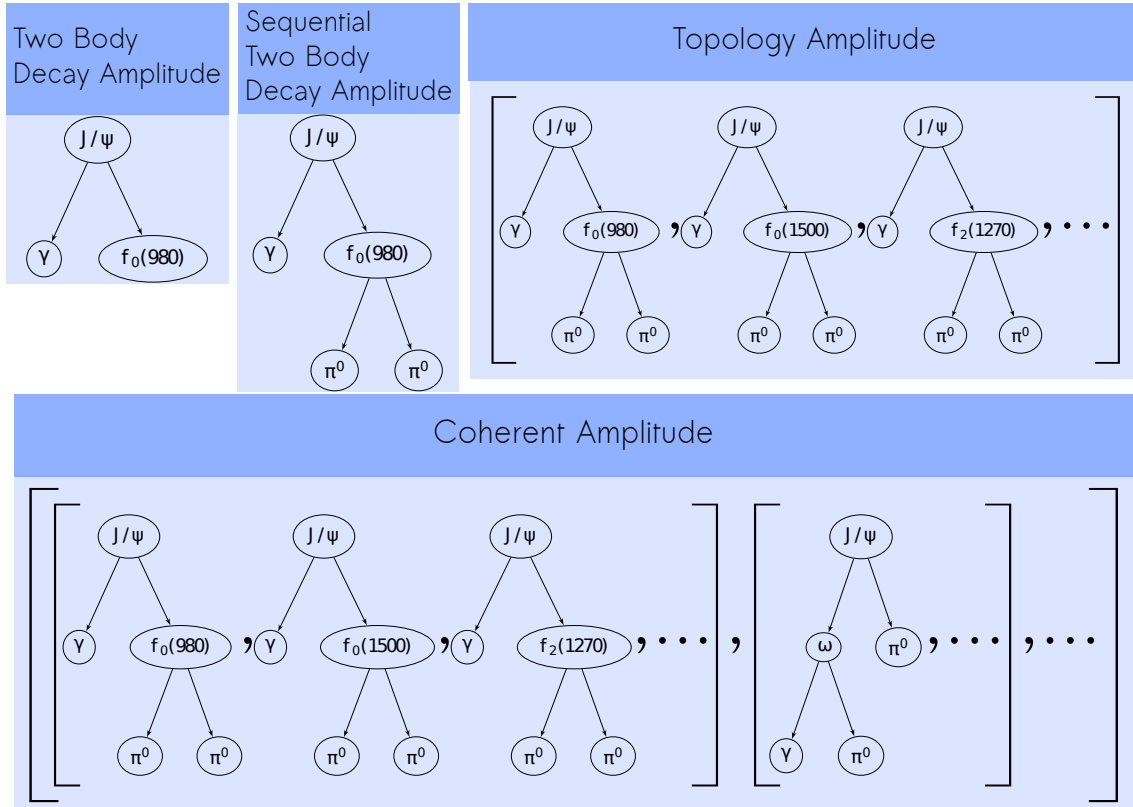


Figure 53: Overview of helicity amplitude hierarchy in CompPWA. On the lowest level is the two-body decay amplitude. A sequential two-body decay amplitude consists of multiple two-body decay amplitudes. The topology amplitude groups together sequential two-body decay amplitudes, based on their decay topology. Finally the coherent amplitude defines the intensity.

described in the next section. Each decay tree contains the complete set of information required to create a sequential two-body decay, which is realized by the topology factory. The factory also sorts the created sequential two-body decays into the appropriate topology group, the topology amplitude. Within the factory connections between complex helicity amplitudes U_i (dynamical part times complex parameter) are established. This takes care of parity conservation, as stated in equation 38. Finally the coherent amplitude, which corresponds to the intensity according to equation 43, can be constructed from a list of topology amplitudes.

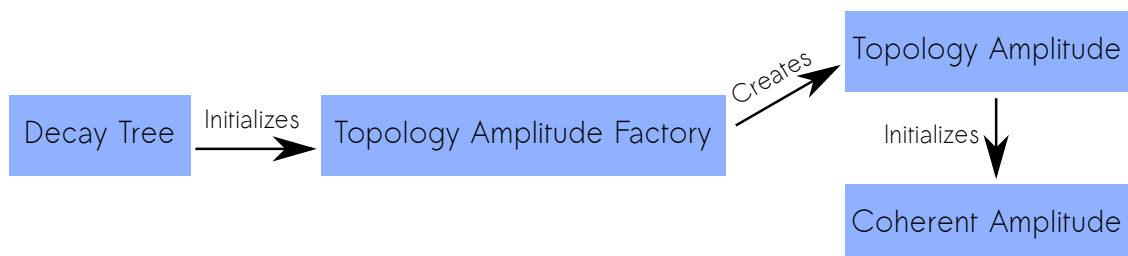


Figure 54: Overview of the creation of coherent amplitudes in CompPWA.

Figure 54 summarizes this workflow. The coherent amplitude is based on the CompPWA function tree [23], which harmonizes with the construction of the intensity while ensur-

ing a high fit performance. According to the principle of CompPWA the construction of the intensity is implemented in a flexible way. Recall that the intensity is an incoherent sum of parts, while each part is a coherent sum of sequential two-body decay amplitudes. Each particle or state occurring in the amplitudes is assigned with a coherency flag. The assessment if two sequential two-body decay amplitudes are summed coherently, now becomes trivial: For two sequential two-body decay amplitudes, all particles flagged as incoherent (not coherent) have to match in both amplitudes for all quantum numbers. In this way coherency is treated individually and generally and is easily comprehensible at the same time.

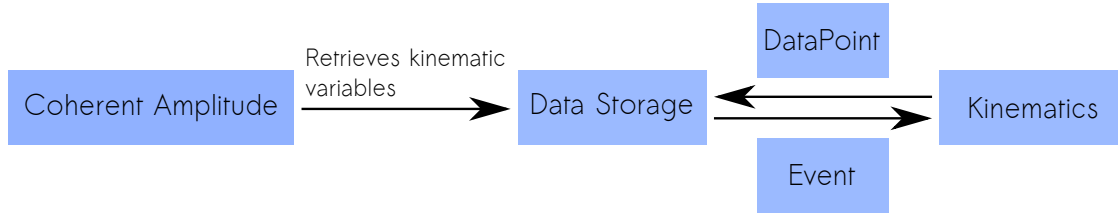


Figure 55: Overview on the evaluation procedure for a Coherent Amplitude in the helicity formalism in CompPWA.

The details of the evaluation of the intensity is shown in diagram 55. When the coherent amplitude is evaluated, the function tree decides which parts have to be recalculated, based on the changes in its leaves. By changing the depth of the function tree, the level of caching can be adjusted in an elegant way. The leaves are on the one hand the parameters of the model, such as masses and widths of resonances and their strengths. Another type of leaves are the kinematic variables, such as invariant masses and decay angles. While the former are direct parameters of the intensity, the latter are domain variables and are retrieved from the data storage. It contains the kinematic variables of all events required from all occurring two-body decays. As an event usually consists of a set of four momenta matching the final state particles, a corresponding kinematics class has to convert this general information into all of the kinematic variables needed by the coherent amplitude first. These kinematic variables are contained in the data point structure. In the helicity formalism the relevant kinematic variables are the helicity angles and invariant masses for each two-body decay. They are calculated by the appropriate boosts and rotations, so that the previously described conditions are satisfied. Because the kinematics class possesses the information about the occurring topologies, only the necessary variables are calculated. These variables have to be calculated only once in a minimization process. With the help of the CompPWA function tree, the caching of these variables is also performed automatically. For the example of the $J/\psi \rightarrow \gamma\pi^0\pi^0$ decay, the two decay topologies result in the two following possible final state particle combinations.

1. $J/\psi : [\gamma\pi_1^0\pi_2^0]$
 $X : [\pi_1^0\pi_2^0]$
2. $J/\psi : [\gamma\pi_1^0\pi_2^0]$
 $X : [\gamma\pi_1^0], [\gamma\pi_2^0]$

Due to the indistinguishable π^0 , topology 2 has two valid combinations of invariant masses for the decay of the intermediate state X that are used in the evaluation: $[\gamma\pi_1^0]$ and $[\gamma\pi_2^0]$. Unique indices are assigned to the indistinguishable final state particles in

order to detect such combinatorics. The coherent amplitude automatically handles this matter, by evaluating the amplitude with both sets of kinematic variables

$$(D \cdot F)^{\text{fsc}} = g \cdot \left(D(\theta_{\gamma\pi_1^0}, \phi_{\gamma\pi_1^0}) H(m_{\gamma\pi_1^0}^2) + D(\theta_{\gamma\pi_2^0}, \phi_{\gamma\pi_2^0}) H(m_{\gamma\pi_2^0}^2) \right).$$

6.3.2 Decay Tree Module and CompPWA Expert System

As stated above the decay trees are a requirement in order to construct a coherent amplitude instance that resembles the helicity intensity (see figure 54). Similar to the HelicityAmplitude module the decay trees are constructed by a decay tree factory, which is initialized with all necessary decay information from the decay configuration. An overview of the decay tree creation process is shown in figure 56. Optionally the decay configura-

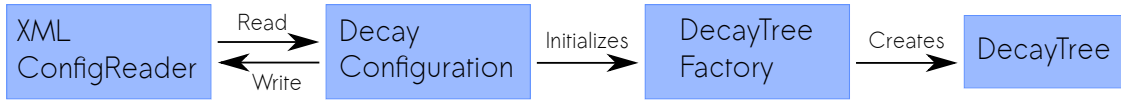


Figure 56: Flowchart of the creation of decay trees.

tion can be loaded from or stored to a file. The decay configuration contains the complete physics information of the decay process that are grouped into two parts:

- All appearing particles, which are assigned with a unique id, all unchangeable quantum numbers (here everything except helicity), as well as an identifier for the dynamical amplitude description. This identifier is used by the factory in the DynamicalFunctions module to generate the appropriate model.
- A list of decay trees, that consist of multiple decay nodes. Each decay node consists of a mother and daughters, and specifies the remaining quantum numbers (here the helicity), plus a complex phase. A decay node is uniquely identified by the quantum numbers of the mother and daughters and their helicities. The nodes are connected to each other via their unique ids.

There are no restrictions on the complexity of the trees from the implementation, hence a decay tree node could in general be directly connected to any number of daughter nodes. The restrictions of two-body decays in the helicity formalism arises from the isobar model assumption.

At last the origin of the configuration information remains to be discussed. It is obtained as advice from the novel CompPWA expert system, based on C Language Integrated Production System (CLIPS) [119]. An expert system consists of two main components, the knowledge base and the inference engine. The knowledge base of the expert system is condensed into the former component as a set of rules. A rule consists of requirement part and an execution body, very similar to the common if-then statement in computer programming. The requirements of rules can be a set of specific facts. A fact can be regarded as a piece of information. When a user asks for the advice of an expert system, usually the so called initial facts have to be supplied. They correspond to the question asked to the expert system. The inference engine starts to process these facts by executing any valid rules. During the execution of rules new facts may be created and others may be deleted or retracted. In CLIPS the execution order of the rules can be adjusted with the salience parameter, which assigns the priority level to rules. Once the

rules are not able to process the information any further, the execution halts and the user can retrieve the advice of the expert system. A more in-depth introduction to expert systems is given in appendix A.2. The creation process of the configuration is summarized in diagram 57.

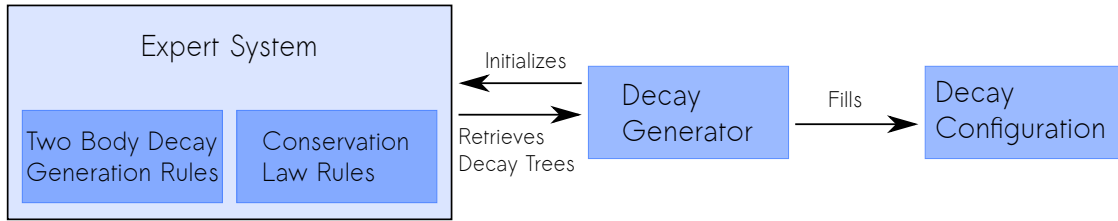


Figure 57: Flowchart of the creation of the decay configuration. The user supplies the expert system with the constraints and basic information of the physics process of interest and obtains the result as advice from the expert system.

In this case of the CompPWA helicity formalism expert system, the initial facts are

- the initial and final state
- the strictly conserved quantum numbers
- a list of restricted value ranges for quantum numbers like the angular momentum L or spin J
- the spin projection constraints for particles (useful for unequal population of the initial states)
- a list of allowed particles as intermediate states.

With this information the decay generator initializes the expert system and the inference engine begins its execution and processes the supplied information with the help of the knowledge base. The helicity formalism knowledge base is filled with rules, that belong either to the decay creation or the conservation law group. All rules belonging to the first group are responsible for the creation of various decay trees, that are retracted by rules of the second category.

In more detail instead of working with particle states (e. g. $f_0(980)$), the expert system uses spin states (e. g. 0^{++}). They are defined as associated lists of quantum number and value pairs. Unlike the particle state the spin state does not have the mass attribute. Therefore following the J^{PC} scheme, the $f_0(980)$ and the $f_0(1500)$ are both 0^{++} spin states, but different particle states. In the following decay is used as a synonym for two-body de-



Figure 58: Example for a basic decay, here for the electric charge quantum number. When charge conservation is active the right charge decay example is forbidden and will be retracted by the expert system charge conservation rule.

Also the term decay tree is used equivalently for a sequential two-body decay. In the beginning rules from the decay creation category, create basic decays for each quantum number. These decays are then checked by the rules of the second category, which

implement the conservation laws. All quantum numbers e. g. spin, angular momentum, parity, C-parity, charge are regarded as independent in general, but can be connected or correlated to other quantum numbers. Figure 58 shows two examples of basic decays for the electric charge. Here the decay on the right is forbidden and would be removed. All of the remaining basic decays are then used to construct spin state decays.

Starting from the initial state also called top decay node, its quantum number content is matched with the mother decay node of all possible basic decays. This creates the spin state decays of the initial state, and during this process the conservation law rules for correlated quantum numbers are executed and remove prohibited decays. Ultimately only decays allowed by the constraints of the user remain. This procedure is applied successively until the required number of final state particle is reached and the spin state decay trees are obtained. An example of a spin state decay is shown in figure 59. As a last step the quantum numbers of the final state supplied from the user are compared to all created spin state decay trees, and only the matching ones remain. All possible combinations for decay trees are created in this way. Currently implemented are the following physics laws:

- angular momentum or spin conservation:
 $|s_1 - s_2| \leq s \leq |s_1 + s_2|$
 $m = m_1 + m_2$
 and the Clebsch-Gordan-Coefficient relations for s_1, m_1 and s_2, m_2 coupling to s, m
- parity conservation: (see equation 38) and
 $\eta^P = \eta_1^P \eta_2^P (-1)^L$
- C-parity conservation:
 $\eta^C = \eta_1^C \eta_2^C$
- isospin conservation:
 $|I_1 - I_2| \leq I \leq |I_1 + I_2|$
 $I_z = I_{z,1} + I_{z,2}$
 and the Clebsch-Gordan-Coefficient relations for $I_1, I_{z,1}$ and $I_2, I_{z,2}$ coupling to I, I_z
- electric charge conservation:
 $q = \sum_i q_i$
- Fermi/Bose state symmetrization:
 if the decay daughters are identical particles, the parity of the mother must satisfy
 $\eta^P = +1$ for boson
 $\eta^P = -1$ for fermion

With the introduction of quantities or quantum numbers which are currently not implemented, e. g. the G-parity, the use of an expert system can reach its full potential. Then simply a rule for the checking of G-parity conservation has to be created, without other alterations.

Once the expert system has ended its calculations, the decay generator asks for the advice and retrieves the results. At this point the spin states of the corresponding decay trees are now instantiated with all possible particles fitting the spin state quantum number description. Afterwards the particle state decay trees can be filtered to allow for requirements on the particle instance level. Currently decay trees are removed, in which

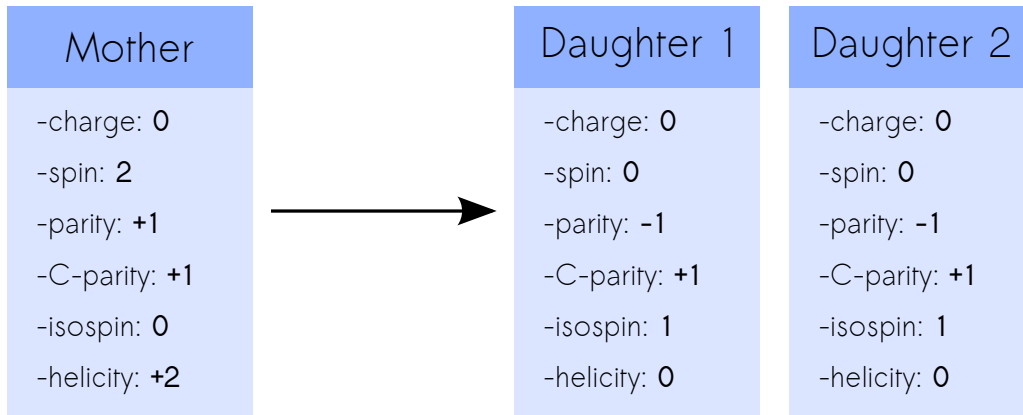


Figure 59: Example of a spin state decay, resembling a $0(2^{++}) \rightarrow 1(0^{-+}) + 1(0^{-+})$ decay. The number in front of the brackets corresponds to the isospin, while all particles have no electric charge. This can correspond to for example a $f_2(1270) \rightarrow \pi^0\pi^0$ decay, when inserting actual particle states.

the net-mass of the decay products is larger than the mass of the decaying state itself to enforce energy conservation. Finally these decay trees are stored into the configuration, which can be saved to a file.

Because the laws of physics are equivalent to the rules of an expert system, the use of such a system is quite natural. The spin state decay trees, that contain the complete physics information of the helicity formalism, are constructed solely by the expert system in a very elegant way. With the separation of the physics knowledge from the construction and evaluation of helicity amplitudes, a high level of structure and transparency to the user is attained. The high modularity, also within the expert system, implicates high flexibility and maintainability. By changing the initial facts, the analyst is able to adjust the decay channel and the underlying physics according to the conservation laws. Of course the expert system can also be used to ask for advice, such as checking the validity or the conservation laws which might be violated for decay trees created by the user.

The use of an expert system for such a field of application is ideal. In the following an exemplary test of the expert system is shown, beside the verification and test of the implementation of the CompPWA helicity formalism.

VALIDATION OF THE HELICITY FORMALISM IMPLEMENTATION

In this chapter the implementation of the helicity formalism in the CompPWA framework is validated. At first the results of the CompPWA expert system are verified. Afterwards the angular distributions for single waves of the $J/\psi \rightarrow \gamma\pi^0\pi^0$ reaction are compared to theory. Then systematic studies in form of input-output checks, comparisons of the angular distributions as well as the analysis of normalized residuals of the fit parameters are performed. This is exercised first for a relatively simple model. Then the complexity of the amplitude model is increased in a second step to reach a similar amplitude that was previously used to describe the BESIII dataset [120]. For this model also data samples were generated with the PAWIAN software package [121], that were in turn fitted with the CompPWA framework. Here also the angular distributions are compared and the normalized residuals of the fit parameters are verified. At last, the first fit result on a large BESIII dataset of the $J/\psi \rightarrow \gamma\pi^0\pi^0$ is presented. This dataset originates from a previously performed analysis that is also used as a reference [51, 120]. No full analysis of the BESIII data is performed, as this goes beyond the scope of this thesis.

For all of the fits presented in this chapter, an unbinned log likelihood estimator was used (see equation 54 in appendix A.1.2). The optimization is performed with the MINUIT2 library [113]. Regarding the helicity amplitude models presented in this chapter, the Breit-Wigner parameterization as stated in equation 44 was used for all of the intermediate resonances.

7.1 TEST OF THE EXPERT SYSTEM

As described in the previous chapter the CompPWA expert system is used to obtain the decay trees that contain the physics information for the reaction of interest, here $J/\psi \rightarrow \gamma\pi^0\pi^0$. The initial facts that have to be supplied to the expert system are declared within a configuration file, e. g.

```
"initial_state": [ "jpsi" ],
"final_state": [
    "gamma",
    "pi0",
    "pi0"
],
"allowed_spins": [ 0, 1, 2 ],
"spin_z_components": {
    "jpsi": [ 1, -1 ]
}.
```

The most basic configuration file only includes the mandatory information, the initial and final state as well as a list of allowed spins that may occur. More constraints like

the conserved quantum numbers and spin projections for particles, etc. can be specified in the configuration file (see section 6.3.2). In this example configuration the spin for particles is restricted to $J = 0, 1, 2$ and the spin projection of the J/ψ of 0 is removed as this is not present for e^+e^- collisions. This condition is used throughout this chapter.

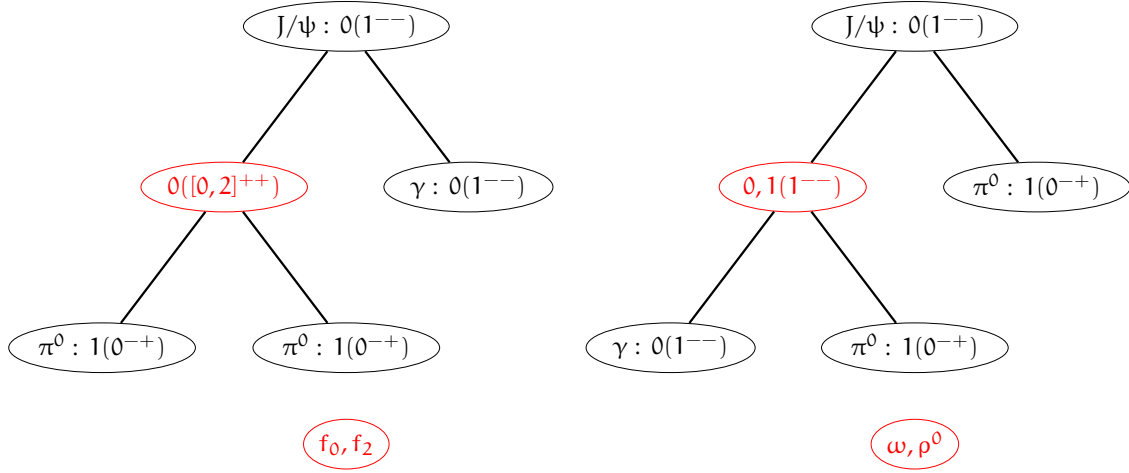


Figure 60: Two examples of decay trees as obtained by the ComPWA expert system for the reaction $J/\psi \rightarrow \gamma \pi^0 \pi^0$. The tree on the left shows the interesting isoscalar intermediate states. On the right the other topology is shown. The $I(J^{PC})$ notation is used.

In the first stage of the expert system, the results are given in form of spin state decay trees. Figure 60 summarizes the advice of the expert system by grouping it into the two topologies. On the left the interesting isoscalar $0^{++}, 2^{++}$ intermediate states appear¹. This topology is restricted to these quantum numbers by isospin conservation, as well as parity conservation and state symmetrization and finally C-parity conservation. The expert system is able to correctly predict the allowed solutions when the rules for these conservation laws are activated. The found $0^{++}, 2^{++}$ intermediate spin states correspond to f_0 and f_2 particle states. On the right of figure 60 the results for the other decay topology are shown. Here the amount of solutions are comparatively large, and the user is required to narrow down the possibilities using additional reasoning. Both the isospin conserving ($I = 1$) and violating ($I = 0$) results are presented. Because the decays are EM, the isospin conservation is not given and both decays occur in nature. However by looking at the branching ratios, one decay can be favored to the other, in this case into the ω or $0(1^{--})$ intermediate state. Also the BESIII dataset indicates evidence for the ω intermediate state, but these ω bands were removed because they are too narrow compared to the mass resolution. The physically interesting states here are the 0^{++} and 2^{++} isoscalars, which appear in the other decay topology.

7.2 ANGULAR DISTRIBUTIONS

For the verification of the implementation of the helicity amplitudes in ComPWA, first a general test is performed. Angular distributions for specific decay modes which can also be calculated analytically were generated with ComPWA helicity formalism modules. The data generation is carried out with hit-and-miss MC sampling of the various helicity amplitudes. All examples shown below relate to the $J/\psi \rightarrow \gamma \pi^0 \pi^0$ process and as already

¹ Note that because the spin is restricted to 2 or below, the 4^{++} intermediate state do not appear.

mentioned only two topologies exist, one with the $\pi^0\pi^0$ and the other with the $\gamma\pi^0$ subsystem. The relevant kinematic variables are $\cos(\theta_a^s)$ and ϕ_a^s , denoting the angles of a in the rest system of s . Both a and s are systems of final state particles. For example with $a = \pi^0\pi^0$, $\cos(\theta_{\pi^0\pi^0}^{\text{cms}})$ and $\phi_{\pi^0\pi^0}^{\text{cms}}$ are the angles of the $\pi^0\pi^0$ system in the $s = \gamma\pi^0\pi^0 = \text{cms}$ system. Similarly $a = \pi^0, s = \pi^0\pi^0$ denotes the angles of a π^0 in the $\pi^0\pi^0$ rest frame.

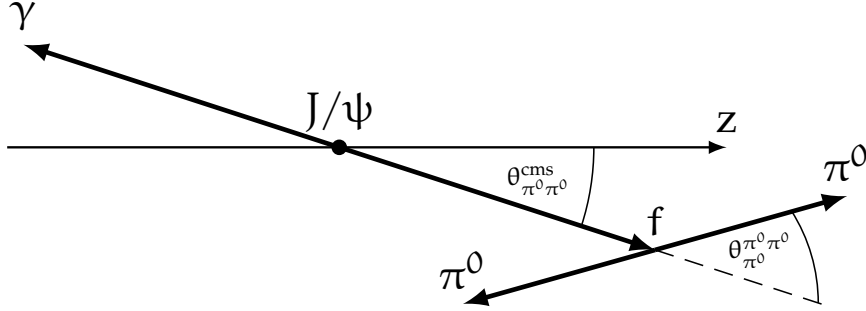


Figure 61: Definition of the θ angles in the $J/\psi \rightarrow \gamma\pi^0\pi^0$ decay via a $\pi^0\pi^0$ sub-system in the helicity formalism.

Figure 61 demonstrates the definitions of the angles $\theta_{\pi^0\pi^0}^{\text{cms}}$ and $\theta_{\pi^0\pi^0}^{\pi^0\pi^0}$, in analogy to the general definitions. To obtain the angles of the $\gamma\pi^0$ topology simply a π^0 has to be exchanged with the γ .

For all of examples shown in this section an incoherent sum over the initial state ($\lambda_{J/\psi} = \pm 1$) and final state helicities ($\lambda_\gamma = \pm 1$) has been performed. Figure 62 depicts the angular distributions for a resonance with 0^{++} quantum numbers in the $\pi^0\pi^0$ subsystem. Evidently the ComPWA generated distributions are in perfect agreement with the analytic solutions, calculated according to the helicity intensity given by equation 43. In addition the $\cos(\theta_{\pi^0\pi^0}^{\text{cms}})$ shows the expected modulation for a spin 1 particle, the J/ψ of the initial state, while the $\cos(\theta_{\pi^0\pi^0}^{\pi^0\pi^0})$ distribution is uniform in accordance with the spin 0 intermediate state. Both of the ϕ distributions are flat, because the amplitude consists only of a single term and hence the ϕ dependence cancels out (see equation 43). Because the performed comparisons in the following also use single resonances with only one helicity setting, the ϕ distributions are uniform as well and are omitted.

When simulating the decay of the J/ψ into a photon and a f_2 or f_4 resonance, which subsequently decays into the two neutral pions, the angular distributions become more interesting. The $\cos(\theta)$ distributions for the decay of the J/ψ initial state into the γ and the intermediate resonance are again in agreement with those of a spin 1 particle. However there are two different versions as can be seen in figure 63. For $|\lambda| = 0, 2$ the distribution is identical to the f_0 case, but for $|\lambda| = 1$ the f_2/f_4 and γ are preferably emitted orthogonal to the quantization axis of the J/ψ . Only these two possibilities for these distributions exist, so that the focus now turns to the kinematic distributions of the subsequent decay.

Figure 64 shows the $\cos(\theta)$ distributions for the intermediate decay of a f_2 or f_4 for various helicities. Here the structure of the distributions is rather complicated but matches perfectly the calculated theoretical description. For the $\lambda = 0$ case there are exactly as many positions of zero intensity as the degree of the spin. Unlike the $\lambda = 0$ distribution, the intensities for $\lambda \neq 0$ vanish at the boundaries ± 1 . The zeros within the spectrum decrease with higher orders of the helicity until finally for the highest possible helicity

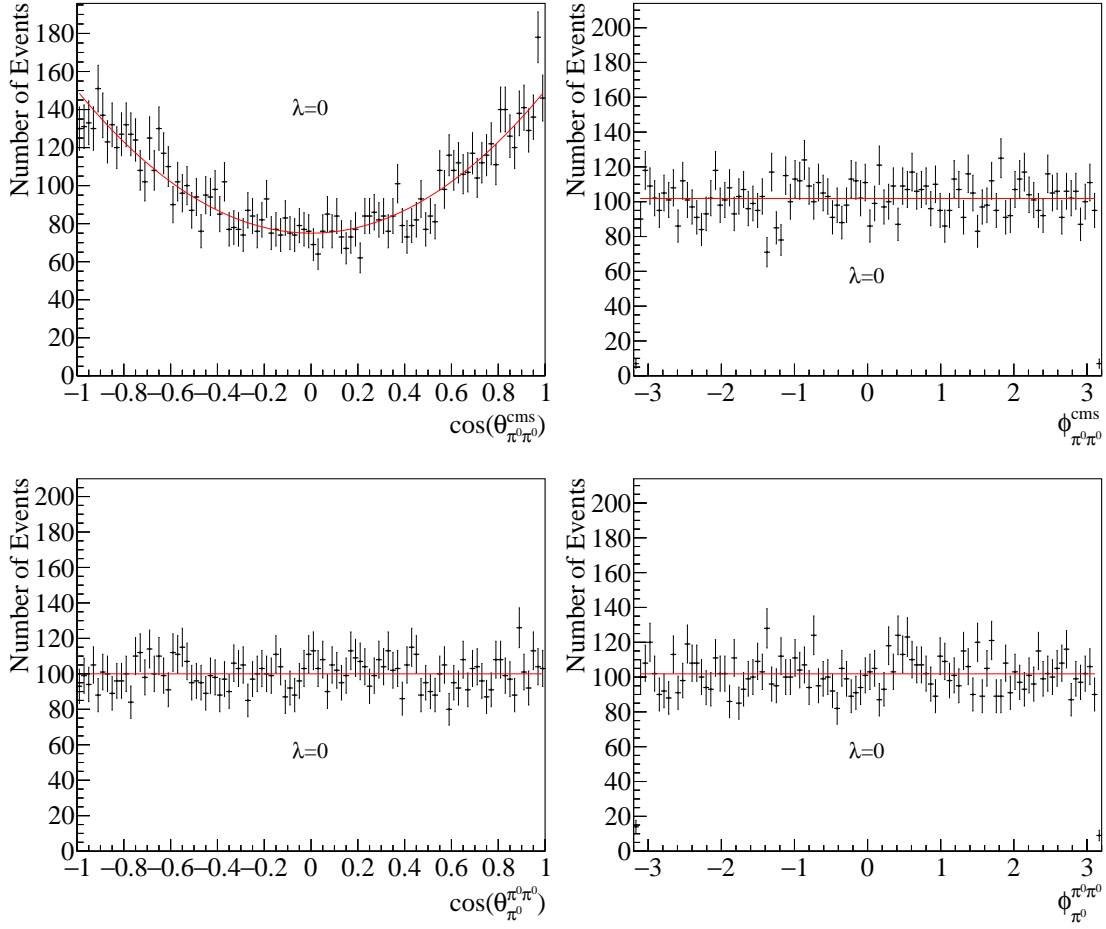


Figure 62: Angular distributions for the $J/\psi \rightarrow \gamma f_0 \rightarrow \gamma \pi^0 \pi^0$ reaction, generated with the CompPWA framework using the HelicityAmplitude module. $\lambda = 0$ denotes the helicity of the intermediate state X . The left shows $\cos(\theta)$ and the right ϕ distributions, in the top for the $\pi^0 \pi^0$ system w.r.t. the $\gamma \pi^0 \pi^0$ rest system and in the bottom for π^0 w.r.t. the $\pi^0 \pi^0$ rest system. The expected theoretical distribution is indicated by the red curve.

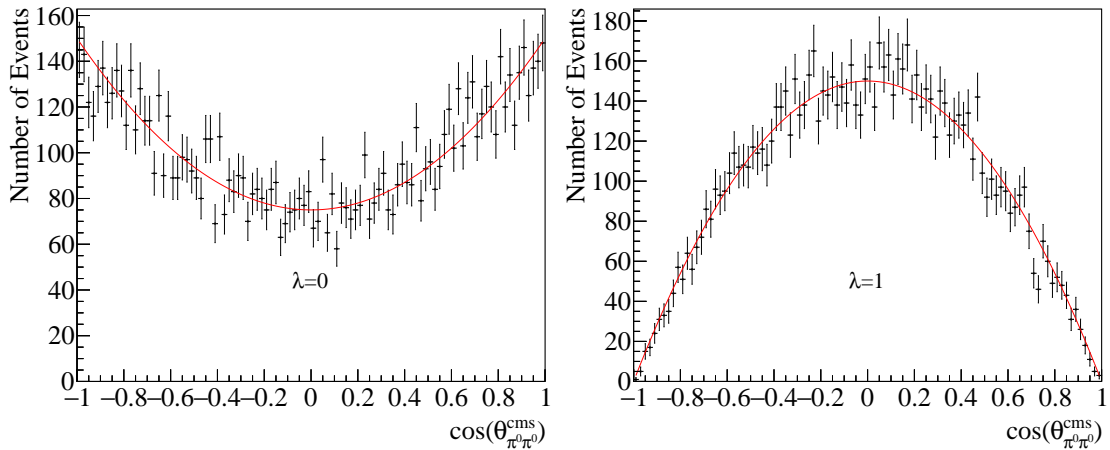


Figure 63: $\cos(\theta_{\pi^0 \pi^0}^{\text{cms}})$ distributions for the $J/\psi \rightarrow \gamma X \rightarrow \gamma \pi^0 \pi^0$ ($X = f_2, f_4$) reaction, generated with the CompPWA framework using the HelicityAmplitude module. On the left with helicity $\lambda = 0, 2$ and on the right with $\lambda = 1$ for the intermediate resonance. Because the $\lambda = 2$ distribution is identical to that of the $\lambda = 0$, it is not shown here. The calculated theoretical distribution is indicated by the red curve.

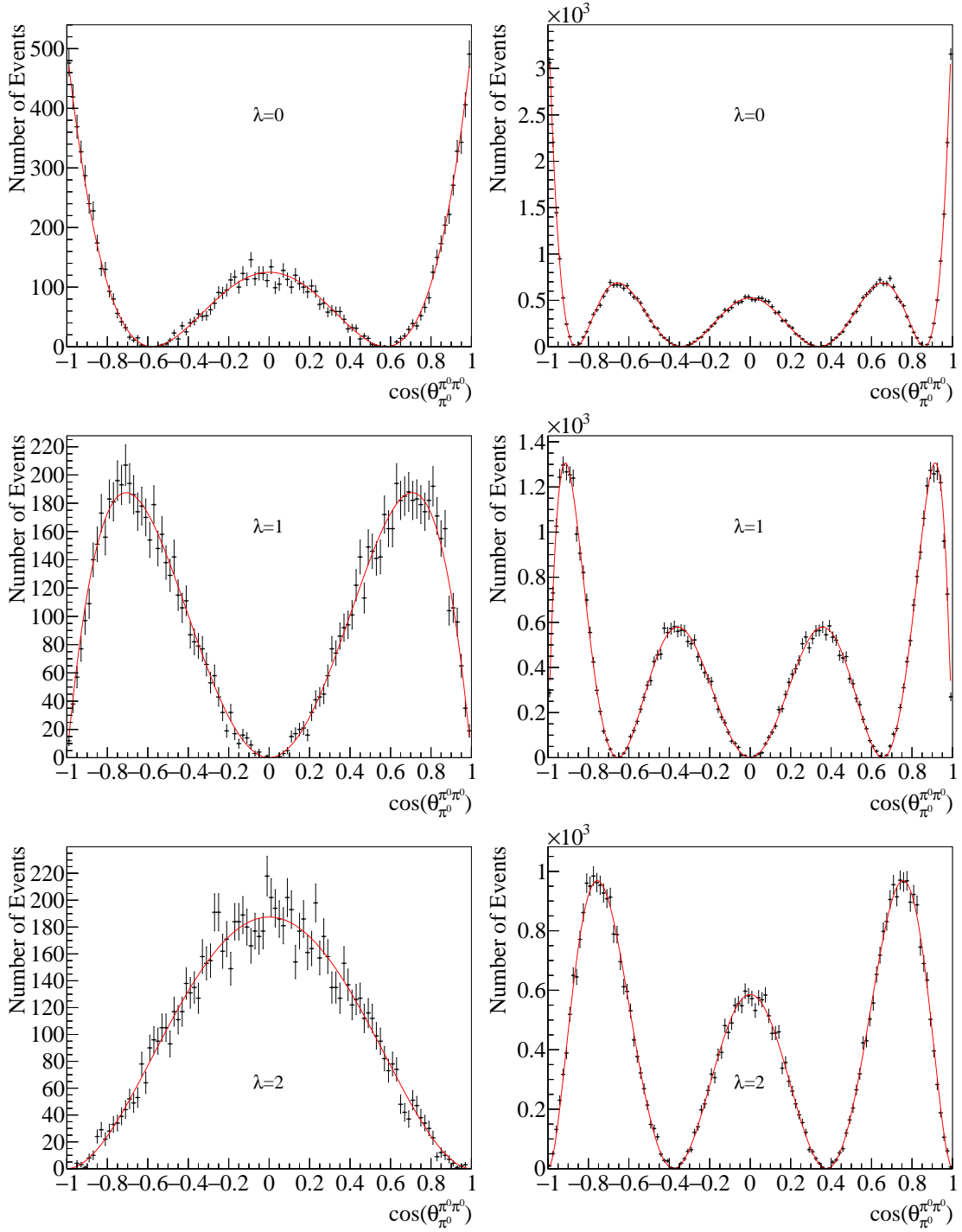


Figure 64: $\cos(\theta_{\pi^0\pi^0})$ distributions for the $J/\psi \rightarrow \gamma X \rightarrow \gamma\pi^0\pi^0$ ($X = f_2, f_4$) reaction, generated with the ComPWA framework using the HelicityAmplitude module. On the left for f_2 and on the right for f_4 as the intermediate resonance. The top shows helicity $\lambda = 0$, the middle $|\lambda| = 1$ and the bottom $|\lambda| = 2$ for the intermediate state X . The calculated theoretical distribution is indicated by the red curve.

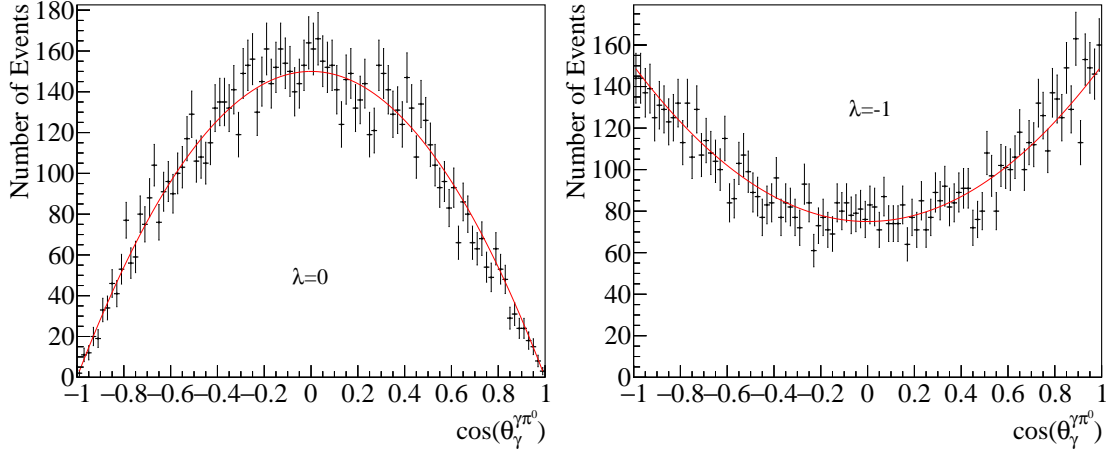


Figure 65: $\cos(\theta_\gamma^{\pi^0})$ distributions for the $J/\psi \rightarrow \pi^0 \omega \rightarrow \gamma \pi^0 \pi^0$ reaction, generated with the CompPWA framework using the HelicityAmplitude module. On the left with $\lambda = 0$ and on the right with $|\lambda| = 1$ for the intermediate resonance. The calculated theoretical distribution is indicated by the red curve.

only the zeros at the boundaries are present. Due to helicity conservation, the helicities for the f_4 resonance are limited to 2 and below.

Finally also the distributions in the other decay topology can be verified. For this data samples with a 1^{--} intermediate resonance, which then decays into the $\gamma \pi^0$, were created. The $\cos(\theta_\gamma^{\pi^0})$ distributions of the decay of the intermediate state are shown in figure 65. Since this is also a spin 1 resonance, just like the mother state J/ψ , their distributions are also identical. Note that the distributions for the $\lambda = 0$ and $|\lambda| = 1$ case are swapped in comparison to the distributions of the J/ψ decay. The reason for this is, that the Wigner D functions are evaluated differently with the denoted λ variable for these two decays. In the J/ψ decay λ refers to the helicity of a decay product, in contrast to the decay of the intermediate state, where λ belongs to the decaying state itself. Therefore the λ variable swaps index positions in the Wigner D functions for these two different decays, which induces the interchange of the distributions. Also it should be noted that the $\lambda = 0$ case does not occur for a parity conserving decay, as the decay of the J/ψ into a π^0 and the ω with $\lambda = 0$ is forbidden. The agreement of the angular distributions with the theory is again perfect.

This perfect agreement was visible consistently, also for rather complex amplitudes of particles of spin 4, which means that the implementation of the angular distributions for single decay channels is implemented correctly. Refer to appendix C.2 for a complete listing of the angular distributions. There also the kinematic distributions in the opposing subsystems are shown, which cannot be calculated analytically and are in general non-trivial distributions with kinematic reflections from the intermediate state subsystem.

7.3 FIRST VALIDATION WITH A SIMPLE MODEL

As a next step in the validation process, input-output checks of the HelicityAmplitude module are performed. For this an amplitude model is constructed that is used for both the data generation and fitting with CompPWA. In this section a simple amplitude was created, using only the $f_0(2020)$ and the $f_2(1270)$ resonance. The choice of these specific

f resonances is based on their strong presence in the BESIII data [120]. All possible helicities for the occurring states are used, except for the spin projection component of the J/ψ equal to zero, as noted above. In addition a coherently added background term, distributed uniformly in phase space, is introduced.

The parameters of the helicity intensity chosen for the data generation are displayed in table 7. Here the values for the masses and widths of the resonances are taken from the Particle Data Group (PDG) [9]. In total 600 independent data samples, each with 20000 events, were generated with the hit-or-miss MC method. For the normalization of the amplitudes in the log-likelihood of the fit, independent phase-space MC data samples with ten times more events are used.

Parameter	Value	Fixed	
$f_0(2020)$	$A_{\lambda=0}$	1.0	
	$\phi_{\lambda=0}$	3.1416	
$f_2(1270)$	$A_{\lambda=0}$	0.75	x
	$\phi_{\lambda=0}$	1.5708	x
	$A_{\lambda=1}$	0.5	
	$\phi_{\lambda=1}$	0.0	
	$A_{\lambda=2}$	0.25	
	$\phi_{\lambda=2}$	-1.5708	
coh. phsp.	A	0.05	
	ϕ	0.7854	

Table 7: Parameters of the simple model for the reaction $J/\psi \rightarrow \gamma\pi^0\pi^0$ including f_0, f_2 as intermediate resonances. For the masses and widths of the intermediate resonances the PDG values are used [9].

Each sample is fitted 7 times with random start values for the fit parameters listed above. The masses and widths are chosen at random from a $[-20, 20]$ % interval around their PDG values. Similarly the start parameters for the magnitudes and phases are random variables of the uniform distributions ranging from $[0, 5]$ and $[-\pi, \pi]$ respectively. The coherent phase space magnitude was limited to $[0, 0.1]$. As denoted in table 7 the $\lambda = 0$ component of the f_2 wave was chosen to be fixed in the fits. This is allowed and needed to stabilize the fitting procedure as explained in the previous chapter. For each data sample only the best fit, based on the likelihood value, was selected and used further. This procedure increases the probability of having found the global minimum.

At first the kinematic distributions of the generated datasets and their fit results can be compared. For this, one of the 600 samples with its best fit result was chosen at random. To visualize the helicity intensity of this fit result another data sample was produced using the weighted MC method. A good overview of the goodness-of-fit is given by the Dalitz plot comparison, which is shown in figure 66².

From the Dalitz plot of the input data (hit-or-miss MC), the two resonances in the $\pi^0\pi^0$ subsystem can be seen nicely. This is indicated by the two bands at around $1.7 \text{ GeV}^2/c^4$ and $4 \text{ GeV}^2/c^4$. Also their spin properties can be identified when comparing the distri-

² Refer to appendix C.1 for basic information about the kinematics of a Dalitz plot

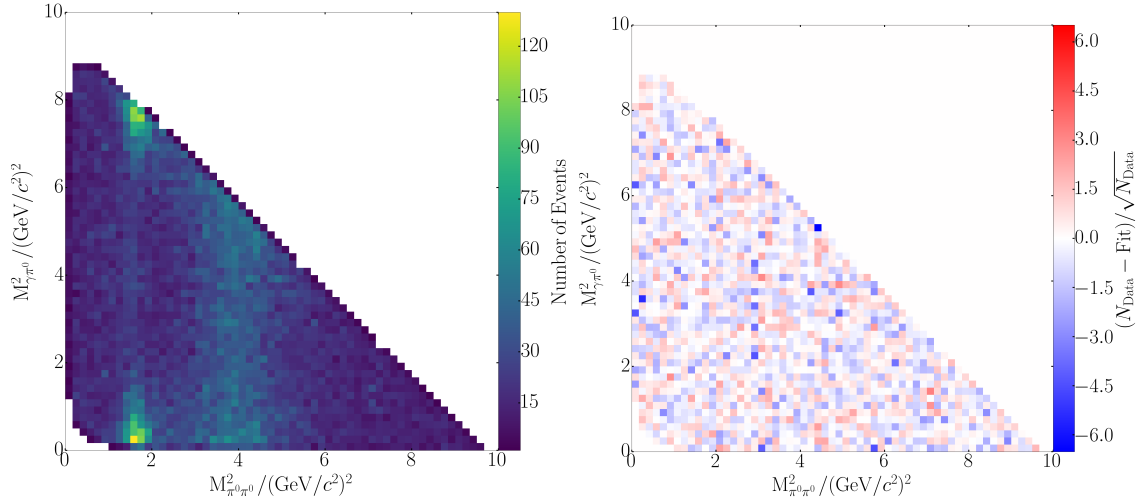


Figure 66: Dalitz plot of the reaction $J/\psi \rightarrow \gamma\pi^0\pi^0$ including f_0, f_2 as intermediate resonances from a MC generated data sample (left) and the normalized residual with the best fit result (right).

bution along the bands with figures 62 and 64. While the f_0 state at a higher mass shows no modulation, which is compatible with a spin 0 particle, the f_2 state at the lower mass resembles the angular distribution for a spin 2 particle with $\lambda = 0$. This can be seen from the peaking at the phase space boundaries. However in this case a more distinct bump in the center of the f_2 band should be present. This in turn is explained by the destructive interference of the $\lambda = 0$ and $\lambda = 2$ waves of the f_2 , which is supported nicely by the parameter values given in table 7.

To obtain an impression on the goodness-of-fit, a normalized residual of the Dalitz histogram of the input data and the fit data sample was created. This is also shown in figure 66. Clearly the fit is able to describe the generated data, since no areas of over- or underestimation are visible.

In the invariant mass spectra of the two possible kinematic combinations $\pi^0\pi^0$ and $\gamma\pi^0$, intermediate states can often already be identified. By looking at the $M_{\pi^0\pi^0}$ spectrum in figure 67, the two peaks can nicely be assigned to the $f_2(1270)$ and $f_0(2020)$ states. However extracting quantitative information from such invariant mass spectra is difficult, due to interference between resonances which can shift and alter the shape of these peaks. In addition so called kinematic reflections of states in one invariant mass combination can generate peaks in the other combination. This can be seen from the $M_{\gamma\pi^0}$ invariant mass spectrum, where a small accumulation of events is visible at around $2.7 \text{ GeV}/c^2$. The peaking structure in the $\cos(\theta)$ distribution of the f_2 wave with $\lambda = 0$ at ± 1 produces this effect. When imagining a projection of the Dalitz plot in figure 66 on the $M_{\gamma\pi^0}^2$ axis, such reflected peak structures are easily comprehensible in a visual way. When comparing the fit result with the generated data in the invariant mass spectra, their consistency is confirmed.

Finally the angular distributions of the decay products are compared. This is shown in figure 68 for $\cos(\theta)$ of the π^0 and γ in the corresponding $\pi^0\pi^0$ and $\gamma\pi^0$ subsystems. As before the agreement between the generated MC data and the fit result is excellent. The shape of the $\cos(\theta_{\pi^0\pi^0})$ distribution can be compared to the analytic calculations in figure 62 and 64. Some insight on the spin properties can be gained, but a comparison in slices of the $\pi^0\pi^0$ invariant mass is favorable here to avoid the mixture of two f

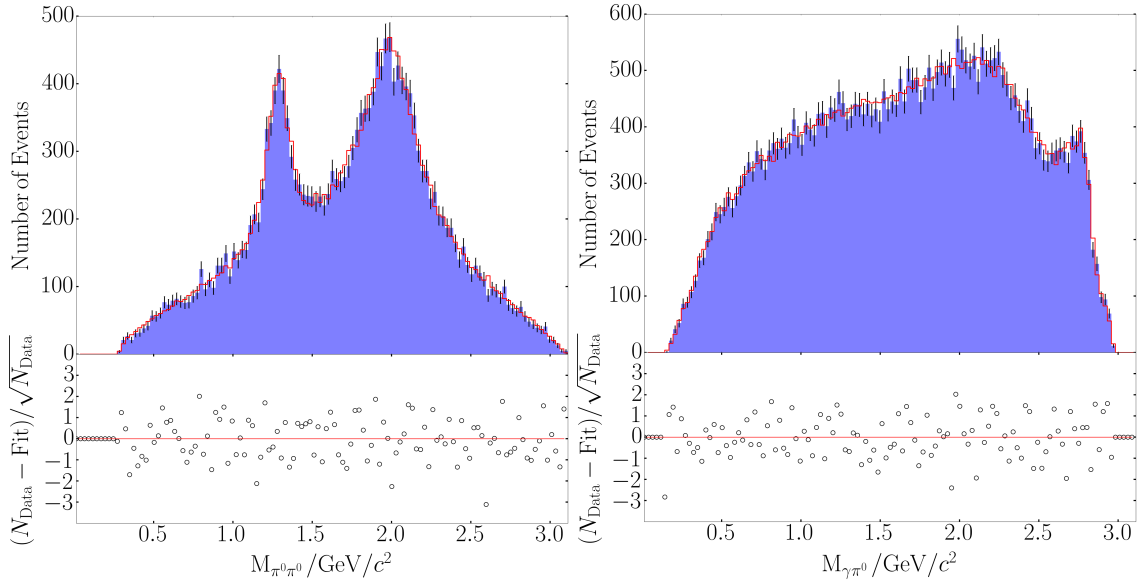


Figure 67: Invariant mass spectra of the $\pi^0\pi^0$ (left) and $\gamma\pi^0$ (right) subsystem of the reaction $J/\psi \rightarrow \gamma\pi^0\pi^0$ including f_0, f_2 as intermediate resonances. While the blue distribution is the MC generated data, the red curve is a weighted MC sample using the best fit result. Below the binwise normalized residuals are shown.

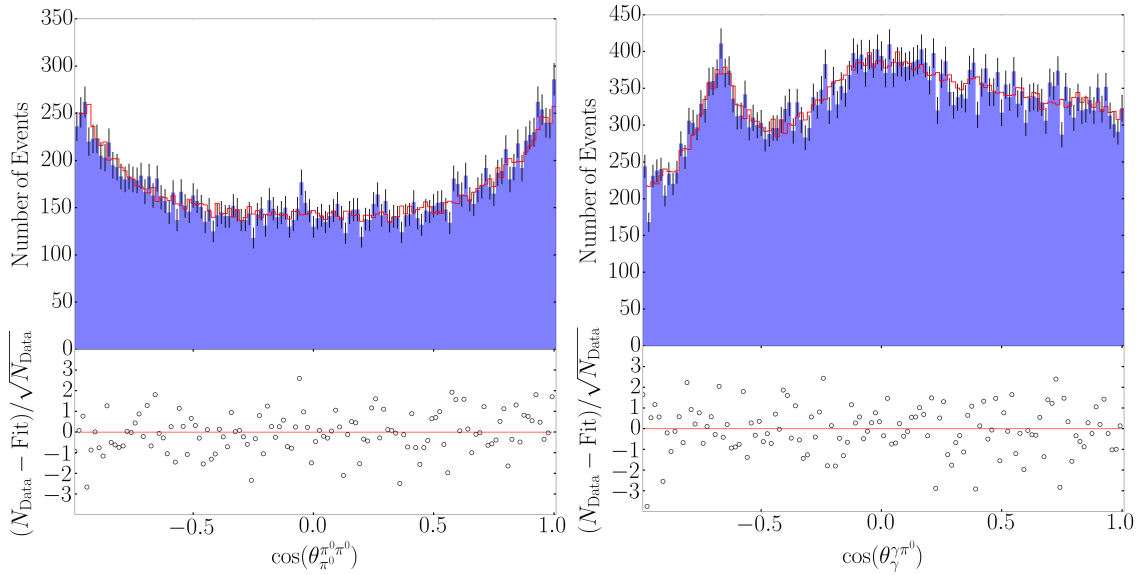


Figure 68: $\cos(\theta_{\pi^0\pi^0})$ (left) and $\cos(\theta_{\gamma\pi^0})$ (right) distributions of the reaction $J/\psi \rightarrow \gamma\pi^0\pi^0$ including f_0, f_2 as intermediate resonances. While the blue distribution is the generated MC data, the red curve is a weighted MC sample using the best fit result. On the bottom the binwise normalized residuals are shown.

states. In the $\gamma\pi^0$ subsystem the $\cos(\theta)$ distribution is non-trivial even though there is no resonance structure present. The reason are the reflections from the other final state particle combination, here $\pi^0\pi^0$, that generate this non-uniform distribution and obscure the interpretation.

Important quantities of the validation process are the accuracy and the error estimation of the extracted parameters. They can be determined from the normalized residuals of the parameters using the 600 generated MC datasets. A selected subset of residuals is shown in figure 69. The complete normalized residual information can be found in the appendix C.4.1. If the extracted parameters are accurate with respect to the generated ones shown in table 7 then the mean \bar{x} should be statistically compatible with zero. A RMS value of one implies a correct error estimation. When reviewing all of the normalized residuals, the mean values are reproduced very well while the majority of RMS values are marginally higher than the required value of 1. Therefore the parameter errors from the fit results, as determined by the minimizer, are slightly underestimated.

From the normalized residuals no measure on the extracted absolute precision is possible. This can be extracted from the unnormalized residuals, for example for the f_2 mass parameter shown in figure 70. The RMS value of $3.56(73) \text{ MeV}/c^2$ defines the 1σ error interval of the fit parameter, under the assumption of a normal distribution. For a data sample of the simple model with 20000 events, the f_2 mass is determined with a precision of approximately 0.3%.

When observing systematic shifts in pull³ distributions, the parameter correlations are useful indicators for possible difficulties in the optimization process. For two random variables X and Y , their correlation is defined as

$$\rho_{XY} = E[(X - \mu_X)(Y - \mu_Y)]/(\sigma_X\sigma_Y) \quad (45)$$

with their mean values μ_X , μ_Y and their standard deviations σ_X , σ_Y . Here E denotes the expectation value operator. The parameter correlations can be collectively visualized in the correlation matrix, which is displayed in figure 71. Here a pair of parameters are independent if their correlation value is zero. Negative or positive values correspond to an anti- or correlation of these parameters, while the magnitude of the correlation scales between 0 and 1. Of course each parameter is fully correlated to itself, hence the diagonal elements are ones. Because this matrix is symmetric the other half is omitted. In general the optimization problem becomes more difficult when the number of fit parameters increase and their correlations are stronger. Consequently the stability of the minimization process decreases. The correlations in the simple model are almost negligible except for example the f_2 mass and the phase of the f_0 or coherently added phase-space. Hypothetically, the anti-correlation of the former and the latter could be reflected in systematic shifts in the normalized residuals of these two variables, but in opposite direction. However when inspecting figure 69, no systematic shifts for these two parameters are apparent and the minimization process can be regarded as stable. In general the instability of a fit increases with the correlations of parameters, which in turn increases with the dimensionality of the fit parameter space.

³ The terms pull and normalized residuals are used as synonyms.

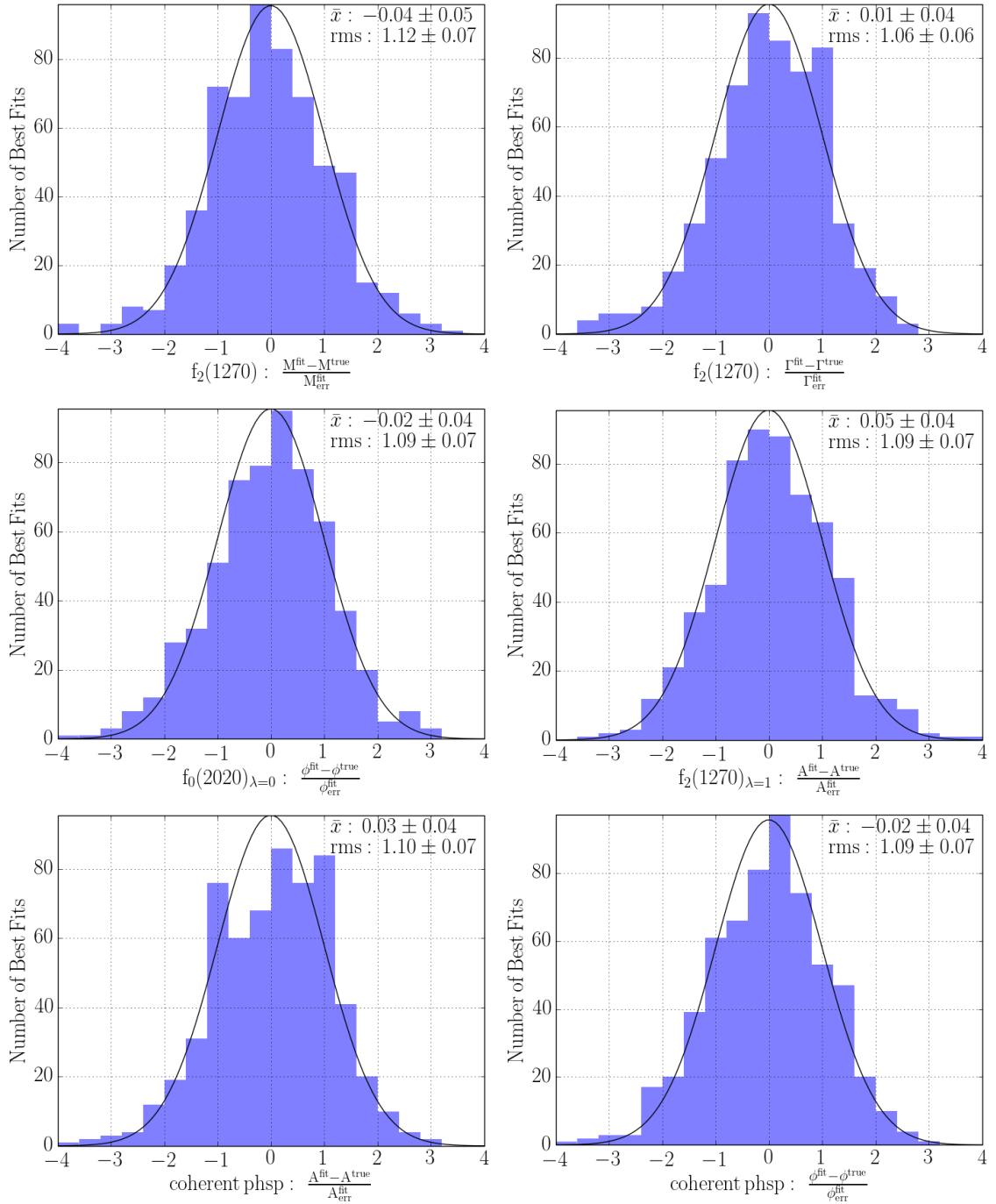


Figure 69: Normalized residuals for a selected subset of parameters in the simple model of the $J/\psi \rightarrow \gamma\pi^0\pi^0$ decay. The blue distributions are created from the best fits results of all generated samples. Drawn in black is a gaussian curve, which indicates the optimal distribution with mean equal to zero and a standard deviation of one. The mean \bar{x} and the RMS values of the distributions are displayed in the plots.

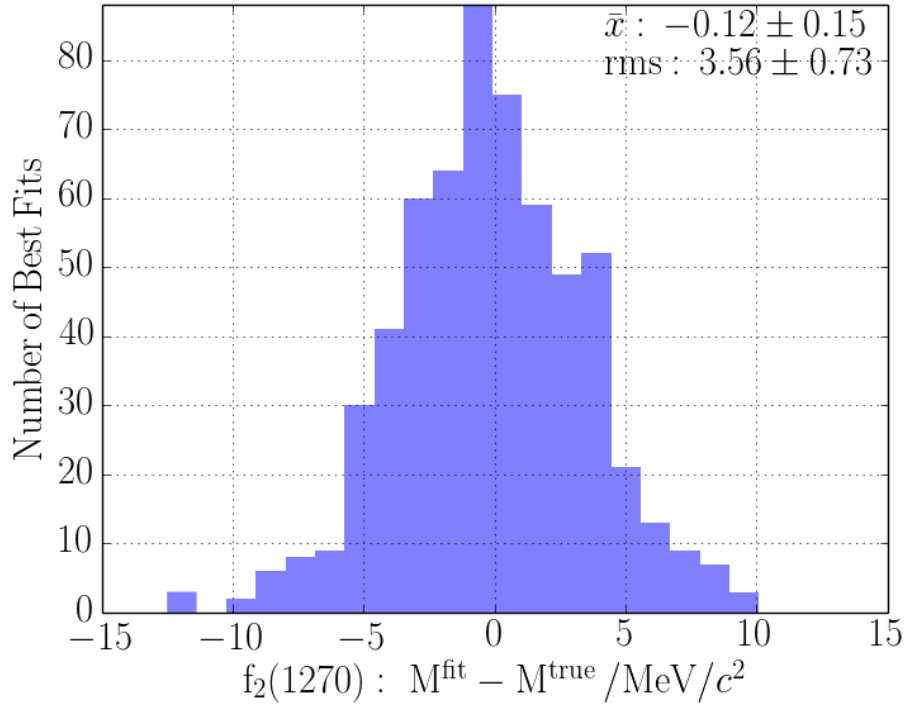


Figure 70: Residual of the f_2 mass in simple model. The mean and RMS values are given in units of MeV/c^2 .

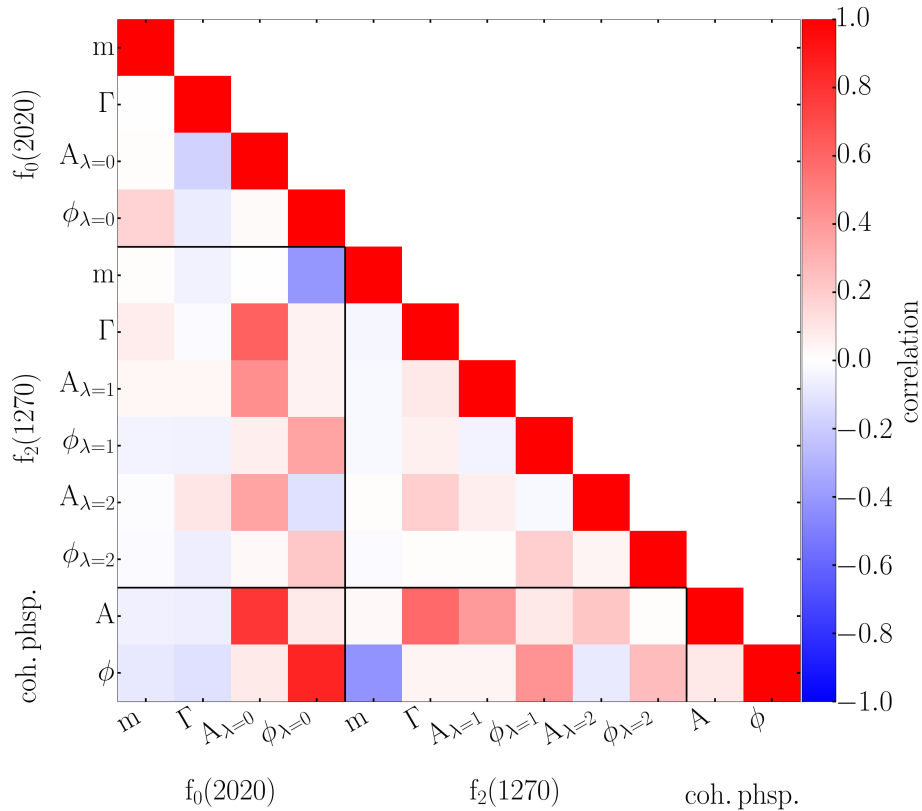


Figure 71: Correlation matrix of the best fit result on a simple model dataset for the reaction $J/\psi \rightarrow \gamma\pi^0\pi^0$ including f_0 and f_2 as intermediate resonances. The black lines serve as visual aids for the grouping of the various states. For the f_2 state the $\lambda = 0$ components are not available as they were fixed parameters in the fit.

7.4 VALIDATION WITH COMPLEX MODEL

In the validation of the implementation of the CompPWA helicity formalism we proceed with the second, more complex model. In this benchmark model more intermediate states compared to the simple model are used. In total three f_0 , two f_2 and one f_4 resonance appear in the sequential decay. The choice of resonances is inspired by the analysis performed in the reference [51], with the exception that a few resonances with fit fractions below 1% were removed. In exchange a f_4 state was inserted to also test the software with higher spin states. The parameters of the benchmark model used for the data generation are listed in table 8. Note that the strength and phases chosen here are arbitrary and do not resemble the parameters of the reference model.

Analogous to the simple model, 600 independent data samples were generated. Each sample contains 50000 events and the corresponding phase-space MC data samples have a factor of ten higher statistic. Every sample was fitted seven times with random start parameters, using the same intervals as specified for the simple model. Again only the best fit results are analyzed further and a total of 551 data samples were used. Some samples could not be used, because at least two successful fits were required in order to make a decision on a better fit result. Consequently the optimization is sometimes not able to find a valid minimum. A minimum is here declared as valid, when the Hesse algorithm successfully probes the minimum region found by the gradient decent method. Two aspects improve the stability of the fit: At first by increasing the ratio of events in a sample to the free parameters of the model, and secondly a reasonable choice of the start parameters.

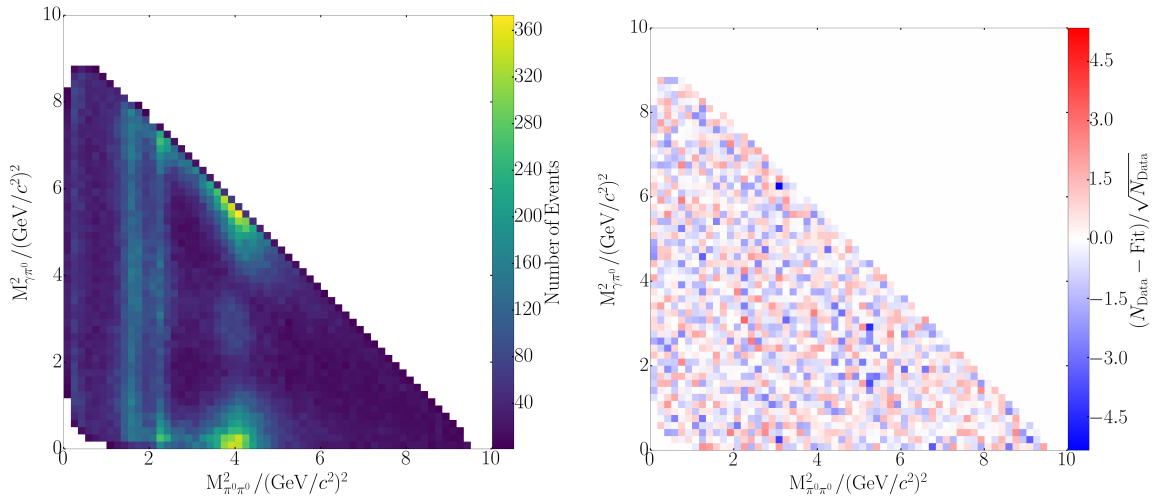


Figure 72: Dalitz plot of CompPWA generated MC data of the reaction $J/\psi \rightarrow \gamma\pi^0\pi^0$ including f_0, f_2, f_4 as intermediate resonances (left) and the normalized residual with the best CompPWA fit result (right).

Again the kinematic distributions between a single dataset and the best fit result are compared first. The Dalitz plot shown in figure 72 gives a informative overview. Foremost four bands in the $\pi^0\pi^0$ invariant mass combination are visible that correspond to all of the f resonances. Three bands are striking compared to the $f_0(500)$ band on the left edge of the Dalitz plot at $0.25 \text{ GeV}^2/c^4$. A remarkable modulation is present in the band at $2.3 \text{ GeV}^2/c^4$, because only the $f_0(1500)$ is found here and a uniform distribution is expected. The explanation for the higher spin modulation in this band are the broad f_2

Parameter		Value	Fixed
$f_0(500)$	$A_{\lambda=0}$	1.0	
	$\Phi_{\lambda=0}$	-1.5	
$f_0(1500)$	$A_{\lambda=0}$	1.5	
	$\Phi_{\lambda=0}$	-1.0	
$f_0(2020)$	$A_{\lambda=0}$	0.5	
	$\Phi_{\lambda=0}$	-0.5	
$f_2(1270)$	$A_{\lambda=0}$	0.5	x
	$\Phi_{\lambda=0}$	-1.5	x
	$A_{\lambda=1}$	1.0	
	$\Phi_{\lambda=1}$	0.0	
	$A_{\lambda=2}$	1.5	
	$\Phi_{\lambda=2}$	1.5	
$f_2(1950)$	$A_{\lambda=0}$	0.3	
	$\Phi_{\lambda=0}$	0.5	
	$A_{\lambda=1}$	0.3	
	$\Phi_{\lambda=1}$	0.5	
	$\Phi_{\lambda=2}$	0.5	
$f_4(2050)$	$A_{\lambda=0}$	1.0	
	$\Phi_{\lambda=0}$	0.0	
	$A_{\lambda=1}$	1.0	
	$\Phi_{\lambda=1}$	0.0	
	$\Phi_{\lambda=2}$	0.0	
coh. phsp.	A	0.05	
	ϕ	0.0	

Table 8: Parameters of the benchmark model used for the data generation of the reaction $J/\psi \rightarrow \gamma\pi^0\pi^0$ including multiple f_0, f_2 resonances and one f_4 resonance as intermediate states. For the masses and widths of the intermediate resonances PDG values are used [9].

and f_4 resonances that can interfere with the $f_0(1500)$. More interference is expected at $4 \text{ GeV}^2/c^4$, where three intermediate states are overlapping strongly: the $f_0(2020)$, the $f_2(1950)$ and the $f_4(2050)$. From the Dalitz plot a higher spin resonance is visible, but also a interference is obvious due to the distortion of the band closer to the phase space boundaries. When inspecting the normalized residual of the Dalitz plot and the fit result (see figure 72), a uniform distribution of the residual values in the Dalitz plot area is on hand. Hence first conclusions on a good description of the data can be drawn.

This excellent agreement is also visible from the comparisons of the one dimensional kinematic variable distributions shown in figure 73. In the $\pi^0\pi^0$ invariant mass spectrum

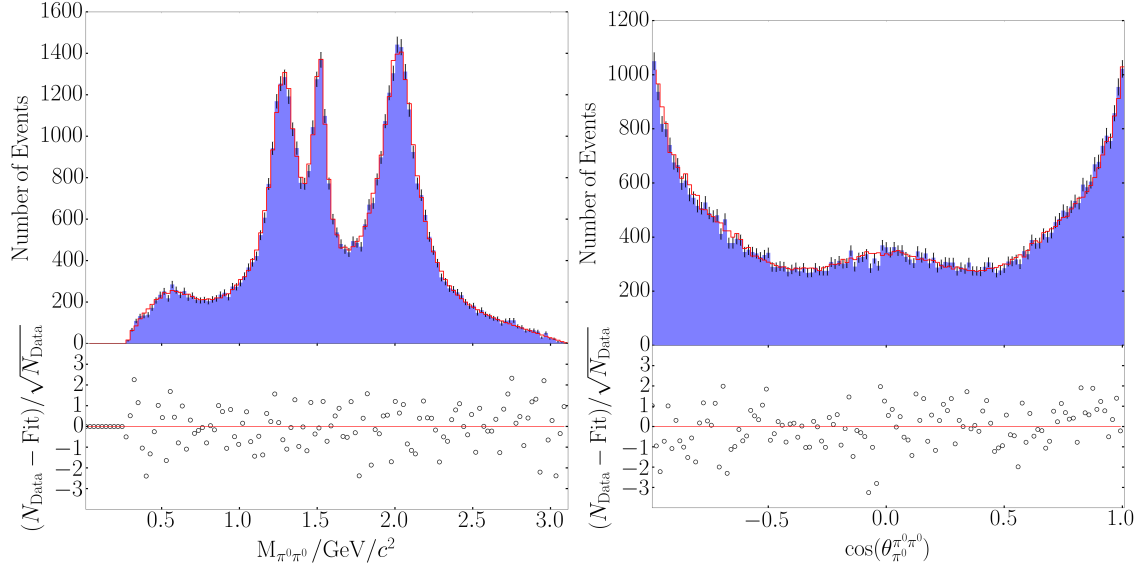


Figure 73: $\pi^0\pi^0$ invariant mass spectrum and $\cos(\theta_{\pi^0\pi^0})$ distribution of the reaction $J/\psi \rightarrow \gamma\pi^0\pi^0$ including f_0, f_2 and f_4 as intermediate resonances from ComPWA generated MC data. While the blue distribution is the ComPWA generated MC data, the red curve is a weighted MC sample using the best fit result. Below the binwise normalized residuals are shown.

three prominent peaks are present, but also a small accumulation at $0.6 \text{ GeV}^2/c^2$ is visible. In this respect all of the f resonances can be found. However at $2 \text{ GeV}^2/c^2$ it is impossible to identify all of the three overlapping resonances. Now the importance of the partial wave analysis becomes clear. Similar to the Dalitz plot, the $\cos(\theta)$ distribution in the $\pi^0\pi^0$ subsystem suggests higher spin components. But as long as this is not used in conjunction with a slicing in the invariant mass, no definite spin information for single resonances can be extracted. This approach was studied in [23]. With regard to the validation of the helicity formalism implementation, once again a perfect agreement of the fit result with the generated data is found.

How accurate the fit parameters are with respect to the parameters used for the MC data generation, is demonstrated by the normalized residual distributions. From the width of the distributions the error estimation performed by the optimizer can be verified. All of the mean and RMS values of the normalized residuals are summarized in table 9. The distributions of the normalized residuals can be found in the appendix in section C.4.2.

Just as in the simple model the RMS values are mostly above one, indicating that the errors for the parameters are slightly underestimated. The pull mean values are statisti-

Parameter	Mean	RMS	
$f_0(500)$	M	0.02 ± 0.05	1.04 ± 0.07
	Γ	-0.09 ± 0.04	1.03 ± 0.07
	$A_{\lambda=0}$	-0.08 ± 0.05	1.04 ± 0.07
	$\phi_{\lambda=0}$	-0.06 ± 0.05	1.09 ± 0.07
$f_0(1500)$	M	0.07 ± 0.05	1.07 ± 0.07
	Γ	-0.06 ± 0.05	1.08 ± 0.07
	$A_{\lambda=0}$	-0.13 ± 0.04	1.01 ± 0.06
	$\phi_{\lambda=0}$	0.00 ± 0.05	1.08 ± 0.07
$f_0(2020)$	M	0.09 ± 0.05	1.11 ± 0.07
	Γ	-0.12 ± 0.05	1.14 ± 0.08
	$A_{\lambda=0}$	-0.09 ± 0.04	1.02 ± 0.06
	$\phi_{\lambda=0}$	0.03 ± 0.05	1.06 ± 0.07
$f_2(1270)$	M	0.09 ± 0.05	1.11 ± 0.08
	Γ	-0.02 ± 0.05	1.07 ± 0.07
	$A_{\lambda=1}$	-0.14 ± 0.04	1.04 ± 0.07
	$\phi_{\lambda=1}$	0.06 ± 0.05	1.08 ± 0.07
	$A_{\lambda=2}$	-0.13 ± 0.04	1.03 ± 0.06
	$\phi_{\lambda=2}$	-0.02 ± 0.05	1.06 ± 0.07
$f_2(1950)$	M	-0.06 ± 0.05	1.06 ± 0.07
	Γ	-0.06 ± 0.05	1.10 ± 0.07
	$A_{\lambda=0}$	-0.02 ± 0.05	1.05 ± 0.07
	$\phi_{\lambda=0}$	0.06 ± 0.04	1.00 ± 0.06
	$A_{\lambda=1}$	0.01 ± 0.04	1.03 ± 0.07
	$\phi_{\lambda=1}$	-0.04 ± 0.04	0.99 ± 0.06
	$A_{\lambda=2}$	-0.07 ± 0.04	1.04 ± 0.07
	$\phi_{\lambda=2}$	0.00 ± 0.04	1.04 ± 0.07
$f_4(2050)$	M	-0.12 ± 0.05	1.10 ± 0.07
	Γ	0.01 ± 0.05	1.12 ± 0.08
	$A_{\lambda=0}$	-0.13 ± 0.04	1.03 ± 0.07
	$\phi_{\lambda=0}$	0.03 ± 0.05	1.07 ± 0.07
	$A_{\lambda=1}$	-0.14 ± 0.04	1.03 ± 0.07
	$\phi_{\lambda=1}$	-0.01 ± 0.05	1.07 ± 0.07
	$A_{\lambda=2}$	-0.15 ± 0.04	1.03 ± 0.07
	$\phi_{\lambda=2}$	-0.03 ± 0.05	1.06 ± 0.07
coh. phsp.	A	-0.14 ± 0.04	1.01 ± 0.06
	ϕ	0.01 ± 0.05	1.08 ± 0.07

Table 9: Normalized residual mean and RMS values for the fit parameters of the benchmark model on CompPWA generated MC data for the reaction $J/\psi \rightarrow \gamma\pi^0\pi^0$ including multiple f_0, f_2 resonances and a f_4 resonance as intermediate states. The values are taken from the appendix C.4.2.

cally compatible with zero taking into account the errors. However it should be noticed that the majority of pull mean values for the magnitude parameters are constantly below zero on a 2 to 3 σ level. This suggests a small bias of the model parameters determined by the fit. However the bias is negligible with respect to the used statistics for this test and is therefore unproblematic.

In conclusion the fit is able to accurately determine the correct parameters. Only a insignificant underestimation of the parameters from MINUIT2 was identified.

7.5 VALIDATION OF THE COMPLEX MODEL USING PAWIAN

So far mainly the self-consistency of the helicity formalism implementation was checked, since a ComPWA helicity amplitude is used for both the data generation and the fitting. To complete the validation of the implementation the correctness of the physics has to be proved. In the beginning of the chapter already the angular distributions for single amplitudes were verified by the comparison with analytic calculations from theory. To ensure a correct description of the physics of this helicity formalism implementation, the validation is extended by an additional step. The data sets are generated with an existing helicity formalism implementation from another software package. This input data is then fitted with ComPWA. The comparison of the fit results with the input data gives information on an identical physics description of the two software packages.

For the data generation the previously defined benchmark model with the same parameter set as stated in table 8 was used in the PAWIAN software package [121]. Because PAWIAN does currently not support background which could be added coherently, this was removed from the model. In total 400 data samples of 30000 events were generated. Again each sample was fitted seven times and only the best fit result, based on the best likelihood value, was used for further analysis. Due to invalid minima found by the minimizer, some results are rejected and only 259 samples with their corresponding best fit results are used in the following. A minimum is declared as invalid, if the Hesse calculation fails, which scans the minimum region obtained by the gradient descent method.

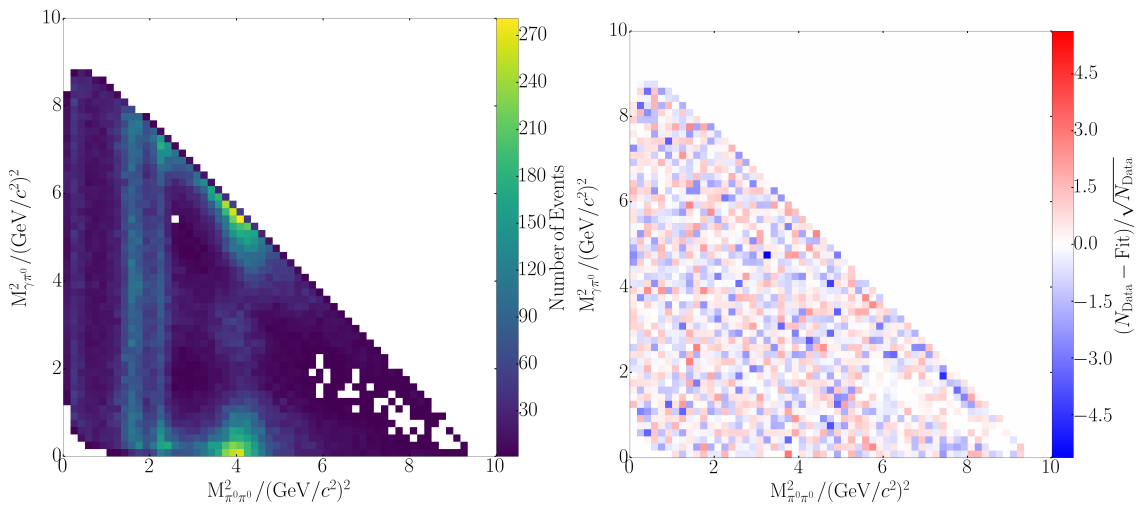


Figure 74: Dalitz plot of PAWIAN generated MC data of the reaction $J/\psi \rightarrow \gamma\pi^0\pi^0$ including f_0, f_2, f_4 as intermediate resonances (left) and the normalized residual with the best CompPWA fit result (right).

At first the decay kinematics of a randomly selected generated data sample is validated. From the resemblance of the Dalitz plots first evidence for an equal description of the helicity formalism in CompPWA and PAWIAN is found. Figure 74 shows the PAWIAN data Dalitz plot, while the one for the CompPWA data was shown in figure 72. The only obvious difference is the missing data at values above $6 \text{ GeV}^2/c^4$ for $M_{\pi^0\pi^0}^2$, which is expectable from the absent coherently added phase space term. A more quantitative validation is given by the comparison of the CompPWA fit result with the PAWIAN data, visualized by the normalized residual plot. Here no regions of under- or overestimation are visible, and a good description of the data can be concluded.

However because the Dalitz plot does not visualize all of the kinematic information of this reaction (see appendix C.1), a more thorough validation is needed. Figure 75 shows distributions for two selected variables not observable in the Dalitz plot.

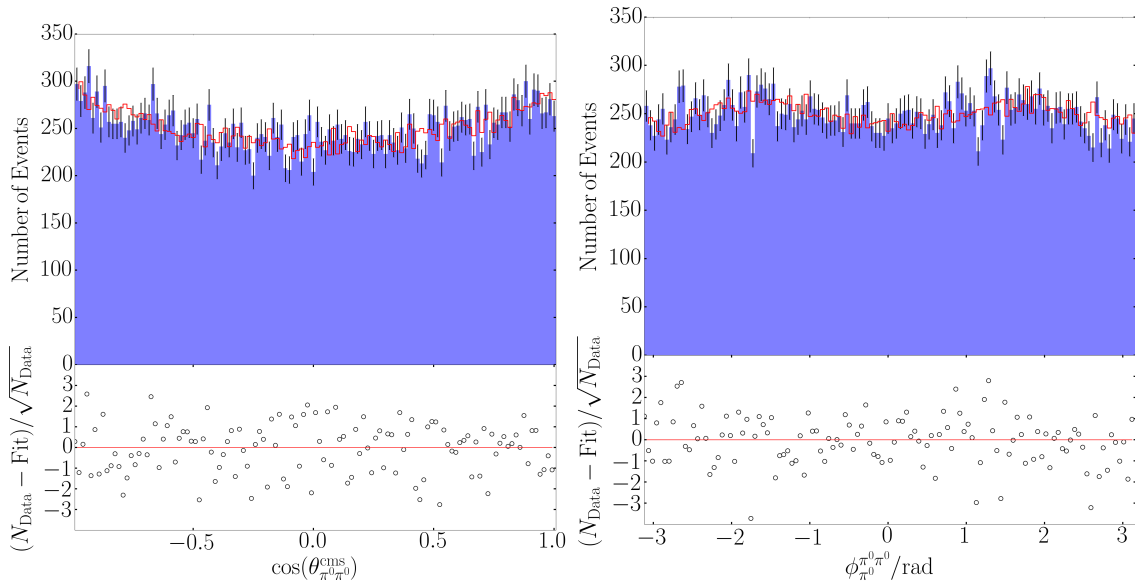


Figure 75: $\cos(\theta_{\pi^0\pi^0}^{\text{cms}})$ and $\phi_{\pi^0\pi^0}$ distributions of the reaction $J/\psi \rightarrow \gamma\pi^0\pi^0$ including f_0 , f_2 and f_4 as intermediate resonances. While the blue distribution is the PAWIAN generated MC data, the red curve is a weighted mc sample using the best fit result on the data. Below the normalized residuals are shown.

Here, the fit result $\cos(\theta_{\pi^0\pi^0}^{\text{cms}})$ distribution matches the data well and also the shape expected by the J/ψ with spin 1 and $\lambda = \pm 1$ is present. Furthermore, because the z axis was chosen for the spin quantization of center-of-mass system (CMS) decay, the physics is invariant under rotations about this axis. This freedom of the orientation of the x and y axis leads to the fact that only differences of the ϕ variables in the CMS and the subsequent decay are relevant. With the chosen convention for the evaluation of the Wigner D functions, this difference is fully mapped to the ϕ distribution of the π^0 in the $\pi^0\pi^0$ system. This is also shown in figure 75. Here a non-trivial modulation is visible and most importantly the fit result correctly describes the distribution. A comparison of all kinematic variable distributions is shown in the appendix C.3.2.

Finally the entity of the best fit results are examined with the normalized residuals of the fit parameters. Hereby the correctness with respect to the generated values (see table 8) is checked. The mean and RMS values for all of the normalized residuals are presented in table 10 (see appendix C.4.3 for the distributions). They give information about the accuracy of the determined parameters and the correctness of their error estimation.

Parameter	Mean	RMS	
$f_0(500)$	M	0.18 ± 0.07	1.03 ± 0.11
	Γ	-0.24 ± 0.07	1.03 ± 0.11
	$A_{\lambda=0}$	-0.09 ± 0.07	0.98 ± 0.10
	$\phi_{\lambda=0}$	-0.06 ± 0.08	1.08 ± 0.12
$f_0(1500)$	M	-0.12 ± 0.08	1.12 ± 0.13
	Γ	-0.04 ± 0.07	1.05 ± 0.11
	$A_{\lambda=0}$	-0.09 ± 0.07	1.01 ± 0.10
	$\phi_{\lambda=0}$	-0.02 ± 0.08	1.08 ± 0.12
$f_0(2020)$	M	0.10 ± 0.08	1.08 ± 0.12
	Γ	-0.24 ± 0.08	1.11 ± 0.12
	$A_{\lambda=0}$	-0.06 ± 0.08	1.11 ± 0.12
	$\phi_{\lambda=0}$	0.10 ± 0.07	1.04 ± 0.11
$f_2(1270)$	M	-0.06 ± 0.08	1.09 ± 0.12
	Γ	-0.03 ± 0.07	1.02 ± 0.10
	$A_{\lambda=1}$	-0.13 ± 0.07	1.01 ± 0.10
	$\phi_{\lambda=1}$	0.12 ± 0.07	1.05 ± 0.11
	$A_{\lambda=2}$	-0.17 ± 0.07	1.05 ± 0.11
	$\phi_{\lambda=2}$	0.03 ± 0.07	1.05 ± 0.11
$f_2(1950)$	M	0.20 ± 0.07	1.06 ± 0.11
	Γ	0.00 ± 0.09	1.24 ± 0.16
	$A_{\lambda=0}$	0.05 ± 0.07	1.01 ± 0.10
	$\phi_{\lambda=0}$	-0.03 ± 0.08	1.11 ± 0.12
	$A_{\lambda=1}$	-0.03 ± 0.08	1.08 ± 0.12
	$\phi_{\lambda=1}$	0.12 ± 0.08	1.10 ± 0.12
	$A_{\lambda=2}$	-0.07 ± 0.08	1.08 ± 0.12
	$\phi_{\lambda=2}$	0.19 ± 0.08	1.09 ± 0.12
$f_4(2050)$	M	-0.06 ± 0.08	1.18 ± 0.14
	Γ	-0.14 ± 0.07	1.01 ± 0.10
	$A_{\lambda=0}$	-0.13 ± 0.07	1.04 ± 0.11
	$\phi_{\lambda=0}$	0.07 ± 0.08	1.08 ± 0.12
	$A_{\lambda=1}$	-0.16 ± 0.07	1.01 ± 0.10
	$\phi_{\lambda=1}$	0.20 ± 0.07	1.06 ± 0.11
	$A_{\lambda=2}$	-0.13 ± 0.07	0.97 ± 0.09
	$\phi_{\lambda=2}$	0.07 ± 0.08	1.15 ± 0.13

Table 10: Normalized residual mean and RMS values for the fit parameters of the benchmark model for the reaction $J/\psi \rightarrow \gamma\pi^0\pi^0$ including multiple f_0, f_2 resonances and a f_4 resonance as intermediate states. The fits were performed with ComPWA on PAWIAN generated datasets. Refer to appendix C.4.3 for pull distributions.

With respect to the statistical errors the mean values are in agreement with the generated parameters, implicating a high accuracy of the fit parameters. Just as in the previous validations, the error are marginally underestimated.

At this point the validation of the helicity formalism implementation in the CompPWA framework is declared as complete.

7.6 A FIRST FIT ON THE BESIII DATA

The BESIII dataset of the decay $J/\psi \rightarrow \gamma\pi^0\pi^0$ originates from the reference [51, 120]. Also a corresponding phase space MC dataset for the efficiency correction is available. It should be emphasized that the goal is not a full analysis of the data, but a first real data test case for the CompPWA helicity formalism implementation. In total the data contains 442562 events and the corresponding acceptance corrected phase space sample amounts to roughly $1.6 * 10^6$ events.

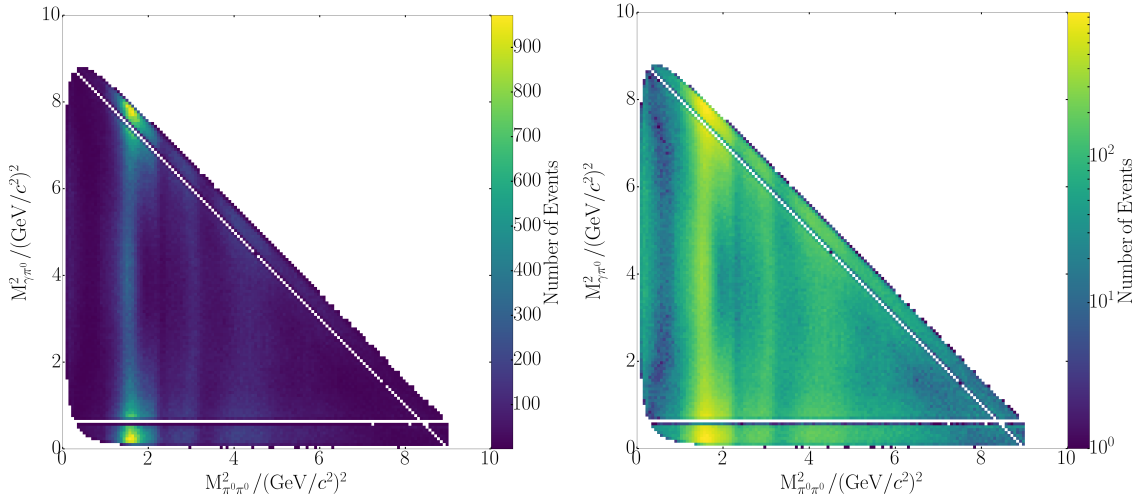


Figure 76: Dalitz plot of the BESIII data of the reaction $J/\psi \rightarrow \gamma\pi^0\pi^0$ (left) and in logarithmic scale (right). The ω bands have been removed [120].

The Dalitz plot of the data is shown in figure 76. Immediately noticeable is the strongest contribution in the $\pi^0\pi^0$ mass combination at a squared mass of roughly $1.6 \text{ GeV}^2/c^4$. Comparing this with the previous Dalitz plots (see figure 72), the $f_2(1270)$ state can be foreshadowed. Both the mass and the spin 2 ($\lambda = 0$) modulation, with peaks at the phase space boundaries and the slight bump in the center of the band, match the $f_2(1270)$. Several other resonances in the squared mass range from $2\text{-}5 \text{ GeV}^2/c^4$ are also visible by eye. A relatively strong uniform spin 0 band is located at around $3 \text{ GeV}^2/c^4$. The broad band at $4 \text{ GeV}^2/c^4$ shows higher spin modulations, thus one would naively suspect multiple intermediate states with interference. However for precise quantitative statements a partial wave analysis is indispensable.

A helicity intensity was generated with CompPWA including all intermediate states as stated in the reference [120, p. 109]. A first fit on the data was performed within the scope of the thesis. In total 48 parameters of the model were optimized by the minimizer. The parameters are again initialized randomly using the same intervals as for the validation tests shown in the previous sections. Generally a single fit is not sufficient to guarantee the finding of the global minimum. In the case of this first fit, the minimizer from the

optimization library MINUIT2 was able to find a valid minimum region and successfully stopped the gradient descent procedure. However to validate the minimum, and obtain a more precise location of the minimum with a symmetric error estimation of fit parameters, the Hesse algorithm is executed afterwards. This additional Hesse calculation failed, which could indicate that not the global minimum was found. Hence no particularly good description of the data is expected, and this result should be interpreted with care. The obtained fit parameters and the errors are listed in table 11.

For most of the parameters the extracted values appear promising, since the masses and width are reasonably close to the PDG values and the strengths of the individual

Parameter	Value	PDG Value	Reference Value
coh. phsp.	A	0.001 ± 0.001	
	ϕ	0.973 ± 1.201	
$f_0(500)$	m	0.273 ± 0.001	0.475
	Γ	1.084 ± 0.007	0.550
	$A_{\lambda=0}$	8.892 ± 0.035	
	$\phi_{\lambda=0}$	-1.258 ± 84.140	
$f_0(1500)$	m	1.462 ± 0.001	1.504 ± 0.006
	Γ	0.099 ± 0.002	0.109 ± 0.007
	$A_{\lambda=0}$	4.360 ± 0.041	
	$\phi_{\lambda=0}$	-1.618 ± 84.136	
$f_0(1710)$	m	1.777 ± 0.000	1.723 ± 0.006
	Γ	0.217 ± 0.001	0.139 ± 0.008
	$A_{\lambda=0}$	7.660 ± 0.026	
	$\phi_{\lambda=0}$	-0.482 ± 84.146	
$f_0(2020)$	m	1.945 ± 0.001	1.992 ± 0.016
	Γ	0.610 ± 0.002	0.442 ± 0.060
	$A_{\lambda=0}$	10.56 ± 0.02	
	$\phi_{\lambda=0}$	-2.292 ± 84.125	
$f_0(2330)$	m	2.240 ± 0.002	2.300
	Γ	0.172 ± 0.004	0.200
	$A_{\lambda=0}$	1.682 ± 0.031	
	$\phi_{\lambda=0}$	1.757 ± 83.875	
$f_2(1270)$	m	1.255 ± 0.000	1.275 ± 0.008
	Γ	0.187 ± 0.001	0.186 ± 0.002
	$A_{\lambda=0}$	11.042 ± 0.027	
	$\phi_{\lambda=0}$	2.642 ± 84.091	
	$A_{\lambda=1}$	8.938 ± 0.026	
	$\phi_{\lambda=1}$	-0.681 ± 84.145	
	$A_{\lambda=2}$	5.298 ± 0.031	
	$\phi_{\lambda=2}$	2.043 ± 84.130	

f ₂ (1565)	m	1.649 ± 0.010	1.562 ± 0.013	1.549 ± 0.002
	Γ	1.860 ± 0.012	0.134 ± 0.008	0.081 ± 0.003
	A _{λ=0}	1.0		
	ϕ _{λ=0}	0.0		
	A _{λ=1}	1.655 ± 0.017		
	ϕ _{λ=1}	1.975 ± 84.069		
	A _{λ=2}	1.844 ± 0.018		
	ϕ _{λ=2}	-1.73 ± 84.06		
f ₂ (1950)	m	1.944	1.944 ± 0.012	1.944
	Γ	0.472	0.472 ± 0.018	0.472
	A _{λ=0}	2.451 ± 0.023		
	ϕ _{λ=0}	-2.972 ± 84.110		
	A _{λ=1}	2.858 ± 0.029		
	ϕ _{λ=1}	-0.308 ± 83.964		
	A _{λ=2}	2.459 ± 0.024		
	ϕ _{λ=2}	2.594 ± 84.090		
f ₂ (2150)	m	2.157	2.157 ± 0.012	2.157
	Γ	0.152	0.152 ± 0.030	0.169
	A _{λ=0}	0.984 ± 0.032		
	ϕ _{λ=0}	-3.075 ± 0.025		
	A _{λ=1}	0.552 ± 0.053		
	ϕ _{λ=1}	-1.316 ± 0.087		
	A _{λ=2}	0.528 ± 0.034		
	ϕ _{λ=2}	-2.964 ± 0.087		

Table 11: Parameters of the helicity amplitude model used for the first fit on the BESIII data of the $J/\psi \rightarrow \gamma\pi^0\pi^0$ process and their extracted values. Also the PDG [9] and reference [120, p. 109] values for the masses and widths are denoted. The mass and width parameters are given in units of GeV/c^2 and GeV respectively. Parameters without specification of their errors have been fixed in the fit or no errors are available.

waves follow the trends of the fit fractions of the reference [120, p. 109]. However several mass and width values stand out with non-credible values far off the PDG values. These are the mass and width of the $f_0(500)$ and the width of the $f_2(1565)$. Actually for the former state, the PDG does not even specify any mass or width values anymore, because the Breit-Wigner parameterization is unsuitable [122]. Other formalisms are preferred for an extraction. Hence it is not surprising that the extraction of these parameters is not easy. Due to the large deviations from the PDG values, the optimization process presumably failed to reach the global minimum. Furthermore the immense width of 1.86 GeV for the f_2 resonance in conjunction with its small amplitude indicates that only a local minimum was reached. Multiple fits with different sets of initial parameters, with a proper adjustment of the intervals from which the start parameters are chosen, have to be performed in the future analysis to ensure the obtainment of the global minimum.

On a closer look, the agreement of the extracted masses and widths of all intermediate states with the PDG values is also not statistically compatible. In the dynamical functions for the f_2 states no barrier terms were used, which could explain the shift of the $f_2(1270)$ to lower masses. However it is remarkable that the reference shows deviations to the PDG values consistent with the result of CompPWA. The same deviation in both fit results support the correct implementation of the helicity formalism in CompPWA. Finally the statistical errors for most of the phases are striking with their large values of about 84. Obviously the error estimation has failed here, which was announced by the optimizer and underlines that a local minimum was found.

Even though the extracted set of parameters is not credible as a whole, it is nevertheless interesting to compare the data and the fit result for various kinematic distributions and obtain a measure for the goodness of the fit.

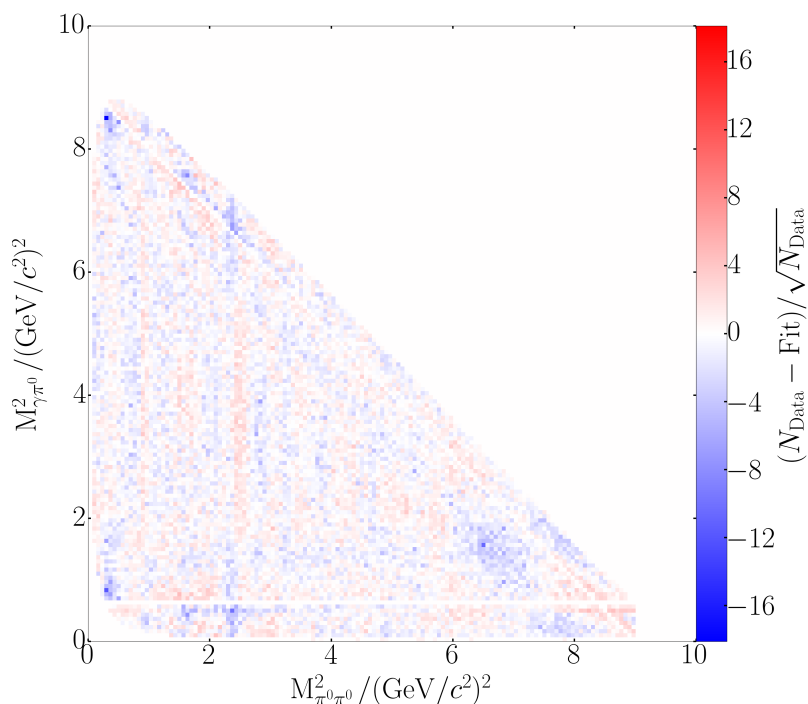


Figure 77: Normalized residual of the BESIII Dalitz plot of the reaction $J/\psi \rightarrow \gamma\pi^0\pi^0$ with the CompPWA helicity amplitude model fit result.

Figure 77 shows the normalized Dalitz plot residual of the data and the phase space sample, which was weighted with the intensity of the fit result. Here many regions of over and underestimation are already visible, implicating that this fit result is not able to describe the data correctly. The periodic modulation in the $\pi^0\pi^0$ mass combination, indicates that the placement of the f resonances and their interference is not properly described in the fit result. Furthermore the band structure at $1.5 \text{ GeV}^2/c^4$ in the $\gamma\pi^0$ mass combination is intriguing, since no resonance is included in our model for this subsystem.

These effects are more easily comprehensible when observing the invariant mass spectra pictured in figure 78. Overall, regarding the fact that some fit parameters are far off the PDG values, the agreement of the fit result with the data is surprisingly good. Some small deviations are visible in the overlap of the distributions, best seen in the normalized residuals below. Because the fit result does not exactly follow the shape of most

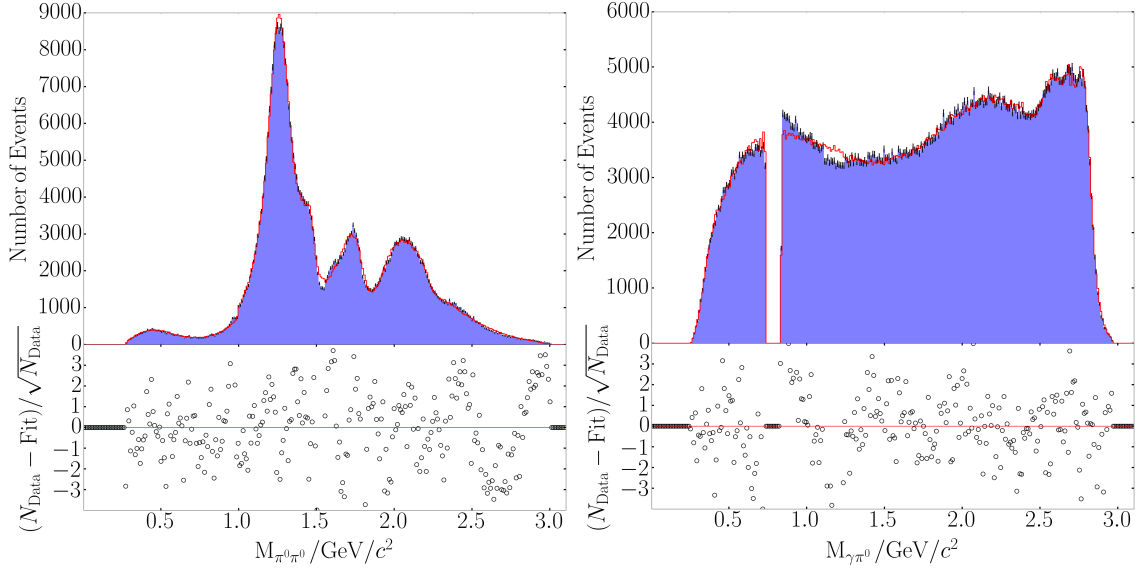


Figure 78: Invariant mass spectra of the the BESIII data for the $\pi^0\pi^0$ (left) and $\gamma\pi^0$ (right) subsystems of the reaction $J/\psi \rightarrow \gamma\pi^0\pi^0$. While the blue distribution is the data, the red curve is the weighted MC sample of the first fit result. Below the normalized residuals are shown.

of the peak structures, the band structures visible in the above normalized Dalitz plot residual now become clear.

In the $\pi^0\pi^0$ invariant mass spectrum, the overestimation at the $f_2(1270)$ peak and at $1.5 \text{ GeV}/c^2$ initially catches the eye. A possible explanation is the dynamical parameterization used here does not include barrier factors. At higher masses the residual also indicates that the agreement is not perfect. The shoulder in the spectrum at a mass of $2.3 \text{ GeV}/c^2$ could be an additional state with no counterpart in the model description. At this mass value also an accumulation of events was visible in the Dalitz plot. The very good description at low masses is astonishing, as the $f_0(500)$ parameters are very far off the PDG values. Also some kinks in the data, that are not reproduced in the fit solution, generate bands in the Dalitz plot. This is especially well visible in the $\gamma\pi^0$ invariant mass spectrum with a drop in the data at $1.2 \text{ GeV}/c^2$. The strong rise near the ω region at around $800 \text{ MeV}/c^2$ suggests that the ω band was not cut out good enough. Although a better solution would be the description of the ω state in the helicity intensity, this may prove to be difficult due to the very small width.

The comparison of further one dimensional kinematic distributions are shown in figure 79. The agreement of the fit result with the data is also very good. Only a minor deviation in the description of the $\cos(\theta_\gamma^{\gamma\pi^0})$ distribution at around 0.5 is visible, especially when checking the normalized residual.

Even though this fit result on the data does not resemble the optimal solution, it describes the main features of the data well. Therefore results of this first fit attempt on real data support the correct implementation of the ComPWA helicity formalism.

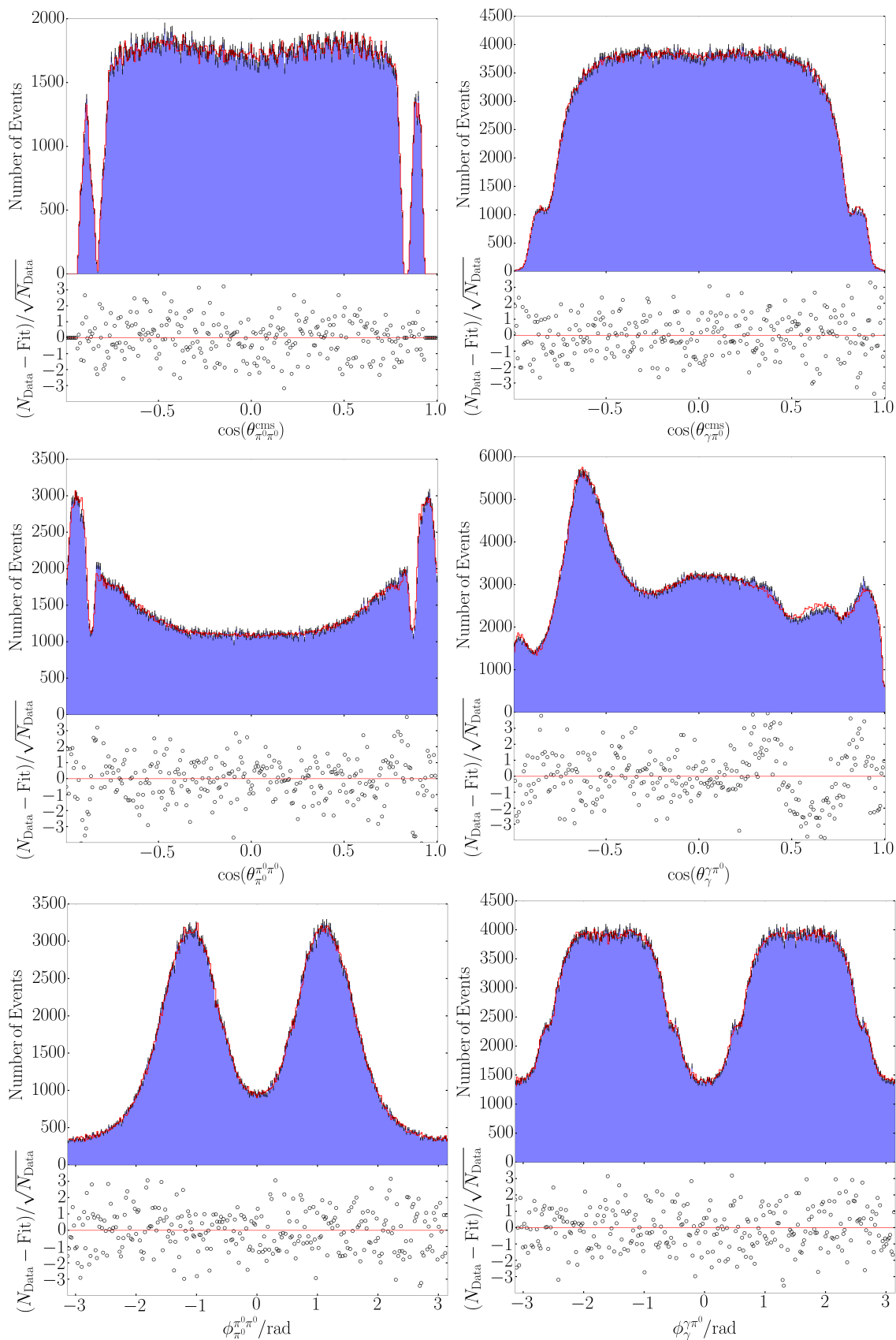


Figure 79: $\cos(\theta)$ and ϕ distributions of the BESIII data of the reaction $J/\psi \rightarrow \gamma\pi^0\pi^0$. The left plots regard the $\pi^0\pi^0$ subsystem topology, while the right ones are for the $\gamma\pi^0$ subsystem. The data is visualized by the blue distributions and the red curve is the weighted MC sample of the first fit result. Below the normalized residuals are shown.

7.7 DISCUSSION & OUTLOOK

In this chapter the helicity formalism implementation of the CompPWA framework was successfully tested. It was shown that the novel expert system approach is able to correctly compute all relevant decay trees, from basic information of the $J/\psi \rightarrow \gamma\pi^0\pi^0$ reaction. By simply enabling or disabling rules, the physics context is modified in a flexible way. Also information about the conserved and violated quantum numbers is provided for each individual decay. Although a second stage was used to narrow down the possible decay trees manually, a growth of the expert system knowledge can improve this situation in the future. Possible extensions are the provision of branching ratios and the ability to automatically determine the type of interaction, and therefore the conserved quantum numbers for each decay. In summary the expert system proves to be a natural and intuitive solution for the task of constructing relevant decay trees. With its high level of transparency, the use of an expert system for this task is beneficial, especially for a large user base.

Next the helicity intensity implementation in CompPWA was verified in a three step process. At first the angular distributions for the $J/\psi \rightarrow \gamma\pi^0\pi^0$ process with only single intermediate states and specific helicities were produced. These distributions are perfectly consistent with the analytic solutions. Next the accuracy of the fit parameters as well as their error estimation using the MINUIT2 minimizer was checked. The accuracy of the parameters is bias free with respect to the statistical errors. Merely the errors are marginally underestimated. These statements hold for both a simple and a more complex model, also underlining the stability of the optimization.

To ensure a correct physics description, $J/\psi \rightarrow \gamma\pi^0\pi^0$ data samples were generated with another software package and fitted with a corresponding CompPWA helicity intensity. Here the data generation was performed with PAWIAN. Also there the systematic studies showed an excellent agreement of the fit results with the data. Consequently, the validation of the CompPWA helicity formalism was declared as complete in connection with the previous steps.

As a first real test-case of the helicity formalism implementation a fit effort on the BESIII data was made. Regarding that only a single fit was performed, the description of the data is already quite good. However some problems in the description of data cannot be disregarded, for example the large deviations in the mass and width parameters of the $f_0(500)$ and some deviations in the invariant mass spectra in general. These observed deviations are understandable, when regarding the fact that the minimization process most likely did not reach the global minimum. Consequently the obtained set of parameters may not represent the optimal solution. Also the simple Breit-Wigner parameterization can account for the observed deviations. Nevertheless the agreement is promising and the extracted parameters are consistent with the results in the reference. A more detailed analysis of the data with an extension of the available dynamical functions is expected as the next step.

With the availability of the helicity formalism in the CompPWA project, a cornerstone for the comparability between various theoretical model descriptions was laid. Analysis of various reactions across many experiments are highly anticipated.

SUMMARY

Several aspects of the strong interaction still remain nebulous, despite large efforts over decades. In the low energy regime, the classification of the bound states and deciphering their structure prove to be difficult in certain areas of the hadron spectrum. Due to the unique properties of the strong interaction, the meson spectrum cannot be calculated analytically and effective models are used. Precise measurements of these bound states and their properties are important, in order to test the validity of the theoretical models. The mass and width of the 0^{++} isoscalars are difficult to extract experimentally, because multiple wide and overlapping states are present. This region is particularly interesting, since there are more states than expected by the constituent quark model and a light glueball state is predicted here by lattice-QCD calculations. Also the unexpected X, Y, Z states in the charmonium sector are compelling, as they are candidates with exotic content with respect to the regular meson quark-antiquark contribution.

One highly accurate method to determine the line shape, i.e. the mass and width, of states is the energy scan. The knowledge of the luminosity is essential to normalize the measured line shape. The energy scans will be performed by the future precision experiment \bar{P} ANDA, for which the luminosity detector (LMD) measures the luminosity. When determining the properties of a broader spectrum of states, the partial wave analysis (PWA) is of great importance. This method allows for the extraction of additional quantum numbers such as the spin and parity. In the 0^{++} isoscalar sector the precise extraction of state masses and widths is hindered by complicated structure of the dynamics. The usual Breit-Wigner parameterization reaches its limits here. To obtain a measure on the ability of a theoretical model to describe the measured data, a comparison of the results with other models is important. This is one of the goals of the CompPWA project, which intends to provide various formalisms and models.

The first part of the thesis was the determination of the luminosity with the highest possible accuracy and precision for the \bar{P} ANDA experiment from the track information of the LMD. For this the versatile LuminosityFit software was developed, providing reliable and accurate luminosity information. Numerous effects influence the stability and accuracy of the luminosity extraction procedure, for which extensive studies were performed. These are the track reconstruction efficiency, the detector resolution, and all effects arising from the distribution and displacement of the IP, as well as the tilt and divergence of the accelerator beam. Furthermore the implementation and performance of the accordant correction algorithms are presented. They enable the high accuracy of the luminosity that is extracted with the fit software. Altogether the luminosity is determined with an accuracy of about 0.5 % for beam momenta up to 5 GeV/c and 0.1 % for the above higher momentum regime.

Besides the luminosity, the developed fit software is able to extract further information regarding the IP and accelerator beam. The mean shift of the IP in the x and y direction is determined with an accuracy of 50 μm . Furthermore the tilt of the anti-proton beam is obtained from the fit with a high accuracy of about 5 μrad for the lower beam momenta up to 5 GeV/c. Going towards higher beam momenta of 15 GeV/c the bias of

the determined tilts is largest with about $30 \mu\text{rad}$. The extracted divergence information is only reliable in the case of divergences above $200 \mu\text{rad}$ in the low beam momentum regime. There, an accuracy of $20 \mu\text{rad}$ is achieved. However the accuracy of the determined divergence values decreases, when the relative magnitude of the divergence in the x and y direction is larger than 50%. Then the accuracy of the divergence can be as low as $200 \mu\text{rad}$. The additional information on the IP and the accelerator beam, that the LuminosityFit software is able to provide, is useful for data analysis and for feedback during the runtime to adjust the reaction rate.

The reason of the splitting into the lower and higher beam momenta for the beam tilt and divergence, is due to the flattening of the elastic cross section in the LMD range at higher momenta. Consequently this insensitivity makes the correction for these effects negligible. In this case especially the divergence correction can be omitted. Alternatively a fixed parameterization from an external measurement can be used.

Overall the systematic deviation of the luminosity is dominated by the large uncertainties of several percent from the hadronic part of the elastic cross section. The KOALA experiment will provide a more precise elastic cross section description to reduce this uncertainty. With the developed LuminosityFit software package, the influence of the luminosity on the relative uncertainty of line shape and absolute cross section measurements is below 0.5%. This uncertainty includes all effects of the accelerator and target beam, as well as the detector efficiency and resolution, which were presented in this thesis. For the measurement of the line shape only the relative luminosity is needed, which can cancel the influence from uncertainties of the background and the hadronic elastic scattering parameterization. Therefore with data sizes in the order of 10^5 events or below, the limiting factor for the accuracy is not the luminosity, but the counting rate.

The second part of the thesis was the implementation of the helicity formalism in the ComPWA framework and was presented in detail. A novel expert system was implemented, which is used for the creation of decay trees. They contain the information required to construct the corresponding helicity intensity. A second module defines a hierarchy of amplitudes of the helicity formalism, that are combined to form the helicity intensity. The implementation was successfully verified in several steps, using the reaction $J/\psi \rightarrow \gamma\pi^0\pi^0$ suitable for the study of the 0^{++} isoscalars.

It was shown that the rule based expert system is intuitive and ideally suited for this task. The expert system is able to correctly calculate the occurring intermediate states of the $J/\psi \rightarrow \gamma\pi^0\pi^0$ decay. Here also details on the conserved quantum numbers are stated by the system. A high level of transparency was achieved for the implemented ComPWA modules with the clear separation of the laws of physics and the evaluation of the helicity intensity. This allows easy adjustments and extension of the physics laws for a wide range of analysis. The validity and correctness of the helicity amplitudes were first checked by direct comparisons to the angular distributions of analytical calculations. Input output checks showed that no statistically significant bias of the extracted parameters was apparent. Only an insignificant underestimation of the parameter errors of the MINUIT2 minimizer was identified. The correctness of the implemented physics was confirmed by fits and comparisons to data generated with the PAWIAN software package. Also a first fit attempt on the BESIII data gave promising results. Even though simple dynamical descriptions were used and the estimations of some parameters indicate that not the optimal solution was found, the data is described well. The determined

parameters and ratios are similar to the results of the reference analysis in the radiative basis.

With the implementation of the helicity formalism, a first general and widespread model is made available in CompWA, and a milestone was laid for the future. In connection to further implementations in CompWA the comparability between these various physics descriptions is possible.

The high accuracy of the determined luminosity, made possible by the LuminosityFit software, allows for the precise measurement of line shapes at the PANDA experiment. With the implementation of the helicity formalism in CompWA, a foundation for the comparability of different physics models is established. From this, one expects to be able to learn more about the dynamics of the hadronic bound states.

APPENDIX - GENERAL

A.1 THE LIKELIHOOD ESTIMATORS

A.1.1 Binominal, Poisson and Normal Distribution Relationship

For a random variable X that follows the binomial statistics, the discrete probability distribution is defined as

$$P(X = x) = \binom{n}{x} p^x (1-p)^{n-x} \quad (46)$$

with

$$\binom{n}{x} = \frac{n!}{x!(n-x)!}$$

with $n \in \mathbb{N}$ the number of trails and $p \in [0, 1]$ the probability for a positive outcome. The mean and variance can be calculated as

$$E[X] = \mu = np$$

$$\text{Var}[X] = np(1-p).$$

This probability distribution is important, as usually measurements can be formulated within this true false categorization. For example take a histogram and select an arbitrary bin ranging from x_l to x_h . The probability for the outcome of a measurement ending up in this random variable range can be associated with p , and with n tries in total, we expect np entries within this bin.

Often one faces the problem that n , and especially p , are unknown, however the mean np is known. Furthermore for large n the computation of the exponential and factorials can become problematic to calculate. In such case the poisson distribution

$$P(X = x) = \lambda^x \frac{e^{-\lambda}}{x!} \quad (47)$$

is a convenient, with the mean and variance $E[X] = \text{Var}[X] = \lambda$. For large n and small p with the condition $\lambda = np$ the binominal distribution 46 becomes equivalent to the poisson distribution, with goodness of the approximation improving as $n \rightarrow \infty$ and $p \rightarrow 0$.

Going further, when the mean $\lambda = np$ is large, so in the histogram example the bin content is large, the poisson distribution turns into the normal distribution

$$P(X = x) = \frac{1}{\sqrt{2\pi}\sigma} e^{-\frac{(x-\mu)^2}{2\sigma^2}} \quad (48)$$

with mean $E[X] = \mu$ and variance $\text{Var}[X] = \sigma^2$. In contrast to the binominal and poisson distributions this is a continuous probability distribution. The transition condition of a large mean is crucial, as this requires the bin content of histograms to be in the order of several hundred events or above. As a consequence of this, the luminosity fit is based on an extended binned log likelihood (see equation 69), which assumes a poisson distributed random variable, giving better results than for example a χ^2 estimator, which assumes normal distributed errors.

A.1.2 Unbinned Loglikelihood

$$p(\vec{x}, \vec{\alpha}) = \frac{f(\vec{x}, \vec{\alpha})}{\int_{x_{\min}}^{x_{\max}} f(\vec{x}', \vec{\alpha}) d\vec{x}'} \quad (49)$$

For observing statistically independent events a probability density function (p.d.f) $p(\vec{x}, \vec{\alpha})$ describes the probability for an outcome \vec{x} in the observable space X , while $\vec{\alpha}$ is the set of parameters of the p.d.f.. A probability density function underlies the condition that the sum of probabilities over all individual outcomes is unity.

$$\int p(\vec{x}, \vec{\alpha}) d\vec{x} = 1 \quad (50)$$

Then the Likelihood is built up as the product of individual probabilities for each made observation \vec{x}_i with a total number of observations of N_{obs} .

$$\mathcal{L}(\vec{\alpha}) = \prod_i^{N_{\text{obs}}} p(\vec{x}_i, \vec{\alpha}) = \prod_i^{N_{\text{obs}}} \frac{f(\vec{x}_i, \vec{\alpha})}{\int_{x_{\min}}^{x_{\max}} f(\vec{x}', \vec{\alpha}) d\vec{x}'} \quad (51)$$

For computational reasons it is advantageous to take the logarithm of the likelihood, which results in the so called loglikelihood. This is possible due to the strictly monotonic behavior of the logarithm.

$$\ln(\mathcal{L}(\vec{\alpha})) = \sum_i^{N_{\text{obs}}} p(\vec{x}_i, \vec{\alpha}) = \sum_i^{N_{\text{obs}}} \ln(f(\vec{x}_i, \vec{\alpha})) - N \cdot \ln \left(\int_{x_{\min}}^{x_{\max}} f(\vec{x}', \vec{\alpha}) d\vec{x}' \right) \quad (52)$$

Defining the expected number of events as

$$\lambda = \int_{x_{\min}}^{x_{\max}} f(\vec{x}', \vec{\alpha}) d\vec{x}' \quad (53)$$

and substituting this into equation (54) one ends up with

$$\ln(\mathcal{L}(\vec{\alpha})) = \sum_i^{N_{\text{obs}}} \ln(f(\vec{x}_i, \vec{\alpha})) - N \cdot \ln \lambda \quad (54)$$

A.1.3 Extended Unbinned Loglikelihood

In case the the probability for an individual measurement is small and the total number of observations large then a poisson statistics factor for the expected number of events λ can be included in 51.

$$\mathcal{L}_{\text{ext}}(\vec{\alpha}) = \frac{\lambda^{N_{\text{obs}}} e^{-\lambda}}{N_{\text{obs}}!} \prod_i^{N_{\text{obs}}} p(\vec{x}_i, \vec{\alpha}) \quad (55)$$

$$= \frac{\lambda^{N_{\text{obs}}} e^{-\lambda}}{N_{\text{obs}}!} \prod_i^{N_{\text{obs}}} \frac{f(\vec{x}_i, \vec{\alpha})}{\int_{x_{\text{min}}}^{x_{\text{max}}} f(\vec{x}', \vec{\alpha}) d\vec{x}'} \quad (56)$$

Again taking the logarithm and use the expected number of events 53

$$\ln(\mathcal{L}_{\text{ext}}(\vec{\alpha})) = N_{\text{obs}} \ln(\lambda) - \lambda - \ln(N_{\text{obs}}!) + \sum_i^{N_{\text{obs}}} \ln(p(\vec{x}_i, \vec{\alpha})) \quad (57)$$

$$= N_{\text{obs}} \ln(\lambda) - \lambda - \ln(N_{\text{obs}}!) + \sum_i^{N_{\text{obs}}} \ln[f(\vec{x}_i, \vec{\alpha})] \quad (58)$$

$$- \sum_i^{N_{\text{obs}}} \ln \left(\int_{x_{\text{min}}}^{x_{\text{max}}} f(\vec{x}', \vec{\alpha}) d\vec{x}' \right) \quad (59)$$

$$= N_{\text{obs}} \ln(\lambda) - \lambda - \ln(N_{\text{obs}}!) + \sum_i^{N_{\text{obs}}} \ln[f(\vec{x}_i, \vec{\alpha})] \quad (60)$$

$$- \sum_i^{N_{\text{obs}}} \ln(\lambda) \quad (61)$$

$$= -\lambda - \ln(N_{\text{obs}}!) + \sum_i^{N_{\text{obs}}} \ln[f(\vec{x}_i, \vec{\alpha})] \quad (62)$$

Dropping the the constant faculty term that is irrelevant for the minimization procedure one ends up with

$$\ln(\mathcal{L}_{\text{ext}}(\vec{\alpha})) = -\lambda + \sum_i^{N_{\text{obs}}} \ln[f(\vec{x}_i, \vec{\alpha})] \quad (63)$$

Note that due to the dropping of this very large negative term, the overall likelihood will be shifted to higher positive values.

A.1.4 Extended Binned Loglikelihood

With increasing number of observed events N_{obs} , the minimization computation costs will eventually reach its limit. In this case binned loglikelihood fits are advantageous. The measurement range is divided into N_b bins. The i_b th bin covers the interval $[x_{i_b}^L - x_{i_b}^H]$

with a bin content of N_{i_b} . The unbinned extended likelihood function 56 then transforms to

$$\mathcal{L}_{\text{ext}}(\vec{\alpha}) = \frac{\lambda^{N_{\text{obs}}} e^{-\lambda}}{N_{\text{obs}}!} \prod_{i_b}^{N_b} \left(\int_{x_{i_b}^L}^{x_{i_b}^H} p(x_{i_b}, \vec{\alpha}) \right)^{N_{i_b}} \quad (64)$$

with $\sum_{i_b}^{N_b} N_{i_b} = N_{\text{obs}}$.

Taking the logarithm once again

$$\ln(\mathcal{L}_{\text{ext}}(\vec{\alpha})) = N_{\text{obs}} \ln(\lambda) - \lambda - \ln(N_{\text{obs}}!) + \sum_{i_b}^{N_b} N_{i_b} \ln \left(\int_{x_{i_b}^L}^{x_{i_b}^H} p(x_{i_b}, \vec{\alpha}) dx_{i_b} \right) \quad (65)$$

Dropping the constant term and making use of 49 and 53

$$\ln(\mathcal{L}_{\text{ext}}(\vec{\alpha})) = N_{\text{obs}} \ln(\lambda) - \lambda + \sum_{i_b}^{N_b} N_{i_b} \ln \left(\frac{\int_{x_{i_b}^L}^{x_{i_b}^H} f(x_{i_b}, \vec{\alpha}) dx_{i_b}}{\int_{x_{\min}}^{x_{\max}} f(\vec{x}', \vec{\alpha}) d\vec{x}'} \right) \quad (66)$$

$$= N_{\text{obs}} \ln(\lambda) - \lambda - \sum_{i_b}^{N_b} N_{i_b} \ln \left(\int_{x_{\min}}^{x_{\max}} f(\vec{x}', \vec{\alpha}) d\vec{x}' \right) \quad (67)$$

$$+ \sum_{i_b}^{N_b} N_{i_b} \ln \left(\int_{x_{i_b}^L}^{x_{i_b}^H} f(x_{i_b}, \vec{\alpha}) dx_{i_b} \right) \quad (68)$$

$$= -\lambda + \sum_{i_b}^{N_b} N_{i_b} \ln \left(\int_{x_{i_b}^L}^{x_{i_b}^H} f(x_{i_b}, \vec{\alpha}) dx_{i_b} \right) \quad (69)$$

From equation 69 it becomes evident that when comparing the function with the bin content, the model has to be integrated over the bin boundaries.

A.2 INTRODUCTION TO EXPERT SYSTEMS

In the branch of artificial intelligence an expert system is a computer system that emulates the decision making ability of a human expert. Its two main components are the knowledge base and the inference engine. The expertise is filled into the knowledge base in form of rules. When a non-expert user request advice from the expert system the inference engine will process available facts with its rules and deliver the result to user. This concept and workflow is visualized in figure 80. The knowledge is condensed in the form rules. Each rule can require a set of facts and when they are satisfied, the body of the rule will be executed. In the execution process facts can be altered, destroyed and created, and depending on the expert system, control parameters for steering the execution such as rule priorities and pausing rules are available. This way complicated knowledge can be modeled efficiently. Since the knowledge exists mainly in form of rules, the level of maintenance work is minimal, as merely new rules have to be added

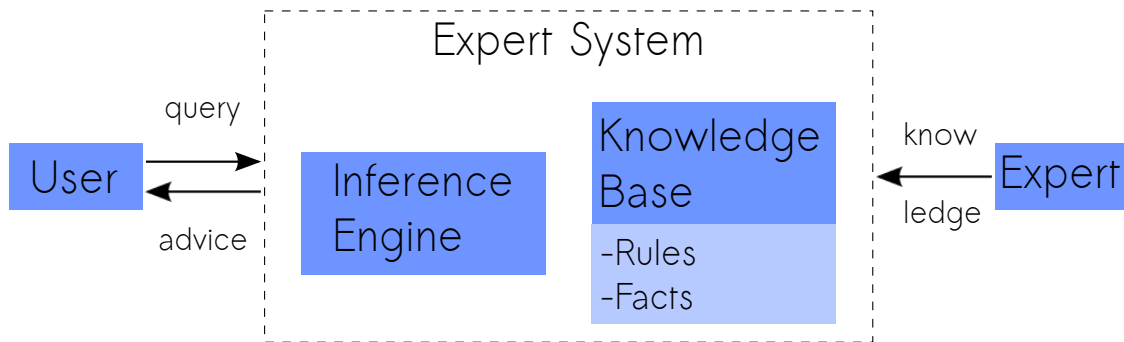


Figure 80: A general design of an expert system.

to the system in order for it to possess the new knowledge. On the downside, expert systems are incapable of adapting to advice request outside of the knowledge base territory. Also the aspect of human common sense is missing in expert systems, which implicates the requirement of more rules in knowledge base. A simple example of an expert system

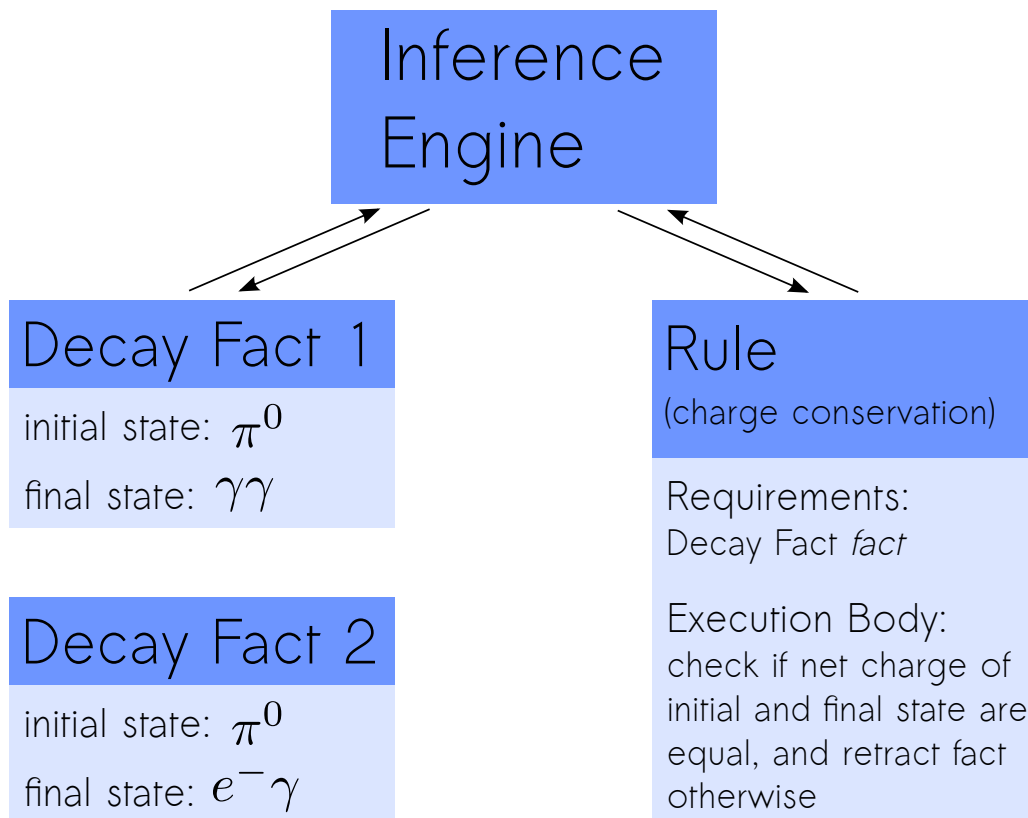


Figure 81: A simple example illustrating the usage of the expert system, which implements charge conservation.

is shown in diagram 81, which illustrates the power of expert systems. It implements charge conservation for reactions. The decay fact, which consists of an initial and a finale state of particles, contains the information about the reaction. The charge conservation rule requires a decay fact for its execution. Within its body the net charge for the initial and final state will be calculated and compared. If they are not equal this decay fact will be retracted/removed. In this way the only reactions that conserve charge remain.

APPENDIX - LMD RELATED

B.1 ACCELERATOR BEAM DYNAMICS

The trajectory of a single particle at each position of the accelerator ring s is described by the two orthogonal spacial dimensions $x(s), y(s)$ with respect to the ideal particle trajectory [123]. Few more words about magnets focusing and defocusing (FODO) These can be calculated by solving the appropriate Hamilton equations of motion for the accelerator.

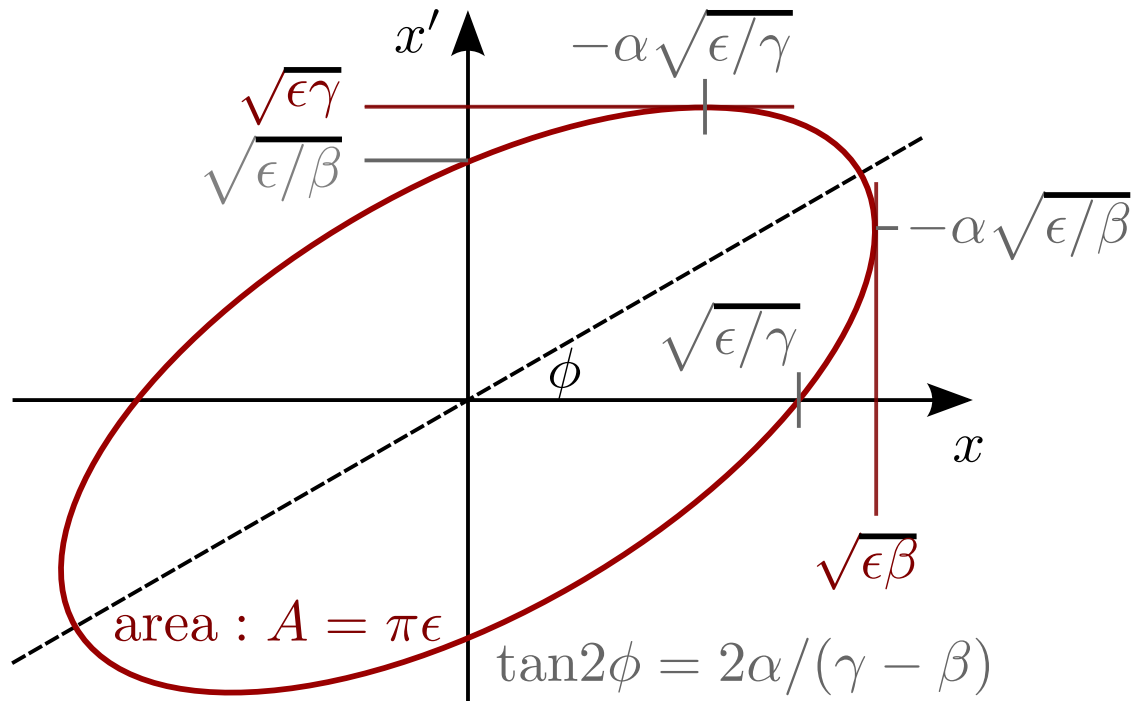


Figure 82: Single particle phase space ellipse

A phase space diagram as illustrated in figure 82 is representing the particle position offset from an ideal closed orbit x and the corresponding gradient offset x' from its reference direction at a position s in a storage ring. Although the shape of the ellipse constantly changes as a function of the position s , due to the focusing magnets, its area stays constant as predicted by Liouville's theorem. This area of the ellipse is also known as the beam emittance, and is one of the accelerator performance parameters. It should be noted that the area of the ellipse is decreased by beam cooling and increased by particle interactions.

The following equations define the maximum displacement and gradient of particle tracks at a position s .

$$x_{\max} = \sqrt{\epsilon\beta(s)} \quad (70)$$

$$x'_{max} = \sqrt{\epsilon\gamma(s)} \quad (71)$$

These values can be computed with the knowledge of the emittance $\epsilon_{x,y}$ and the $\beta_{x,y}(s)$ and $\gamma_{x,y}(s)$ functions, often referred to as the Twiss functions. Those functions are provided by accelerator experts, who solve the equations of motion for each lattice setting individually. Note that the maximum track displacement equals the beam spot size, while the maximum gradient offset is better known as the beam divergence.

For small rotations of the ellipse the beam divergence can be expressed as

$$x'_{max} = \sqrt{\frac{\epsilon}{\beta(s)}} \quad (72)$$

The values for the beam divergence can now be approximated by first calculating the betatron amplitude or beta function value with equation 70 and then approximating the divergence with equation 72.

B.2 FROM MOMENTUM TRANSFER t TO LABORATORY FRAME θ

The theoretical calculations of the cross section for elastic antiproton proton scattering is expressed as usual in the lorentz invariant four momentum transfer t . In order to compare the model with the measured data, which is the scattering angle in the laboratory frame, a transformation is required.

As the momentum transfer t is a lorentz invariant, it can be directly calculated from kinematical variables in the lab frame. However rewriting the formula to contain only known quantities of the experiment, the complexity increases dramatically.

Alternatively one can make use of the simple relationship of the scattering angle and the 4-momentum transfer t in the center-of-mass (cms) frame. The kinematics of the elastic scattering process in the cms frame are shown in Figure 83. The cms frame is defined by the requirement of the total momentum to equal zero. This defines the initial 4-momenta¹ of the two scattering partners as

$$p_{cms}^{\bar{p}} = \begin{pmatrix} E_{cms} \\ \vec{p}_{cms} \end{pmatrix}, \quad p_{cms}^p = \begin{pmatrix} E_{cms} \\ -\vec{p}_{cms} \end{pmatrix} \quad (73)$$

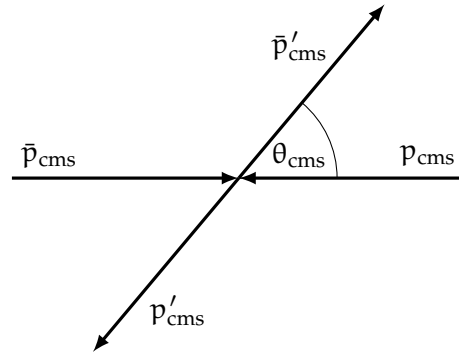


Figure 83: A kinematic drawing elastic $\bar{p}p$ scattering in the cms frame.

¹ Note that in this definition the first dimension is energy/time and the latter three the momentum/space dimensions. In this compact notation the three momentum/space dimensions are grouped into a single vector element and the dimension variable of the 4-vector was dropped for simplicity.

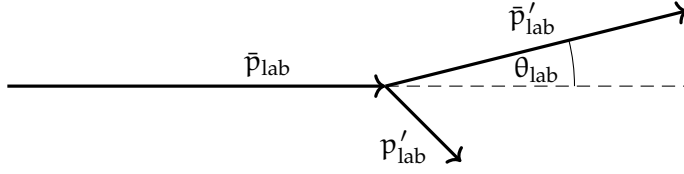


Figure 84: A kinematic drawing of the lab frame

and the final 4-momenta as

$$p_{\text{cms}}^{\prime\bar{p}} = \begin{pmatrix} E_{\text{cms}} \\ \vec{p}'_{\text{cms}} \end{pmatrix}, \quad p_{\text{cms}}^{\prime p} = \begin{pmatrix} E_{\text{cms}} \\ -\vec{p}'_{\text{cms}} \end{pmatrix}. \quad (74)$$

Using 73 and 74 and the condition of elastic scattering ($p_{\text{cms}} = |\vec{p}'_{\text{cms}}| = |\vec{p}_{\text{cms}}|$) the four momentum transfer in the cms frame is now given by

$$t = (p_{\text{cms}}^{\prime\bar{p}} - p_{\text{cms}}^{\bar{p}})^2 = p_{\text{cms}}^{\prime\bar{p}2} + p_{\text{cms}}^{\bar{p}2} - 2p_{\text{cms}}^{\prime\bar{p}} p_{\text{cms}}^{\bar{p}} \quad (75)$$

$$= 2m_p^2 - 2(E_{\text{cms}}^2 - \vec{p}'_{\text{cms}} \cdot \vec{p}_{\text{cms}}) \quad (76)$$

$$= -2p_{\text{cms}}^2 + 2p_{\text{cms}}^2 \cdot \cos \theta_{\text{cms}} \quad (77)$$

$$= -2p_{\text{cms}}^2 (1 - \cos \theta_{\text{cms}}). \quad (78)$$

Next p_{cms} and θ_{cms} have to be expressed in terms of laboratory frame variables. A kinematic drawing of the scattering process is shown in Figure 84

In a fixed target experiment the initial 4-vectors are simply defined as

$$p_{\text{lab}}^{\bar{p}} = \begin{pmatrix} E_{\text{lab}} \\ \vec{p}_{\text{lab}} \end{pmatrix}, \quad p_{\text{lab}}^p = \begin{pmatrix} m_p \\ 0 \end{pmatrix} \quad (79)$$

The absolute momentum in the cms frame p_{cms} can easily be described by the center of mass energy s , which is lorentz invariant.

$$s = (p_{\text{cms}}^{\bar{p}} + p_{\text{cms}}^p)^2 = \begin{pmatrix} 2E_{\text{cms}} \\ 0 \end{pmatrix}^2 = 4(m_p + p_{\text{cms}})^2 \quad (80)$$

Using 79 the center of mass energy in the laboratory system can be written as

$$s = (p_{\text{lab}}^{\bar{p}} + p_{\text{lab}}^p)^2 = 2m_p^2 + 2E_{\text{lab}} m_p. \quad (81)$$

When equating 80 and 81 and solving for p_{cms}^2 one obtains the following relation.

$$4(m_p + p_{\text{cms}})^2 = 2m_p^2 + 2E_{\text{lab}} m_p \quad (82)$$

$$p_{\text{cms}}^2 = 2m_p(E_{\text{lab}} - m_p) \quad (83)$$

Finally the scattering angle in the cms frame θ_{cms} has to be expressed as a function of the lab frame scattering angle θ_{lab} . For this we define the scattering plane to be spanned by the z- and x-axis, while the incoming beam particles travel along the z-axis. Hence the initial four vectors in the lab frame (see 79) can be rewritten as

$$p_{\text{lab}}^{\bar{p}} = \begin{pmatrix} E_{\text{lab}} \\ 0 \\ 0 \\ p_{\text{lab}} \end{pmatrix}, \quad p_{\text{lab}}^p = \begin{pmatrix} m_p \\ 0 \\ 0 \\ 0 \end{pmatrix} \quad (84)$$

Next the velocity (or $\beta = \frac{v}{c}$) of the lorentz transformation along the z-axis, that boosts from the lab to the cms-frame, has to be determined. To obtain the four momenta in the cms frame this lorentz boost simply has to be applied to both the beam and target four vectors in the lab frame.

$$p_{\text{cms}}^{\bar{p}} = \begin{bmatrix} \gamma & 0 & 0 & -\beta\gamma \\ 0 & 1 & 0 & 0 \\ 0 & 0 & 1 & 0 \\ -\beta\gamma & 0 & 0 & \gamma \end{bmatrix} \begin{pmatrix} E_{\text{lab}} \\ 0 \\ 0 \\ p_{\text{lab}} \end{pmatrix} = \begin{pmatrix} \gamma(E_{\text{lab}} - \beta p_{\text{lab}}) \\ 0 \\ 0 \\ \gamma(p_{\text{lab}} - \beta E_{\text{lab}}) \end{pmatrix}, \quad (85)$$

$$p_{\text{cms}}^p = \begin{bmatrix} \gamma & 0 & 0 & -\beta\gamma \\ 0 & 1 & 0 & 0 \\ 0 & 0 & 1 & 0 \\ -\beta\gamma & 0 & 0 & \gamma \end{bmatrix} \begin{pmatrix} m_p \\ 0 \\ 0 \\ 0 \end{pmatrix} = \begin{pmatrix} \gamma m_p \\ 0 \\ 0 \\ -\beta\gamma m_p \end{pmatrix}$$

From the requirement of the net momentum to be zero, the sum of the z-components of the momenta of the two particles have to be zero.

$$\gamma(p_{\text{lab}} - \beta E_{\text{lab}}) = \beta\gamma m_p \quad (86)$$

$$\beta = \frac{p_{\text{lab}}}{E_{\text{lab}} + m_p} \quad (87)$$

To obtain the relation between the cms and the lab scattering angle, the 4 momenta of the scattered antiproton from the cms definition has to be compared to the lab definition applied with the boost.

$$p_{\text{cms}}^{\bar{p}} = \begin{bmatrix} \gamma & 0 & 0 & -\beta\gamma \\ 0 & 1 & 0 & 0 \\ 0 & 0 & 1 & 0 \\ -\beta\gamma & 0 & 0 & \gamma \end{bmatrix} \begin{pmatrix} E'_{\text{lab}} \\ p'_{\text{lab}} \sin\theta_{\text{lab}} \\ 0 \\ p'_{\text{lab}} \cos\theta_{\text{lab}} \end{pmatrix} \quad (88)$$

$$= \begin{pmatrix} \gamma(E'_{\text{lab}} - \beta p'_{\text{lab}} \cos\theta_{\text{lab}}) \\ p'_{\text{lab}} \sin\theta_{\text{lab}} \\ 0 \\ \gamma(p'_{\text{lab}} \cos\theta_{\text{lab}} - \beta E'_{\text{lab}}) \end{pmatrix} \quad (89)$$

comparing this to the cms frame scattered antiproton definition

$$\vec{p}'_{\text{cms}} = \begin{pmatrix} E'_{\text{cms}} \\ p'_{\text{cms}} \sin \theta_{\text{cms}} \\ 0 \\ p'_{\text{cms}} \cos \theta_{\text{cms}} \end{pmatrix} \quad (90)$$

$$p'_{\text{cms}} \sin \theta_{\text{cms}} = p'_{\text{lab}} \sin \theta_{\text{lab}} \quad (91)$$

$$p'_{\text{cms}} \cos \theta_{\text{cms}} = \gamma(p'_{\text{lab}} \cos \theta_{\text{lab}} - \beta E'_{\text{lab}}) \quad (92)$$

$$\tan \theta_{\text{cms}} = \frac{p'_{\text{lab}} \sin \theta_{\text{lab}}}{\gamma(p'_{\text{lab}} \cos \theta_{\text{lab}} - \beta E'_{\text{lab}})} \quad (93)$$

$$= \frac{\sin \theta_{\text{lab}}}{\gamma(\cos \theta_{\text{lab}} - \beta \frac{E'_{\text{lab}}}{p'_{\text{lab}}})} \quad (94)$$

So far no approximation was made, everything is perfectly exact! However the scattered antiproton momentum/energy is unknown in the above formula. It differs from the momentum/energy of the incoming beam particle by the recoil energy of the target proton. For the small scattering angles the recoil energy is negligible and one can insert the incoming beam parameters. By inserting equation 94 into 75, one finally ends up with the complete formula that takes the scattering angle of the laboratory frame θ_{lab} ² to the 4-momentum transfer t .

$$t = -2p_{\text{cms}}^2 \left(1 - \cos \left(\text{atan} \left(\frac{\sin \theta_{\text{lab}}}{\gamma(\cos \theta_{\text{lab}} - \beta \frac{E'_{\text{lab}}}{p'_{\text{lab}}})} \right) \right) \right) \quad (95)$$

To improve the computational performance³, this equation is rewritten using the following trigonometrical relation.

$$\cos(\theta_{\text{cms}}) = \frac{1}{\sqrt{1 + \tan^2(\theta_{\text{cms}})}} \quad (96)$$

Then equation 95 becomes

$$t = -2p_{\text{cms}}^2 \left(1 - \frac{1}{\sqrt{1 + \left(\frac{\sin \theta_{\text{lab}}}{\gamma(\cos \theta_{\text{lab}} - \beta \frac{E'_{\text{lab}}}{p'_{\text{lab}}})} \right)^2}} \right). \quad (97)$$

The correct 4 momentum values can be determined by solving the problem numerically. We define the difference function of the specified θ_{lab} and the lab angle calculated from a boost from a defined θ_{cms} angle in the cms coordinate system into the laboratory

² When elastically scattering two particles of equal mass, the maximal scattering angle in the fixed target frame (lab frame) is $\pi/2$.

³ Roughly a speed gain of 20% per evaluation is achieved with this transformation. Of course this result depends on the compiler and machine.

system. Using Newton's root finding method the correct θ_{cms} can be found and inserted into equation 75. Finally the validity of the approximation can be determined by checking the relative difference between the approximation and the correct transformation, which is shown in figure 85.

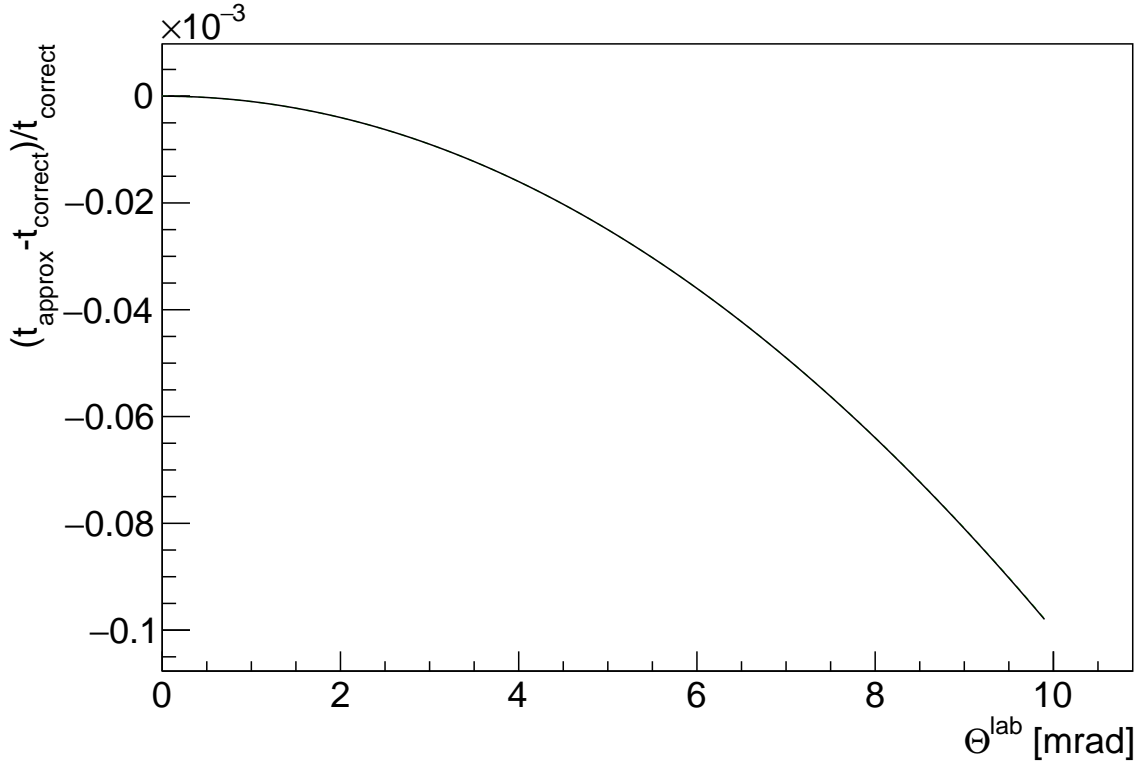


Figure 85: Relative Difference approximate and correct t versus θ_{lab}

It should be clear to the reader that this is very computation intensive, for which reason this approximation is mandatory in the first place, as this transformation function is evaluated numerous times during the fit.

B.3 PROTON RECOIL ENERGY

In elastic scattering the kinetic energy of the recoil proton can easily be calculated using the 4-vectors of the frame in which the particle is initially at rest. In a fixed target experiment this coincides with the laboratory frame. So defining the initial and final target proton 4-vectors as

$$p_{p,\text{lab}} = \begin{pmatrix} m_p \\ 0 \end{pmatrix}, \quad p'_{p,\text{lab}} = \begin{pmatrix} E'_{p,\text{lab}} \\ \vec{p}'_{p,\text{lab}} \end{pmatrix} \quad (98)$$

the 4-momentum transfer can be calculated to

$$t = (p'_{p,\text{lab}} - p_{p,\text{lab}})^2 \quad (99)$$

$$= p'^2_{p,\text{lab}} + p^2_{p,\text{lab}} - 2p'_{p,\text{lab}}p_{p,\text{lab}} \quad (100)$$

$$= 2m_p^2 - 2E'_{p,\text{lab}}m_p. \quad (101)$$

Using equation 101 and defining the recoil energy as the kinetic part of the final state recoil proton one obtains

$$E_r = E'_{p,\text{lab}} - m_p = -\frac{t}{2m_p} \quad (102)$$

Note that the value of the 4-momentum transfer is defined as a negative number so the recoil energy is always positive.

B.4 CONVOLUTION VS. RESOLUTION SMEARING ALGORITHM

In reality the number of scattered anti-protons inside an angular element $\Delta\theta$ at an angle θ_{rec} is measured. This is described by equation 103.

$$\frac{dN(\theta_{\text{rec}})}{d\theta_{\text{rec}}} = L \cdot \int d\theta_{\text{mc}} \frac{d\sigma(\theta_{\text{mc}})}{d\theta_{\text{mc}}} \cdot \epsilon(\theta_{\text{mc}}) \cdot \frac{d\text{Res}(\theta_{\text{rec}} - \theta_{\text{mc}}, \theta_{\text{mc}})}{d\theta_{\text{rec}}} \quad (103)$$

Here $\frac{d\sigma(\theta_{\text{mc}})}{d\theta_{\text{mc}}}$ is the probability that the antiproton was scattered into a infinitesimal θ ring element $\Delta\theta_{\text{mc}}$ at a certain θ_{mc} value. Propagating this particle through the magnetic fields and/or material, eventually the particle may leave behind signals in the detectors. $\epsilon(\theta_{\text{mc}})$ describes the probability, that the particle within the angular element $\Delta\theta_{\text{mc}}$ at a specific value of θ_{mc} is actually reconstructed. Finally due to the detector resolution and scattering effects in material, the reconstructed angle θ_{rec} deviates from the true angle θ_{mc} . The probability for a particle within the angular element $\Delta\theta_{\text{mc}}$ at θ_{mc} to be reconstructed at an angle θ_{rec} within $\Delta\theta_{\text{rec}}$ is given by $\frac{d\text{Res}(\theta_{\text{rec}} - \theta_{\text{mc}}, \theta_{\text{mc}})}{d\theta_{\text{rec}}}$. To obtain the probability of measuring scattered antiprotons inside an angular element $\Delta\theta$ at an angle θ_{rec} , an integral over all initial scattering angles has to be performed. To obtain the number of particles scattered into this angular element within a unit of time, the overall probability has to be scaled with the time-integrated luminosity. Putting everything together one ends up with equation 103.

For the special case that $\frac{d\text{Res}(\theta_{\text{rec}} - \theta_{\text{mc}}, \theta_{\text{mc}})}{d\theta_{\text{rec}}}$ only depends on the difference $\theta_{\text{rec}} - \theta_{\text{mc}}$, equation 103 can be simplified to 104.

$$\frac{dN(\theta_{\text{rec}})}{d\theta_{\text{rec}}} = L \cdot \int d\theta_{\text{mc}} \frac{d\sigma(\theta_{\text{mc}})}{d\theta_{\text{mc}}} \cdot \epsilon(\theta_{\text{mc}}) \cdot \frac{d\text{Res}(\theta_{\text{rec}} - \theta_{\text{mc}})}{d\theta_{\text{rec}}} \quad (104a)$$

$$= L \cdot [(\sigma \cdot \epsilon) * \text{Res}](\theta_{\text{rec}}) \quad (104b)$$

In this case the integral over θ_{mc} turned into the convolution expressed by the operator $*$. Figure 86 visualizes the equality in this special case. Here the red curve is the probability density function $\frac{d\sigma(\theta_{\text{mc}})}{d\theta_{\text{mc}}} \cdot \epsilon(\theta_{\text{mc}})$ of particles scattered at an angles θ_{mc}

and leave behind information to be reconstructed by the detector. The black and black dashed curves are normal distributions with equal widths, which resemble the resolution of the detector $\frac{dRes(\theta_{rec}-\theta_{mc})}{d\theta_{rec}}$. Note that the width of the normal distributions was set to this arbitrary large value to clarify the mathematical concept. The overall probability of measuring a particle in the neighborhood of $\theta_{rec} = 2.5\text{mrad}$, that originated from the vicinity of $\theta_{mc} = 4.0\text{mrad}$, is calculated by the product of the values of the red and black-dashed functions at these positions. On the other hand the solid black curve shows the same normal function shifted to the position of 2.5mrad . Evaluating this function at 4.0mrad , one can see that the probability is equal to the dashed black curve at 2.5mrad . Integrating over all possible θ_{mc} , the overall probability is obtained. The integral of the product of the solid black and red curve is the convolution of these functions evaluated at the position 2.5mrad .

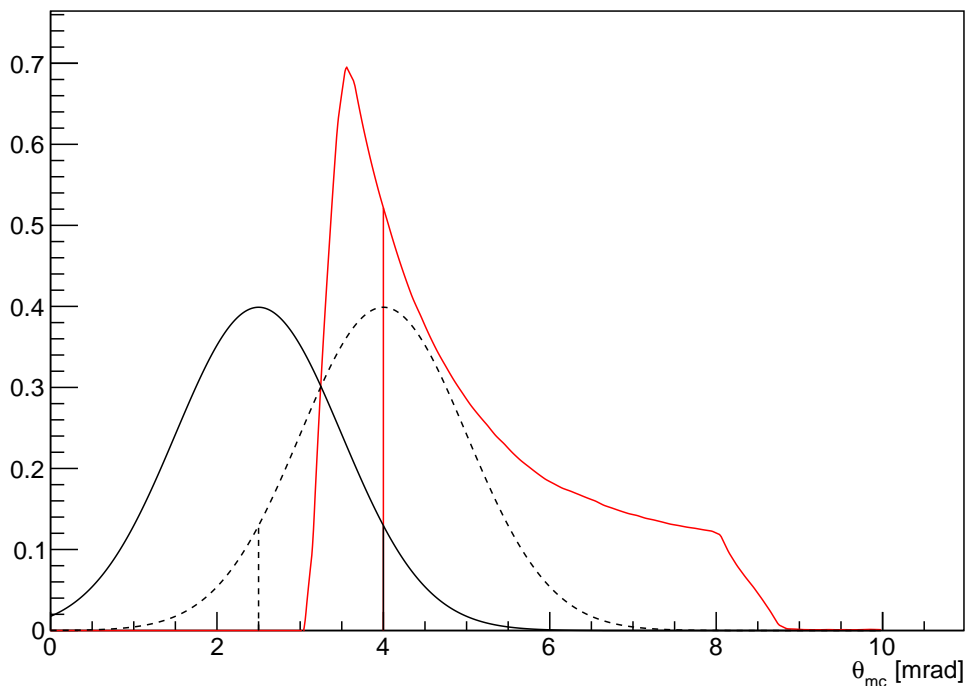


Figure 86: Special case of the detector resolution in which the equality to a convolution operation is obtained. The red curve shows the probability density function before accounting for smearing. The gaussian functions indicate an exemplary special case for the resolution.

APPENDIX - PWA RELATED

C.1 DALITZ PLOT KINEMATICS

In general the N particle phase space is fully specified by $3N - 4$ variables [91, p. 139f]. Each particle has three momentum components and an energy that specifies its kinematics. However through the energy-momentum relation $E^2 = (\mathbf{p} \cdot \mathbf{c})^2 + (m \cdot c^2)^2$ the mass of the particle defines its energy by the momentum and only three independent variables remain. From momentum and energy conservation another four variables can be eliminated and $3N - 4$ particles remain.

In the special case of a scalar initial state, or when averaging over all initial spin states, the orientation of the initial state with respect to the final state particles is arbitrary. In consequence the degrees of freedom for a three particle final state can be reduced further to two independent variables [9, p. 56of]. Typically two Lorentz-invariant masses are chosen, e. g. $m_{12}^2 = (\mathbf{p}_1 + \mathbf{p}_2)^2/c^4$ and $m_{23}^2 = (\mathbf{p}_2 + \mathbf{p}_3)^2/c^4$. The visualization of those variables is more commonly known as the Dalitz plot, with an example shown in figure 87. What makes the Dalitz plot powerful, is its ability to conclude on the existence of

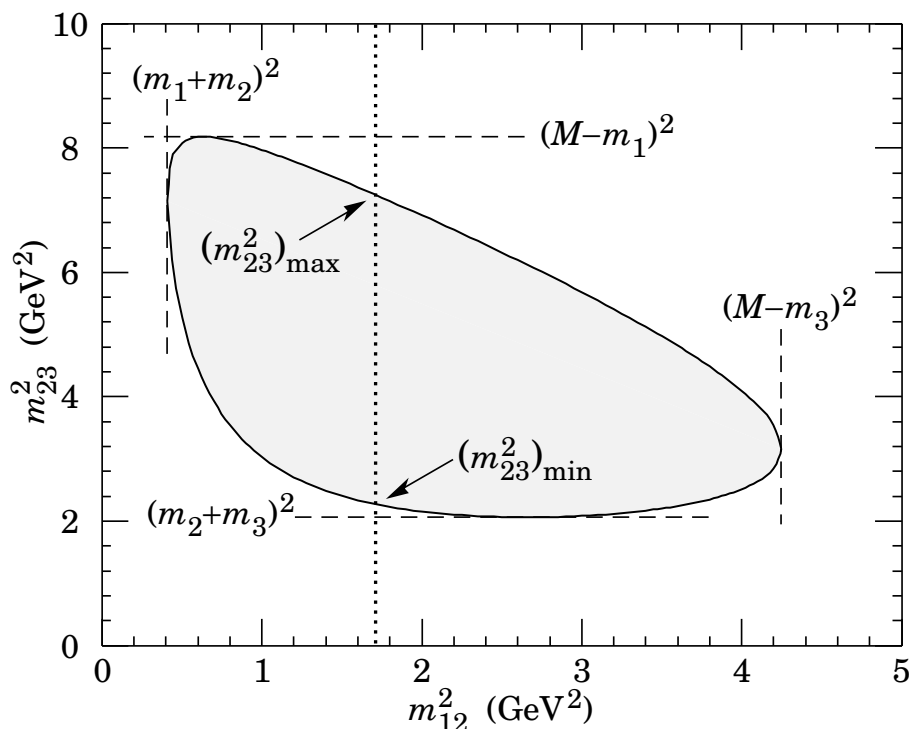


Figure 87: An example of a Dalitz plot for the decay of a particle with mass M into three particles with masses m_1, m_2, m_3 . The kinematics limits restrict the shape of the Dalitz plot. Here natural units with $c = 1$ were chosen [9].

any intermediate states and their spin properties. Here a intermediate state will appear

as a band in a invariant mass combination and the modulation along the band is characteristic for its spin. In section C.2 examples for $\cos(\theta)$ distributions are shown, which resemble the angular distributions of the daughters dependent on the spin properties of the decaying particle. These $\cos(\theta)$ distributions are visible in the bands of the Dalitz plot as indicated by figure 88.

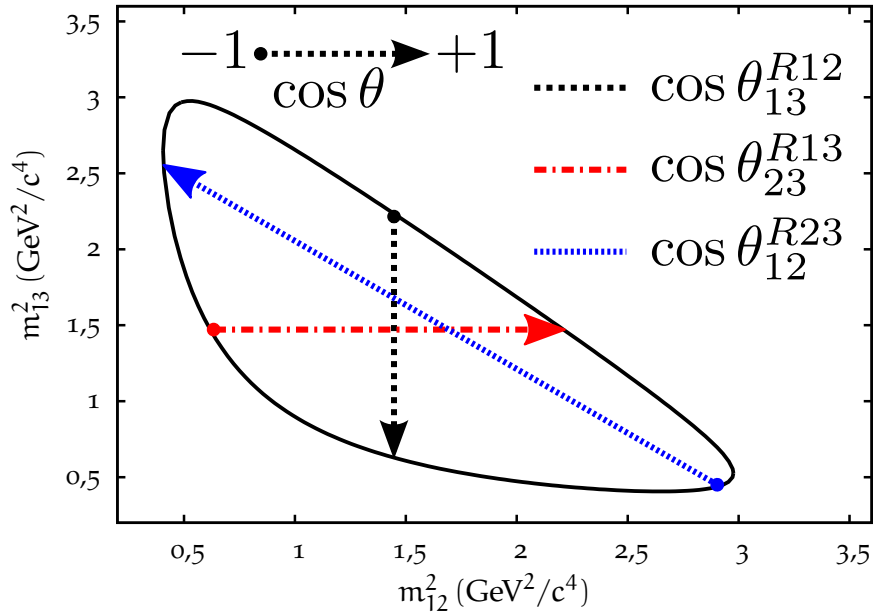


Figure 88: The helicity angle distributions within the Dalitz plot [124]. The extreme values of $\cos(\theta)$ are taken at the boundaries of the Dalitz plot.

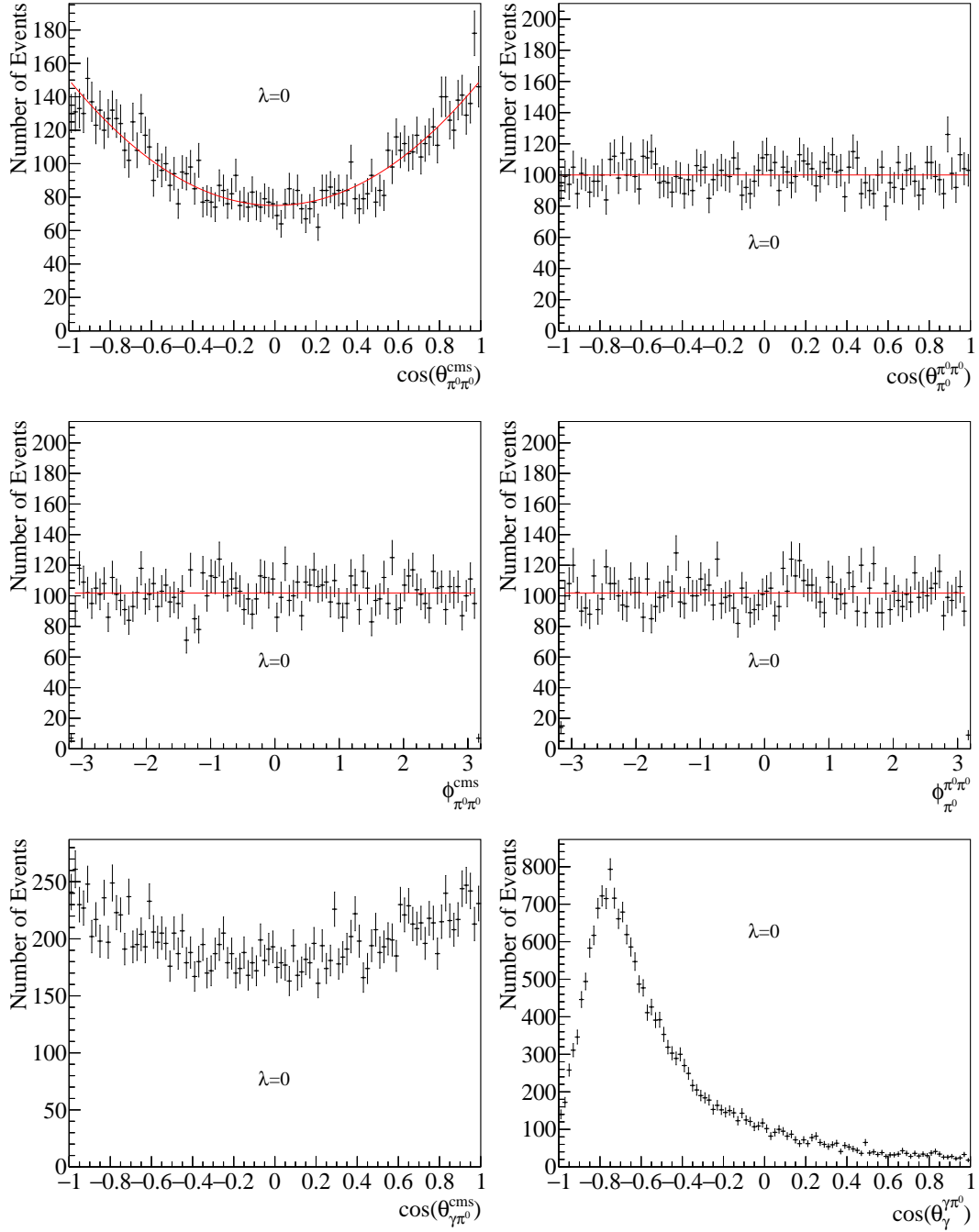
C.2 SINGLE CHANNEL $\gamma\pi^0\pi^0$ KINEMATIC DISTRIBUTIONS

Figure 89: Angular distributions of the $J/\psi \rightarrow \gamma\pi^0\pi^0$ decay in the $f_0(\lambda=0)$ channel generated by the CompWA framework using the HelicityAmplitude module. The left column shows distributions in the CMS and the right column for the two particle subsystems. The analytic solution is indicated by the red curve.

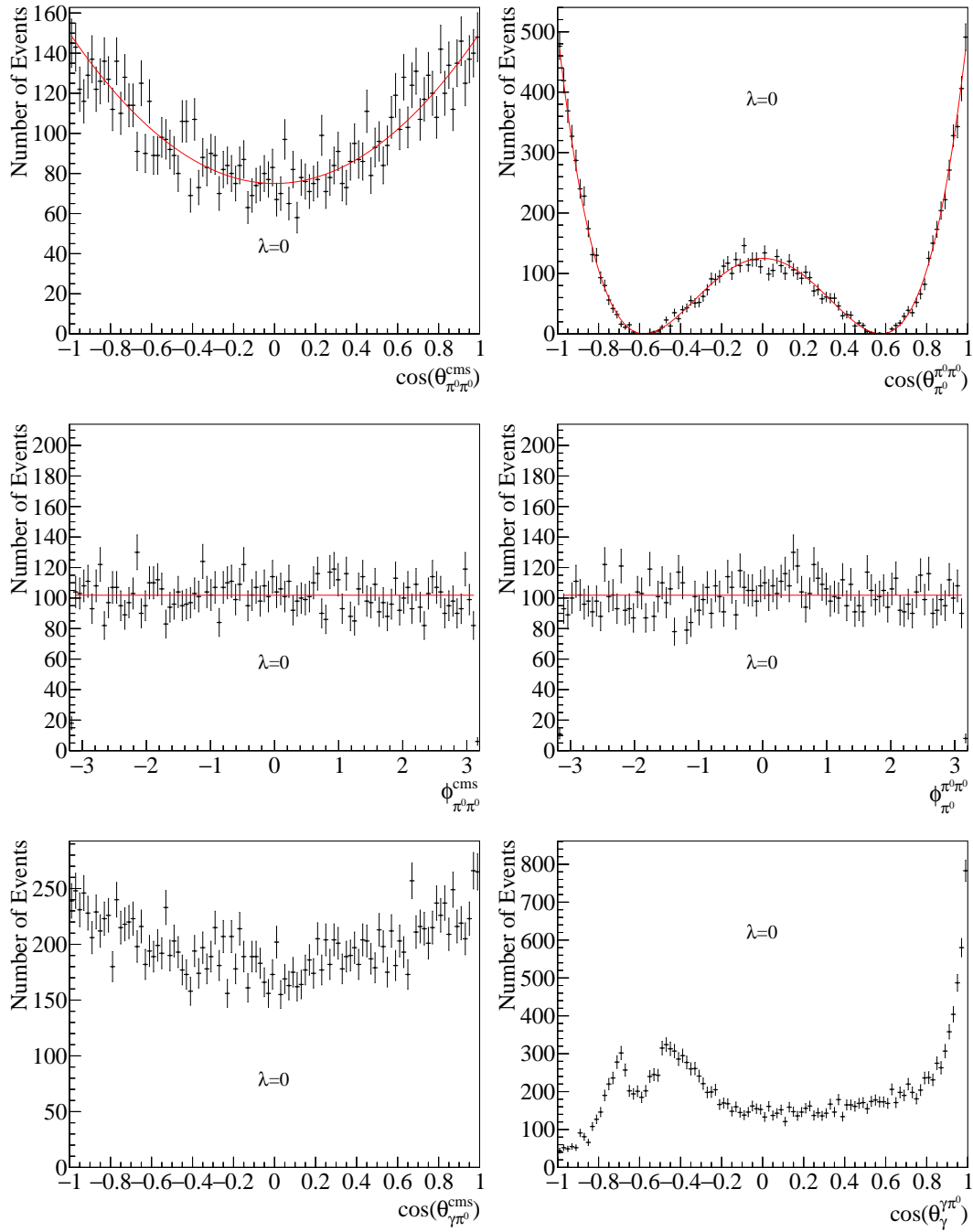


Figure 90: Angular distributions of the $J/\psi \rightarrow \gamma\pi^0\pi^0$ decay in the $f_2(\lambda=0)$ channel generated by the ComPWA framework using the HelicityAmplitude module. The left column shows distributions in the CMS and the right column for the two particle subsystems. The analytic solution is indicated by the red curve.

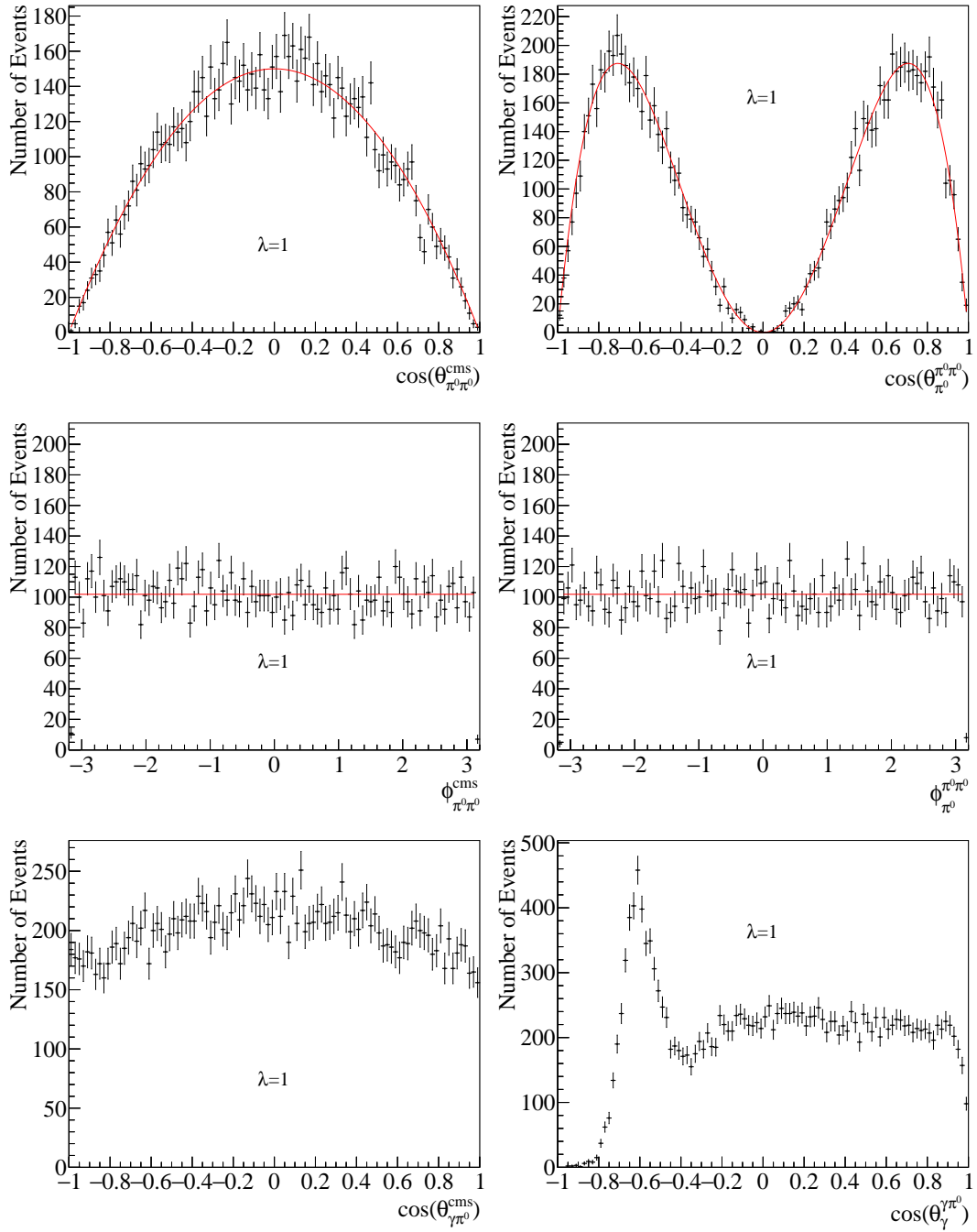


Figure 91: Angular distributions of the $J/\psi \rightarrow \gamma\pi^0\pi^0$ decay in the $f_2(|\lambda|=1)$ channel generated by the ComPWA framework using the HelicityAmplitude module. The left column shows distributions in the CMS and the right column for the two particle subsystems. The analytic solution is indicated by the red curve.

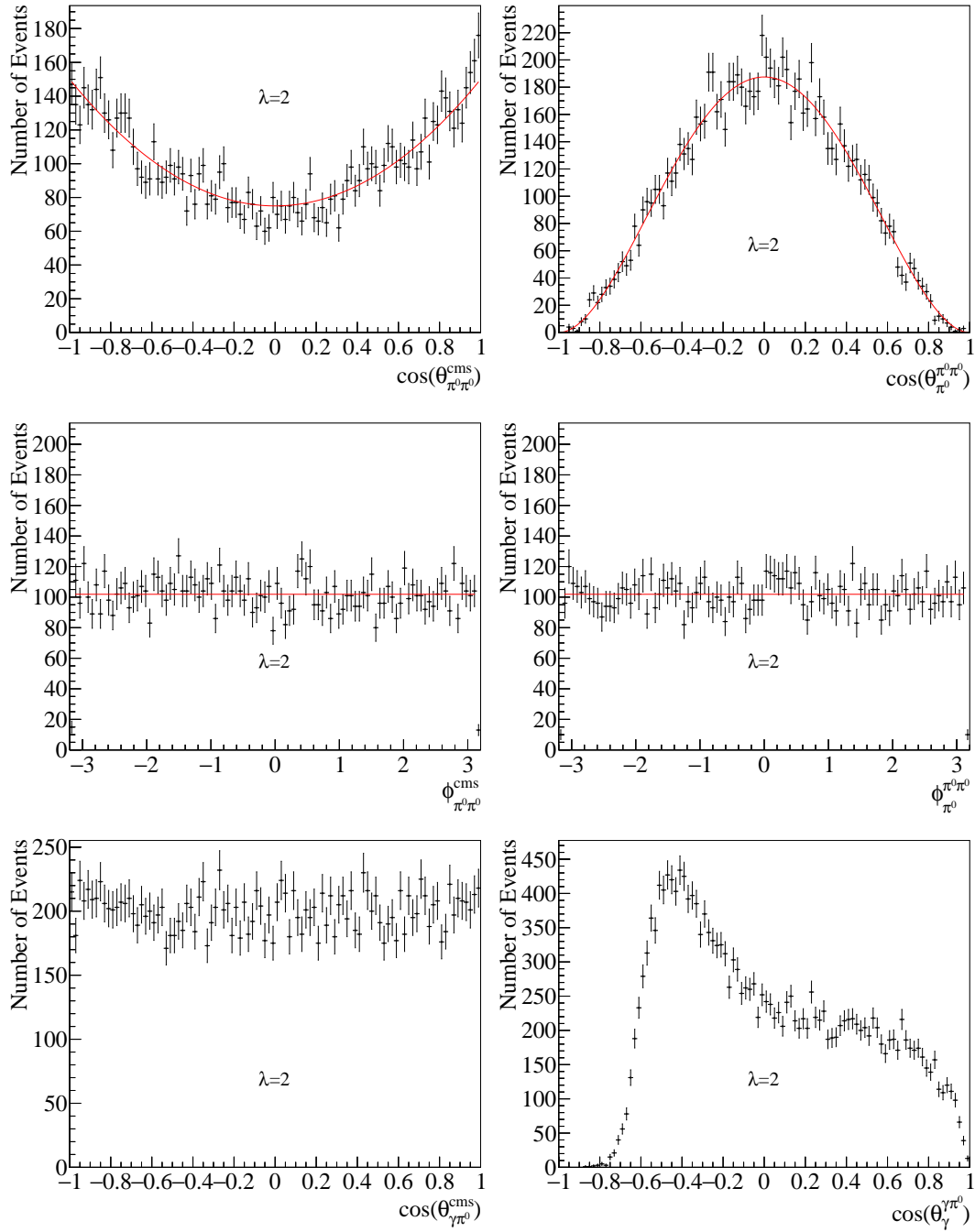


Figure 92: Angular distributions of the $J/\psi \rightarrow \gamma\pi^0\pi^0$ decay in the $f_2(|\lambda| = 2)$ channel generated by the ComPWA framework using the HelicityAmplitude module. The left column shows distributions in the CMS and the right column for the two particle subsystems. The analytic solution is indicated by the red curve.

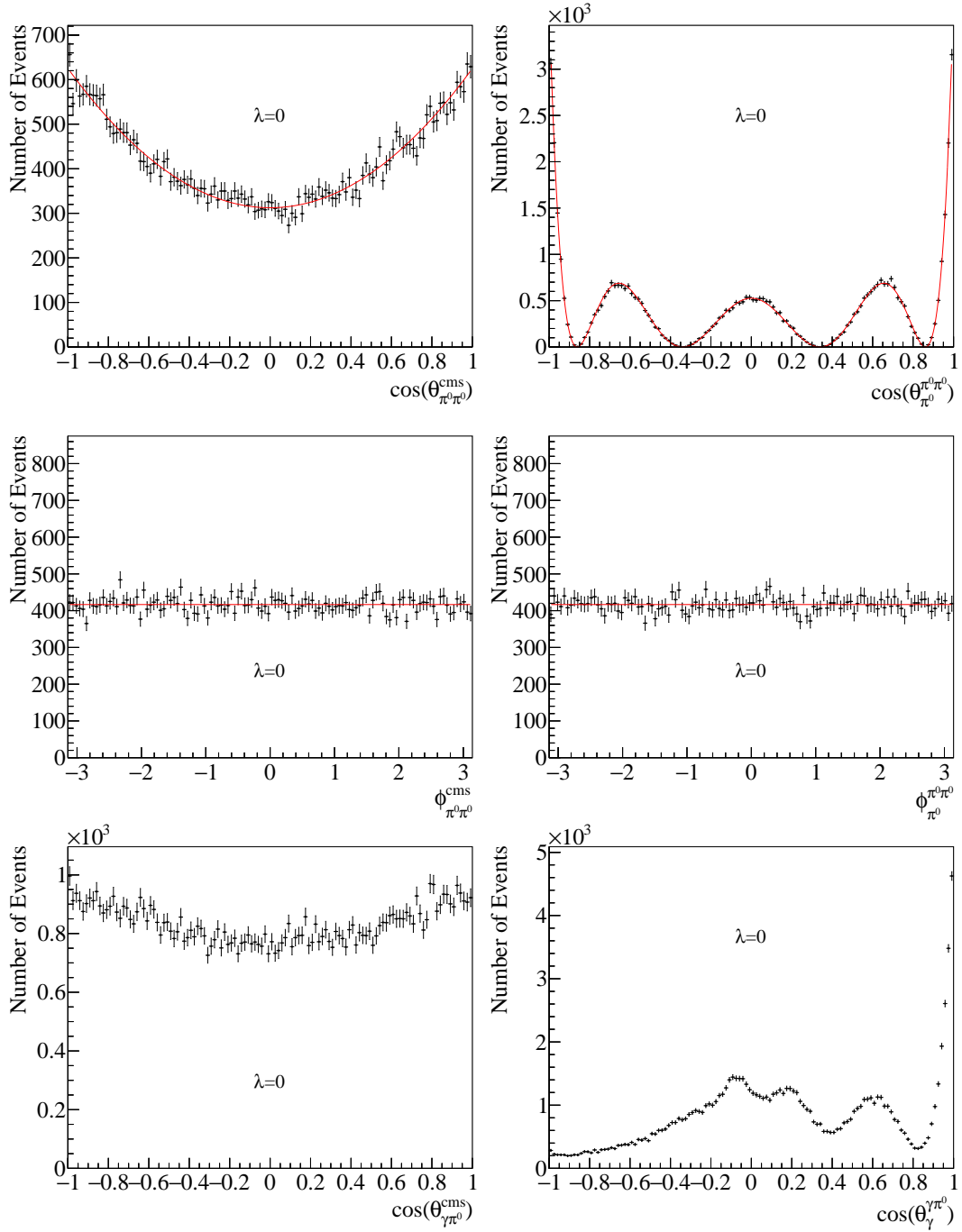


Figure 93: Angular distributions of the $J/\psi \rightarrow \gamma\pi^0\pi^0$ decay in the $f_4(\lambda=0)$ channel generated by the ComPWA framework using the HelicityAmplitude module. The left column shows distributions in the CMS and the right column for the two particle subsystems. The analytic solution is indicated by the red curve.

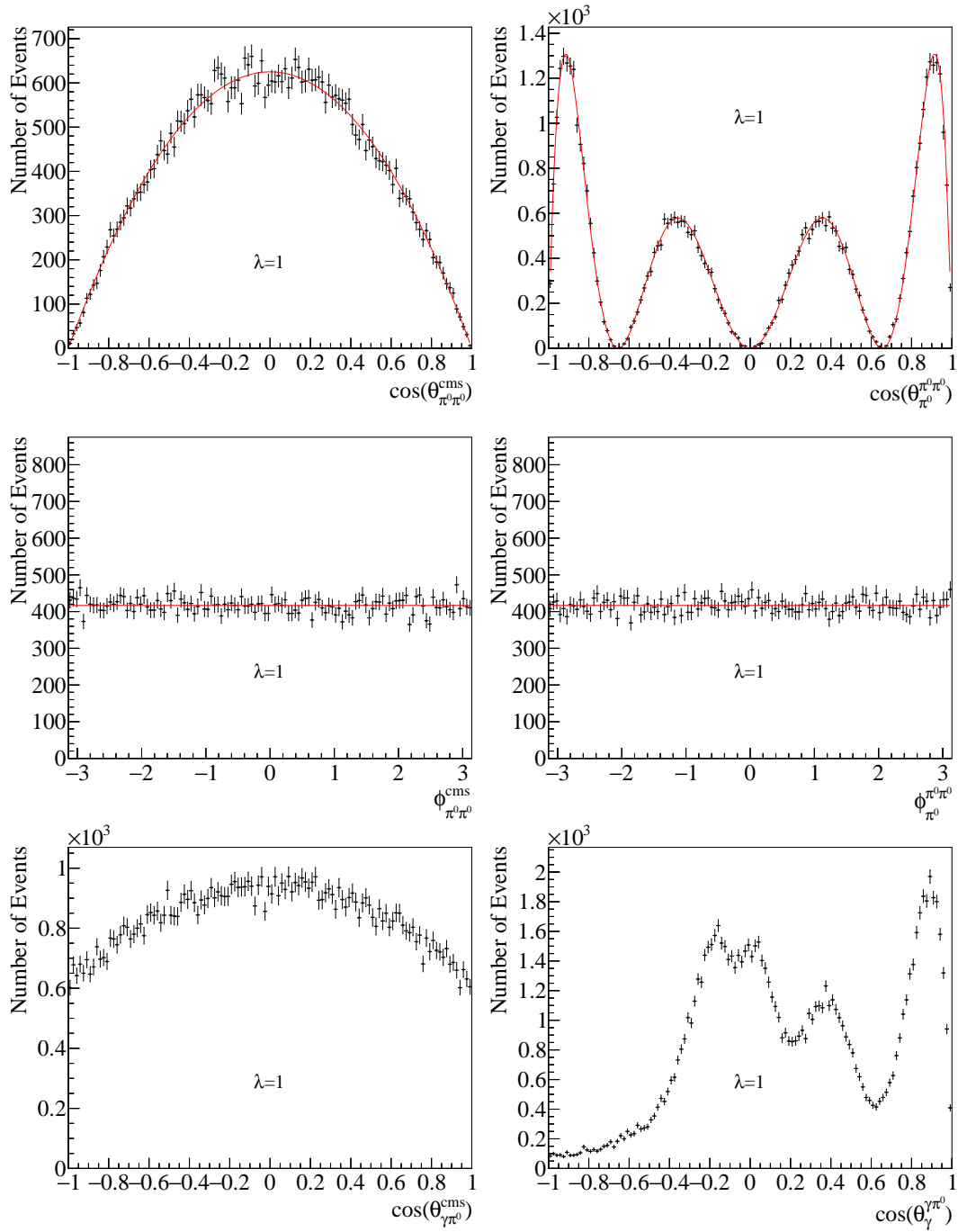


Figure 94: Angular distributions of the $J/\psi \rightarrow \gamma\pi^0\pi^0$ decay in the $f_4(|\lambda| = 1)$ channel generated by the ComPWA framework using the HelicityAmplitude module. The left column shows distributions in the CMS and the right column for the two particle subsystems. The analytic solution is indicated by the red curve.

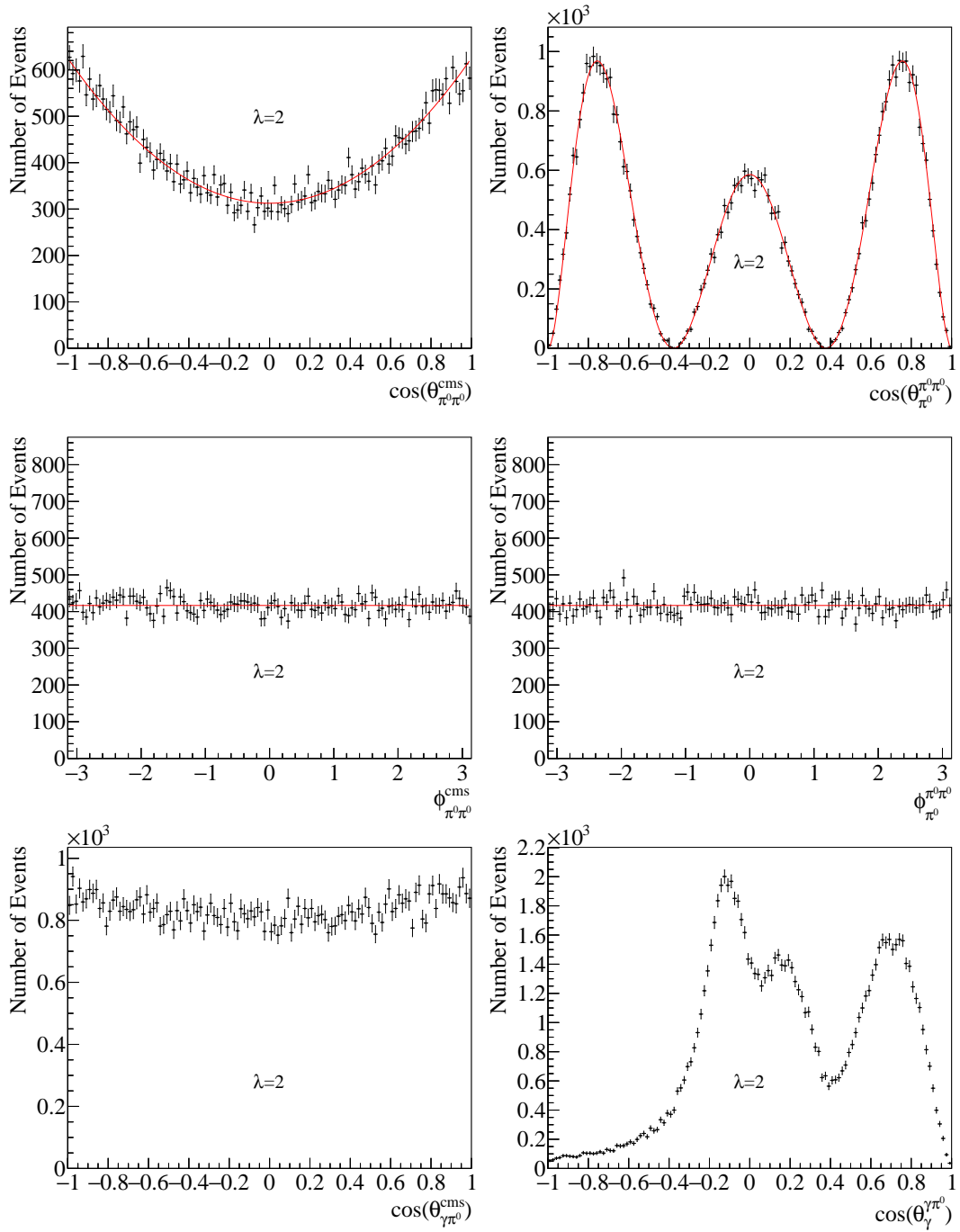


Figure 95: Angular distributions of the $J/\psi \rightarrow \gamma\pi^0\pi^0$ decay in the $f_4(|\lambda|=2)$ channel generated by the ComPWA framework using the HelicityAmplitude module. The left column shows distributions in the CMS and the right column for the two particle subsystems. The analytic solution is indicated by the red curve.

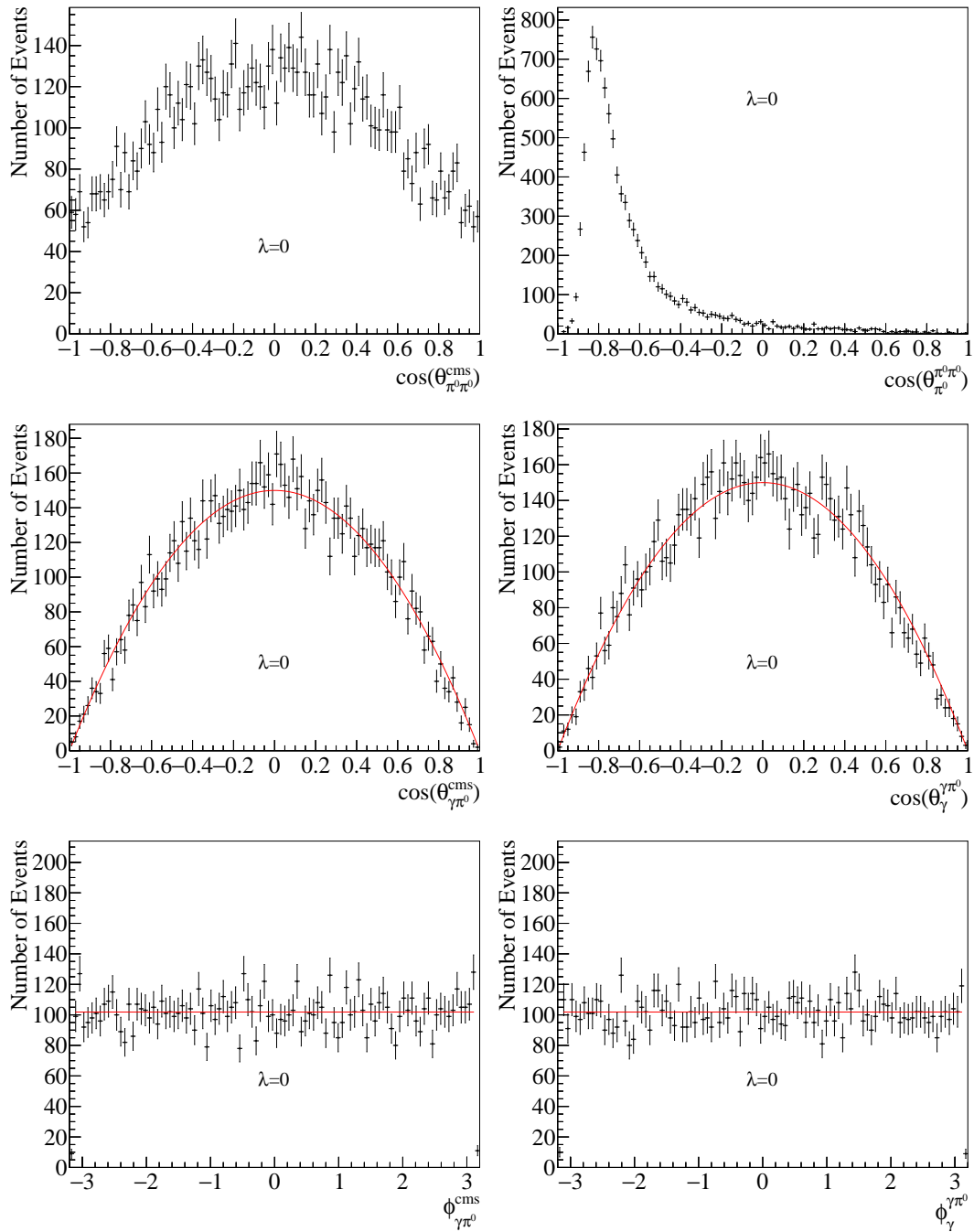


Figure 96: Angular distributions of the $J/\psi \rightarrow \gamma\pi^0\pi^0$ decay in the $\omega(\lambda = 0)$ channel generated by the CompPWA framework using the HelicityAmplitude module. The left column shows distributions in the CMS and the right column for the two particle subsystems. The analytic solution is indicated by the red curve and the π^0 are made distinguishable here. Note that this decay channel is parity violating.

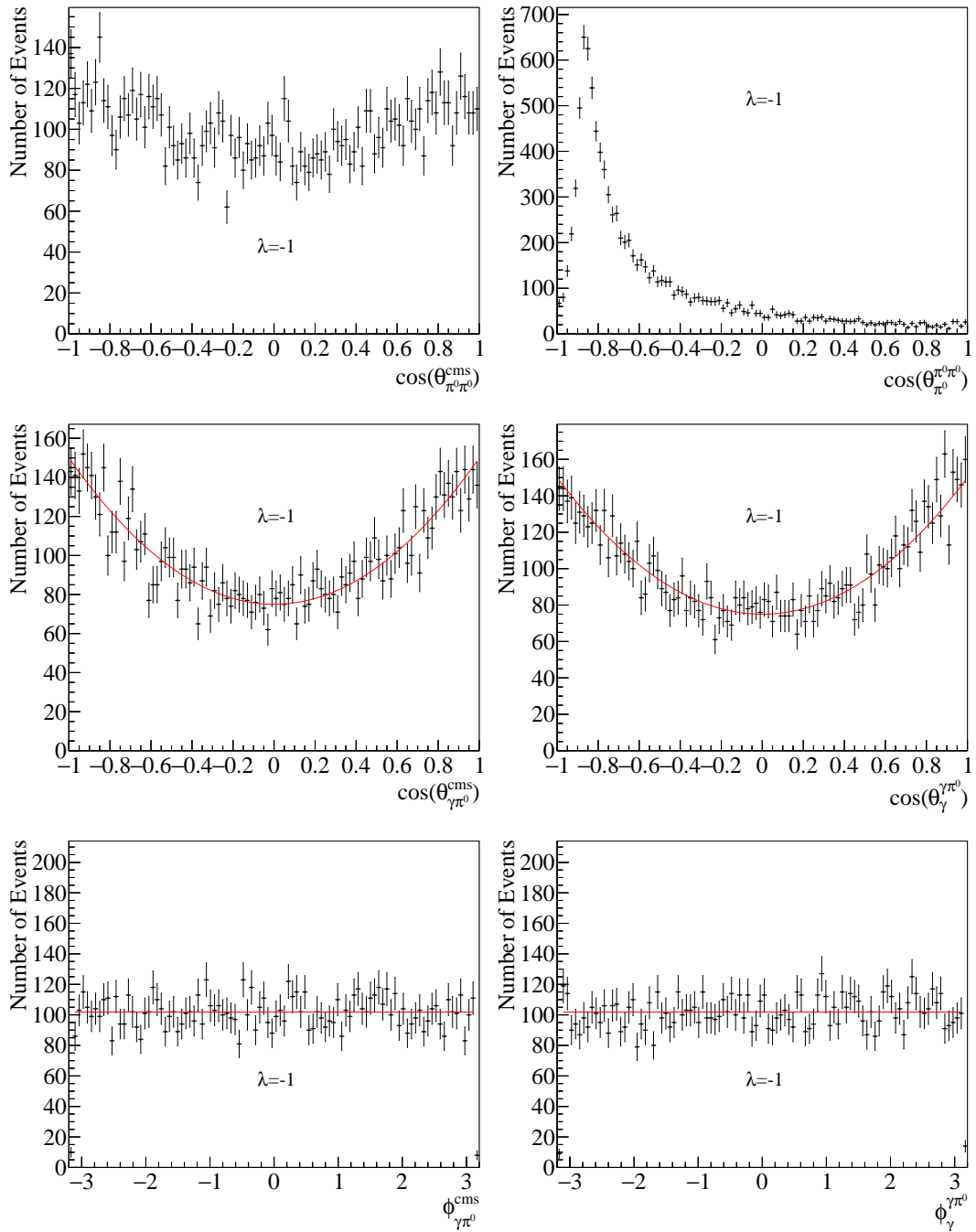


Figure 97: Angular distributions of the $J/\psi \rightarrow \gamma\pi^0\pi^0$ decay in the $\omega(|\lambda|=1)$ channel generated by the ComPWA framework using the HelicityAmplitude module. The left column shows distributions in the CMS and the right column for the two particle subsystems. The analytic solution is indicated by the red curve and the π^0 are made distinguishable here.

C.3 1D KINEMATIC VARIABLE COMPARISONS

C.3.1 CompPWA $J/\psi \rightarrow \gamma\pi^0\pi^0$ benchmark model MC data and CompPWA best fit result

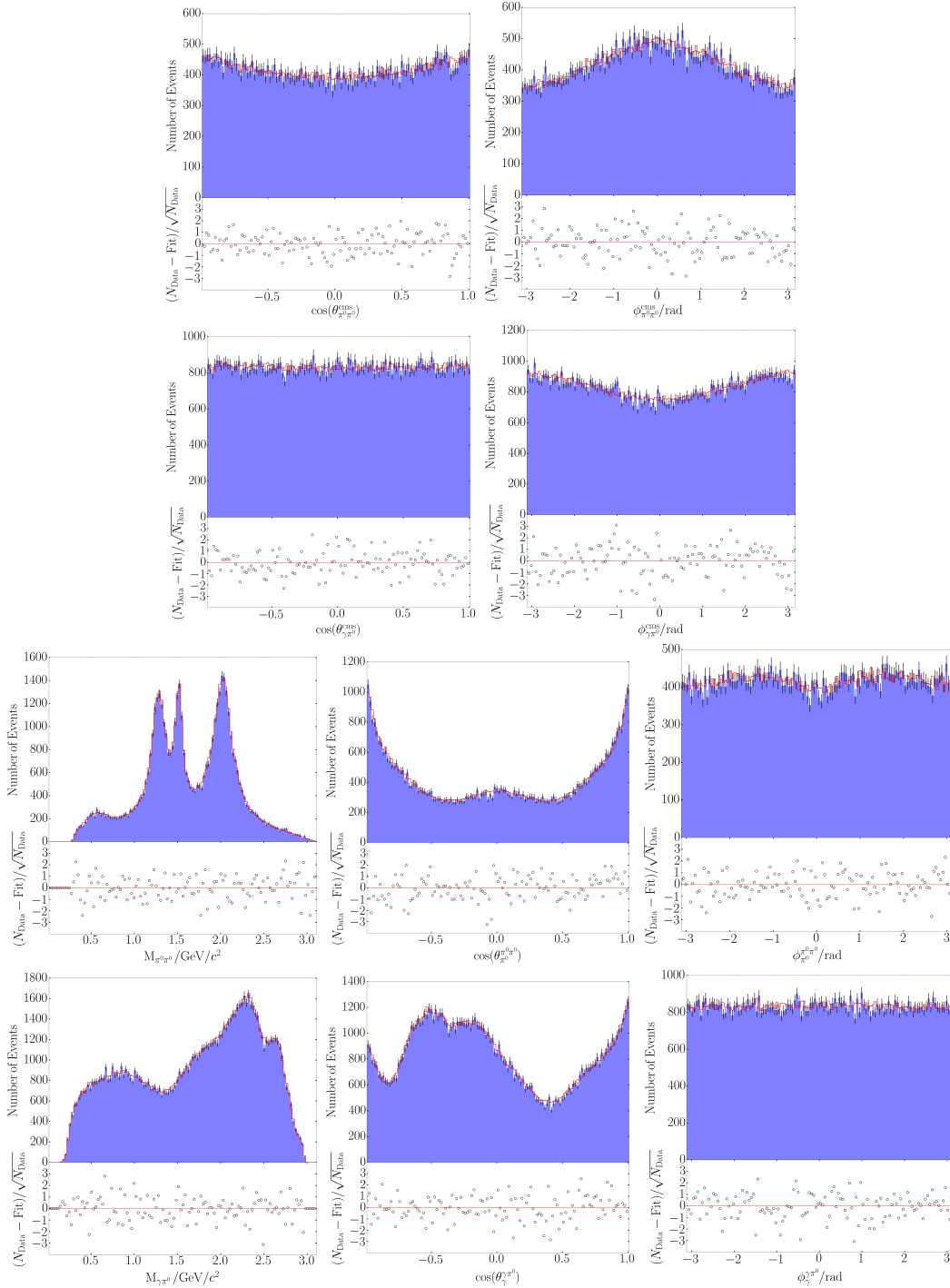


Figure 98: 1D kinematic distributions of CompPWA generated benchmark model data. The data is shown in blue while the CompPWA best fit result is indicated with the red line. Below are normalized residuals.

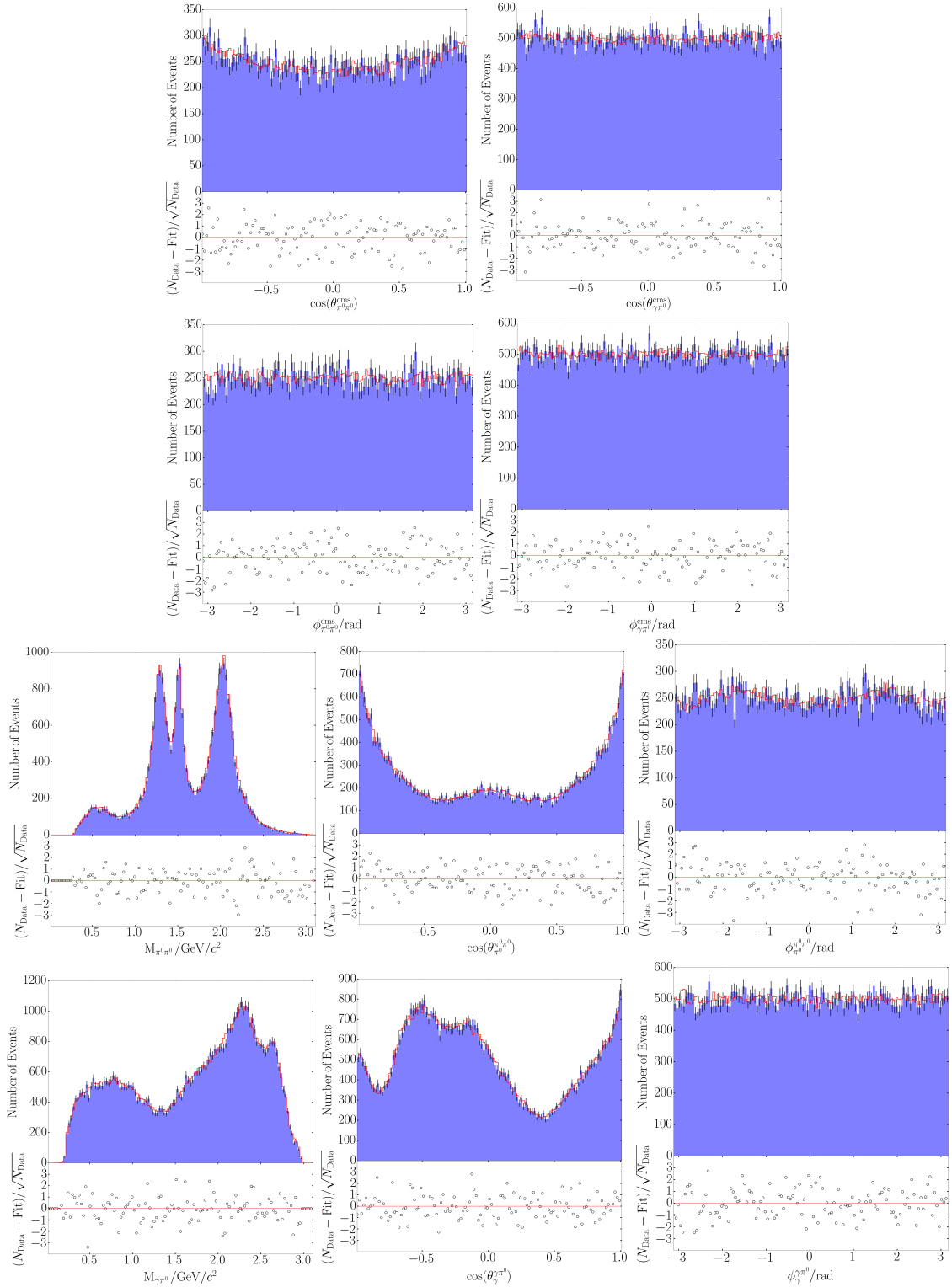
c.3.2 PAWIAN $J/\psi \rightarrow \gamma\pi^0\pi^0$ benchmark model MC data and CompPWA best fit result

Figure 99: 1D kinematic distributions of PAWIAN generated benchmark model data. The data is shown in blue while the CompPWA best fit result is indicated with the red line. Below are normalized residuals.

C.4 NORMALIZED RESIDUALS FOR COMPWA FITS ON $J/\psi \rightarrow \gamma\pi^0\pi^0$ MC DATA

C.4.1 Simple model data generated with CompPWA

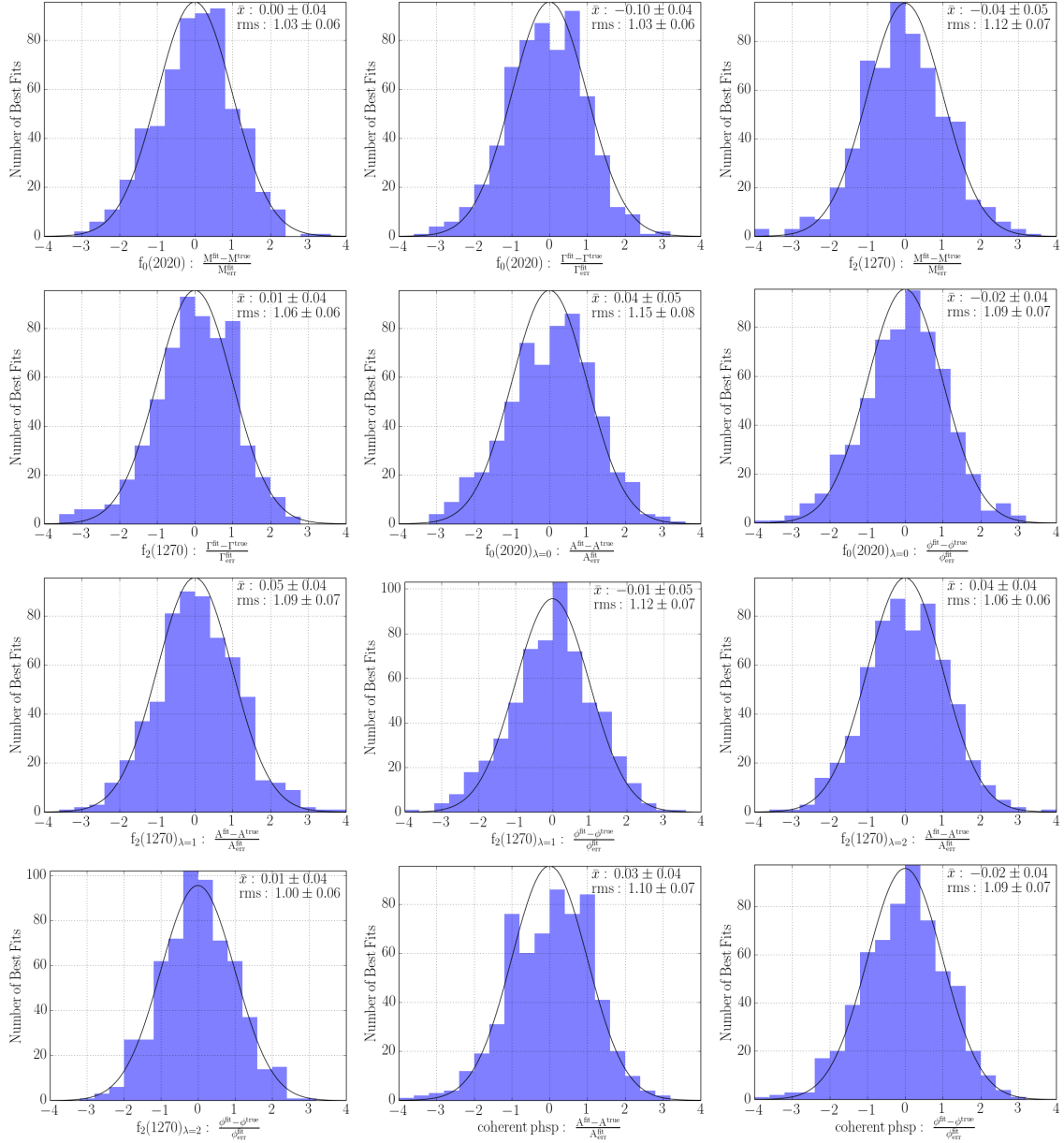


Figure 100: Normalized residuals of parameters of the simple model from fits on CompPWA generated data. The black curve indicates the ideal distribution with mean $\bar{x} = 0$ and a RMS value of 1.

C.4.2 Benchmark model data generated with CompWA

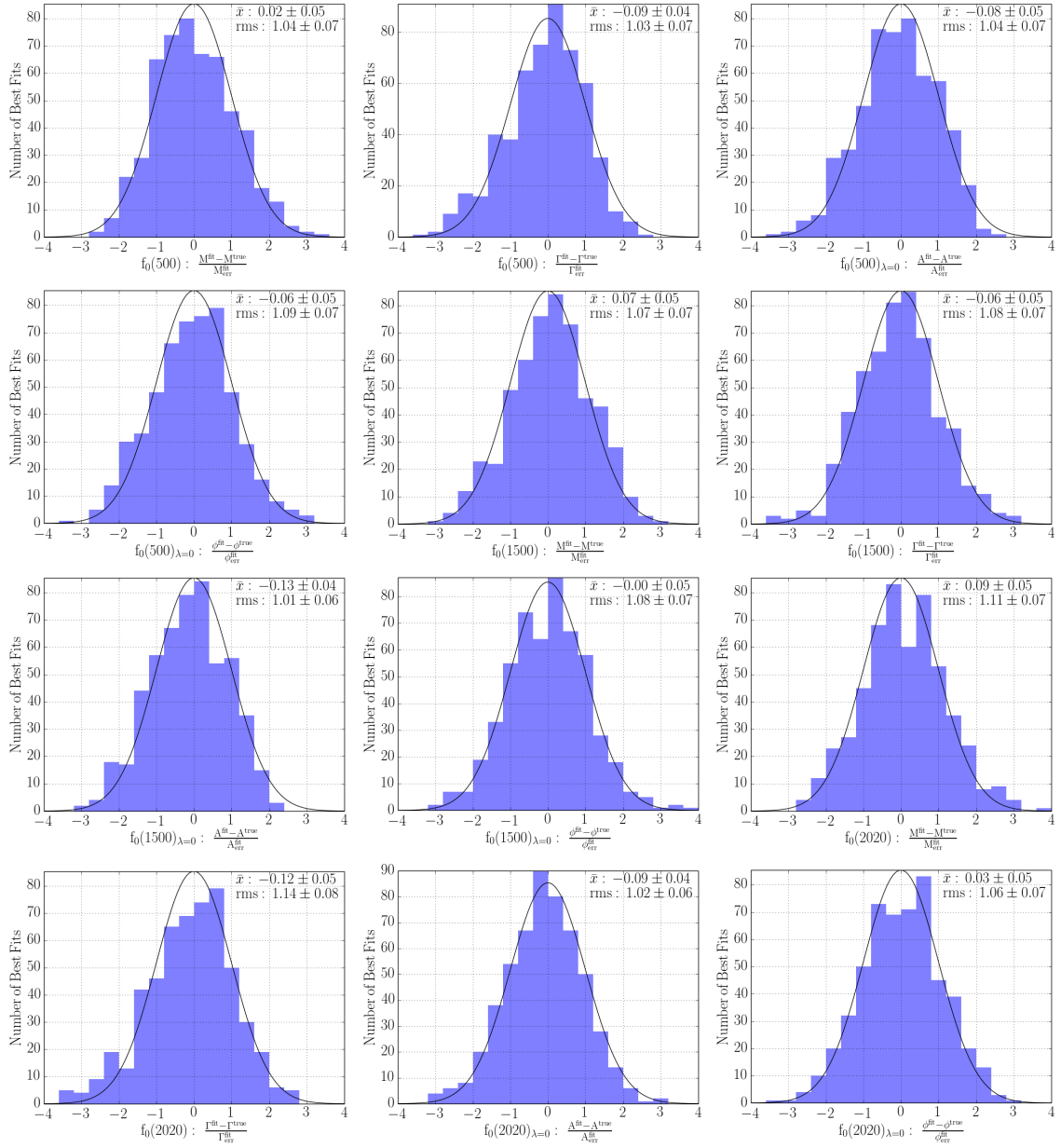


Figure 101: Normalized residuals of parameters of the benchmark model from fits on CompWA generated data. The black curve indicates the ideal distribution with mean $\bar{x} = 0$ and a RMS value of 1.

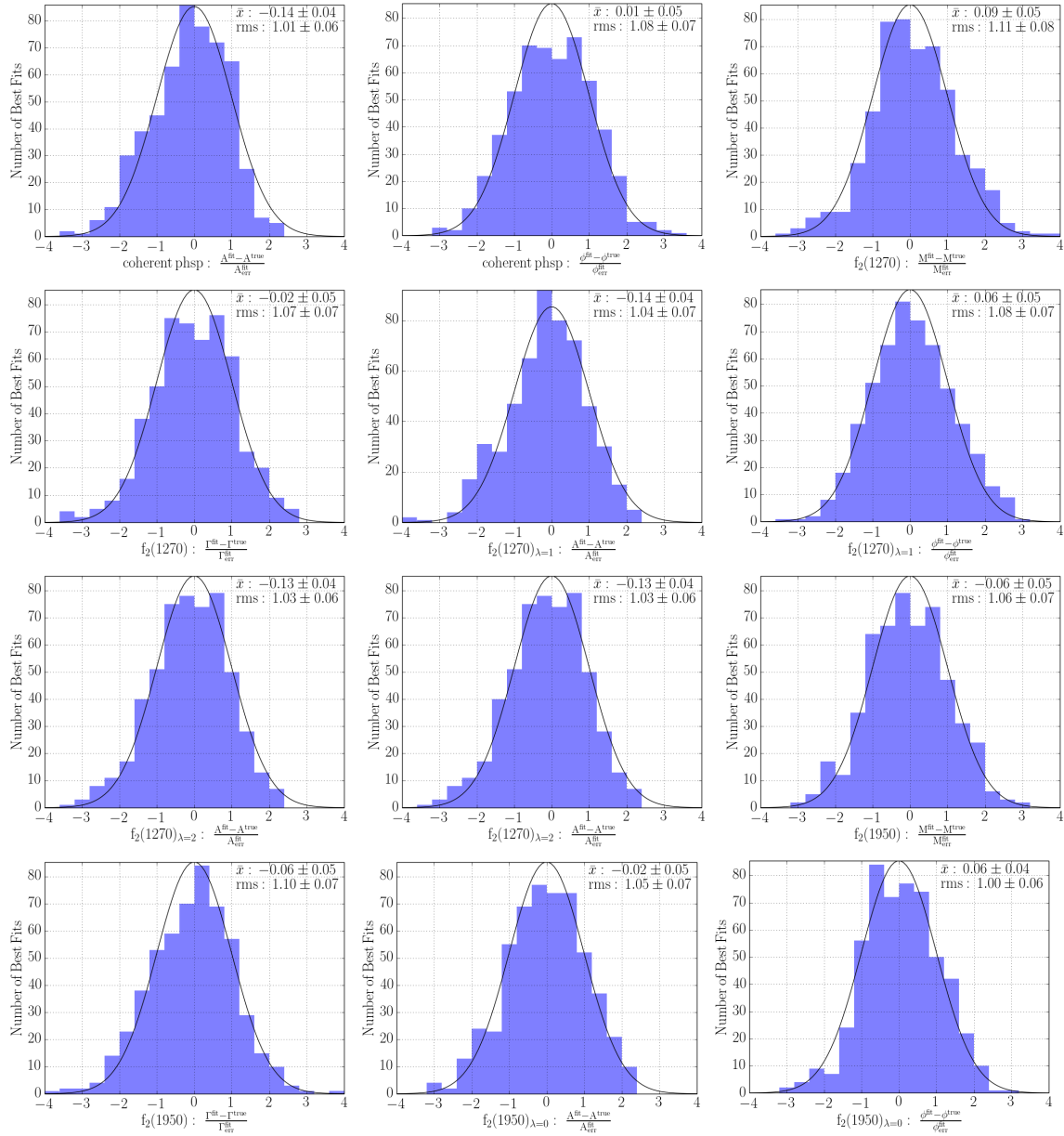


Figure 102: Normalized residuals of parameters of the benchmark model from fits on CompPWA generated data (cont.). The black curve indicates the ideal distribution with mean $\bar{x} = 0$ and a RMS value of 1.

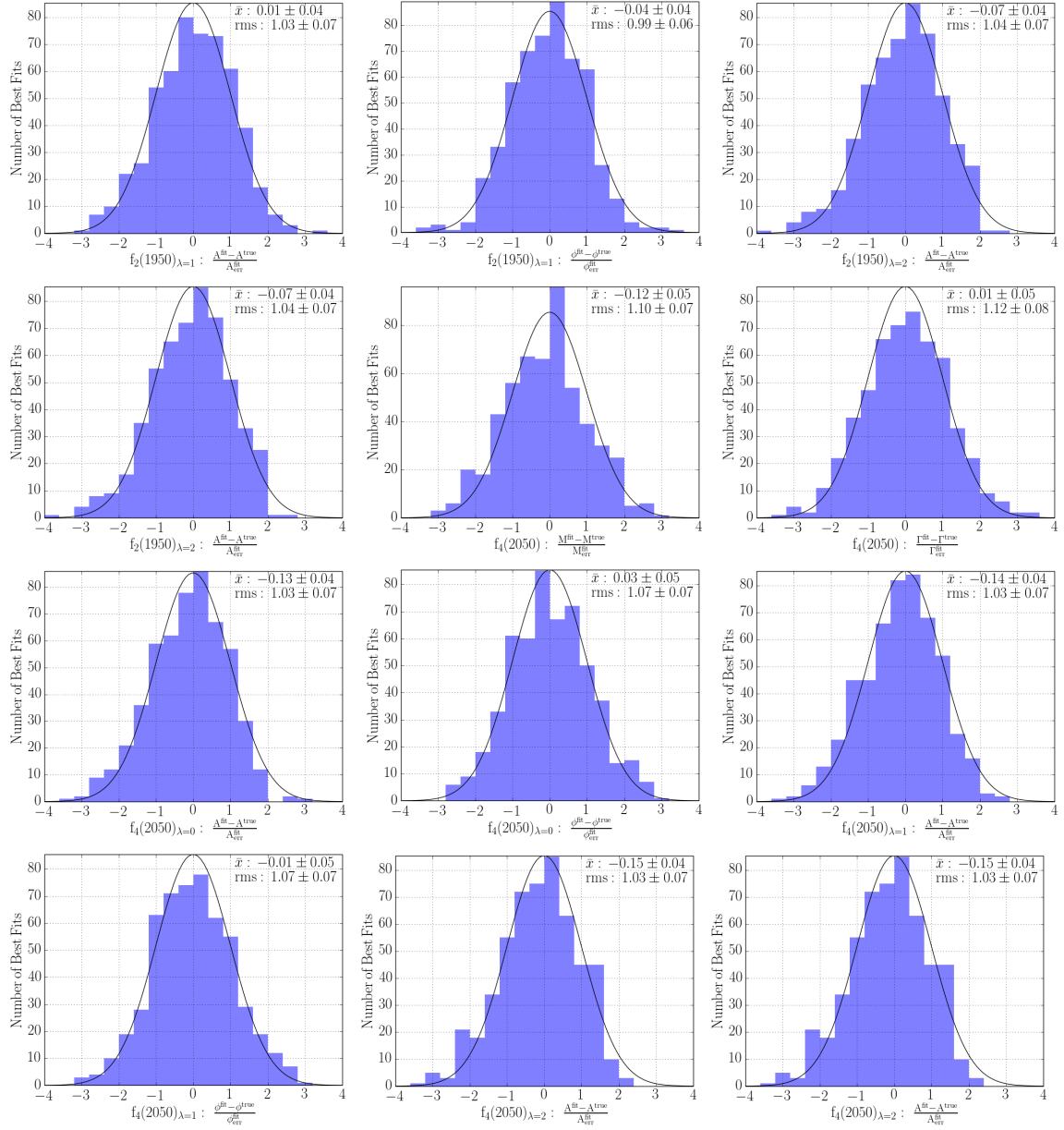


Figure 103: Normalized residuals of parameters of the benchmark model from fits on CompWA generated data (cont.). The black curve indicates the ideal distribution with mean $\bar{x} = 0$ and a RMS value of 1.

C.4.3 Benchmark model data generated with PAWIAN

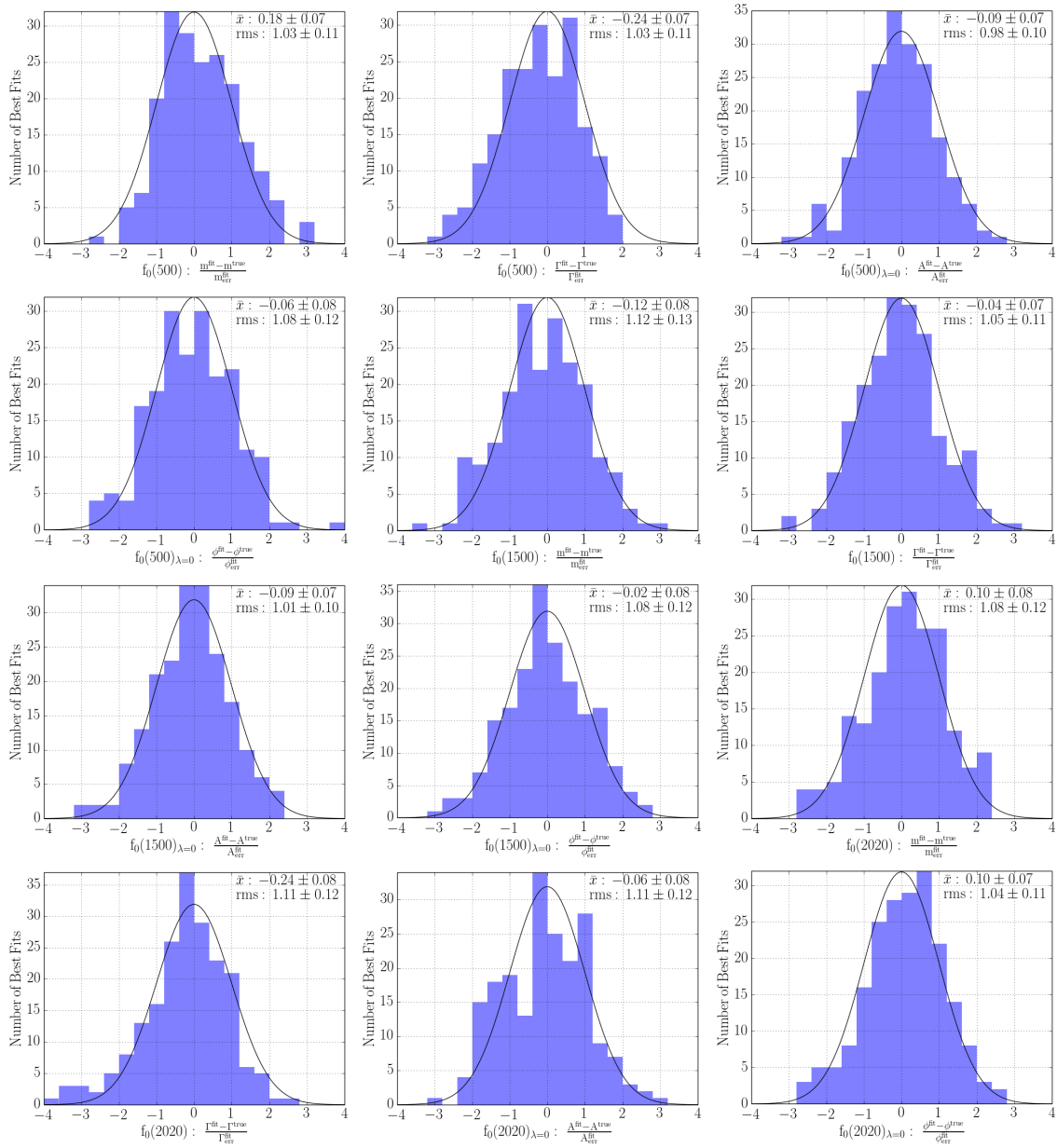


Figure 104: Normalized residuals of parameters of the benchmark model from fits on PAWIAN generated data. The black curve indicates the ideal distribution with mean $\bar{x} = 0$ and a RMS value of 1.

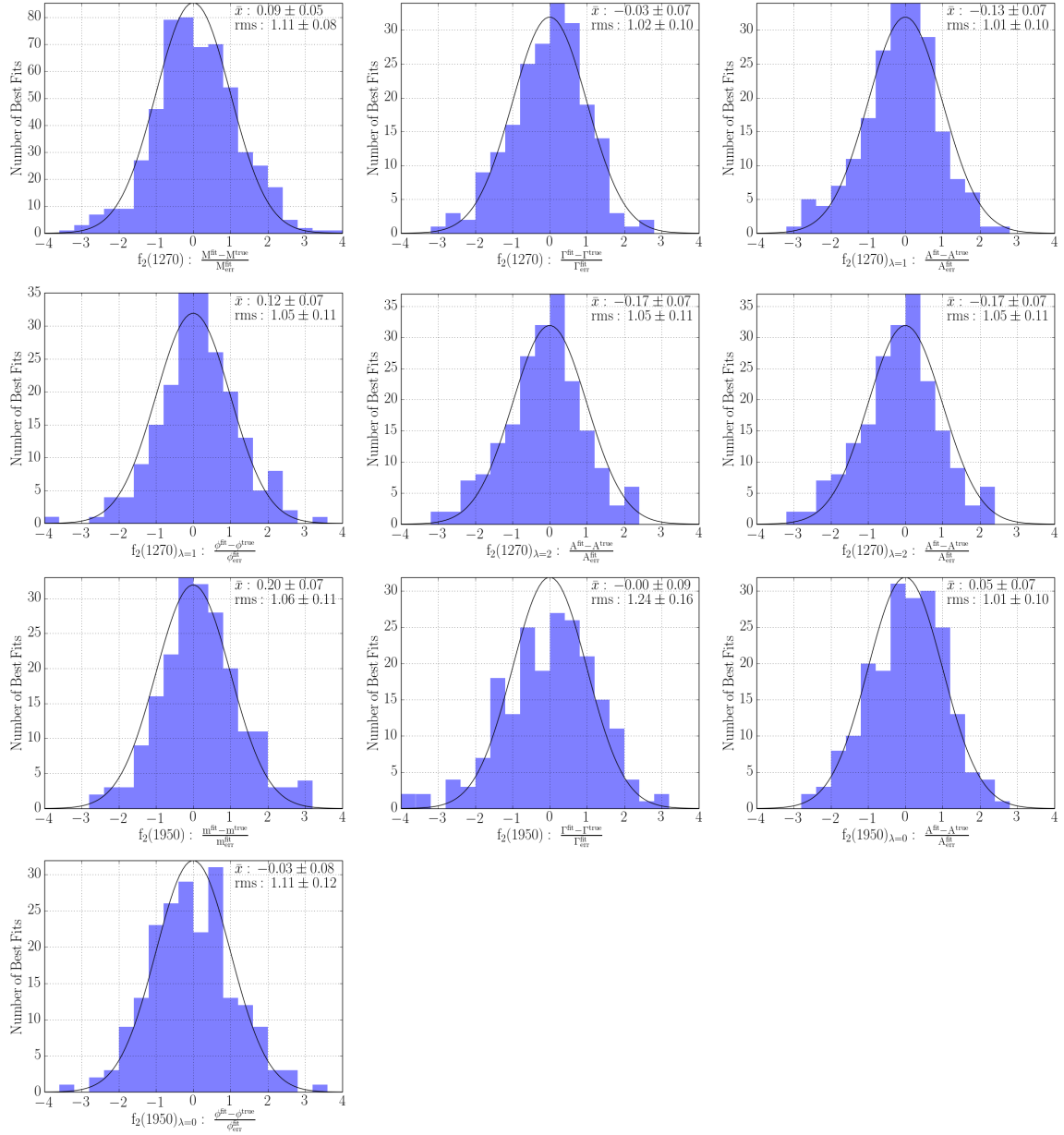


Figure 105: Normalized residuals of parameters of the benchmark model from fits on PAWIAN generated data (cont.). The black curve indicates the ideal distribution with mean $\bar{x} = 0$ and a RMS value of 1.

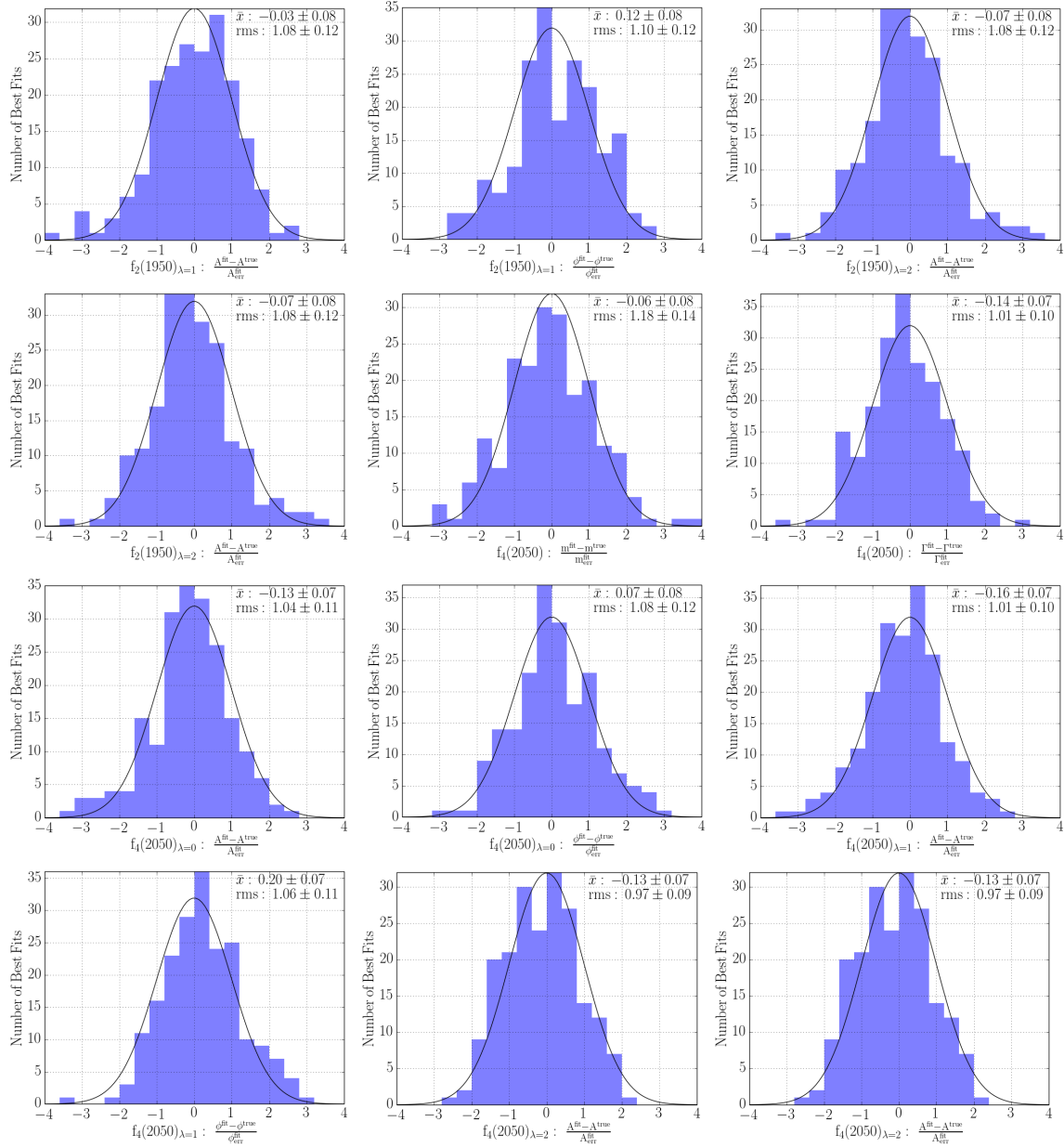


Figure 106: Normalized residuals of parameters of the benchmark model from fits on PAWIAN generated data (cont.). The black curve indicates the ideal distribution with mean $\bar{x} = 0$ and a RMS value of 1.

LIST OF FIGURES

Figure 1	Standard Model Elementary Particles	1
Figure 2	Measurements of α_s at various energy scales Q	3
Figure 3	Pseudoscalar & vector meson multiplets	8
Figure 4	Simplest conventional and exotic components of hadron states within the constituent quark picture	9
Figure 5	Isoscalar meson spectrum with $J^{PC} = 0^{++}$	11
Figure 6	Quenched lattice glueball spectrum	12
Figure 7	Meson Summary	13
Figure 8	BESIII side view	17
Figure 9	The FAIR Complex	19
Figure 10	The HESR	20
Figure 11	HESR cycle with the RESR	21
Figure 12	PANDA side view	26
Figure 13	Illustration of fixed target luminosity	31
Figure 14	Sketch of a general scattering process	32
Figure 15	Relative DPM cross section uncertainty	35
Figure 16	$ t $ ranges for previous elastic $\bar{p}p$ measurements, the LMD and KOALA	35
Figure 17	LMD side view	37
Figure 18	HV-MAPS sensor scheme	38
Figure 19	Illustration of a half plane	38
Figure 20	Rendered luminosity detector simulation model.	40
Figure 21	Overall LMD software flow	41
Figure 22	LMD data reconstruction software flow	41
Figure 23	Sensor overlap	42
Figure 24	Exemplary reconstructed track 2D angular distribution at 1.5 GeV/c	43
Figure 25	Contributions of the elastic $\bar{p}p$ scattering cross section	46
Figure 26	The $\theta_x\theta_y$ coordinate system	47
Figure 27	$\theta_x\theta_y$ transformation validity	49
Figure 28	Divergence smearing example	50
Figure 29	Ideal LMD $\theta_x\theta_y$ angular acceptance	51
Figure 30	Illustration of paired acceptance inefficiency structure	52
Figure 31	LMD 2D Angular Resolution @ 1.5 GeV/c and 15 GeV/c	53
Figure 32	Momentum dependence of the LMD angular resolution	53
Figure 33	Relative luminosity versus fit model and data binning	56
Figure 34	Luminosity fit results - ideal case	58
Figure 35	Beam shift and tilt sketch	59
Figure 36	Expected LMD $\theta_x\theta_y$ angular acceptance	60
Figure 37	Uncorrected and corrected LMD fit results for the gaussian distributed IP 1.5 GeV/c	62
Figure 38	Uncorrected and corrected LMD fit results for the gaussian distributed IP 15 GeV/c	63

Figure 39	Influence of IP displacements on luminosity precision	64
Figure 40	Example of reconstructed IP distributions of x_{IP}, y_{IP}	65
Figure 41	Reconstructed mean x_{IP}, y_{IP} precision at $p_{lab} = 1.5 \text{ GeV}/c$ and $p_{lab} = 15 \text{ GeV}/c$	65
Figure 42	Luminosity determination precision with IP displacement correction	66
Figure 43	Influence of accelerator beam tilts on the luminosity precision	67
Figure 44	Reconstructed beam tilt $tilt_x, tilt_y$ precision at $p_{lab} = 1.5 \text{ GeV}/c$ and $p_{lab} = 15 \text{ GeV}/c$	68
Figure 45	Luminosity determination precision with beam tilt correction	68
Figure 46	Influence of accelerator beam divergence on the luminosity precision	69
Figure 47	Reconstructed beam divergence div_x, div_y precision at $p_{lab} = 1.5 \text{ GeV}/c$ and $p_{lab} = 15 \text{ GeV}/c$	70
Figure 48	Luminosity determination precision with beam tilt correction	71
Figure 49	Residuals of luminosity fit parameters of realistic scenario	76
Figure 50	Sketch of the definition of the helicity angles	85
Figure 51	CompPWA design overview	87
Figure 52	CompPWA helicity formalism modules overview	88
Figure 53	HelicityAmplitude module: the amplitude hierarchy	89
Figure 54	HelicityAmplitude module: coherent amplitude construction flowchart	89
Figure 55	HelicityAmplitude module: amplitude evaluation structure	90
Figure 56	DecayTree module: decay tree creation flowchart	91
Figure 57	DecayTree module: flowchart of the creation of the decay configuration	92
Figure 58	Basic decay example: electric charge	92
Figure 59	Spin state decay example	94
Figure 60	Two example $J/\psi \rightarrow \gamma\pi^0\pi^0$ decay trees obtained by the CompPWA expert system	96
Figure 61	Definition of the θ angles in the $J/\psi \rightarrow \gamma\pi^0\pi^0$ decay via a $\pi^0\pi^0$ sub-system in the helicity formalism	97
Figure 62	$J/\psi \rightarrow \gamma f_0 \rightarrow \gamma\pi^0\pi^0$ angular distributions	98
Figure 63	$\cos(\theta_{\pi^0\pi^0}^{cms})$ distributions for the $J/\psi \rightarrow \gamma X \rightarrow \gamma\pi^0\pi^0$ ($X = f_2, f_4$) reaction for various helicities	98
Figure 64	$\cos(\theta_{\pi^0\pi^0}^{\pi^0})$ distributions for the $J/\psi \rightarrow \gamma X \rightarrow \gamma\pi^0\pi^0$ ($X = f_2, f_4$) reaction for various helicities	99
Figure 65	$\cos(\theta_{\gamma\pi^0}^{\pi^0})$ distributions for the $J/\psi \rightarrow \pi^0\omega \rightarrow \gamma\pi^0\pi^0$ reaction for various helicities	100
Figure 66	Dalitz plot of the reaction $J/\psi \rightarrow \gamma\pi^0\pi^0$ including f_0, f_2 as intermediate resonances and the normalized residual with the best fit result	102
Figure 67	Invariant mass spectra of the $\pi^0\pi^0$ and $\gamma\pi^0$ subsystem of the reaction $J/\psi \rightarrow \gamma\pi^0\pi^0$ including f_0, f_2 as intermediate resonances	103
Figure 68	$\cos(\theta_{\pi^0\pi^0}^{\pi^0})$ and $\cos(\theta_{\gamma\pi^0}^{\pi^0})$ distributions of the reaction $J/\psi \rightarrow \gamma\pi^0\pi^0$ including f_0, f_2 as intermediate resonances	103
Figure 69	Normalized residuals for a selected subset of parameters in the simple model of the $J/\psi \rightarrow \gamma\pi^0\pi^0$ decay.	105

Figure 70	Residual of the f_2 mass in simple model	106
Figure 71	Correlation matrix of the best fit result on a simple model dataset for the reaction $J/\psi \rightarrow \gamma\pi^0\pi^0$ including f_0 and f_2 as intermediate resonances	106
Figure 72	Dalitz plot of CompPWA generated MC data of the reaction $J/\psi \rightarrow \gamma\pi^0\pi^0$ including f_0, f_2, f_4 as intermediate resonances and the normalized residual with the CompPWA fit result	107
Figure 73	$\pi^0\pi^0$ invariant mass spectrum and $\cos(\theta_{\pi^0\pi^0}^{\text{cms}})$ distribution of the reaction $J/\psi \rightarrow \gamma\pi^0\pi^0$ including f_0, f_2 and f_4 as intermediate resonances from CompPWA generated MC data	109
Figure 74	Dalitz plot of PAWIAN generated MC data of the reaction $J/\psi \rightarrow \gamma\pi^0\pi^0$ including f_0, f_2, f_4 as intermediate resonances and the normalized residual with the CompPWA fit result	111
Figure 75	$\cos(\theta_{\pi^0\pi^0}^{\text{cms}})$ and $\phi_{\pi^0\pi^0}$ distributions of the reaction $J/\psi \rightarrow \gamma\pi^0\pi^0$ including f_0, f_2 and f_4 as intermediate resonances from PAWIAN generated MC data	112
Figure 76	Dalitz plot of the BESIII data of the reaction $J/\psi \rightarrow \gamma\pi^0\pi^0$	114
Figure 77	Normalized residual of the BESIII Dalitz plot of the reaction $J/\psi \rightarrow \gamma\pi^0\pi^0$ with the CompPWA helicity amplitude model fit result	117
Figure 78	Invariant mass spectra of the the BESIII data for the $\pi^0\pi^0$ and $\gamma\pi^0$ subsystems of the reaction $J/\psi \rightarrow \gamma\pi^0\pi^0$	118
Figure 79	$\cos(\theta)$ and ϕ distributions of the BESIII data of the reaction $J/\psi \rightarrow \gamma\pi^0\pi^0$	119
Figure 80	General expert system design	129
Figure 81	Usage example of the expert system	129
Figure 82	Phase space ellipse	131
Figure 83	A kinematic drawing elastic $\bar{p}p$ scattering in the cms frame.	132
Figure 84	A kinematic drawing of the lab frame	133
Figure 85	Relative Difference approximate and correct t versus θ_{lab}	136
Figure 86	Special case of the detector resolution in which the equality to a convolution operation is obtained. The red curve shows the probability density function before accounting for smearing. The gaussian functions indicate an exemplary special case for the resolution.	138
Figure 87	Dalitz plot example and kinematics limits	139
Figure 88	The helicity angle distributions within the Dalitz plot	140
Figure 89	Angular distributions of the $J/\psi \rightarrow \gamma\pi^0\pi^0$ decay in the $f_0(\lambda = 0)$ channel	141
Figure 90	Angular distributions of the $J/\psi \rightarrow \gamma\pi^0\pi^0$ decay in the $f_2(\lambda = 0)$ channel	142
Figure 91	Angular distributions of the $J/\psi \rightarrow \gamma\pi^0\pi^0$ decay in the $f_2(\lambda = 1)$ channel	143
Figure 92	Angular distributions of the $J/\psi \rightarrow \gamma\pi^0\pi^0$ decay in the $f_2(\lambda = 2)$ channel	144
Figure 93	Angular distributions of the $J/\psi \rightarrow \gamma\pi^0\pi^0$ decay in the $f_4(\lambda = 0)$ channel	145
Figure 94	Angular distributions of the $J/\psi \rightarrow \gamma\pi^0\pi^0$ decay in the $f_4(\lambda = 1)$ channel	146

Figure 95	Angular distributions of the $J/\psi \rightarrow \gamma\pi^0\pi^0$ decay in the $f_4(\lambda = 2)$ channel	147
Figure 96	Angular distributions of the $J/\psi \rightarrow \gamma\pi^0\pi^0$ decay in the $\omega(\lambda = 0)$ channel	148
Figure 97	Angular distributions of the $J/\psi \rightarrow \gamma\pi^0\pi^0$ decay in the $\omega(\lambda = 1)$ channel	149
Figure 98	1D kinematic distributions of ComPWA generated benchmark model data and normalized residuals with the best ComPWA fit result.	150
Figure 99	1D kinematic distributions of PAWIAN generated benchmark model data and normalized residuals with the best ComPWA fit result.	151
Figure 100	Normalized residuals of parameters of the simple model from fits on ComPWA generated data	152
Figure 101	Normalized residuals of parameters of the benchmark model from fits on ComPWA generated data	153
Figure 102	Normalized residuals of parameters of the benchmark model from fits on ComPWA generated data (cont.)	154
Figure 103	Normalized residuals of parameters of the benchmark model from fits on ComPWA generated data (cont.)	155
Figure 104	Normalized residuals of parameters of the benchmark model from fits on PAWIAN generated data	156
Figure 105	Normalized residuals of parameters of the benchmark model from fits on PAWIAN generated data (cont.)	157
Figure 106	Normalized residuals of parameters of the benchmark model from fits on PAWIAN generated data (cont.)	158

LIST OF TABLES

Table 1	Beam parameters of the HESR	21
Table 2	Expected HESR beam parameters HL mode	22
Table 3	Expected HESR beam parameters HR mode	23
Table 4	PANDA target parameters	27
Table 5	Accuracy of the luminosity determination for various random realistic scenarios	72
Table 6	Influence of various fit settings on the beam tilts and luminosity	74
Table 7	Parameters of the simple model for the reaction $J/\psi \rightarrow \gamma\pi^0\pi^0$ including f_0, f_2 as intermediate resonances	101
Table 8	Parameters of the benchmark model used for the data generation of the reaction $J/\psi \rightarrow \gamma\pi^0\pi^0$ including multiple f_0, f_2 resonances and one f_4 resonance as intermediate states	108
Table 9	Normalized residual mean and RMS values for the fit parameters of the benchmark model on CompPWA generated MC data for the reaction $J/\psi \rightarrow \gamma\pi^0\pi^0$ including multiple f_0, f_2 resonances and one f_4 resonance as intermediate states	110
Table 10	Normalized residual mean and RMS values for the CompPWA fit parameters of the benchmark model on PAWIAN generated MC data for the reaction $J/\psi \rightarrow \gamma\pi^0\pi^0$ including multiple f_0, f_2 resonances and one f_4 resonance as intermediate states	113
Table 11	Parameters of the helicity amplitude model used for the first fit on the BESIII data of the $J/\psi \rightarrow \gamma\pi^0\pi^0$ process and their extracted values	116

ACRONYMS

BEPCII Beijing Electron Positron Collider II
BESIII Beijing Electron Spectrometer III
BOPET Biaxially-oriented polyethylene terephthalate
BPM Beam positioning monitors
CA Cellular automaton
CHPT Chiral perturbation theory
CKM Cabibbo-Kobayashi-Maskawa
CLIPS C Language Integrated Production System
CMS Center-of-mass system
COMPWA Common Partial Wave Analysis
CPA Closest point of approach
CQM Constituent quark model
CR Collector Ring
CVD Chemical vapor deposition
DAQ Data acquisition
DIRC Detector of internally reflected Cherenkov light
DPM Dual parton model
EM Electromagnetic
EMC Electromagnetic calorimeter
FAIR Facility for Antiproton and Ion Research
FODO Focusing and defocusing
FT Forward tracker
GEANE Average tracking and error propagation package
GEANT4 Geometry and tracking
GEM Gas electron multiplier
GPD Generalized parton distribution

GSI GSI Helmholtzzentrum für Schwerionenforschung GmbH
HESR High-Energy Storage Ring
HL High luminosity
HR High resolution
HV-MAPS High voltage monolithic active pixel sensors
IHEP Institute of High Energy Physics
IP Interaction point
LHC_B Large Hadron Collider beauty
LMD Luminosity detector
MC Monte Carlo
MCP-PMT Micro-channel plate photomultiplier tube
MDC Multi-layer drift chamber
MDT Mini drift tube
MINUIT2 Function Minimization and Error Analysis 2
MVD Micro vertex detector
OZI Okubo-Zweig-Iizuka
PANDA Antiproton Annihilations at Darmstadt
PANDAROOT
PAWIAN Partial Wave Interactive Analysis
PDG Particle Data Group
PID Particle identification
p-LINAC Proton linear accelerator
PMT Photomultiplier tube
PWA Partial wave analysis
QCD Quantum chromodynamics
QED Quantum electrodynamics
QFT Quantum field theory
RESR Recuperated experimental storage ring
RICH Ring imaging Cherenkov
RMS Root mean square

RPC Resistive plate chamber

SIS Schwerionen Synchrotron

SM Standard Model

SODA Synchronization of data acquisition

STT Straw tube tracker

TOF Time-of-flight

UNILAC Universal linear accelerator

BIBLIOGRAPHY

- [1] Wikipedia. "Standard Model." URL: https://en.wikipedia.org/wiki/Standard_Model.
- [2] F. J. Dyson. "The Radiation Theories of Tomonaga, Schwinger, and Feynman." *Phys. Rev.* 75 (3 1949), pp. 486–502.
- [3] S. L. Glashow. "Partial Symmetries of Weak Interactions." *Nucl. Phys.* 22 (1961), pp. 579–588.
- [4] S. Weinberg. "A Model of Leptons." *Phys. Rev. Lett.* 19 (1967), pp. 1264–1266.
- [5] A. Salam. "Elementary Particle Theory: Relativistic Groups and Analyticity (Nobel Symposium No. 8), edited by N. Svartholm." 1968.
- [6] A. Collaboration. "Observation of a new particle in the search for the Standard Model Higgs boson with the ATLAS detector at the LHC." *Physics Letters B* 716.1 (2012), pp. 1–29.
- [7] C. Collaboration. "Observation of a new boson at a mass of 125 GeV with the CMS experiment at the LHC." *Physics Letters B* 716.1 (2012), pp. 30–61.
- [8] G. Hooft. "Renormalization of massless Yang-Mills fields." *Nuclear physics: B* 33.1 (1971), pp. 173–199.
- [9] C. Patrignani et al. "Review of Particle Physics." *Chin. Phys.* C40.10 (2016), p. 100001.
- [10] J. D. Bjorken and E. A. Paschos. "Inelastic electron-proton and γ -proton scattering and the structure of the nucleon." *Physical Review* 185.5 (1969), p. 1975.
- [11] D. J. Gross and F. Wilczek. "Ultraviolet behavior of non-abelian gauge theories." *Physical Review Letters* 30.26 (1973), p. 1343.
- [12] H. D. Politzer. "Reliable perturbative results for strong interactions?" *Physical Review Letters* 30.26 (1973), p. 1346.
- [13] Y. Nambu. "The confinement of quarks." *Scientific American* 235 (1976), pp. 48–61.
- [14] O. W. Greenberg. "Quarks: Resource Letter Q-1." *Am. J. Phys.* 50 (1982), pp. 1074–1089.
- [15] S. Dürr et al. "Ab Initio Determination of Light Hadron Masses." *Science* 322.5905 (2008), pp. 1224–1227.
- [16] S. Scherer. "Introduction to chiral perturbation theory." *Adv. Nucl. Phys.* 27 (2003), p. 277.
- [17] M. e. a. Ablikim. "Observation of a Charged Charmoniumlike Structure in $e^+e^- \rightarrow \pi^+\pi^-J/\psi$ at $\sqrt{s}=4.26$ GeV." *Phys. Rev. Lett.* 110 (25 2013), p. 252001.
- [18] T. Xiao et al. "Observation of the Charged Hadron $Z_c^\pm(3900)$ and Evidence for the Neutral $Z_c^0(3900)$ in $e^+e^- \rightarrow \pi\pi J/\psi$ at $\sqrt{s} = 4170$ MeV." *Phys. Lett.* B727 (2013), pp. 366–370.
- [19] M. e. a. Ablikim. "Observation of $e^+e^- \rightarrow \pi^0\pi^0 h_c$ and a Neutral Charmonium-like Structure $Z_c(4020)^0$." *Phys. Rev. Lett.* 113 (21 2014), p. 212002.

- [20] T. Weber. "High-Voltage Monolithic Active Pixel Sensors for the PANDA Luminosity Detector and Search for the Decay $e^+e^- \rightarrow \eta_c \eta \pi^+ \pi^-$ at Center of Mass Energies between 4.23 - 4.36 GeV at BES-III." PhD thesis. University of Mainz, 2016.
- [21] M. Gell-Mann. "The Eightfold Way: A Theory of strong interaction symmetry" (1961).
- [22] O. W. Greenberg. "Spin and unitary-spin independence in a paraquark model of baryons and mesons." *Physical Review Letters* 13.20 (1964), p. 598.
- [23] M. Michel. "Extraction of the scalar wave in $J/\psi \rightarrow \gamma \pi^0 \pi^0$ using the ComPWA Framework." PhD thesis. Mainz, 2016.
- [24] F. Halzen and A. D. Martin. "Quark & Leptons: An Introductory Course In Modern Particle Physics." 2008.
- [25] M. A. DeWitt. "The spectrum and decays of scalar mesons in the light-front quark model." PhD thesis. North Carolina State University, 2008.
- [26] C. Patrignani et al. "Review of Particle Physics - Note on scalar mesons below 2 GeV." *Chin. Phys.* C40.10 (2016), p. 100001.
- [27] J. R. Peláez. "From controversy to precision on the sigma meson: a review on the status of the non-ordinary $f_0(500)$ resonance." *Physics Reports* 658 (2016), pp. 1–111.
- [28] B. Moussallam. "Couplings of light I=0 scalar mesons to simple operators in the complex plane." *The European Physical Journal C* 71.12 (2011), p. 1814.
- [29] J. Weinstein and N. Isgur. " $K\bar{K}$." *Phys. Rev. D* 41 (7 1990), pp. 2236–2257.
- [30] F. E. Close, N. Isgur, and S. Kumano. "Scalar mesons in ϕ radiative decay: Their implications for spectroscopy and for studies of CP violation at ϕ factories." *Nuclear Physics B* 389.2 (1993), pp. 513–533.
- [31] R. J. Jaffe. "Multiquark hadrons. I. Phenomenology of $Q^2\bar{Q}^2$ mesons." *Phys. Rev. D* 15 (1 1977), pp. 267–280.
- [32] G. 't Hooft et al. "A Theory of Scalar Mesons." *Phys. Lett.* B662 (2008), pp. 424–430.
- [33] Y. Chen et al. "Glueball spectrum and matrix elements on anisotropic lattices." *Phys. Rev. D* 73 (2006), p. 014516.
- [34] C. Amsler and F. E. Close. "Is $f_0(1500)$ a scalar glueball?" *Phys. Rev. D* 53 (1996), pp. 295–311.
- [35] F. E. Close and A. Kirk. "Scalar glueball q anti- q mixing above 1-GeV and implications for lattice QCD." *Eur. Phys. J.* C21 (2001), pp. 531–543.
- [36] M. S. Chanowitz. "Chiral Suppression of Scalar-Glueball Decay." *Phys. Rev. Lett.* 95 (17 2005), p. 172001.
- [37] E. Eichten et al. "Charmonium: The Model." *Phys. Rev. D* 17 (1978), p. 3090.
- [38] S. Okubo. "Phi meson and unitary symmetry model." *Phys. Lett.* 5 (1963), pp. 165–168.
- [39] G. Breit and E. Wigner. "Capture of Slow Neutrons." *Phys. Rev.* 49 (1936), pp. 519–531.

- [40] S. K. Choi et al. "Observation of a narrow charmonium-like state in exclusive $B^\pm \rightarrow K^\pm \pi^+ \pi^- J/\psi$ decays." *Phys. Rev. Lett.* 91 (2003), p. 262001.
- [41] R. Aaij et al. "Determination of the X(3872) meson quantum numbers." *Phys. Rev. Lett.* 110 (2013), p. 222001.
- [42] R. Aaij et al. "Quantum numbers of the X(3872) state and orbital angular momentum in its $\rho^0 J/\psi$ decay." *Phys. Rev. D* 92.1 (2015), p. 011102.
- [43] N. A. Tornqvist. "Isospin breaking of the narrow charmonium state of Belle at 3872-MeV as a deuson." *Phys. Lett.* B590 (2004), pp. 209–215.
- [44] D. Gamermann and E. Oset. "Isospin breaking effects in the X(3872) resonance." *Phys. Rev. D* 80 (2009), p. 014003.
- [45] S. Prelovsek. "Hadron Spectroscopy." *PoS LATTICE2014* (2014), p. 015.
- [46] S. Prelovsek and L. Leskovec. "Evidence for X(3872) from DD^* scattering on the lattice." *Phys. Rev. Lett.* 111 (2013), p. 192001.
- [47] R. e. a. Aaij. "Amplitude analysis of $B^+ \rightarrow J/\psi \phi K^+$ decays." *Phys. Rev. D* 95 (1 2017), p. 012002.
- [48] D. M. Asner et al. "Physics at BES-III." *Int. J. Mod. Phys. A* 24 (2009), S1–794.
- [49] M. e. a. Ablikim. "Observation of a Charged Charmoniumlike Structure $Z_c(4020)$ and Search for the $Z_c(3900)$ in $e^+e^- \rightarrow \pi^+\pi^-h_c$." *Phys. Rev. Lett.* 111 (24 2013), p. 242001.
- [50] M. e. a. Ablikim. "Observation of $Z_c(3900)^0$ in $e^+e^- \rightarrow \pi^0\pi^0 J/\psi$." *Phys. Rev. Lett.* 115 (11 2015), p. 112003.
- [51] M. e. a. Ablikim. "Amplitude analysis of the $\pi^0\pi^0$ system produced in radiative J/ψ decays." *Phys. Rev. D* 92 (5 2015), p. 052003.
- [52] A. Denig. "Measurements of the Hadronic Cross Section and of Meson Transition Form Factors at BESIII for an improved Standard Model Prediction of $(g-2)_\mu$." *Nucl. Part. Phys. Proc.* 260 (2015), pp. 79–84.
- [53] F. Jegerlehner and A. Nyffeler. "The muon $g-2$." *Physics Reports* 477.1 (2009), pp. 1–110.
- [54] M. Ablikim et al. "Measurement of the proton form factor by studying $e^+e^- \rightarrow p\bar{p}$." *Phys. Rev. D* 91.11 (2015), p. 112004.
- [55] BESIII-Collaboration. "BESIII Detector Drawing."
- [56] FAIR. "FAIR Green Paper - The Modularized Start Version" (2009).
- [57] H. Gutbrod et al. "FAIR - Baseline Technical Report" (2006).
- [58] L. Groening et al. "The 70-MeV Proton Linac for the Facility for Antiproton and Ion Research FAIR." *Proceedings of the Linear Accelerator Conference LINAC2006* (2006), pp. 186–188.
- [59] N. Tahir et al. "Design of a Target for Antiproton Production at the Future FAIR Facility." *GSI Annual Report* (2007).
- [60] F. Nolden et al. "TDR - Collector Ring (CR)" (2008).
- [61] O. Kester et al. "Status of the FAIR Facility." *Proceedings of IPAC13, Shanghai, China* (2013).

- [62] C. Donlinski et al. "TDR - Recuperated Experimental Storage Ring (RESR)" (2008).
- [63] R. Maier et al. "The high energy storage ring (HESR)." *Proceedings of PAC2011, New York, USA* (2011).
- [64] Q. Hu et al. "A recoil detector for the measurement of antiproton-proton elastic scattering at angles close to 90° ." *Eur. Phys. J. A* 50.10 (2014), p. 156.
- [65] T. Stöhlker et al. "SPARC Collaboration: New Strategy for Storage Ring Physics at FAIR." *Hyperfine Interact.* 227 (2014), pp. 45–53.
- [66] H. Stockhorst et al. "Cooling Scenario for the HESR Complex." *AIP Conf. Proc.* 821 (2006), p. 190.
- [67] A. Lehrach et al. "Beam dynamics of the High-Energy Storage Ring (HESR) for FAIR." *Int.J.Mod.Phys.* E18 (2009), pp. 420–429.
- [68] A. Lehrach et al. "Beam performance and luminosity limitations in the high-energy storage ring (HESR)." *Nuc. Instrum. Meth. Phys. A* 561.2 (2006), pp. 289–296.
- [69] D. Welsch. "Investigation and Optimization of Transverse Non-Linear Beam Dynamics in the High-Energy Storage Ring HESR." PhD thesis. University of Bonn, 2009.
- [70] E. Wilson and E. J. Wilson. *An introduction to particle accelerators*. Clarendon Press, 2001.
- [71] D. Reistad et al. "Calculations on high-energy electron cooling in the HESR." *COOL 2007 Proceedings*. 2007.
- [72] J. Biri et al. "Beam position monitor electronics at the cooler synchrotron COSY Jülich." *Nuclear Science, IEEE Transactions on* 41.1 (1994), pp. 221–224.
- [73] W. Erni et al. "Physics Performance Report for PANDA: Strong Interaction Studies with Antiprotons." *arXiv preprint arXiv:0903.3905* (2009).
- [74] PANDA-Collaboration. "Letter of Intent for: PANDA" (2004).
- [75] PANDA-Collaboration. "PANDA Physics Webpage." URL: <https://panda.gsi.de/oldwww/framework/content/physics>.
- [76] M. F. M. Lutz et al. "Physics Performance Report for PANDA: Strong Interaction Studies with Antiprotons" (2009).
- [77] K. Goeke, M. V. Polyakov, and M. Vanderhaeghen. "Hard exclusive reactions and the structure of hadrons." *Prog. Part. Nucl. Phys.* 47 (2001), pp. 401–515.
- [78] A. V. Belitsky and A. V. Radyushkin. "Unraveling hadron structure with generalized parton distributions." *Phys. Rept.* 418 (2005), pp. 1–387.
- [79] M. Fritsch et al. "Technical Design Report for the PANDA Luminosity Detector." *to be published* (2015).
- [80] A. Khoukaz et al. "TDR for the PANDA Internal Targets" (2012).
- [81] A. Khoukaz et al. "Internal note" (2014).
- [82] O. Nordhage et al. "Tracked pellets: A Way to improve the efficiency of charmonium studies." *Nucl. Instrum. Meth.* A568 (2006), pp. 561–565.
- [83] M. Steinen. "The germanium detector array for the PANDA experiment." PhD thesis. University of Mainz, ongoing.

- [84] S. Bleser. "Production and decay of double Λ hypernuclei in \bar{p} -nucleus reactions." PhD thesis. University of Mainz, ongoing.
- [85] W. Erni et al. "Technical Design Report for the: PANDA Micro Vertex Detector." *arXiv preprint arXiv:1207.6581* (2012).
- [86] J. Boucher et al. "Technical Design Report for the: PANDA Straw Tube Tracker" (2012).
- [87] W. Erni et al. "Technical Design Report for PANDA Electromagnetic Calorimeter (EMC)." *arXiv preprint arXiv:0810.1216* (2008).
- [88] H. Xu et al. "Introduction to PANDA Data Acquisition System." *Physics Procedia* 37 (2012), pp. 1855–1860.
- [89] K. Korcyl et al. "Modeling event building architecture for the triggerless data acquisition system for PANDA experiment at the HESR facility at FAIR/GSI." *Journal of Physics: Conference Series*. Vol. 396. 1. IOP Publishing. 2012, p. 012027.
- [90] W. Herr and B. Muratori. "Concept of luminosity." *Proceedings of CERN Accelerator School, Zeuthen* (2003).
- [91] S. Weinberg. *The quantum theory of fields*. Vol. 1. Cambridge university press, 1996.
- [92] K. Zapfe et al. "Detailed studies of a high density polarized hydrogen gas target for storage rings." *Nucl. Instrum. Meth. A* 368 (1996), pp. 293–306.
- [93] H. Stein et al. "Determination of target thickness and luminosity from beam energy losses." *Physical Review Special Topics-Accelerators and Beams* 11.5 (2008), p. 052801.
- [94] S. Trokenheim et al. "A pp- luminosity monitor for Fermilab experiment E760." *Nucl. Instrum. Meth Phys. A* 355.2-3 (1995), pp. 308–319.
- [95] T. Armstrong et al. "Precision measurements of antiproton-proton forward elastic scattering parameters in the 3.7 to 6.2 GeV/c region." *Physics Letters B* 385.1-4 (1996), pp. 479–486.
- [96] A. Capella et al. "Dual parton model." *Physics Reports* 236.4-5 (1994), pp. 225–329.
- [97] A. Galoyan et al. "Parametrization of the anti-P P Elastic Scattering Differential Cross Section Between 2-GeV/c \leq P(lab) \leq 16-GeV/c." *arXiv preprint arXiv:0809.3804* (2008).
- [98] A. Karavdina. "Preparation for the accurate luminosity measurement by antiproton-proton elastic scattering and feasibility study for observation of h_c hadronic decay modes at the PANDA experiment." PhD thesis. Johannes-Gutenberg Universität Mainz, 2015.
- [99] I. Perić. "A novel monolithic pixelated particle detector implemented in high-voltage CMOS technology." *Nucl. Instrum. Meth. Phys. A* 582.3 (2007), pp. 876–885.
- [100] S. Spataro, P. collaboration, et al. "The PandaRoot framework for simulation, reconstruction and analysis." *Journal of Physics: Conference Series*. Vol. 331. 3. IOP Publishing. 2011, p. 032031.
- [101] S. Agostinelli et al. "GEANT4—a simulation toolkit." *Nucl. Instrum. Meth. Phys. A* 506.3 (2003), pp. 250–303.

- [102] R. Klasen. "Bestimmung der relativen Position der Siliziumpixel-Sensoren des PANDA Luminositätsdetektors." MA thesis. Johannes-Gutenberg Universität Mainz, 2014.
- [103] M. Michel. "Simulation des PANDA-Luminositätsmonitor-Systems." MA thesis. Johannes-Gutenberg Universität Mainz, 2010.
- [104] I. Abt et al. "CATS: a cellular automaton for tracking in silicon for the HERA-B vertex detector." *Nucl. Instrum. Meth. Phys. A* 489.1 (2002), pp. 389–405.
- [105] G. Lutz. "Optimum track fitting in the presence of multiple scattering." *Nucl. Instrum. Meth. Phys. A* 273.1 (1988), pp. 349–361.
- [106] V. Innocente, M. Maire, and E. Nagy. "GEANE: average tracking and error propagation package." *CERN Program Library W5013-E* (1991).
- [107] S. Pflüger. "Panda Luminosity Detector Fit Software." 2013. URL: <https://github.com/spflueger/LuminosityFit>.
- [108] "Wikipedia: bilinear interpolation." URL: https://en.wikipedia.org/wiki/Bilinear_interpolation.
- [109] S. Pflüger. "Model Framework." 2013. URL: <https://github.com/spflueger/ModelFramework>.
- [110] S. Baker and R. D. Cousins. "Clarification of the use of chi-square and likelihood functions in fits to histograms." *Nucl. Instrum. Meth. Phys.* 221.2 (1984), pp. 437–442.
- [111] W. Erni et al. "Technical Design Report for the PANDA Solenoid and Dipole Spectrometer Magnets" (2009).
- [112] A. Khoukaz et al. "Two-dimensional visualization of cluster beams by microchannel plates." *Nucl. Instrum. Meth. A* 735 (2014), pp. 12–18.
- [113] F. James and M. Roos. "Minuit - a system for function minimization and analysis of the parameter errors and correlations." *Computer Physics Communications* 10.6 (1975), pp. 343–367.
- [114] S. U. Chung. *Spin formalisms*. Tech. rep. Brookhaven Nat. Lab., 2014.
- [115] M. Jacob and G. Wick. "On the general theory of collisions for particles with spin." *Annals of Physics* 7.4 (1959), pp. 404–428.
- [116] R. Kutschke. "An angular distribution cookbook." *CLEO internal note* (1996).
- [117] T. F. Degener. "TARA — An object-oriented program for a partial wave analysis of sequential two body decays." *Computer Physics Communications* 118.1 (1999), pp. 34–48.
- [118] "ComPWA Webpage." URL: <https://github.com/ComPWA/ComPWA>.
- [119] "CLIPS Webpage." URL: <http://clipsrules.sourceforge.net>.
- [120] J. V. Bennett. "An amplitude analysis of the $\pi^0\pi^0$ system produced in radiative J/ψ decays." PhD thesis. Indiana University, 2014.
- [121] B. Kopf et al. "Partial wave analysis for $\bar{p}p$ and e^+e^- annihilation processes." *Hyperfine Interactions* 229.1 (2014), pp. 69–74.
- [122] J. R. Peláez. "From controversy to precision on the sigma meson: A review on the status of the non-ordinary resonance." *Physics Reports* 658 (2016), pp. 1–111.

- [123] J. Buon. "Beam phase space and emittance" (1992).
- [124] A. B. Pitka. " $D_0 - \bar{D}_0$ -Mischung im Zerfall $D_0 \rightarrow K_s \pi^+ \pi^-$ am PANDA-Experiment." PhD thesis. Gießen: Justus-Liebig-Universität, 2015.

Stefan Pflüger

✉ spfluege@gmail.com

Personal Info

Name Stefan Pflüger
 Date of Birth 2. May 1986
 Place of Birth Stuttgart, Germany

Education

- 1992–1996 **Elementary School Graduation**, *Ludwig-Uhland-Schule*, Leinfelden-Echterdingen, Germany.
 Elementary School
- 1996–1998 , *Immanuel-Kant-Gymnasium*, Leinfelden-Echterdingen, Germany.
 Secondary school
- 1998–2000 **Middle School Graduation**, *Todd Middle School - Spackenkill High School*, Poughkeepsie, NY, USA.
 Middle School & High School
- 2000–2005 **Secondary School Diploma**, *Immanuel-Kant-Gymnasium*, Leinfelden-Echterdingen, Germany.
 Secondary School
- 2005–2011 **Diploma in Physics**, *Technical University of Munich*, Munich, Germany.
 University
- 20012–2017 **PhD in Physics**, *Ruhr University Bochum/Helmholtz Institute Mainz*, Bochum/Mainz, Germany.
 University

Diploma Thesis (available on request)

title *Investigations of the Light Meson Spectrum with COMPASS using Final States containing Neutral Particles*
 supervisors Prof. Dr. Stephan Paul, Dr. Bernhard Ketzer, Dr. Boris Grube, Florian Haas

PhD Thesis (available on request)

title *Precise determination of the Luminosity with the PANDA-Luminosity Detector and Implementation of the helicity formalism for the ComPWA framework for an extraction of the scalar wave in the channel $J/\psi \rightarrow \pi^0 \pi^0 \gamma$*
 supervisors Prof. Miriam Fritsch

Experience

Vocational

- 2008–2009 **Software Engineer**, *DVC-München*, Munich, Germany.
Lead software engineer of a touch-screen based screening system, which was successfully operated at the TV film festivals at Cannes.
- 2009–2010 **Tutor**, *Technical University Munich*, Munich, Germany.
Leading a tutorial for students of the course “Experimental Physics 1”.
- 2010–2011 **Diploma Student**, *TUM Physics Department E18*, Munich, Germany & CERN (Geneva), CH.
Work at the COMPASS experiment at CERN during time of diploma thesis. Participation in multiple international workshops/meetings
- 2011–2011 **Research Assistant**, *TUM Physics Department E18*, Munich, Germany.
Various work on reconstructions improvements for data of the year 2008. Additionally some studies on neutral channel acceptance corrections using kaons.
- 2012–2017 **PhD Student**, *Helmholtz Insitute Mainz*, Mainz, Germany.
Precise determination of the Luminosity with the PANDA-Luminosity Detector and Implementation of the helicity formalism for the CompPWA framework for an extraction of the scalar wave in the channel $J/\psi \rightarrow \pi^0\pi^0\gamma$
- 2017– **Postdoctoral Research Assistant**, *Helmholtz Insitute Mainz / GSI*, Mainz, Germany.
Various work on the PANDA-Luminosity Detector software and the CompPWA framework.

Practical Internships

- 2003–2003 **Intern**, *Lasso GmbH*, Leinfelden-Echterdingen, Germany.
Stress Simulations using the Finite Element Method.
- 2005–2005 **Intern**, *Bodensee Wasser Versorgung eV*, Stuttgart, Germany.
Metal working and maintenance of the pipeline network.
- 2005–2005 **Intern**, *Frama GmbH*, Merklingen, Weil der Stadt, Germany.
Metal working using CNC milling machines and lasers.

Languages

German	<i>native</i>
English	<i>fluent</i>
Chinese	<i>elementary</i>
French	<i>elementary</i>

Computer Skills

Micro-controller	TI MSP430, Atmel	OS	Unix/Linux/Mac OS, Windows
Programming	C/C++, Java, Python, Bash	Database	SQL: MySQL, PostgreSQL
WWW Programming	Django, PHP, React, JavaScript, HTML, CSS		

Interests

-Sports (Soccer, Basketball, Biking,
Swimming, Snowboarding)
-Cooking

-Technology & Science
-Handcrafting

References (available on request)

Prof. Miriam Fritsch Full professor of the experimental physics chair (EP1) at the Ruhr University Bochum

Prof. Stephan Paul Full professor and head of the experimental physics chair (E18) at the Technical University of Munich

Richard Thes CEO DVC-Munich